

# **Theoretical Studies of OME-synthesis and Ammonia SCR in Zeolite Catalysis**

Zur Erlangung des akademischen Grades eines  
DOKTORS DER NATURWISSENSCHAFTEN  
(Dr. rer. nat)

von der KIT-Fakultät für Chemie und Biowissenschaften  
des Karlsruher Instituts für Technologie (KIT)

genehmigte  
DISSERTATION

von

**Tiago João Ferreira Gonçalves**

1. Referent: Prof. Dr. Felix Studt  
2. Referent: Priv.-Doz. Dr. Karin Fink  
Tag der mündlichen Prüfung: 20.04.2020



*When you have eliminated all which is impossible, then whatever remains, however improbable, must be the truth.*

Sir Arthur Conan Doyle



# Abstract

Emissions of global and local pollutants are a growing concern in terms of climate change and public health. Greenhouse gases are constituted by more than 80% of carbon dioxide. The use of oxymethylene dimethyl ethers (OMEs) as fuels or fuel additives in the transportation sector has the advantage of low CO<sub>2</sub> and nitrogen oxide (NO<sub>x</sub>) emissions without the need of adapting the engine. NO<sub>x</sub> emissions, that contribute to local pollution, can also be controlled by exhaust gas aftertreatment.

Density functional theory (DFT) is commonly used to model catalysts. Here, we test the accuracy of DFT, for acid-catalyzed reactions (methanol to olefins) and redox reactions (selective catalytic reduction) by comparing it with higher-level methods. Cluster models were used to model a cavity of the zeolite within the chabazite framework by extracting 46 tetrahedral atoms from the periodic structure. Mean absolute errors of DFT depend on the functional used, which vary between 10 and 40 kJ/mol for MTO reactions and between 20 and 50 kJ/mol for SCR reactions, when compared to DLPNO-CCSD(T) calculations.

In this thesis, we investigate reaction mechanisms for polyoxymethylene ether (POME) synthesis and selective catalytic reduction, an exhaust gas aftertreatment, of NO<sub>x</sub> gases to molecular nitrogen and water, by using theoretical methods such as density functional theory, Möller-Plesset second-order perturbation theory (MP2) and domain-based local pair natural orbitals coupled cluster with single, double and perturbative triple excitations (DLPNO-CCSD(T)). We found that for OME synthesis using the H-BEA zeolite, the rate-determining step is the trioxane ring-opening with a transition state of 60 kJ/mol, which indicates fast reaction rates. OME synthesis in homogeneous catalysis has been found to have a similar Gibbs free energy profile while the initiation step, that corresponds to OME protonation, is based on the catalyst's acidity. For the SCR, a reaction mechanism based on the fast SCR cycle and NO activation cycle is investigated using the Cu-SSZ-13 zeolite, where the rate-determining step is expected to be the NO oxidation, with transition states close to 300 kJ/mol on isolated copper sites. Structures in the NO activation cycle have shown multi-reference character and may require an evaluation using more refined methods such as complete active space (CAS) methods.



# Kurzfassung

Die Emissionen globaler und lokaler Schadstoffe sind ein wachsendes Problem im Hinblick auf den Klimawandel und die öffentliche Gesundheit. Treibhausgase bestehen zu mehr als 80% aus Kohlendioxid. Die Verwendung von Oxymethyldimethylethern (OMEs) als Kraftstoffe oder Kraftstoffadditive im Transportsektor hat den Vorteil geringerer  $\text{CO}_2$ - und Stickoxidemissionen ( $\text{NO}_x$ ) ohne dass der Motor angepasst werden muss.  $\text{NO}_x$ -Emissionen, die zur lokalen Verschmutzung beitragen, können auch durch Abgasnachbehandlung reduziert werden.

Auf Dichtefunktionaltheorie (DFT) basierende Berechnungen werden oft zur Modellierung von Katalysatoren verwendet. In dieser Arbeit habe ich die Genauigkeit von DFT für säurekatalysierte Reaktionen (Methanol zu Olefinen) und Redoxreaktionen (selektive katalytische Reduktion) in Bezug auf übergeordnete Methoden getestet. Clustermodelle wurden verwendet, um einen Hohlraum des Zeolithen innerhalb des Chabazitgerüsts zu modellieren, indem 46 tetraedrische Atome aus der periodischen Struktur extrahiert wurden. Die mittleren absoluten Fehler der DFT hängen von der verwendeten Funktion ab, die im Vergleich zu DLPNO-CCSD(T)-Berechnungen zwischen 10 und 40 kJ/mol für MTO-Reaktionen und zwischen 20 und 50 kJ/mol für SCR-Reaktionen variieren.

In dieser Arbeit habe ich die Reaktionsmechanismen für die Synthese von Polyoxymethylenether (POME) und die selektive katalytische Reduktion, die eine Abgasnachbehandlung ist, von  $\text{NO}_x$ -Gasen zu molekularem Stickstoff und Wasser unter Verwendung theoretischer Methoden wie der Dichtefunktionaltheorie, Möller-Plesset-Störungstheorie zweiter Ordnung (MP2) und "domain-based local pair natural orbital coupled cluster with single, double and perturbative triple excitations" (DLPNO-CCSD(T)) untersucht. Die Untersuchungen zeigten, dass für die OME-Synthese unter Verwendung des H-BEA-Zeolithen die Trioxanringöffnung mit einem Übergangszustand von 60 kJ/mol, der ratebestimmende Schritt ist. Es wurde gefunden, dass die OME-Synthese in der homogenen Katalyse während des Initiationsschritts ein ähnliches Gibbs-Profil der freien Energie aufweist, welches der OME-Protonierung entspricht und auf der Acidität des Katalysators basiert. Für die SCR wurden Reaktionsmechanismen untersucht, die auf dem schnellen SCR-Zyklus und dem NO-Aktivierungszyklus basieren. Hierzu habe ich den Cu-SSZ-13-Zeolith untersucht und gefunden, dass der geschwindigkeitsbestimmende Schritt die NO-Oxidation mit Übergangszuständen nahe 300 kJ/mol ist. Strukturen im NO-Aktivierungszyklus haben einen Multireferenzcharakter gezeigt und erfordern wahrscheinlich die Verwendung von CAS-Methoden (Complete Active Space).



# Contents

|   |            |
|---|------------|
| <b>Abstract</b> . . . . .   | <b>i</b>   |
| <b>Kurzfassung</b> . . . . .  | <b>iii</b> |
| <b>1 Introduction</b> . . . . .   | <b>1</b>   |
| 1.1 Challenges of CO <sub>2</sub> and NO <sub>x</sub> emissions . . . . .     | 1          |
| 1.2 Oxymethylene Ethers as Renewable Fuels . . . . .                          | 3          |
| 1.3 Exhaust Gas Aftertreatment . . . . .                                      | 5          |
| 1.4 Zeolites as Catalysts . . . . .   | 8          |
| 1.5 Scope of the Thesis . . . . .   | 9          |
| <b>2 Computational Chemistry of Molecules and Solids</b> . . . . .            | <b>11</b>  |
| 2.1 Rate and Equilibrium Constants . . . . .                                  | 12         |
| 2.2 Treatment of the Motion of the Nuclei . . . . .                           | 13         |
| 2.2.1 Born-Oppenheimer Approximation . . . . .                                | 13         |
| 2.2.2 Rigid Rotator and Harmonic Oscillator . . . . .                         | 14         |
| 2.3 Electronic Structure Theory . . . . .                                     | 15         |
| 2.3.1 Hartree-Fock Theory . . . . .   | 16         |
| 2.3.2 Møller-Plesset Perturbation Theory . . . . .                            | 18         |
| 2.3.3 Coupled Cluster Theory . . . . .  | 19         |
| 2.3.4 Density Functional Theory . . . . .                                     | 21         |
| 2.3.5 Localized Basis sets . . . . .  | 24         |
| 2.3.6 Approximations . . . . .  | 25         |
| 2.4 Description of Solvation . . . . .  | 26         |
| 2.4.1 Implicit Solvation . . . . .  | 26         |
| 2.4.2 Explicit Solvation . . . . .  | 27         |
| <b>3 Accuracy of Density Functional Theory in Zeolite Catalysis</b> . . . . . | <b>29</b>  |
| 3.1 Introduction . . . . .  | 29         |
| 3.2 Methods . . . . .   | 29         |

---

|          |   |             |
|----------|---|-------------|
| 3.3      | Cluster models . . . . .  | 30          |
| 3.4      | Results . . . . .   | 32          |
| 3.4.1    | Methanol to Olefins . . . . .   | 32          |
| 3.4.2    | Selective Catalytic Reduction . . . . .   | 37          |
| 3.5      | Conclusion . . . . .  | 41          |
| <b>4</b> | <b>Selective Catalytic Reduction of NO<sub>x</sub> by Ammonia using Cu-SSZ-13 . . . . .</b> | <b>43</b>   |
| 4.1      | Introduction . . . . .  | 43          |
| 4.2      | Methods . . . . .   | 44          |
| 4.3      | Results . . . . .   | 45          |
| 4.4      | Conclusion . . . . .  | 50          |
| <b>5</b> | <b>Synthesis of Oxymethylene Dimethyl Ethers using H-BEA . . . . .</b>                      | <b>51</b>   |
| 5.1      | Introduction . . . . .  | 51          |
| 5.2      | Methods . . . . .   | 52          |
| 5.3      | Active Site and Solvation Models . . . . .  | 53          |
| 5.3.1    | Active Site . . . . .   | 53          |
| 5.3.2    | Explicit Solvation and Hydrogen-bonding . . . . .   | 54          |
| 5.3.3    | Thermodynamics . . . . .  | 57          |
| 5.4      | Results . . . . .   | 58          |
| 5.5      | Conclusion . . . . .  | 62          |
| <b>6</b> | <b>OME Synthesis through Homogeneous Acid Catalysis . . . . .</b>                           | <b>63</b>   |
| 6.1      | Introduction . . . . .  | 63          |
| 6.2      | Methods . . . . .   | 64          |
| 6.3      | Results . . . . .   | 65          |
| 6.4      | Conclusion . . . . .  | 71          |
| <b>7</b> | <b>Final conclusion and outlook . . . . .</b>   | <b>73</b>   |
|          | <b>References . . . . .</b>   | <b>75</b>   |
|          | <b>Appendix . . . . .</b>   | <b>viii</b> |
| <b>A</b> | <b>Accuracy of Density Functional Theory in Zeolite Catalysis . . . . .</b>                 | <b>ix</b>   |
| A.1      | Details on Convergence Tests . . . . .  | ix          |
| A.1.1    | MTO . . . . .   | ix          |
| A.1.2    | SCR . . . . .   | xiv         |
| A.2      | Tables and Figures . . . . .  | xx          |

---

|   |               |
|---|---------------|
| <b>B Selective Catalytic Reduction of NO<sub>x</sub> by Ammonia using Cu-SSZ-13</b> | <b>xxix</b>   |
| B.1 Tables and Figures  | xxix          |
| <b>C Synthesis of Oxymethylene Dimethyl Ethers using H-BEA</b>                      | <b>xxxiii</b> |
| C.1 Gas phase free energy diagrams  | xxxiii        |
| C.2 Tables and Figures  | xxxiv         |
| <b>D OME Synthesis through Homogeneous Acid Catalysis</b>                           | <b>xxxix</b>  |
| D.1 Accuracy of DFT   | xxxix         |
| D.2 Solvent corrections   | xl            |
| D.2.1 Calculation of Protonation Energies with Solvation                            | xl            |
| D.2.2 Solvent parameterizations in the SMD model                                    | xli           |
| D.3 Tables and Figures  | xlii          |
| <b>Acknowledgements</b>   | <b>xlix</b>   |
| <b>Acronyms</b>   | <b>li</b>     |
| <b>List of Publications</b>   | <b>liii</b>   |
| <b>Eidesstattliche Erklärung</b>  | <b>lv</b>     |



# Chapter 1

## Introduction

### 1.1 Challenges of CO<sub>2</sub> and NO<sub>x</sub> emissions

Air pollution is a dominant concern as it plays a relevant role both in climate change and human health. [1–12] With the growth of the population, arises the growth of energy consumption for domestic use, for the transportation sector and industry, along with the growth of CO<sub>2</sub> emissions. [6–8] Levels of carbon dioxide in the atmosphere change cyclically based on Earth’s glacial and interglacial periods. However, recent studies show that the levels of CO<sub>2</sub> in the atmosphere were never as high as the values of today in 8 glacial periods (800,000 years), [9–12] which is shown in Figures 1.1 and 1.2.

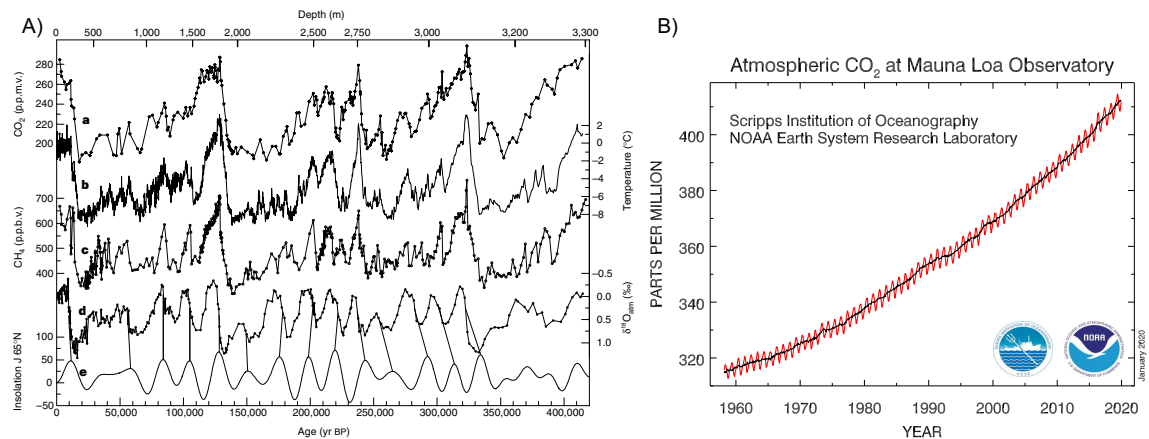


**Figure 1.1:** A) Vostok time series and insolation. Series with respect to time (GT4 timescale for ice on the lower axis) of: a) CO<sub>2</sub>, each point is approximately separated by 2k years, with the first point showing CO<sub>2</sub> levels around 2000 years ago; b) isotopic temperature (based on isotopic content  $\delta D$  or  $\delta^{18}O$  which is linearly related to the temperature above the inversion level); c) CH<sub>4</sub>; d)  $\delta^{18}O_{atm}$ ; and e) mid-June insolation at 65° N (in  $W m^{-2}$ ). [10, 13] Figure provided by [10]. Reprinted by permission from Springer Nature: Nature, 'Climate and atmospheric history of the past 420,000 years from the Vostok ice core, Antarctica', Petit, J. R. et al. Copyright (1999), Springer Nature. B) Mean carbon dioxide measured at Mauna Loa Observatory, Hawaii. The red lines show the monthly mean values, centered on the middle of each month, while the black lines show the same, after correction for the average seasonal cycle. Image provided by NOAA ESRL Global Monitoring Division, Boulder, Colorado, USA (<http://esrl.noaa.gov/gmd/>). [11]

Figure 1.1 A), shows the amount of carbon dioxide present in the atmosphere in the past 400,000 years while B) shows the amount of CO<sub>2</sub> in the past few decades until 2020. The combination of data from Figures 1.1 A) and B), [10,11] along with data from ref. [9] were used to reproduce the graph from Figure 1.2, [12] in which oscillations of carbon dioxide from the past 800,000 years until the current date are observed.

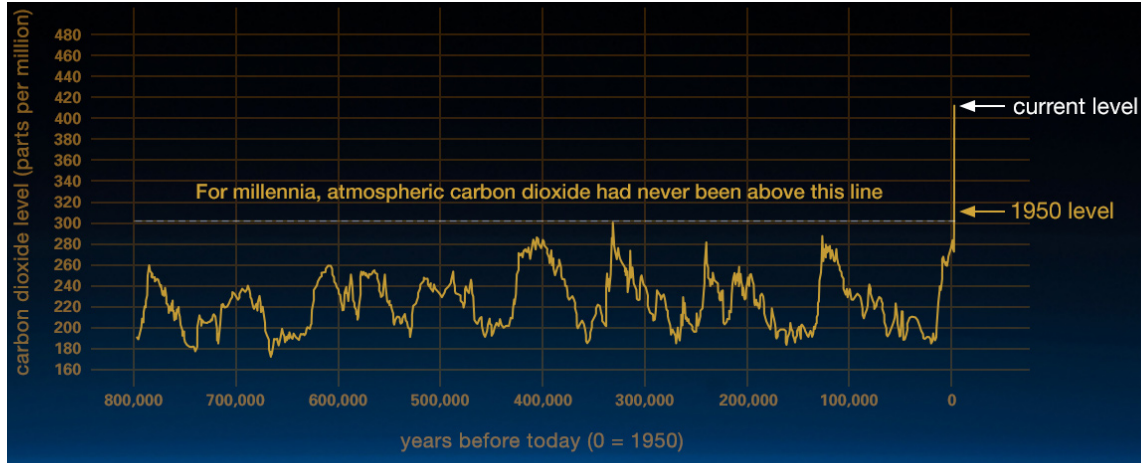


**Figure 1.2:** Carbon dioxide in ppmv in the past 800,000 years. This graph is based on the comparison of atmospheric samples contained in ice cores and more recent direct measurements. [9–12] Figure provided by NASA [12].

During ice ages and warmer interglacial periods, CO<sub>2</sub> levels have been fluctuating between 200 and 280 parts per million. However, the carbon dioxide levels are above 300 ppm since 1950 and keep rising until today, reaching 420 ppm. This implies that the rise of atmospheric CO<sub>2</sub> is related to the Industrial Revolution and has a constant relationship with fossil-fuel burning. [12]

Carbon dioxide is a primary greenhouse gas, representing around 82% amongst the global pollutants, which are methane (10%), nitrous acid (6%) and fluorinated gases (2%). [14] The relation of CO<sub>2</sub>, CH<sub>4</sub> and insolation levels with the difference in temperature is depicted in Figure 1.1 A), in which a shift of around 80 ppm of CO<sub>2</sub>, 0.7 ppm of CH<sub>4</sub> and 100 W m<sup>-2</sup> of insolation triggers a difference in temperature of more than 10 °C. This means that CO<sub>2</sub> emissions need to be reduced to prevent temperature rising that may lead to catastrophic events.

The other source of air pollution is local pollutants such as particulate matter and nitrogen oxides that form smog and can trigger severe health effects on the human population. [1–5] NO<sub>2</sub> for instance, under exposures of 2.0 – 5.0 ppm, is responsible for problems such as coughing and wheezing, headache, dyspnea, chest pain, diaphoresis, fever, bronchospasm and pulmonary edema. [4] Diesel engines are one of the main sources of nitrogen oxide emissions. [2]

Controlling CO<sub>2</sub> and NO<sub>x</sub> emissions from diesel engines is one way to mitigate the progress of climate decay and to attenuate the number health issues of the world’s population from harmful and toxic gases. Figure 1.3 depicts the trend in NO<sub>x</sub> emissions by different continents. Emissions from North America and Europe have been steady since the 80s. After the 90s there is an apparent decrease in NO<sub>x</sub> emissions from Europe likely due to stringent emission controls in Western European countries. [3]

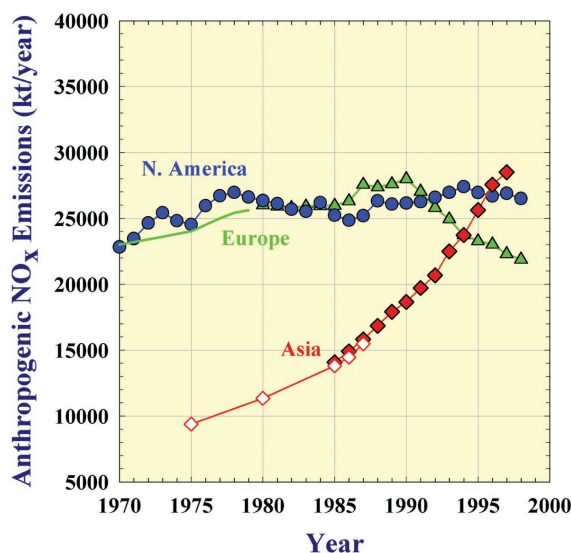


**Figure 1.3:** Changes in anthropogenic NO<sub>x</sub> emissions over North America (United States and Canada) [15], Europe (including Russia and the near and middle East) [16], and Asia (East, Southeast, and South Asia) in solid squares [17] and open squares [18]. The extrapolated line for Europe in the 1970s is based on OECD data. [19] Figure taken from ref. [3]. From Akimoto, H. (2003). Global air quality and pollution. *Science*, 302(5651), 1716-1719. Reprinted with permission from AAAS.

In Sections 1.2 and 1.3 alternatives to control CO<sub>2</sub> and NO<sub>x</sub> emissions will be discussed. Section 1.2 will focus on CO<sub>2</sub> and soot control through *Oxymethylene Dimethyl Ethers* or OMEs, which are synthetic fuels or fuel additives that can potentially be synthesized from biomass or CO<sub>2</sub>, while Section 1.3 will target *exhaust gas aftertreatment*, more specifically, the Selective Catalytic Reduction using ammonia, in which a catalyst is used to convert NO<sub>x</sub> into molecular nitrogen and water.

## 1.2 Oxymethylene Ethers as Renewable Fuels

Oxymethylene ethers (OMEs) are oxygen-containing synthetic fuels that follow the formula depicted in Equation 1.2.1.



Figure 1.4 is an example of OME<sub>n</sub> with a single formaldehyde unit ( $n = 1$ ).

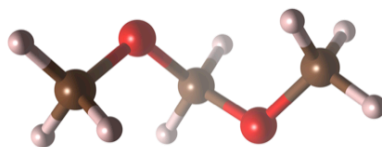


**Figure 1.4:** Illustration of an OME<sub>1</sub> molecule. Color scheme: C – Brown; H – White; O – Red.

The absence of carbon-carbon bonds along with the higher oxygen content lead to a complete

combustion of fuel significantly reducing the soot and particulate-matter formation, reduction in fuel consumption and more power. [20] OMEs as fuel or fuel additives also have the advantage of having lower peak temperatures during combustion. By having lower temperatures, less  $\text{NO}_x$  is formed and exhaust gas recirculation can be done at higher rates.

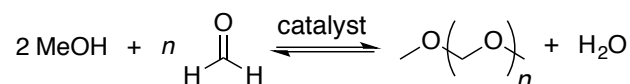
OMEs are also non-toxic and are not limited to high vapor pressures at ambient temperatures, which is an improvement when compared to MeOH or dimethyl ether (DME). [21] Formaldehyde (FA) and equivalents thereof are the building blocks to form  $\text{OME}_n$ .

Different synthesis routes for OME oligomerization were investigated before. [22–25] One route consists of the reaction of methanol with formaldehyde, in which 2 mol of MeOH along with  $n$  mol of formaldehyde leads to the formation of  $\text{OME}_n$  and water (Scheme 1.1). This leads to accumulation of water in which hydroxyl groups may react to form hemiformals and glycols that are recycled. An alternative to the use of methanol is to use  $\text{OME}_1$  with  $n/3$  mol of trioxane or  $n$  mol of formaldehyde instead (Scheme 1.2), which leads to the production of  $\text{OME}_n$  without the formation of water. [23, 25, 26]

---

**Scheme 1.1** OME Synthesis from FA and methanol.

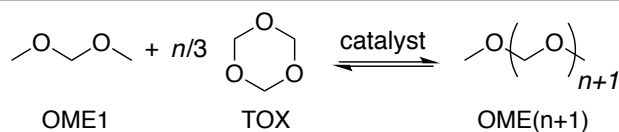
---




---

**Scheme 1.2** Synthesis of OMEs from TOX and  $\text{OME}_1$ .

---



Studies found that for the latter route in OME synthesis, the selectivity in solution follows a Schulz-Flory distribution, which indicates that there is a relevant amount of OME molecules within the desired chain length. [25] Also, separation of  $\text{OME}_{3-5}$  from the product mixtures can be carried out via distillation.  $\text{OME}_{1-2}$ ,  $\text{OME}_{6-10}$  and trioxane can be completely recycled and fed back to the OME synthesis. [25]

Different catalysts such as different ion exchange resins and zeolites were tested for the oligomerization process with BEA25 excelling in terms of activity. [25, 27] Using zeolites (aluminosilicate structures with pores) as catalysts may hold an advantage in terms of activity due to their array of textural properties and acidity (which is related to Si/Al ratio), they also limit the formation of byproducts such as hemiformals and glycols when the starting materials are dried. [25, 26] The surface area and pore size, for instances, have impact on the activity of zeolites due to small channels that induce transport limitations if large OME molecules are involved, specially in solution. Studies suggest that when using H-ZSM-5, accessibility to the acid sites in the micropores is important. A way to circumvent this problem is to insert intracrystalline mesopores, [28, 29] through desilication by alkaline treatment, which will improve its diffusion properties, boosting the catalytic activity significantly. [30] Good activity and selectivity towards  $\text{OME}_{3-5}$  was also found for H-BEA, without the need of desilication, as it presents larger pores compared to H-ZSM-5. [25]

OME synthesis can also proceed via homogeneous catalysis, in which the reaction is dependent on the acid (H-BEA, HCl, amongst others) to protonate one  $\text{OME}_1$  molecule that acts as a catalyst

for the oligomerization process.

### 1.3 Exhaust Gas Aftertreatment

Fuel combustion often leads to emissions of harmful gases that have impact on human health. [4] Despite certain additives such as oxymethylene ethers (Section 1.2) reducing local pollutants (e.g.  $\text{NO}_x$  and soot), there is still non-negligible formation of these particular byproducts due to high-temperature combustion in diesel engines. [31] These emissions can be controlled using various exhaust gas aftertreatment procedures.

$\text{NO}_x$ , a mixture which is typically 95 % of  $\text{NO}$  and 5 % of  $\text{NO}_2$  is generally a product of combustion processes by the oxidation of atmospheric nitrogen at very high temperatures and follow equations 1.3.1 and 1.3.2. [32]



The removal of  $\text{NO}_x$  requires an exhaust gas aftertreatment. [33] This thesis will focus on the *Selective Catalytic Reduction* (SCR) for this process, where ammonia is used as a hydrogen donor to form molecular nitrogen and water through a stoichiometric reaction that is shown in Equation 1.3.3, which is defined as the *Standard SCR*.



$\text{NH}_3$ -SCR has shown to be effective compared to conventional three-way catalysts when the engine is operated under highly oxidizing conditions, which is required to achieve better fuel efficiency and to convert  $\text{NO}_x$  into  $\text{N}_2$  (since the standard SCR, Equation 1.3.3, depends on the oxidation of  $\text{NO}$ ). [34] It has also been observed that the use of  $\text{NH}_3$  as a selective reductant was preferred when compared to methane, a mixture of light hydrocarbons, kerosene vapors and hydrogen. [33, 35]

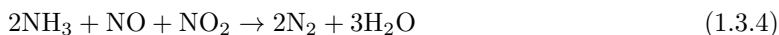
The exhaust temperature in most diesel engines range between 373 and 673 K (depending on a number of factors such as speed, slope and state of the terrain) rarely exceeding 520 K [36] which is within the low-temperature regime for SCR. This poses a problem as catalysts need to function on a broader temperature window to avoid reheating the exhaust gas.

Copper and iron exchanged zeolites have become increasingly attractive due to their excellent catalytic activity, selectivity towards  $\text{NO}_x$  reduction and hydrothermal stability, [34, 37–58] which broadens the temperature window under lean conditions for SCR reactions. [34] However, high end temperatures ( $> 920$  K) may lead to structural collapse of the catalyst and outmigration of the active component followed by its agglomeration. At around 770 K, if Cu-exchanged zeolites are used, it is expected that dealumination from zeolites occurs. This will lead to an irreversible loss of activity from the catalyst. [33, 59]

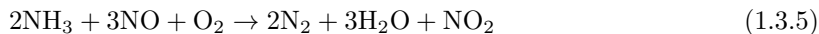
Specifically, Cu-SSZ-13 has shown to have high activity and selectivity towards  $\text{N}_2$ , with  $\text{NO}_x$  conversions of 90–100% over a wide temperature range, due to its small porosity, which prevents hydrocarbons to react with active sites. However, it also poses a problem when ammonia and sulfur react to form ammonium sulfate and ammonium bisulfate, which potentially clogs the catalyst, blocking active sites and gas flow paths. [60] The formation of byproducts such as  $\text{N}_2\text{O}$  has also

been found to be lower compared to Cu-ZSM5 and Cu-BEA zeolites. [34] Copper exchanged zeolites have the advantage of having a redox active copper atom in the active site which has been shown to be relevant for SCR reactions. [41–53]

The reaction cycle studied here (Chapters 3 and 4) is based on the *standard SCR* (Equation 1.3.3), which is evaluated as a combination of two cycles with different catalytic rates. The *fast SCR* (Equation 1.3.4) involves a direct nitrogen dioxide consumption, which above 473 K is at least 10 times faster than the standard SCR.



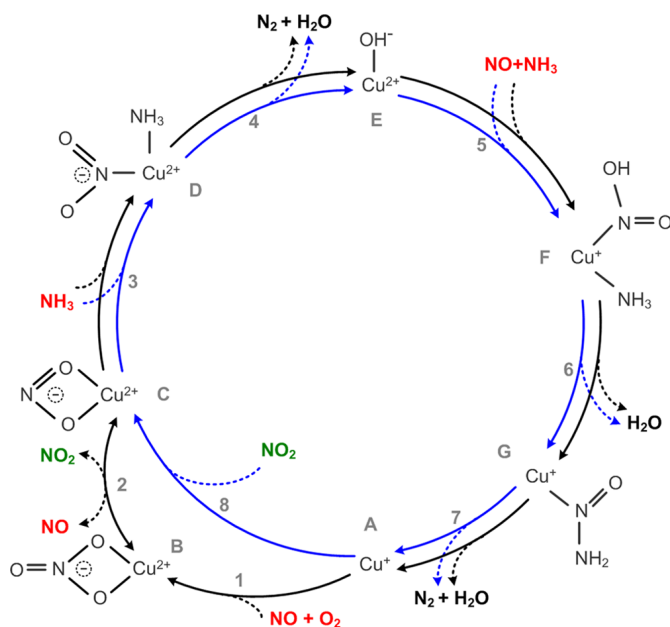
The issue is that  $\text{NO}_2$  is available in very low quantities when compared to  $\text{NO}$ . For that reason  $\text{NO}$  has to be oxidized in a set of reactions that involve oxygen splitting, this is called *NO activation cycle* (equation 1.3.5).



Due to the standard SCR being dependent on the amounts of nitrogen dioxide present in the gas mixture, reaction rates are limited by the slowest process, which is the oxidation of nitric oxide. Studies found that despite the possibility that the fast SCR takes place on isolated copper sites in zeolite catalysts, the oxidation process, which involves the splitting of molecular oxygen, is prohibitive under such conditions. [61] Janssens et al. proposed a consistent reaction scheme (1.3) based on Equations 1.3.4 and 1.3.5, where a single copper site is used to catalytically convert  $\text{NO}_x$  and  $\text{NH}_3$  into  $\text{N}_2$ , water and potentially more  $\text{NO}_2$ . [45] In their study, it was determined that the rate-determining step is indeed the oxygen splitting in the  $\text{NO}$  activation cycle.

This work is the first more comprehensive study of the reaction mechanism of  $\text{NO}_x$  reduction and also employs the first theoretical studies of the catalytic  $\text{NH}_3$ -SCR processes with Cu-SSZ-13 at a molecular level. The reaction scheme, however, still lacks fundamental details. Some of the steps in the study seem to be instantaneous (simultaneous adsorption of  $\text{NO}$  and  $\text{NH}_3$ , or simultaneous release of  $\text{N}_2$  and  $\text{H}_2\text{O}$ ), while in fact reactions occur in multiple elementary steps, and no barriers are investigated in the fast SCR as they are assumed to be very low. The only relevant barriers investigated are the oxygen splitting and nitrate reduction from the  $\text{NO}$  activation cycle. The other issue is that DFT with PBE-D3 functional is used to study this mechanism, which has relatively high errors. In Chapter 3 a comparison between DFT with different functionals and higher-level methods for reactions based on Scheme 1.3 is made, and in Chapter 4 a complete study of  $\text{NH}_3$ -SCR is done.

**Scheme 1.3** Proposed reaction mechanism for the SCR reaction in a Cu-zeolite. The fast SCR cycle is shown in blue, and the NO activation cycle in black. Reactants are indicated in red, products in black and the  $\text{NO}_2$  intermediate in green. Reprinted with permission from Janssens, T. V. et al. (2015). A consistent reaction scheme for the selective catalytic reduction of nitrogen oxides with ammonia. *ACS Catalysis*, 5(5), 2832-2845. Copyright (2015) American Chemical Society.



Dynamic multinuclear sites formed from copper complexes were proposed by Paolucci et al. [47] as an alternative approach to split oxygen.

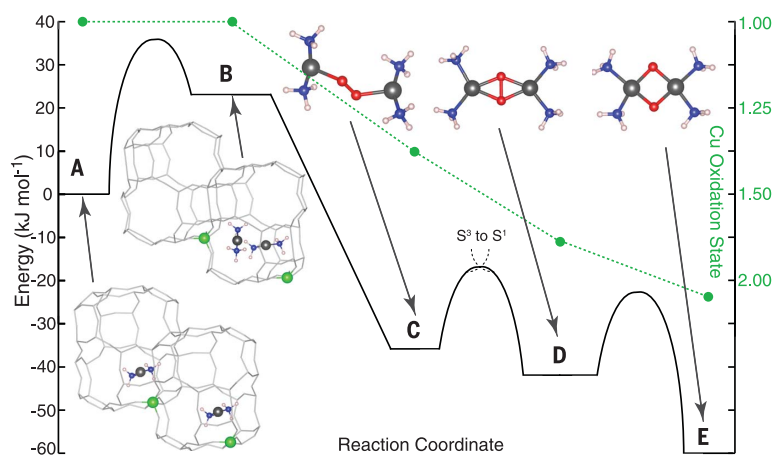
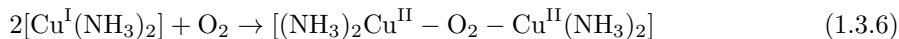


**Figure 1.5:** Simulation of  $\text{O}_2$  adsorption and oxidation of two  $\text{Cu}^{\text{I}}(\text{NH}_3)_2$  equivalents. DFT-computed energy landscape is shown for the diffusion of  $\text{Cu}^{\text{I}}(\text{NH}_3)_2$  through an 8-MR CHA window into an adjacent cage and subsequent bimolecular reaction with  $\text{O}_2$ . Color scheme: Cu – Gray; Al – Green; O – Red; N – Blue; H – White. From Paolucci, C. et al. (2017). Dynamic multinuclear sites formed by mobilized copper ions in  $\text{NO}_x$  selective catalytic reduction. *Science*, 357(6354), 898-903. Reprinted with permission from AAAS.

This suggestion has been shown to have considerably lower reaction barriers in this part of the mechanism. [45,47,61] It was found that copper atoms are able to detach from the catalyst, moving freely within the cavities and eventually interact with ammonia and other copper atoms creating complexes as shown in Figure 1.5 (also depicted in Equation 1.3.6), with an energy barrier of around 30 kJ/mol.



Note that reproducing copper diffusion with cluster models (description in Section 1.4) and higher-level theory may be challenging, because the model of the zeolite is now limited to the size of the cluster and bigger clusters lead to computationally demanding calculations.

Another alternative is to consider active sites in the catalyst close to each other so that both have NO adsorbed and are simultaneously oxidized consuming one molecule of oxygen, this leads to a low energy barrier (close to 60 kJ/mol). The same approach with clean copper atoms instead, leads to one oxygen atom adsorbed to each of the copper atoms, which has a significantly higher energy barrier (around 200 kJ/mol). The barrier height is comparable to the splitting of oxygen using an isolated NO-adsorbed Cu atom (also around 200 kJ/mol), where a nitrate is formed as an intermediate that is an extremely stable species. [45,61,62]

Increasing the Cu loading is thus thought to enhance the activity of the catalyst, and can be explained by the promotion of the formation of more Cu dimers. [45]

## 1.4 Zeolites as Catalysts

Zeolites are porous aluminosilicate minerals that are composed of silicon tetrahedral atoms that are connected through the oxygen atoms. Substitution of silica with alumina leads to a negative charge. If that is compensated by a proton, an acid site is created. Other substitutions comprise  $\text{Na}^+$ , or transition metals such as  $\text{Cu}^+$ .

The properties of a zeolite play an important role in terms of its catalytic effects. The pore size and shape from a framework has influence on the selectivity, in which large molecules have transport limitations as reactants or products may not be formed at all. [63,64] The Si/Al ratio is important in terms of the catalyst's activity, where more aluminum atoms lead to more acid sites within the framework, which may increase its reactivity. [65–69] The Si/Al ratio may also influence the zeolite's morphology, crystal size and surface area as well as hydrophilic/hydrophobic properties, which may also be relevant for certain processes. [64–66,69] The catalytic cracking to light olefins is one example of the large dependence on the shape and size of pores in the cracking activity of Brønsted acid sites. [70–72]

From a theoretical perspective, modeling a zeolite framework and the active sites is relevant to predict the stability of intermediates and reaction barriers. Despite the specific location of the active site, where the reaction occurs, being experimentally very hard to determine, a number of symmetry-inequivalent points per unit cell can be studied theoretically, depending on the framework. Chabazite for instances, contains 36 symmetry equivalent T-sites, which means that any atom in a unit cell (containing 36 tetrahedra) can be picked to model a reaction as it will lead to the same result. For frameworks that contain multiple symmetry inequivalent T-sites, all have to be considered and compared to evaluate which one is more reactive, so that that site is used consistently for the entire study. Also, for each T-site, there is 4 symmetry inequivalent oxygen atoms that also need to be compared. In principle, having  $n$  symmetry-inequivalent T-sites will

lead to  $4 \times n$  different active sites to test. Despite the reaction taking place in an active site, modeling the vicinity of the zeolite is also important due to long-range interactions between the zeolite framework and reactants/products and possible steric effects. Periodic cells and cluster models [73–77] are two methods to model zeolites.

## 1.5 Scope of the Thesis

This thesis aims at investigating the reaction mechanism of OME synthesis using different synthesis routes with quantum chemical calculations. The second reaction that is investigated is the selective catalytic reduction of  $\text{NO}_x$  using ammonia over Cu-SSZ-13 as the catalyst. Since these reactions are challenging to study from a computational point of view, the accuracy of the most commonly used quantum mechanical methods (DFT) is addressed and alternatives are discussed.

The contents of this thesis are divided into four different chapters, dealing with (1) the accuracy of different methods that were used throughout the thesis, (2) a detailed investigation of how Cu-SSZ-13 facilitates the catalytic reduction of  $\text{NO}_x$  with ammonia, as well as (3) a computational study of the reaction mechanism of OME synthesis employing acidic BEA and (4) through a homogeneous acid catalyst.

- Chapter 3, Accuracy of Density Functional Theory in Zeolite Catalysis: In this chapter, the accuracy of one of the most commonly used theoretical quantum mechanical tools in catalysis is discussed. A meticulous comparison between DFT and higher-level methods is performed for reaction energies and barriers of methanol to olefin (MTO) processes, as well as for reaction energies of SCR. The hierarchical cluster approach is used to accurately describe the reactivity of the active site on smaller cluster models with higher-level methods and to extrapolate that reactivity to the periodic model.
- Chapter 4, Selective Catalytic Reduction of  $\text{NO}_x$  by Ammonia using Cu-SSZ-13: Here, a detailed mechanism of the SCR is evaluated. The fast SCR and oxidation of nitric oxide at the low temperature regime (around 473 K) are the main cycles studied.
- Chapter 5, Synthesis of Oxymethylene Dimethyl Ethers using H-BEA: The oligomerization of formaldehyde units is studied using H-BEA as the catalyst, with TOX/FA and OME1 as the reactants. Solvation corrections are treated by explicitly including OME1 molecules in different possible orientations, as implicit models often fail to describe vdW-based solvent-solute interactions and also fail to construct a consistent solvent-solute cavity for zeolites.
- Chapter 6, OME Synthesis through Homogeneous Acid Catalysis: A similar reaction mechanism is studied in comparison with the one evaluated for H-BEA. A protonated OME1 acts as a catalyst to perform the initiation reaction to form the resting state structure, which is now a cationic methoxymethylated OME1 molecule. For the solvent treatment, the implicit “SMD” model is used as zeolites are no longer involved in the reaction process, which facilitates the solute-solvent cavity construction. Also, this model is more accurate than standard polarizable continuum models in treating solvent interactions as it is more empirical. A set of parameters for each solvent from the SMD-database is included to accurately treat solvent-solute interactions.



## Chapter 2

# Computational Chemistry of Molecules and Solids

Catalysts are important in chemical industry due to the ability of lowering reaction barriers of slow processes by interacting with reactants as Figure 2.1 illustrates. An accurate description of systems at the molecular level is essential to predict catalytic performance.

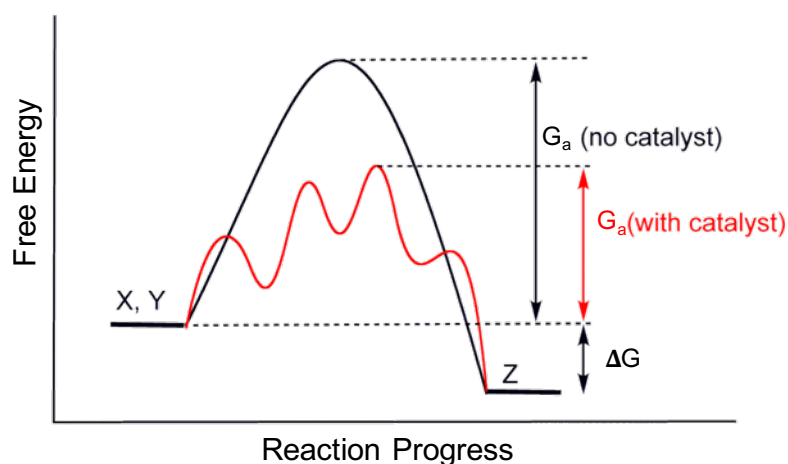


**Figure 2.1:** Activation free energies of the formation of product “Z” from reactants “X” and “Y” without a catalyst (black line) and with a catalyst (red line).  $\Delta G$  is the difference in Gibbs free energy of the conversion of reactants into products.

Thermodynamics determines the direction of chemical reactions and predicts the quantities of reactants and products in equilibrium, through equilibrium constants. These equilibrium constants depend on the difference of the Gibbs free energies between reactants and products. The Gibbs free energy is defined in Equation 2.0.1.

$$G = H - T\Delta S \quad (2.0.1)$$

Where  $T$ ,  $H$  and  $S$  are the temperature of the system, enthalpy and entropy respectively. While thermodynamics describes chemical reactions towards equilibrium, it provides no information about

---

This chapter is based on refs. [78–83]

its rate. With kinetics, it is possible to calculate reaction rates based on the rate constant of elementary processes.

## 2.1 Rate and Equilibrium Constants

In Transition State Theory (TST), the phase space is divided into two distinct regions. The reactant region and the product region. In Harmonic Transition State Theory (HTST), the transition state is defined as the maximum of the minimum energy pathway on the Potential Energy Surface (PES), a first-order saddle point. The rate constant for an elementary process, under the assumption that the reactant follows a specific pathway, determines the reaction rate [79] and is given by

$$k = \frac{k_B T}{h} e^{-\Delta G^\ddagger/k_B T} \quad (2.1.1)$$

Where  $\Delta G^\ddagger$  is the Gibbs free energy of the difference between the transition state and the reactant. When the PES is reasonably well represented by a second-order Taylor expansion, the Harmonic Transition State Theory (HTST) is applicable. The Gibbs free energy is obtained using the relation in Equation 2.0.1, where entropy and enthalpy are calculated using the rigid rotator/free translator and harmonic oscillator approximation (Sections 2.2.2), at temperature  $T$ .

Finding transition states (first-order saddle points) is often a difficult task. Several methods have been used in this work. Two examples of transition-state optimization methods are described below.

- *Nudged Elastic Band* is a technique that involves optimizing several images (sum of the energies of the images are minimized) usually created with an interpolation technique using the initial and final structures. Images are evenly distributed along the reaction path with a spring constant. [84]
- *Automated Relaxed Potential Energy Scans* consist of constrained optimizations where differences of bonds between atoms  $ij$  and  $jk$ ,  $b_{ijk} = |\mathbf{x}_{ij}| - |\mathbf{x}_{jk}|$  are kept fixed in each optimization cycle. An  $S_N2$  reaction  $AB + C \rightarrow A + BC$  would have a constraint defined as  $|\mathbf{x}_{AB}| - |\mathbf{x}_{BC}|$  varying in each optimization cycle until the derivative of the energy along the reaction path is zero (reaching a saddle point). [85]

Chemical equilibrium is achieved when the rates of forward and back reactions are identical, which is determined by the equilibrium constant, defined in Equation 2.1.2.

$$K_{\text{eq}} = \frac{k_f}{k_b} = e^{-\Delta G/k_B T} \quad (2.1.2)$$

Where  $\Delta G$  represents the Gibbs free energy difference between the product and reactant, which is independent of the transition state.  $k_f$  and  $k_b$  are rates of forward and back reactions respectively. For a simple reaction of the type  $A \rightleftharpoons B$ , the equilibrium constant is given by

$$K_{\text{eq}} = \frac{[B]}{[A]} = \frac{k_f}{k_b} \quad (2.1.3)$$

## 2.2 Treatment of the Motion of the Nuclei

The motion of nuclei and electrons as well as their interactions in their stationary states are the foundation of the properties of materials studied in catalysis. The time-independent Schrödinger equation describes such systems and is given by

$$\mathbf{H}\Psi_{\text{tot}}(\mathbf{r}, \mathbf{R}) = E_{\text{tot}}\Psi_{\text{tot}}(\mathbf{r}, \mathbf{R}) \quad (2.2.1)$$

Where the solutions are derived by applying the Hamiltonian operator  $\mathbf{H}$  on a wave function  $\Psi_i(\mathbf{r}, \mathbf{R})$  that depends on all-electron ( $\mathbf{r}$ ) and all-nuclear coordinates ( $\mathbf{R}$ ) and “tot” is the state of the coupled system. The multi-electronic-nonrelativistic Hamiltonian is depicted in Equation 2.2.2, where kinetic and potential energies of electrons and nuclei are considered.

$$\mathbf{H} = \mathbf{T}_n + \mathbf{T}_e + \mathbf{V}_{ne} + \mathbf{V}_{ee} + \mathbf{V}_{nn} \quad (2.2.2)$$

By substituting the kinetic and potential terms with their equivalent expressions, in atomic units, the Hamiltonian is given by

$$\begin{aligned} \mathbf{H} = & - \sum_A^{N_{\text{nuclei}}} \frac{1}{2M_A} \nabla_A^2 - \sum_i^{N_{\text{elec}}} \frac{1}{2} \nabla_i^2 - \sum_A^{N_{\text{nuclei}}} \sum_i^{N_{\text{elec}}} \frac{Z_A}{|\mathbf{R}_A - \mathbf{r}_i|} \\ & + \sum_i^{N_{\text{elec}}} \sum_{j>i}^{N_{\text{elec}}} \frac{1}{|\mathbf{r}_i - \mathbf{r}_j|} + \sum_A^{N_{\text{nuclei}}} \sum_B^{N_{\text{nuclei}}} \frac{Z_A Z_B}{|\mathbf{R}_A - \mathbf{R}_B|} \end{aligned} \quad (2.2.3)$$

### 2.2.1 Born-Oppenheimer Approximation

Calculating full solutions of the Schrödinger equation using the exact Hamiltonian is a very difficult task and some approximations need to be considered. A commonly used approximation is that wave functions of electrons and nuclei are separable. This is generally a good approximation as nuclei are about 1800 times heavier than electrons, which means that electrons can be assumed to move around frozen nuclei. This approximation is known as the Born-Oppenheimer approximation. The total wave functions for a given state of the coupled electron-nuclear system is a combination of functions of the nuclear coordinates  $\chi_{ni}(\mathbf{R})$  and the electronic wave function  $\psi_i(\mathbf{r}, \mathbf{R})$  (Equation 2.2.4), where  $\mathbf{R}$  is now just a parameter in  $\psi_i$ .

$$\Psi_{\text{tot}}(\mathbf{r}, \mathbf{R}) = \sum_i \chi_{ni}(\mathbf{R}) \psi_i(\mathbf{r}, \{\mathbf{R}\}) \quad (2.2.4)$$

The electronic and nuclear Schrödinger equations are written as

$$(\mathbf{T}_e + \mathbf{V}_{ne} + \mathbf{V}_{ee})\psi_i(\mathbf{r}, \mathbf{R}) = E_i\psi_i(\mathbf{r}, \{\mathbf{R}\}) \quad (2.2.5)$$

$$(\mathbf{T}_n + E_i(\mathbf{R}))\chi_{ni}(\mathbf{R}) = E_{\text{tot}}\chi_{ni}(\mathbf{R}) \quad (2.2.6)$$

Where electronic and nuclear terms are decoupled. For the rigid rotator and harmonic oscillator approximation, nuclear vibrations, rotations and translations are also decoupled.

### 2.2.2 Rigid Rotator and Harmonic Oscillator

In the rigid rotator and harmonic oscillator approximation, the total energy of a molecule is approximated as a sum of terms involving translational, rotational, vibrational and electronic states. A 1-dimensional potential energy  $U(x)$  of a molecular vibration can be expanded in Taylor series as

$$\begin{aligned} U(x) &= U(x_0) + \left. \frac{dU(x)}{dx} \right|_{x_0} (x - x_0) + \frac{1}{2!} \left. \frac{d^2U(x)}{dx^2} \right|_{x_0} (x - x_0)^2 + \dots \\ &= U(x_0) + \sum_{i=1}^{\infty} \frac{1}{i!} \left. \frac{d^i U(x)}{dx^i} \right|_{x_0} (x - x_0)^i \end{aligned} \quad (2.2.7)$$

In the harmonic approximation, only terms up to the second order of Taylor's expansion are considered. The first term is the minimum of the potential energy, the second term is zero (minimum is a stationary point) and the third term is written as

$$\frac{1}{2} \left. \frac{d^2U(x)}{dx^2} \right|_{x_0} (x - x_0)^2 = \frac{1}{2} k (x - x_0)^2 \quad (2.2.8)$$

Where  $k$  is the curvature of the potential energy curve (harmonic oscillator force constant). The multi-dimensional potential energy can be approximated to

$$U(\mathbf{q} + \Delta\mathbf{q}) \approx U(\mathbf{q}) + \frac{1}{2} \Delta\mathbf{q}^T \mathbf{H}(\mathbf{q}) \Delta\mathbf{q} \quad (2.2.9)$$

Where  $\mathbf{H}$  is the Hessian matrix,  $\mathbf{q}$  is a vector with the coordinates and  $\mathbf{q}^T$  is the transpose of  $\mathbf{q}$ . The rigid rotator approximation neglects the vibrational anharmonicity, it only treats rotation at the equilibrium geometry. In this work, molecular rotations, translations and vibrations are always approximated in this way.

The total contributions to the Gibbs free energy are enthalpy and entropy. Where enthalpy depends on the electronic energy, zero point energy (Equation 2.2.10) and heat capacity.

$$\text{ZPE} = \sum_{i=1}^{N_{\text{modes}}} \frac{1}{2} h \omega_i \quad (2.2.10)$$

In the ideal gas approximation, enthalpy is defined in Equation 2.2.11. [86,87] Partition functions of the canonical ensemble (NVT ensemble) are considered to calculate heat capacity and entropy. [88]

$$H(T) = \text{ZPE} + E_{\text{electronic}} + \int_0^T C_P dT \quad (2.2.11)$$

Where the total heat capacity is given as the sum of its rotational, translational, vibrational and electronic components (Equation 2.2.12).  $k_B$  is an additional term for the conversion of heat capacity at constant pressure to heat capacity at constant volume, following Mayer's relation.

$$C_P = k_B + C_{V,\text{rot}} + C_{V,\text{trans}} + C_{V,\text{vib}} + C_{V,\text{electronic}} \quad (2.2.12)$$

Where the electronic heat capacity is assumed to be zero, the translational heat capacity is  $3/2k_B$ , the rotational heat capacity is 0 for monoatomic,  $k_B$  for linear and  $3/2k_B$  for non-linear molecules. The vibrational heat capacity is given by Equation 2.2.13.

$$\int_0^T C_{V,\text{vib}} dT = \sum_i^{N_{\text{modes}}} \frac{h\omega_i}{e^{h\omega_i/k_B T} - 1} \quad (2.2.13)$$

Temperature and pressure-dependent entropy is also decomposed into its translational, rotational, vibrational and electronic components, as Equation 2.2.14 shows.

$$S_{P,T} = S_{\text{rot}} + S_{\text{trans}} + S_{\text{vib}} + S_{\text{electronic}} - k_B \ln \frac{P}{P_0} \quad (2.2.14)$$

Where  $P_0$  corresponds to the reference pressure. Translational entropy is given by Equation 2.2.15.

$$S_{\text{trans}} = k_B \left\{ \ln \left[ \left( \frac{2\pi M k_B T}{h^2} \right)^{3/2} \frac{k_B T}{P_0} \right] + \frac{5}{2} \right\} \quad (2.2.15)$$

Rotational entropy is zero for a monoatomic species, whereas for a linear molecule it is defined in Equation 2.2.16 and for a non-linear system in Equation 2.2.17.

$$S_{\text{rot}} = k_B \left[ \ln \left( \frac{8\pi^2 I k_B T}{\sigma h^2} \right) + 1 \right] \quad (2.2.16)$$

$$S_{\text{rot}} = k_B \left\{ \ln \left[ \frac{\sqrt{\pi I_A I_B I_C}}{\sigma} \left( \frac{8\pi^2 k_B T}{h^2} \right)^{3/2} \right] + \frac{3}{2} \right\} \quad (2.2.17)$$

Here,  $I$  is the inertial moment and  $\sigma$  the symmetry number. Vibrational entropy is defined in Equation 2.2.18, where  $N_{\text{modes}}$  is either  $3N_{\text{atoms}} - 5$  or  $3N_{\text{atoms}} - 6$ , if it is a linear molecule or non-linear system.

$$S_{\text{vibs}} = k_B \sum_i^{N_{\text{modes}}} \left[ \frac{h\omega_i}{k_B T (e^{h\omega_i/k_B T} - 1)} - \ln \left( 1 - e^{-h\omega_i/k_B T} \right) \right] \quad (2.2.18)$$

Electronic entropy follows the relation  $S_{\text{electronic}} = k_B \ln(2s + 1)$ . The constant  $s$  corresponds to the total spin of the system. The combination of the gas-phase enthalpies (electronic energies, ZPE and heat capacity) and entropy gives the temperature and pressure-dependent Gibbs free energy shown in Equation 2.2.19.

$$G(P, T) = H(T) - TS(P, T) \quad (2.2.19)$$

In the harmonic limit of solids and surfaces, there is no rotation and translation contributions. The only terms considered are the vibrations for heat capacity and entropy.

## 2.3 Electronic Structure Theory

As discussed before, the Schrödinger equation describes the nuclei and electrons in a molecular system. Single-electron systems such as an hydrogen atom are simple to be described and have analytical solutions. However, multi-electronic systems are complex to describe due to electron-electron interactions.

### 2.3.1 Hartree-Fock Theory

As a solution of the Born-Oppenheimer approximation, the electronic Schrödinger equation is depicted in Equation 2.2.5. In HF theory, each state in a multi-electronic system is occupied respecting the Pauli principle, i.e. two electrons cannot have the same quantum state. The Slater determinant (Equation 2.3.1) treats the antisymmetry of the wave function by adding orthonormal spin-orbitals.

$$\Phi_{\text{SD}} = \frac{1}{\sqrt{N!}} \begin{vmatrix} \phi_1(1) & \phi_2(1) & \cdots & \phi_N(1) \\ \phi_1(2) & \phi_2(2) & \cdots & \phi_N(2) \\ \vdots & \vdots & \ddots & \vdots \\ \phi_1(N) & \phi_2(N) & \cdots & \phi_N(N) \end{vmatrix} \quad (2.3.1)$$

Each column shows a single-electron wave function that depends on its spin-orbital, while rows represent different electrons. The term  $1/\sqrt{N!}$  is a normalization factor.

Equation 2.3.1 can be rewritten as the action of the antisymmetrizing operator  $\mathbf{A}$  on the orbital product  $\mathbf{\Pi}$  (Equation 2.3.2).  $\mathbf{A}$  is the sum of permutation operators  $\mathbf{P}$  weighted with a sign according to the number of permutations.

$$\Phi = \mathbf{A}[\phi_1(1)\phi_2(2)\cdots\phi_N(N)] = \mathbf{A}\mathbf{\Pi} \quad (2.3.2)$$

The operator  $\mathbf{P}$  generates all permutations of  $n$  electrons. The one-electron operator  $\mathbf{h}_i$  that describes the motion of electron  $i$  under a potential created by nuclei can be written as Equation 2.3.3 shows.

$$\mathbf{h}_i = -\frac{1}{2}\Delta_i^2 - \sum_A^{N_{\text{nuclei}}} \frac{Z_A}{|\mathbf{R}_A - \mathbf{r}_i|} \quad (2.3.3)$$

The two-electron operator  $\mathbf{g}_{ij}$  that provides electron-electron interaction is shown in Equation 2.3.4.

$$\mathbf{g}_{ij} = \frac{1}{|\mathbf{r}_i - \mathbf{r}_j|} \quad (2.3.4)$$

Replacing the terms from the Hamiltonian in Equation 2.2.3 and considering that nuclei are static ( $\mathbf{T}_n = 0$ ), the electronic Hamiltonian is written as the following equation shows.

$$\mathbf{H}_e = \sum_i^{N_{\text{elec}}} \mathbf{h}_i + \sum_i^{N_{\text{elec}}} \sum_{j>i}^{N_{\text{elec}}} \mathbf{g}_{ij} + \mathbf{V}_{nn} \quad (2.3.5)$$

The energy may be written with the permutation operator introduced in Equation 2.3.2, which gives Equation 2.3.6.

$$E = \langle \Phi | \mathbf{H} | \Phi \rangle = \langle \mathbf{A}\mathbf{\Pi} | \mathbf{H} | \mathbf{A}\mathbf{\Pi} \rangle \quad (2.3.6)$$

As  $\mathbf{V}_{nn}$  is independent of electron coordinates,  $\langle \Phi | \mathbf{V}_{nn} | \Phi \rangle = V_{nn}$ . The contributions of the one-electron operator are the same as for the orbital product  $\mathbf{\Pi}$ :

$$\langle \mathbf{\Pi} | \mathbf{h}_i | \mathbf{\Pi} \rangle = \langle \phi_i(i) | \mathbf{h}_i | \phi_i(i) \rangle = h_i \quad (2.3.7)$$

The contributions from the two-electron operator is split into terms arising from the identity operator (Equation 2.3.8), leading to the Coulomb integral  $J_{ij}$ , representing classical repulsion between two charge distributions, and from the permutation operator  $\mathbf{P}$  (Equation 2.3.9), leading to the exchange integral  $K_{ij}$ .

$$\langle \mathbf{\Pi} | \mathbf{g}_{ij} | \mathbf{\Pi} \rangle = \langle \phi_i(i) \phi_j(j) | \mathbf{g}_{ij} | \phi_i(i) \phi_j(j) \rangle = J_{ij} \quad (2.3.8)$$

$$\langle \mathbf{\Pi} | \mathbf{g}_{ij} | \mathbf{P}_{ij} \mathbf{\Pi} \rangle = \langle \phi_i(i) \phi_j(j) | \mathbf{g}_{ij} | \phi_j(i) \phi_i(j) \rangle = K_{ij} \quad (2.3.9)$$

The energy can now be written in terms of Equations 2.3.7, 2.3.8 and 2.3.9.

$$E = \sum_{i=1}^{N_{\text{elec}}} h_i + \frac{1}{2} \sum_{i=1}^{N_{\text{elec}}} \sum_{j=1}^{N_{\text{elec}}} (J_{ij} - K_{ij}) + V_{nn} \quad (2.3.10)$$

Note that the Coulomb self-interaction term is canceled by its corresponding exchange term ( $J_{ii} - K_{ii} = 0$ ). We can write the Coulomb part in terms of the operator

$$\mathbf{J}_i | \phi_j(2) \rangle = \langle \phi_i(1) | \mathbf{g}_{12} | \phi_i(1) \rangle \phi_j(2) \quad (2.3.11)$$

And the exchange part in terms of the operator

$$\mathbf{K}_i | \phi_j(2) \rangle = \langle \phi_i(1) | \mathbf{g}_{12} | \phi_j(1) \rangle \phi_i(2) \quad (2.3.12)$$

The Fock operator can be defined in Equation 2.3.13 by using Equations 2.3.11 and 2.3.12.

$$\mathbf{F}_i = \mathbf{h}_i + \sum_j^{N_{\text{elec}}} (\mathbf{J}_j - \mathbf{K}_j) \quad (2.3.13)$$

Minimization of the energy is done with the Lagrangian, where a small change in the orbitals should not change the Lagrange function (Equation 2.3.14).

$$L = E - \sum_{ij}^{N_{\text{elec}}} \lambda_{ij} (\langle \phi_i | \phi_j \rangle - \delta_{ij}) \quad (2.3.14)$$

The term  $\lambda_{ij}$  is the Lagrange multiplier. The minimization of the Lagrangian is done so that the molecular orbitals remain orthogonal and normalized. The minimization of  $L$  leads to the Hartree-Fock equations (2.3.15) with the Fock operator  $\mathbf{F}_i$ .

$$\mathbf{F}_i \phi_i = \sum_j^{N_{\text{elec}}} \lambda_{ij} \phi_j \quad (2.3.15)$$

The Hartree-Fock equation can be simplified by performing a unitary transformation, where  $\lambda_{ij} = 0$  and  $\lambda_{ii} = \epsilon_i$ , which yields

$$\mathbf{F}_i \phi'_i = \epsilon_i \phi'_i \quad (2.3.16)$$

This equation is solved self-consistently and the functions that are the solutions to the HF equation are called the Self-Consistent Field (SCF) orbitals.

Now, by expanding each orbital  $\phi$  in terms of basis functions  $\chi$ , we get

$$\phi_i = \sum_{\alpha}^{M_{\text{basis}}} c_{\alpha i} \chi_{\alpha} \quad (2.3.17)$$

Where the Hartree-Fock Equation can now be rewritten as Equation 2.3.18 shows.

$$\mathbf{F}_i \sum_{\alpha}^{M_{\text{basis}}} c_{\alpha i} \chi_{\alpha} = \epsilon_i \sum_{\alpha}^{M_{\text{basis}}} c_{\alpha i} \chi_{\alpha} \quad (2.3.18)$$

Integrating the multiplication of the Hartree-Fock equation with a specific basis function from the left, yields the *Roothaan-Hall* equation for a closed-shell system (2.3.19).

$$\mathbf{F}\mathbf{C} = \mathbf{S}\mathbf{C}\epsilon \quad (2.3.19)$$

In Equation 2.3.19,  $\mathbf{F}$  is a matrix that contains the Fock elements,  $\mathbf{S}$  a matrix that contains the overlap elements between basis functions,  $\epsilon$  is a diagonal matrix of the orbital energies  $\epsilon_i$  and  $\mathbf{C}$  is a square matrix of expansion coefficients  $c_{\alpha i}$ . For open-shell systems, the Unrestricted Hartree-Fock approach is usually considered, where Roothaan-Hall equations are calculated separately for different spin-functions  $\alpha$  and  $\beta$ , where no restriction is applied. This leads to deviations of  $\langle S \cdot S \rangle$  from the exact solution  $S(S+1)$ , which is called spin contamination, where  $S$  is the total spin of the system. This problem can be avoided by using restricted-type wave functions, where orbitals occupied both by  $\alpha$  and  $\beta$  spins are forced to be the same. This is called Restricted Open-shell Hartree-Fock.

In Hartree-Fock theory, the exchange interaction is explicitly calculated, while the remaining electron-electron interactions are treated as electronic interaction with an average repulsion from the electronic cloud. For instantaneous electron-electron interaction, or correlation, different configurations (multiple Slater determinants) have to be used with HF reference. Configuration Interaction (CI), Møller-Plesset second order perturbation theory (MP2) and coupled cluster (CC) are three examples of methods that go beyond a single determinant wave function. In wave function theory, the correlation energy is defined as  $E_{\text{corr}} = E_{\text{exact}} - E_{\text{HF}}$ .

### 2.3.2 Møller-Plesset Perturbation Theory

To account for the correlation energy, several methods have been developed. Møller-Plesset perturbation theory considers the sum over the Fock operators to be the unperturbed Hamiltonian (Equation 2.3.20), and treats the difference to the full Hamiltonian as the perturbation.

$$\begin{aligned} \mathbf{H}_0 &= \sum_{i=1}^{N_{\text{elec}}} \left( \mathbf{h}_i + \sum_{j=1}^{N_{\text{elec}}} (\mathbf{J}_j - \mathbf{K}_j) \right) \\ &= \sum_{i=1}^{N_{\text{elec}}} \mathbf{h}_i + \sum_{i=1}^{N_{\text{elec}}} \sum_{j=1}^{N_{\text{elec}}} \langle \mathbf{g}_{ij} \rangle = \sum_{i=1}^{N_{\text{elec}}} \mathbf{h}_i + 2\langle \mathbf{V}_{ee} \rangle \end{aligned} \quad (2.3.20)$$

Equation 2.3.21 shows the perturbation, that is defined as the difference between the exact electron-electron repulsion and twice the  $\langle \mathbf{V}_{ee} \rangle$  operator. As the Fock operator counts the average electron-electron repulsion twice.

$$\mathbf{H}' = \mathbf{H} - \mathbf{H}_0 = \sum_{i=1}^{N_{\text{elec}}} \sum_{j>i}^{N_{\text{elec}}} \mathbf{g}_{ij} - \sum_{i=1}^{N_{\text{elec}}} \sum_{j=1}^{N_{\text{elec}}} \langle \mathbf{g}_{ij} \rangle = \mathbf{V}_{ee} - 2\langle \mathbf{V}_{ee} \rangle \quad (2.3.21)$$

The zeroth-order wave function is the HF determinant and the zeroth order energy (Equation 2.3.22) is the sum of molecular orbital energies, counting  $\langle \mathbf{V}_{ee} \rangle$  twice.

$$\text{MP0} = E(\text{MP0}) = W_0 = \langle \Phi_0 | \mathbf{H}_0 | \Phi_0 \rangle \quad (2.3.22)$$

The first-order energy correction (Equation 2.3.23) is the average of the perturbation operator over the zeroth order wave function.

$$W_1 = \langle \Phi_0 | \mathbf{H}' | \Phi_0 \rangle = \langle \mathbf{V}_{ee} \rangle - 2\langle \mathbf{V}_{ee} \rangle = -\langle \mathbf{V}_{ee} \rangle \quad (2.3.23)$$

By summing the zeroth-order energy with the first-order energy correction, we obtain Equation 2.3.24, which gives the energy of the first-order Møller-pletset perturbation theory. Equation 2.3.24 is also the HF energy because  $W_1$  corrects the double counting terms from the Fock operator.

$$\text{MP1} = E(\text{MP0}) + E(\text{MP1}) = E(\text{HF}) \quad (2.3.24)$$

The second-order energy correction (Equation 2.3.25) is the first contribution to correlation energy, generated by exciting two electrons from occupied orbitals  $i$  and  $j$  to virtual orbitals  $a$  and  $b$ .

$$\begin{aligned} E(\text{MP2}) = W_2 &= \sum_{i<j}^{\text{occ}} \sum_{a<b}^{\text{vir}} \frac{\langle \Phi_0 | \mathbf{H}' | \Phi_{ij}^{ab} \rangle \langle \Phi_{ij}^{ab} | \mathbf{H}' | \Phi_0 \rangle}{E_0 - E_{ij}^{ab}} \\ &= \sum_{i<j}^{\text{occ}} \sum_{a<b}^{\text{vir}} \frac{(\langle \phi_i \phi_j | \phi_a \phi_b \rangle - \langle \phi_i \phi_j | \phi_b \phi_a \rangle)^2}{\epsilon_i + \epsilon_j - \epsilon_a - \epsilon_b} \end{aligned} \quad (2.3.25)$$

The summation is restricted to avoid double-counting.

### 2.3.3 Coupled Cluster Theory

The coupled cluster wave function follows the *ansatz* defined in Equation 2.3.26.

$$\Psi_{\text{CC}} = e^{\mathbf{T}} \Phi_0 \quad (2.3.26)$$

Where  $\Phi_0$  is the HF wave function and  $\mathbf{T}$  is an excitation operator defined as

$$\mathbf{T} = \mathbf{T}_1 + \mathbf{T}_2 + \mathbf{T}_3 + \cdots + \mathbf{T}_{N_{\text{elect}}} \quad (2.3.27)$$

The  $\mathbf{T}_i$  operator acting on the HF reference wave function, gives all  $i$ th excited Slater determinants.  $\mathbf{T}_1$  and  $\mathbf{T}_2$  are defined in Equations 2.3.28 and 2.3.29 with the excited determinants  $\Phi_i^a$  and  $\Phi_{ij}^{ab}$ .

$$\mathbf{T}_1 \Phi_0 = \sum_i^{\text{occ}} \sum_a^{\text{vir}} t_i^a \Phi_i^a \quad (2.3.28)$$

$$\mathbf{T}_2\Phi_0 = \sum_{i<j}^{\text{occ}} \sum_{a<b}^{\text{vir}} t_{ij}^{ab} \Phi_{ij}^{ab} \quad (2.3.29)$$

The expansion coefficient  $t$  is defined as amplitude. The exponential term is now written in terms of a Taylor expansion:

$$e^{\mathbf{T}} = \mathbf{1} + \mathbf{T} + \frac{1}{2}\mathbf{T}^2 + \frac{1}{6}\mathbf{T}^3 + \dots = \sum_{k=0}^{\infty} \frac{1}{k!}\mathbf{T}^k \quad (2.3.30)$$

Replacing the exponential operator (Equation 2.3.30) with Equation 2.3.27, yields

$$e^{\mathbf{T}} = \underbrace{\mathbf{1}}_{\text{HF}} + \underbrace{\mathbf{T}_1}_{\text{S}} + \underbrace{(\mathbf{T}_2 + \frac{1}{2}\mathbf{T}_1^2)}_{\text{D}} + \underbrace{(\mathbf{T}_3 + \mathbf{T}_2\mathbf{T}_1 + \frac{1}{6}\mathbf{T}_1^3)}_{\text{T}} + \dots \quad (2.3.31)$$

The first term generates the HF reference, while S, D and T, generate all singly, doubly and triply excited states. Doubly excited states for instance, include connected ( $\mathbf{T}_2$ ) and disconnected ( $\mathbf{T}_1^2$ ) excitation terms. The Schrödinger equation with the coupled cluster wave function becomes

$$\mathbf{H}e^{\mathbf{T}}\Phi_0 = E_{\text{CC}}e^{\mathbf{T}}\Phi_0 \quad (2.3.32)$$

Multiplying the Schrödinger equation from the left by  $\Phi_0^*$  and integrating yields

$$\begin{aligned} \langle \Psi_0 | \mathbf{H}e^{\mathbf{T}} | \Psi_0 \rangle &= E_{\text{CC}} \langle \Psi_0 | (\mathbf{1} + \mathbf{T}_1 + \mathbf{T}_2 + \frac{1}{2}\mathbf{T}_1^2 + \dots) | \Psi_0 \rangle \\ \langle \Psi_0 | \mathbf{H}e^{\mathbf{T}} | \Psi_0 \rangle &= E_{\text{CC}} \end{aligned} \quad (2.3.33)$$

Due to the Hamiltonian having one- and two-electron operators, Equation 2.3.33 is rewritten as

$$\begin{aligned} E_{\text{CC}} &= \langle \Phi_0 | \mathbf{H}(\mathbf{1} + \mathbf{T}_1 + \mathbf{T}_2 + \frac{1}{2}\mathbf{T}_1^2) | \Phi_0 \rangle \\ &= E_0 + \sum_{i<j}^{\text{occ}} \sum_{a<b}^{\text{vir}} (t_{ij}^{ab} + t_i^a t_j^b - t_i^b t_j^a) \langle \Phi_0 | \mathbf{H} | \Phi_{ij}^{ab} \rangle \\ &= E_0 + \sum_{i<j}^{\text{occ}} \sum_{a<b}^{\text{vir}} (t_{ij}^{ab} + t_i^a t_j^b - t_i^b t_j^a) (\langle \phi_i \phi_j | \phi_a \phi_b \rangle - \langle \phi_i \phi_j | \phi_b \phi_a \rangle) \end{aligned} \quad (2.3.34)$$

With Equation 2.3.34, the correlation energy can be determined by singles and doubles amplitudes, which are obtained by projecting the Schrödinger equation to the space of single, doubly, triply, ..., excited determinants:

$$\begin{aligned} \langle \Phi_i^a | \mathbf{H}e^{\mathbf{T}} | \Psi_0 \rangle &= E_{\text{CC}} \langle \Psi_i^a | e^{\mathbf{T}} \Psi_0 \rangle \\ \langle \Phi_{ij}^{ab} | \mathbf{H}e^{\mathbf{T}} | \Psi_0 \rangle &= E_{\text{CC}} \langle \Psi_{ij}^{ab} | e^{\mathbf{T}} \Psi_0 \rangle \\ \langle \Phi_{ijk}^{abc} | \mathbf{H}e^{\mathbf{T}} | \Psi_0 \rangle &= E_{\text{CC}} \langle \Psi_{ijk}^{abc} | e^{\mathbf{T}} \Psi_0 \rangle \\ &\vdots \end{aligned} \quad (2.3.35)$$

Energies calculated with Coupled Cluster with Single and Double excitations (CCSD) method are obtained by truncating the excitation operator  $\mathbf{T} = \mathbf{T}_1 + \mathbf{T}_2$ , where the exponential operator is written as

$$e^{\mathbf{T}_1 + \mathbf{T}_2} = \mathbf{1} + \mathbf{T}_1 + (\mathbf{T}_2 + \frac{1}{2}\mathbf{T}_1^2) + (\mathbf{T}_2\mathbf{T}_1 + \frac{1}{6}\mathbf{T}_1^3) + (\frac{1}{2}\mathbf{T}_2^2 + \frac{1}{2}\mathbf{T}_2\mathbf{T}_1^2 + \frac{1}{24}\mathbf{T}_1^4) + \dots \quad (2.3.36)$$

The CCSD energy is obtained by using Equation 2.3.34, where amplitudes are derived by projecting against a singly and doubly excited Slater determinant. Projectors involve matrix elements of triple and quadruple excitations, which lead to identical matrix elements between reference and doubly excited state.

Coupled Cluster with Single, Double, and perturbative Triple excitations (CCSD(T)) follow Equation 2.3.37.

$$E_{\text{CCSD(T)}} = E_{\text{CCSD}} + \underbrace{E^{(4)} + E^{(5)}}_{E_{(\text{T})}} \quad (2.3.37)$$

Where  $E_{(\text{T})}$  is calculated using Møller-Plesset fourth-order perturbation theory, using CCSD amplitudes rather than perturbation coefficients, adding a term arising from the fifth-order perturbation theory, which describes the coupling between singles and triples.

### 2.3.4 Density Functional Theory

DFT aims to describe the electronic structure by using density functionals rather than wave functions. The ground state density (Equation 2.3.38) is given by the expectation value of the density operator.

$$\rho_0(\mathbf{r}) = \langle \Psi_0 | \boldsymbol{\rho}(\mathbf{r}) | \Psi_0 \rangle \quad (2.3.38)$$

The density operator  $\boldsymbol{\rho}$  is defined by Equation 2.3.39, where  $\mathbf{r}_i$  is a set of coordinates for electron  $i$  and  $\delta(\mathbf{r} - \mathbf{r}_i)$  is the Kronecker delta.

$$\boldsymbol{\rho}(\mathbf{r}) = \sum_{i=1}^N \delta(\mathbf{r} - \mathbf{r}_i) \quad (2.3.39)$$

The foundations of density functional theory are the Hohenberg-Kohn (HK) theorems and Kohn-Sham (KS) equations.

#### 2.3.4.1 Hohenberg-Kohn Theorems

The Hamiltonian of a multi-electronic system can be written in terms of an external potential (Equation 2.3.40), that in principle determines all properties of the system.

$$\mathbf{H} = \mathbf{T} + \mathbf{V}_{\text{ext}} + \mathbf{V}_{ee} \quad (2.3.40)$$

The terms  $\mathbf{T}$ ,  $\mathbf{V}_{\text{ext}}$  and  $\mathbf{V}_{ee}$  are the kinetic energy, external potential and electron-electron interaction operators respectively.

The first HK theorem states that the electron density of the ground state  $\rho_0(\mathbf{r})$  determines uniquely the external potential  $\mathbf{V}_{\text{ext}}$ , phased by a constant.

The second HK theorem states that an universal functional of energy  $E[\rho(\mathbf{r})]$  can be defined and the global minimum represents the exact ground state energy of the system for one particular

$\mathbf{V}_{\text{ext}}$ . The density  $\rho(\mathbf{r})$  that minimizes the functional is the exact ground state density  $\rho_0(\mathbf{r})$ . The Hohenberg-Kohn energy functional is defined as

$$E_{\text{HK}}[\rho] = \langle \Psi[\rho] | \mathbf{H} | \Psi[\rho] \rangle = F_{\text{HK}}[\rho] + \int d\mathbf{r} \mathbf{V}_{\text{ext}}(\mathbf{r}) \rho(\mathbf{r}) + E_{II} \quad (2.3.41)$$

Where  $F_{\text{HF}}[\rho]$  includes all internal kinetic and potential energies (Equation 2.3.42), and  $E_{II}$  is the interaction energy of the nuclei.

$$F_{\text{HK}}[\rho] = T + E_{\text{int}} \quad (2.3.42)$$

The challenge in this approach is that  $F_{\text{HK}}$  is not known exactly and needs to be approximated.

### 2.3.4.2 The Kohn-Sham approach

The Kohn-Sham *ansatz* implies that the ground state density of the original interacting system is equivalent to a chosen non-interacting system, with the interacting terms included in an exchange and correlation functional of the density. This is known as non-interacting-V-representability. Also, the Hamiltonian is chosen to have the usual kinetic operator and an effective local potential  $\mathbf{V}_{\text{eff}}^\sigma$  acting on an electron of spin  $\sigma$  at point  $\mathbf{r}$ . The potential  $\mathbf{V}_{\text{eff}}^\sigma$  is also called the Kohn-Sham potential and is defined as

$$\mathbf{V}_{\text{KS}}^\sigma(\mathbf{r}) = \mathbf{V}_{\text{ext}}(\mathbf{r}) + \mathbf{V}_{\text{Hartree}}(\mathbf{r}) + \mathbf{V}_{xc}^\sigma(\mathbf{r}) \quad (2.3.43)$$

Where  $\mathbf{V}_{\text{Hartree}}(\mathbf{r})$  is the Hartree potential and  $\mathbf{V}_{xc}^\sigma(\mathbf{r})$  is exchange and correlation potential. In the KS approach, the exact exchange operator is not considered, only the Coulomb operator, which gives the Hartree energy. Exchange and correlation is calculated in an exchange and correlation functional  $E_{xc}$ . The KS energy is defined in Equation 2.3.44.

$$E_{\text{KS}} = T_s[\rho] + \int d\mathbf{r} \mathbf{V}_{\text{ext}}(\mathbf{r}) \rho(\mathbf{r}) + E_{\text{Hartree}}[\rho] + E_{II} + E_{xc}[\rho] \quad (2.3.44)$$

$T_s[\rho]$  is the independent particle kinetic energy for  $N = N^\uparrow + N^\downarrow$  independent electrons, which is trivial to calculate from the orbital.  $E_{II}$  is the interaction between the nuclei,  $E_{\text{Hartree}}[\rho]$  is the Hartree energy and  $E_{xc}[\rho]$  is the exchange and correlation energy. Note that since exchange is only approximated, there is an error associated with self-electronic Coulomb interaction, which is otherwise canceled with exact exchange energy. Similar to HF theory, Lagrange multipliers are also used to minimize energy leading to KS equations.

### 2.3.4.3 Density Functionals

The exact exchange and correlation functional is not known. Two approaches to obtain an approximate  $E_{xc}$  are discussed here. The first is the Local Spin Density Approximation (LDA), where the electronic structure is treated as an homogeneous electron gas. The spin-dependent exchange and correlation energy (Equation 2.3.45) is an integral over all space with  $\epsilon_{xc}^{\text{hom}}$  derived from homogeneous electron gas.

$$E_{xc}^{\text{LDA}}[\rho^\uparrow, \rho^\downarrow] = \int d\mathbf{r} \rho(\mathbf{r}) \epsilon_{xc}^{\text{hom}}(\rho^\uparrow(\mathbf{r}), \rho^\downarrow(\mathbf{r})) \quad (2.3.45)$$

The individual exchange and correlation energy for the homogeneous electron gas can be written as the sum of exchange energy and correlation energy, where the exchange component is computed from an analytical formula and the correlation component is fit to Quantum Monte Carlo (QMC) results.

The second approach is by considering the Generalized Gradient Approximation (GGA), in which gradients of the density  $|\nabla\rho^\sigma|$  are also included:

$$E_{xc}^{\text{GGA}}[\rho^\uparrow, \rho^\downarrow] = \int d\mathbf{r} \rho(\mathbf{r}) \epsilon_{xc}(\rho^\uparrow(\mathbf{r}), \rho^\downarrow(\mathbf{r}), \nabla\rho^\uparrow(\mathbf{r}), \nabla\rho^\downarrow(\mathbf{r}), \dots) \quad (2.3.46)$$

The term  $\epsilon_{xc}$  can be redefined as Equation 2.3.47 shows.

$$\epsilon_{xc}(\rho^\uparrow(\mathbf{r}), \rho^\downarrow(\mathbf{r}), \nabla\rho^\uparrow(\mathbf{r}), \nabla\rho^\downarrow(\mathbf{r}), \dots) = \epsilon_x^{\text{hom}} F_{xc}(\rho^\uparrow(\mathbf{r}), \rho^\downarrow(\mathbf{r}), \nabla\rho^\uparrow(\mathbf{r}), \nabla\rho^\downarrow(\mathbf{r}), \dots) \quad (2.3.47)$$

The function  $F_{xc}$  is the enhancement factor and  $\epsilon_x^{\text{hom}}$  is the exchange energy for the unpolarized gas.

The PBE functional, developed by Perdew, Burke and Ernzerhof, [89–91] parametrizes  $F_{xc}$  so that the local approximation is recovered for low values of density gradients ( $F(0) = 1$ ), is constant for large density gradients and satisfies specific conditions.

Other types of functionals include meta-GGA and hybrid functionals. Meta-GGA include second derivatives of the density, M06-L [92] is one example of such. Hybrid functionals such as M06, B3LYP and PBE0 [93–96] include different percentages of the explicit HF exchange to reduce the Coulomb self-interaction error.

#### 2.3.4.4 Dispersion Corrections

London dispersion, or van der Waals interactions are multipolar interactions between molecules that are not directly bonded. Electronic correlation is responsible for these intermolecular interactions. Usually, density functionals do not account for long-range correlation effects. The general equation for the van der Waals interactions between atoms A and B is shown in Equation 2.3.48.

$$E_{\text{vdW}}(r_{AB}) = E_{\text{repulsion}}(r_{AB}) - \frac{C^{AB}}{(r_{AB})^6} \quad (2.3.48)$$

The term  $C^{AB}$  is a constant. Dispersion in DFT depends on the functional used, as each treats correlation differently. Dispersion corrections used in this thesis are based on zero damping Grimme's dispersion corrections "D3" [97] that introduces a damping function that converges the vdW energy correction to zero in the short-range limit. The DFT-D3 energies are defined as

$$E_{\text{DFT-D3}} = E_{\text{KS-DFT}} - E_{\text{disp}} \quad (2.3.49)$$

$E_{\text{disp}}$  is the dispersion correction that is given by  $E_{\text{disp}} = E^{(2)} + E^{(3)}$ , which are the two body and three body terms. The two body term is the most important and is defined as

$$E^{(2)} = \sum_{AB} \sum_{n=6,8,10,\dots} s_n \frac{C_n^{AB}}{r_{AB}^n} f_{d,n}(r_{AB}) \quad (2.3.50)$$

The term  $C_n^{AB}$  denotes the averaged  $n$ th-order dispersion coefficient (with orders of  $n = 6, 8, 10, \dots$ ) for atom pair  $AB$ , where  $r_{AB}$  is their internuclear distance.  $s_n$  are scaling factors that are adjusted

for  $n > 6$  to ensure asymptotic exactness. Damping functions  $f_{d,n}$  avoids near singularities for small distances and mid-range double counting effects. The three body term is defined as

$$E^{(3)} = \sum_{ABC} f_{d,(3)}(\bar{r}_{ABC}) \frac{C_9^{ABC} (3 \cos \theta_a \cos \theta_b \cos \theta_c + 1)}{(r_{AB} r_{BC} r_{CA})^3} \quad (2.3.51)$$

Where the sum is over all atom triples  $ABC$  in the system and  $f_{d,(3)}(\bar{r}_{ABC})$  is the damping function, used with well-defined parameters and with a geometrically averaged radii  $\bar{r}_{ABC}$ .  $\theta_a$ ,  $\theta_b$  and  $\theta_c$  are internal angles of the triangle formed by  $r_{AB}$ ,  $r_{BC}$  and  $r_{CA}$  and  $C_9^{ABC}$  is the triple-dipole constant.

### 2.3.4.5 Projector Augmented Wave method

The PAW method divides space in two regions. Non-overlapping atomic regions, called augmentation spheres and an interstitial region, where the KS wave functions are expected to be smooth and easily described by an uniform discretization such as an uniform grid or plane waves with a certain cutoff. Despite the smooth discretization spanning to the atomic regions, each atomic region has spherical augmentation functions called partial waves. The idea is to describe the augmentation region (that has a rapidly oscillating atomic wave function) as accurately as possible by adding a linear combination of partial waves and by removing the smooth wave function that is used to describe the interstitial region (smooth region). The total wave function  $\Psi_k(\mathbf{r})$  is written as

$$\Psi_k(\mathbf{r}) = \tilde{\Psi}_k(\mathbf{r}) + \sum_a^{N_{\text{atoms}}} \sum_{nlm} c_{k,nlm}^a \left[ \xi_{nlm}^a(r_a, \theta_a, \phi_a) - \tilde{\xi}_{nlm}^a(r_a, \theta_a, \phi_a) \right] \quad (2.3.52)$$

Which represents a combination of a smooth pseudo wave function  $\tilde{\Psi}_k(\mathbf{r})$ , with the difference of the atomic all-electron partial waves  $\xi_{nlm}^a(r_a, \theta_a, \phi_a)$  and smooth partial waves  $\tilde{\xi}_{nlm}^a(r_a, \theta_a, \phi_a)$ .  $n$ ,  $m$ ,  $l$  are the principal, angular and magnetic quantum numbers while  $r$ ,  $\theta$  and  $\phi$  are the radial distance, polar angle and the azimuthal angle.  $c_{k,nlm}$  is a coefficient given by a projection in each sphere for the partial-wave transformation to be linear.

### 2.3.5 Localized Basis sets

A molecular orbital (MO) is described with a set of basis functions. There are two types of basis functions that define a molecular orbital. Slater-Type Orbitals (STOs) are defined in Equation 2.3.53.

$$\chi_{\zeta,n,l,m}(r, \theta, \varphi) = NY_{l,m}(\theta, \varphi) r^{n-1} e^{-\zeta r} \quad (2.3.53)$$

Where  $N$  is a normalization constant and  $Y_{l,m}$  are spherical harmonic functions that depend on polar and azimuthal angles and are related to angular momentum. Gaussian-Type Orbitals (GTOs) are defined as follows:

$$\chi_{\zeta,n,l,m}(r, \theta, \varphi) = NY_{l,m}(\theta, \varphi) r^{2n-2-l} e^{-\zeta r^2} \quad (2.3.54)$$

The smallest basis set that just uses enough functions for a minimum description of the occupied orbitals, is called Single Zeta (SZ) basis set, which is based on the variable  $\zeta$  from Equations 2.3.53 and 2.3.54. Double zeta and triple zeta basis sets use twice and thrice as many orbitals

for each atomic orbital. A split-valence basis uses one basis function for each core atomic orbital and a larger basis for valence atomic orbitals. High angular momentum functions are relevant for interaction between different orbitals, that also describe unoccupied orbitals. Polarization adds high angular momentum (e.g. adds  $p$ -orbitals to  $s$ -orbitals). Correlated methods require higher angular momentum (polarization functions) to achieve reliable results, which lead to different (slower) rate of energy convergence with the increase of basis functions.

Karlsruhe-type basis sets are one type of GTO basis-sets that are constructed using a linear combination of primitive functions (individual GTOs) that have been found to have good performance in describing chemical reactions with DFT.

Dunning and coworkers proposed basis sets that are built to recover the correlation energy from the valence electrons. [98] The basis sets are constructed so that the variation of the HF and correlation energies with the size of the basis set fit to well-defined functions. The HF and correlation limits are then calculated by complete basis-set extrapolation methods.

### 2.3.5.1 Complete Basis-set extrapolation

The complete basis-set extrapolation is done separately for the Hartree-Fock and the correlation part, as these components converge at different rates. Considering Dunning's correlation-consistent basis sets, [98] three points are used (has two undetermined parameters) to extrapolate the basis-set limit for the HF energy, hence three different basis-sets (cc-pVXZ with X=D, T or Q are used), following the Equation 2.3.55.

$$E_{\text{HF}}^{\infty} = E_{\text{HF}}^{\text{X}} - \alpha \exp^{-\beta X} \quad (2.3.55)$$

The second part is the convergence of the correlation component using two points (one parameter to be determined). Either the energy values obtained from cc-pVDZ and cc-pVTZ (2,3) or cc-pVTZ and cc-pVQZ (3,4), following the curve from Equation 2.3.56.

$$E_{\text{Corr}}^{\infty} = E_{\text{Corr}}^{\text{X}} - \frac{\gamma}{X^3} \quad (2.3.56)$$

The sum of the CBS-extrapolated HF and correlation components leads to the CBS-extrapolated total energies to the basis-set limit  $E_{\text{tot}} = E_{\text{HF}} + E_{\text{Corr}}$ , which are then compared with energies obtained with other basis-sets (Figure A.11). [99–102]

## 2.3.6 Approximations

### 2.3.6.1 Resolution of the Identity

The Resolution of the Identity (RI- $J$ ) is an approximate treatment of Coulomb operators based on the expansion of molecular electron densities in atom-centered auxiliary basis sets. The Coulomb energy is written in terms of electron density (Equation 2.3.57).

$$J = \frac{1}{2} \int \rho(\mathbf{r}_1) \frac{1}{r_{12}} \rho(\mathbf{r}_2) d^3 r \quad (2.3.57)$$

An approximate representation of the density  $\rho$  in terms of an atom-centered auxiliary basis-set, denoted as  $\alpha$ , is shown in Equation 2.3.58. [103]

$$\rho(\mathbf{r}) \approx \sum_{\alpha} c_{\alpha} \alpha(\mathbf{r}) = \tilde{\rho}(\mathbf{r}) \quad (2.3.58)$$

This is also known as density-fitting.

### 2.3.6.2 Chain of Spheres

The Chain-of-Spheres exchange approximation (COSX) is a combination of semi-numerical integration and overlap screening. The exchange energy is calculated using Equation 2.3.59. [104]

$$E_x = \frac{1}{2} \sum_{\mu\nu} P_{\mu\nu} K_{\mu\nu}(\mathbf{P}) \quad (2.3.59)$$

Where  $\mathbf{P}$  is the density matrix and

$$K_{\mu\nu} = \sum_{k\tau} P_{k\tau} \int \mu(\mathbf{r}_1) k(\mathbf{r}_1) \nu(\mathbf{r}_1) \tau(\mathbf{r}_2) r_{12}^{-1} d\mathbf{r}_1 d\mathbf{r}_2 \quad (2.3.60)$$

The terms  $\mu$ ,  $k$ ,  $\nu$  and  $\tau$  are matrix elements of an exchange-type matrix  $K$  that are approximated as follows

$$K_{\mu\nu} \approx \sum_g X_{\mu g} \sum_{\tau} A_{\nu\tau}(\mathbf{r}_g) \sum_k P_{k\tau} X_{kg} \quad (2.3.61)$$

Here, the index “ $g$ ” refers to grid points  $\mathbf{r}_g$ .  $X_{kg}$  denotes the basis function  $k(\mathbf{r}_g)$  multiplied by  $w_g^{1/2}$ , where the term  $w_g$  represents the grid weights and

$$A_{\nu\tau}(\mathbf{r}_g) = \int \frac{\nu(\mathbf{r}) \tau(\mathbf{r})}{|\mathbf{r} - \mathbf{r}_g|} d\mathbf{r} \quad (2.3.62)$$

### 2.3.6.3 Domain based Local Pair Natural Orbitals

The DLPNO approximation is a combination of Local Pair Natural Orbitals (LPNO), that construct natural localized internal orbitals for electron pairs, with Projected Atomic Orbitals (PAO), which are obtained by projecting the occupied orbital space out of the atomic orbitals while preserving the localized character of the atomic orbitals. This set of localized atomic orbitals are also referred as orbital domains (D). Correlation is captured by interactions of multipoles from local orbitals, which linearizes the computational cost with respect to the size of the system. In DLPNO-CCSD(T), single excitations are truncated, whereas for LPNO-CCSD(T), all amplitudes for single excitations are preserved. However, the correlation energy loss due to the domains remains low. DLPNO-CCSD(T) is a good approximation when compared to canonical CCSD(T). [105–107]

## 2.4 Description of Solvation

### 2.4.1 Implicit Solvation

Several reactions in catalysis occur in solution. Implicit solvent models are models that rely on replacing vacuum with a continuum medium, where the corresponding solvent’s dielectric constant

is used. The environment is split in two regions, the solvent region is dominated by the dielectric constant while the solute region is dominated by the solute interactions. A cavity is constructed with a radius that provides accurate solvation energies when compared to experiments, in which the parameter that smoothens the solvent-solute transition is also controlled. Figure 2.2 shows an illustration of a solvent-solute cavity.

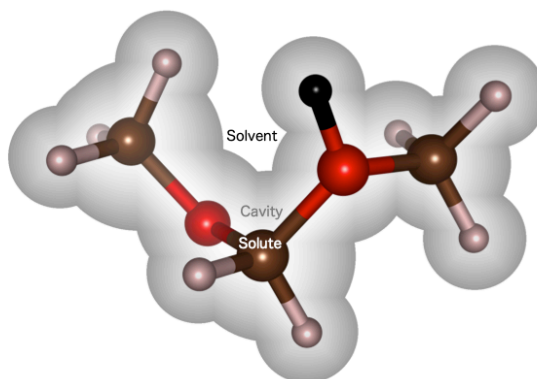


**Figure 2.2:** Illustration of the solvent-solute cavity in implicit models surrounding a protonated oxymethylene dimethyl ether. Color code: H – White; O – Red; C – Brown; H<sup>+</sup> – Black.

The Solvation Model based on Density (SMD) is a more accurate model than standard Polarizable Continuum Models (PCM) since, in addition, it uses a set of empirical parameters (depicted in Table D.2) for each solvent in a database with more than 100 molecules. This model predicts the formation of hydrogen bonds. [108]

### 2.4.2 Explicit Solvation

Explicit solvation models include solvent molecules in the vicinity that interact with the solute. This method of solvation is rather complex since there is no unique method of incorporating solvent molecules. Different numbers of molecules with different possible orientations are generating a large number of local minima. Molecular dynamics is often used to predict the global minima of the system but these methods are computationally demanding. Mixed methods (explicit+implicit solvation) are also commonly used.



## Chapter 3

# Accuracy of Density Functional Theory in Zeolite Catalysis

### 3.1 Introduction

Density Functional Theory (DFT) is considered by many the most suitable quantum chemical tool to calculate reaction energies and transition states for complex catalysts, such as zeolites or similar materials, [109–126] which constitute a widely used class of heterogeneous catalysts in the chemical industry. [127–130] As the popularity of this method increased over time, due to the computationally low cost and often good results, its overall accuracy is questioned. [131] It has been observed that, in transition metal catalysis, the mean absolute error is below 20 kJ/mol for the best density functionals, when compared to experimentally obtained adsorption energies. [132, 133] Despite DFT displaying a systematic underestimation of barriers, when functionals such as PBE-D3 are used, the GGA functional BEEF-vdW surprisingly appeared to have a less systematic trend, with an error below 15 kJ/mol. [134]

This chapter will focus primarily on Brønsted-Lowry acid catalytic reactions and transition states of methanol to olefins (MTO) processes as well as reaction energies for the selective catalytic reduction (SCR) to compare DFT with MP2 and CCSD(T) methods. For these processes, it is common to work with H-SSZ-13 and Cu-SSZ-13 zeolites, [41–45, 135–165] respectively, with the latter involving a change of the oxidation state from Cu<sup>I</sup> to Cu<sup>II</sup>. [41–53] However, not only modeling periodic systems constitute a problem for higher-level methods, even though recent advancements are being made, [166–173] but also a unit cell of a zeolite contains 100 to 300 atoms, which is affordable for DFT but very demanding for higher-level methods.

### 3.2 Methods

Non-periodic DFT calculations were performed using the TURBOMOLE program package [175, 176] with the Resolution of Identity approximation for the Coulomb energy [103] along with the def2-TZVPP basis-set. [177, 178] Additionally, M06/def2-QZVPP calculations were performed,

---

This chapter is based on the following publication: [174] Goncalves, T. J.; Plessow, P. N.; Studt, F., On the Accuracy of Density Functional Theory in Zeolite Catalysis. *ChemCatChem* 2019, 11, 4368–4376. Copyright (2019) Wiley. Used with permission from Goncalves, T. J.; Plessow, P. N.; Studt, F., On the Accuracy of Density Functional Theory in Zeolite Catalysis. *ChemCatChem*. Wiley.

which changed the MAE of M06 with respect to CCSD(T)/CBS(3,4) by about 0.5 kJ/mol (see Figure A.5). We thus conclude that the def2-TZVPP basis-set is sufficient for DFT calculations. The PBE functional [89–91] with zero damping Grimme’s dispersion corrections ”D3” [97] was used for geometry optimization and single-point calculations. Single points were also performed with the hybrid functionals PBE0-D3, [96] B3LYP-D3 [94, 95] and M06 [93] and Møller-Plesset second order perturbation theory MP2 [179–181] in TURBOMOLE, all with the def2-TZVPP/def2-QZVPP basis-sets and a corresponding auxiliary basis-set. [182–184]

For CCSD(T) [180, 181] both TURBOMOLE and ORCA program packages were used. TURBOMOLE for canonical CCSD(T) calculations and ORCA [106, 107] to compare the accuracy of the DLPNO approximation [99, 185] with the canonical values obtained for the smallest cluster model T1. Then, DLPNO-CCSD(T) was carried out for the largest cluster and canonical CCSD for T1 with cc-pVXZ (X=D, T, Q) basis-sets, for the complete basis-set limit extrapolation (CBS). [99–102]

For the periodic and gas-phase DFT calculations, an optimized unit cell of the chabazite zeolite was used (PBC) as well as the T46 cluster model in vacuum, with the standard Projector Augmented Wave (PAW) method, and the PBE-D3 functional for geometry optimization and more accurate, hard-PAWs [186, 187] for single-points and the BEEF-vdW functional [188] as well, using the VASP program package [186, 187, 189–191], version 5.4.

DFT single-points are calculated with different program packages, because BEEF-vdW, for instance, is not available in TURBOMOLE.

The RIJCOSX approximation [104] was used both for MP2 and CCSD(T) for the MTO reactions as it leads to a significant increase in the performance without impacting the accuracy.

Tables A.8 and A.9 show the different methods used, along with the plane-waves/basis-sets applied on the different cluster models for the MTO and SCR reactions respectively.

### 3.3 Cluster models

Sauer and co-workers have introduced a hierarchical cluster approach, which consists of cutting the active site and its vicinity from the periodic structure to be able to perform non-periodic Møller-Plesset perturbation theory or even coupled-cluster calculations. [73–77, 135, 136, 192] Studies have revealed that while larger clusters produce more reliable results, errors in reaction energies tend to converge with the number of tetrahedral atoms cut. [74] In this work, the entire cavity of the chabazite structure was cut from the periodic structure, containing 46 tetrahedral atoms, to model the full effects of the steric repulsion of the framework. Silicon atoms at the edge of the cluster are saturated with hydrogen atoms that have reference Si-H bond lengths and have the same orientation of the former oxygen atoms. Single-point calculations are performed on this cluster model.

While the T46 cluster model is still a challenge for canonical coupled-cluster calculations, i.e. the computational cost of a canonical CCSD(T) calculation scales as  $N^7$  with  $N$  being the size of the system, the DLPNO-CCSD(T) developed by Neese and co-workers, scales almost linearly with the size of the system while capturing around 99.9% of the canonical correlation energy, with reported deviations of around 1 to 5 kJ/mol for reaction enthalpies. [99, 106, 107, 185] The T1 cluster model, consisting only of the active site, was also considered to evaluate the accuracy of DLPNO-CCSD(T) with respect to canonical CCSD(T). The clusters have OH terminations that are fully optimized due to possible reorientations during reactions. The different cluster models are depicted in Figure

3.1 .

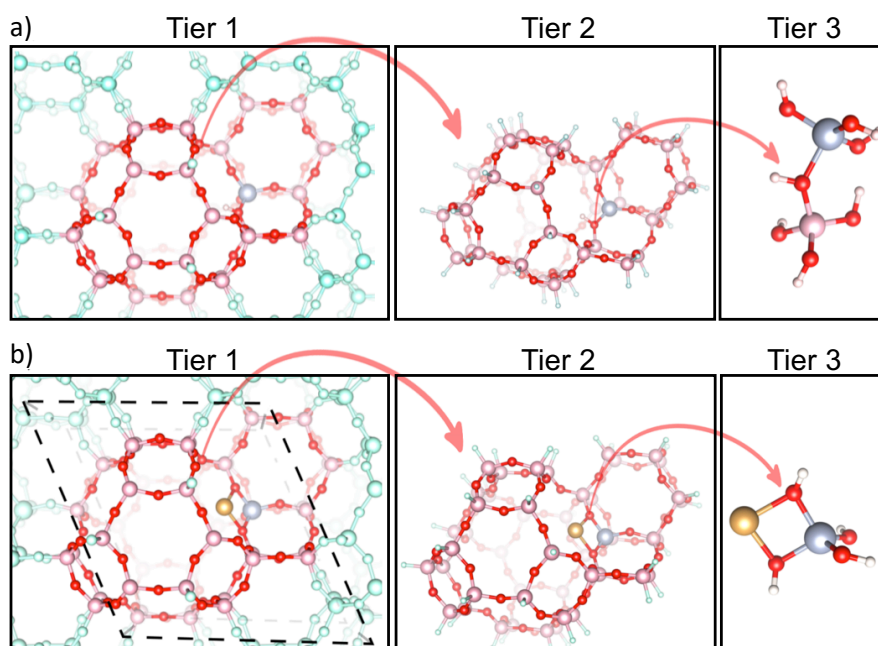


**Figure 3.1:** a) Illustration of the different tiers of models of the H-SSZ-13 zeolite. b) Illustration of the different tiers of models of the Cu-SSZ-13 zeolite. Color scheme: Cu - Brown; Al - Gray; O - Red; Si - Pink; H - White; Solid crystal structure/Termination - Green.

The three tiers illustrated in Figure 3.1 are defined as follows

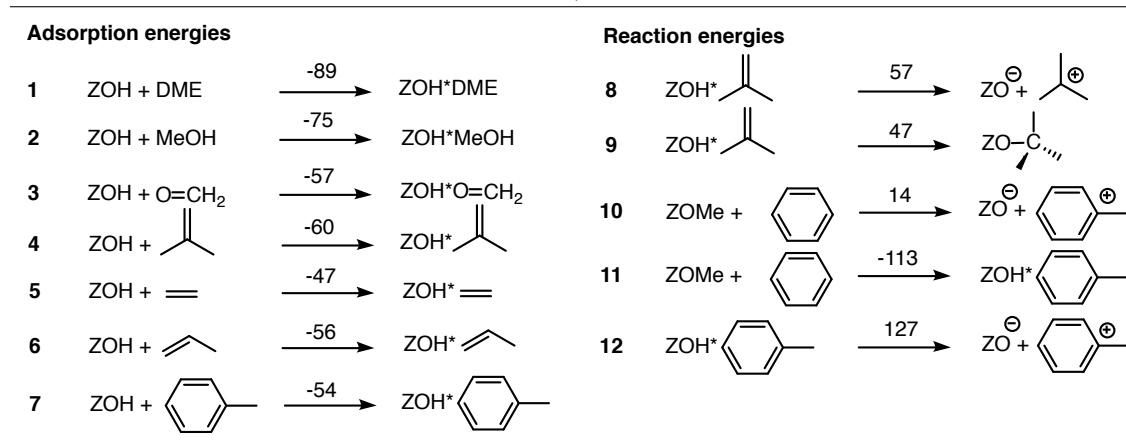
- Tier 1 is a periodic model of the zeolite H-SSZ-13 (Figure 3.1 a) and Cu-SSZ-13 (Figure 3.1 b) with an optimized rhombohedral unit cell containing 36 tetrahedral atoms, one of which is an aluminum atom, leading to a Si/Al ratio of 35. Typical ratios of Si/Al can vary between 6 and 50 depending on which reactions are studied. [45, 138, 152, 160] For SCR reactions, Cu/Al ratios are relevant to boost the catalytic activity, usually ranging from 0 to 0.5. [41, 43, 45] Here, one copper per active site exists, which gives a Cu/Al ratio of 1. The ratio used in this work has the purpose of capturing the reactivity of an isolated active site, it also depicts a realistic model. The aluminum substitution formally introduces a charge that is balanced either by a proton in acid catalysis or by a copper(I) ion in the case of copper-catalyzed SCR.
- Tier 2 depicts 46 tetrahedral atoms cut from the repeated unit cell of the tier 1 structure and terminated with hydrogen atoms. In Figure 3.1, the 6-membered ring is shown directly on the top-right side of the aluminum atom, whereas the 8-membered ring is on the left-hand side and approximately orthogonal to the 6-membered ring. Here, we strictly evaluate the energy error for a given T46-cluster derived from a PBE-D3 optimized periodic structure, but stress that reoptimization of the structures at a different level of theory will affect these errors. Approaches that optimize periodic structures using more accurate forces from cluster models show that deviations from proton-exchange reactions of alkenes are on the order of 1 kJ/mol between optimized and single-point calculations. [77]
- Tier 3 is the smallest cluster possible. Despite being representative of the active site, it differs significantly from the other tiers and does not consider the steric effects of the framework. For that reason, it is only used to study the influence of the size of the basis-sets and the accuracy of DLPNO-CCSD(T) with respect to canonical CCSD(T).

## 3.4 Results

### 3.4.1 Methanol to Olefins

Various MTO-related acid-catalyzed reactions (Schemes 3.1 and 3.2) are selected from a reaction mechanism proposed by Plessow et al., [135,136,142] which are used as test structures to benchmark the accuracy of DFT. Adsorption and reaction energies will be investigated first (Scheme 3.1), followed by the study of transition states (Scheme 3.2).

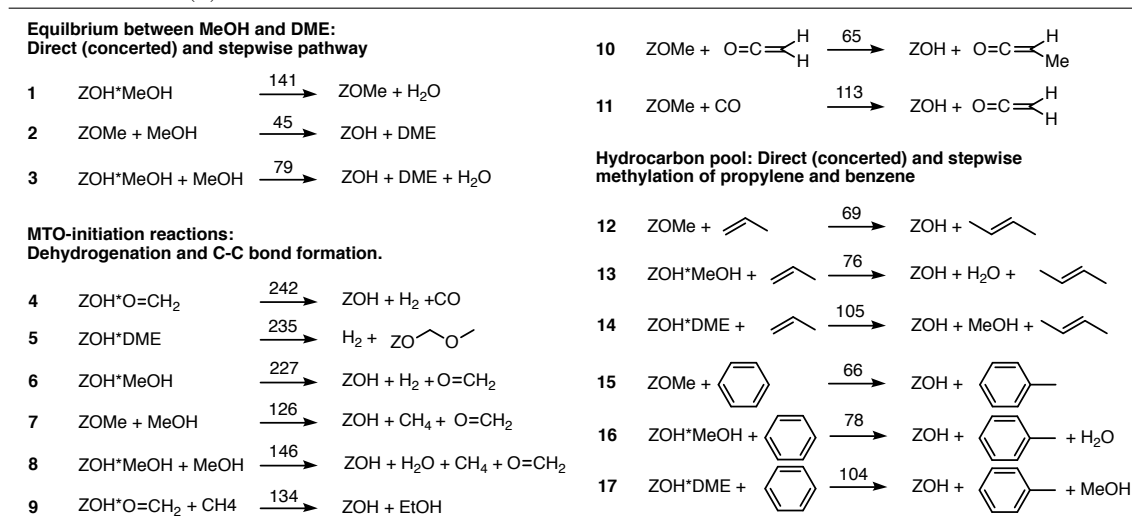
**Scheme 3.1** Overview over MTO-related acid-catalyzed reactions studied in this Section. Our best estimate for the adsorption and reaction energies is  $E_{\text{PBE-D3}}^{\text{PBC}} + (E_{\text{DLPNO-CCSD(T)}}^{\text{T46}} - E_{\text{PBE-D3}}^{\text{T46}})$ . Adsorption and reaction energies are given in kJ/mol above the reaction arrow.



In Scheme 3.1, reactions 1-7 consist of the adsorption of oxygenates such as methanol (MeOH), formaldehyde and dimethyl ether (DME), which are precursors and intermediates in the MTO process as well as the produced olefins (ethylene, propylene and isobutene) and aromatics (toluene). The adsorption energies are computed to be in the range of -89 to -47 kJ/mol, -75 kJ/mol for MeOH and -54 kJ/mol for toluene. The deviations of these values are shown in Figure 3.2 b). Reactions 8-12 consist of protonation and methylation reactions of isobutene, benzene and toluene that take place at the active site, either through a proton or a surface methoxy species (SMS). Many of these reactions involve the formation of zwitterions (reactions 8, 10 and 12). It can be seen in Figure 3.2 b) that these zwitterionic intermediates are computed to be too stable with non-hybrid functionals (PBE-D3 and BEEF-vdW) with errors as high as 40 kJ/mol, as also observed before for isobutene and PBE. [125]

Reaction barriers, which can be used to predict kinetics using harmonic transition state theory, are depicted in Scheme 3.2, that shows 17 different reactions, ordered by its type. Reactions 1-3 consist of the stepwise and direct mechanism for the formation of DME from methanol, where the first reaction of the stepwise process is the formation of an SMS. Reactions 4-11 are elementary steps that may be relevant for the initiation of the MTO process and include hydride transfers from MeOH, formaldehyde and DME to the acid site (both proton and SMS) leading to the formation of H<sub>2</sub> and CH<sub>4</sub>. Some of the involved barriers are very high (up to 242 kJ/mol for reaction 4). Additionally, methylation of ketene and CO are considered (reactions 10 and 11). Reactions 12-17 are typical reactions from the hydrocarbon pool of the MTO process [193–196] and consist of the methylation of propylene and benzene both with SMS (stepwise mechanism) and MeOH and DME (direct mechanism).

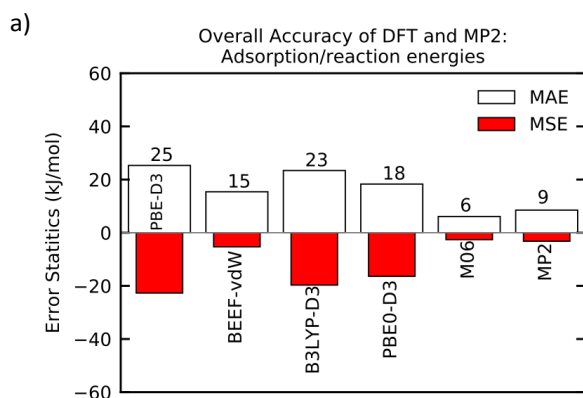
**Scheme 3.2** Overview over MTO-related acid-catalyzed transition states studied in this Section. Our best estimation for the adsorption and reaction energies is  $E_{\text{PBE-D3}}^{\text{PBC}} + \Delta E_{\text{T46}}$ , in which  $\Delta E_{\text{T46}}$  is  $E_{\text{DLPNO-CCSD(T)}}^{\text{T46}} - E_{\text{PBE-D3}}^{\text{T46}}$ . Energy barriers are given in kJ/mol above the reaction arrow.

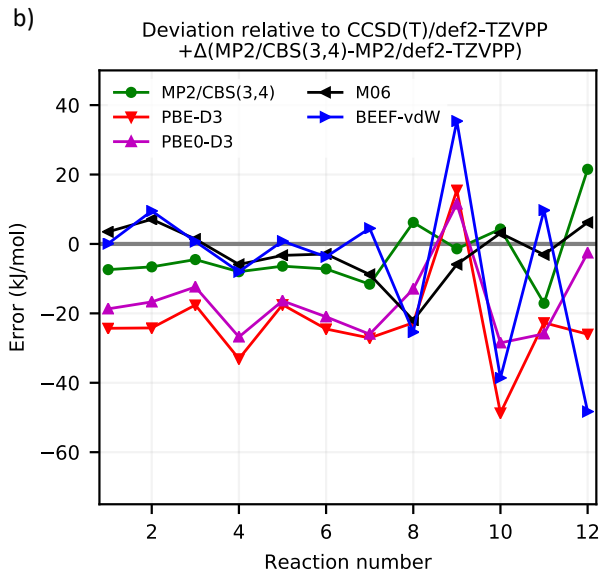


Our reference T46 adsorption/reaction energies and barriers are obtained using Equation 3.4.1.

$$E_{\text{DLPNO-CCSD(T)}}^{\text{T46}} = E_{\text{DLPNO-CCSD(T)/def2-TZVPP}}^{\text{T46}} + \Delta E_{\text{CBS}}^{\text{T46}} \quad (3.4.1)$$

In which  $\Delta E_{\text{CBS}}^{\text{T46}} = E_{\text{DLPNO-MP2/CBS}}^{\text{T46}} - E_{\text{DLPNO-MP2/def2-TZVPP}}^{\text{T46}}$  represents the complete basis-set extrapolation increment. With that, we can now compare the achieved results with DFT/def2-TZVPP using TURBOMOLE, [175, 176] BEEF-vdW/hard-PAW [186–188] using VASP [186, 187, 189–191] and MP2/CBS(3,4), with CCSD(T)/CBS(3,4) using ORCA (Figures 3.2 and 3.3). [106, 107] The mean absolute errors (MAE) and mean signed errors (MSE) for all reactions from Scheme 3.1 are shown in Figure 3.2 a). Overall, the best performing approaches are M06 and MP2 with mean absolute errors below 10 kJ/mol with a maximum deviation of 22 kJ/mol for both cases (Table A.1).

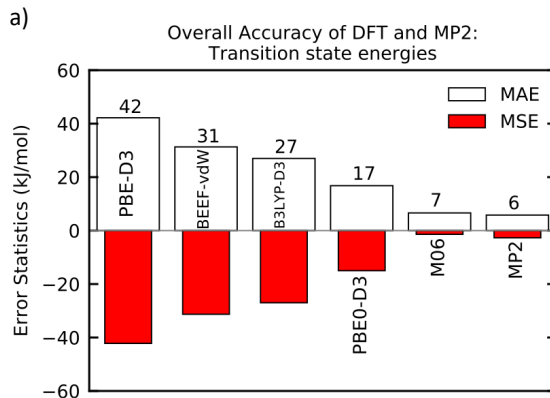




**Figure 3.2:** Comparison of CCSD(T)/CBS(3,4) reaction energies with several DFT/def2-TZVPP methods, BEEF-vdW/hard-PAWs and MP2/CBS(3,4) for the T46 clusters. a) shows the mean absolute error and mean signed error (values are explicitly shown in Table A.1), while b) lists the individual contributions of all reactions. Note that CCSD(T) and MP2 calculations were performed using the DLPNO approximation with "TightPNO" thresholds for the T46 cluster model.

We observe that the D3-corrected functionals PBE-D3 [89–91] and PBE0-D3 [96] systematically lead to too strong adsorption by around 20 kJ/mol which can be attributed to vdW, in agreement with the results obtained by Sauer et al. for the adsorption energies for ethene, benzene and ethylbenzene in H-ZSM-5, which leads to an overestimation of binding energies from 7-26 kJ/mol using PBE-D/QZVP when compared to MP2/TZVP(P). [75] MP2 shows systematically too strong adsorption, however with an error below 10 kJ/mol. M06 [93] and BEEF-vdW [188] have no systematic error and have also a low MAE for adsorption. Figure A.17 shows the energy contribution from the D3 dispersion corrections for PBE, PBE0 and B3LYP functionals.

The results shown in Figure 3.3 correspond to the barriers described in Scheme 3.2, where Figure 3.3 a) shows the MAE and MSE while Figure 3.3 b) shows the individual errors for the corresponding reactions. For adsorption and reaction energies, B3LYP-D3 shows an identical trend as PBE-D3 or PBE0-D3 whereas for transition states, the trend is similar to BEEF-vdW.



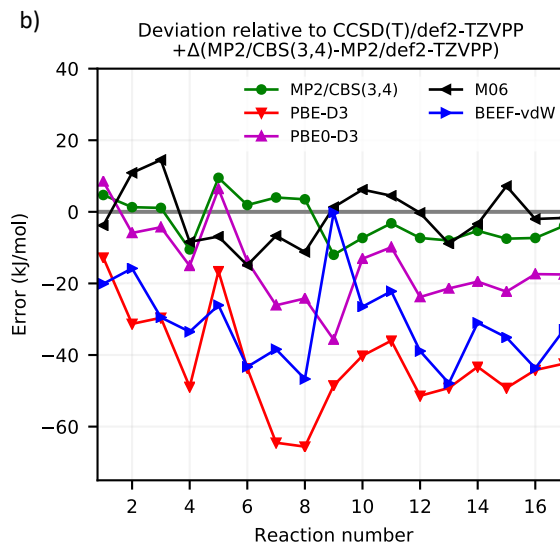


**Figure 3.3:** Comparison of CCSD(T)/CBS(3,4) transition states with several DFT/def2-TZVPP methods, BEEF-vdW/hard-PAWs and MP2/CBS(3,4) for the T46 clusters. a) Shows the mean absolute error and mean signed error (values are explicitly shown in Table A.2), while b) lists the individual contributions of all reactions. Note that CCSD(T) and MP2 calculations were performed using the DLPNO approximation with "TightPNO" thresholds for the T46 cluster model.

Both PBE-D3 and BEEF-vdW severely underestimate barriers with errors often in the range of 40 kJ/mol or higher. Some of the reaction barriers in Scheme 3.2 are intrinsic barriers and do not involve an adsorption step, as the reactant is already adsorbed (for example MeOH in reactions 1 and 6). Many reactions, however, require the adsorption of additional reactants. Generally, these reactants get larger with the reaction number in Scheme 3.2, leading up to the methylation of benzene. The error observed for these species is therefore a combination of the error in adsorption and the actual barrier. This is likely the reason for the systematic underestimation of the barriers for the methylation reactions 12-17 by PBE0-D3 (error around -20 kJ/mol) and MP2 (error around -7 kJ/mol). These errors can thus be attributed to too strong adsorption, while the trend is less clear for reactions 1-11, where the error is unsystematic, in particular for MP2. Overall, we again obtain the lowest MAE for MP2 and M06, both below 10 kJ/mol, while all other density functionals perform significantly worse with PBE-D3 showing the largest errors (MAE=42 kJ/mol), as can be observed in Table A.2.

To obtain our best guess for the adsorption/reaction energies and transition states (values above arrows in Schemes 3.1 and 3.2), we extrapolate  $E_{\text{PBE-D3}}^{\text{PBC}}$  results into  $E_{\text{CCSD(T)}}^{\text{PBC}}$  as shown in Equation 3.4.2.

$$E_{\text{CCSD(T)}}^{\text{PBC}} = E_{\text{PBE-D3}}^{\text{PBC}} + (E_{\text{CCSD(T)}}^{\text{T46}} - E_{\text{PBE-D3}}^{\text{T46}}) \quad (3.4.2)$$

$E_{\text{PBE-D3}}^{\text{PBC}}$  represents energies obtained using the periodic model with the PBE-D3/hard-PAW functional,  $E_{\text{CCSD(T)}}^{\text{T46}}$  corresponds to energies computed using the T46 cluster model with the DLPNO-CCSD(T)/CBS(3,4) (see Equation 3.4.1) and  $E_{\text{PBE-D3}}^{\text{T46}}$  refers to energies achieved using also the T46 cluster model with PBE-D3/def2-TZVPP.

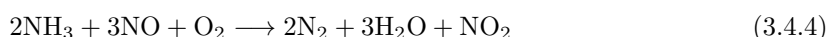
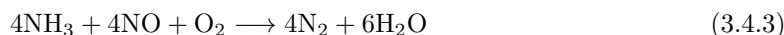
In this section, to calculate accurate values for reaction energies and barriers:

- The approximate HF exchange (COSX) was employed to speed up the calculations on T46 cluster model;
- A complete basis-set study was performed for post-HF and DFT methods;
- Comparison between MP2 and CCSD(T) was done;
- Difference between BEEF-vdW and PBE-D3 for T46 and PBC was done.

For more information about convergence tests and its implications, check Section A.1.1.

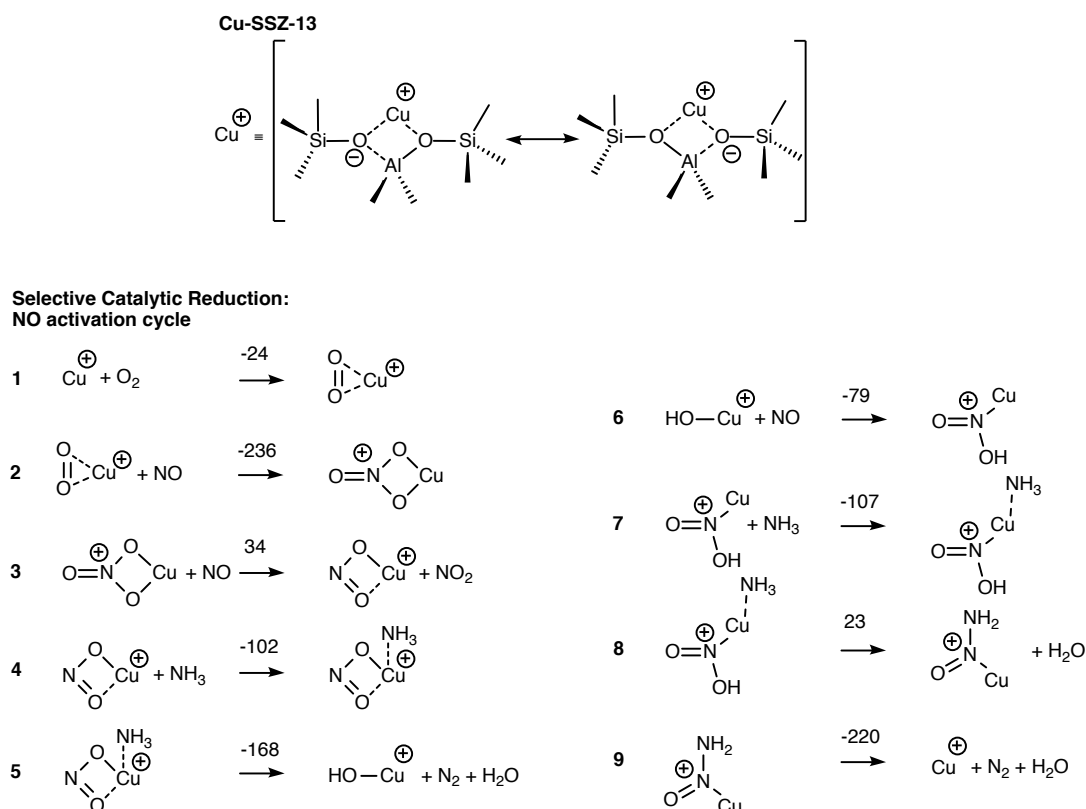
### 3.4.2 Selective Catalytic Reduction

In this section, the accuracy of DFT will be studied for the redox chemistry of ammonia SCR using Cu-SSZ-13. Similar to H-SSZ-13, we have modeled this catalytic material by exchanging one Si with one Al atom per unit cell with the charge being compensated by a single Cu atom with an oxidation state of +1. Extensive experimental and theoretical work has led to the establishment of a standard SCR reaction (Equation 3.4.3), which is a combination of the NO activation cycle and fast SCR (Equations 3.4.4 and 3.4.5) [197] with a recent contribution showing a consistent reaction scheme for both. [45, 198]



In contrast to the acid-catalyzed reactions discussed in Section 3.4.1, reaction energies prove to be very challenging for DFT. In this early stage of the SCR study, it is sufficient to simply look at energy minima based on selected reactions proposed in ref. [45] as part of the catalytic cycle, rather than comparing also energy barriers. These reactions are shown in Scheme 3.3. It is important to note that not all of these reactions are elementary reactions. In particular, reactions 5 and 9 contain multiple elementary reactions in which several bonds are formed and broken.

**Scheme 3.3** Resonance structures of Cu-SSZ-13 and the reactions from the NO activation cycle of the SCR, based on the reaction mechanism proposed by Janssens et al. [45] Reaction energies above arrow are extrapolated using the correction  $E_{\text{PBE-D3/hard-PAW}}^{\text{PBC}} + \Delta E_{\text{T46}}$ , in which  $\Delta E_{\text{T46}}$  is  $E_{\text{DLPNO-CCSD(T)/CBS(3,4)}}^{\text{T46}} - E_{\text{PBE-D3/def2-TZVP}}^{\text{T46}}$ .



In reaction 1,  $\text{O}_2$  is activated by the active site and reacts with two  $\text{NO}$  molecules to form adsorbed  $\text{NO}_2$  and free  $\text{NO}_2$  (reactions 2 and 3). This reaction is accompanied by a change of the oxidation state of copper from +1 to +2. The first three steps could therefore be bypassed in the presence of  $\text{NO}_2$ , e.g. in the fast SCR. In steps 4 and 5,  $\text{Cu-NO}_2$  adsorbs and reacts with  $\text{NH}_3$  to form  $\text{N}_2$  and  $\text{H}_2\text{O}$ , while a hydroxyl group remains at the active site ( $\text{Cu-OH}$ ). Next,  $\text{NO}$  is adsorbed and inserted into the hydroxyl group and reacts with  $\text{NH}_3$  to form a N-N bond. In two consecutive steps,  $\text{H}_2\text{O}$  and  $\text{N}_2+\text{H}_2\text{O}$  are released, eventually returning  $\text{Cu}$  to oxidation state +1.

In order to perform an extensive benchmark analysis, several different models of  $\text{Cu-SSZ-13}$  have been tested and compared with different levels of theory, similar as described for  $\text{H-SSZ-13}$ . While  $\text{CCSD(T)}$  is an established benchmark method for the acid-catalyzed reactions studied in the previous section, [73–77] this is less clear for  $\text{Cu-SSZ-13}$ . D1 and T1 diagnostics were checked (see Table A.4), and do not indicate multireference character, as  $\text{D1} \leq 0.15$  and  $\text{T1} \leq 0.05$  indicates single-reference character for transition metal catalysis, according to a study published by Wilson and co-workers. [181] The smallest model, the T1 cluster, corresponds to one  $\text{Cu}^+$  ion coordinated to an  $\text{Al(OH)}_4$  tetrahedron as shown in Figure 3.1 b) and has already been used previously for theoretical studies. [199–202] This model has been used to calculate the reaction energies shown in Scheme 3.3 not only to compare canonical and  $\text{DLPNO-CCSD(T)}$  calculations, but also to carry out a complete basis-set study using the Dunning’s basis-sets. [98–102]

Similar to the description in the last sections, the T46 clusters were generated by performing first DFT calculation employing periodic boundary conditions and then cutting the cluster from the periodic structures. As a reference method, we perform  $\text{DLPNO-CCSD(T)/def2-TZVPP}$  calculations introduced above, which are additionally corrected evaluating the difference between canonical and  $\text{DLPNO-CCSD(T)}$  on the T1 cluster model and also corrected using  $\text{CCSD/CBS(3,4)}$  extrapolation techniques, with Dunning’s  $\text{cc-pVXZ}$  basis-sets, as depicted in Equation 3.4.6.

$$E_{\text{CCSD(T)/CBS(3,4)}}^{\text{T46}} = E_{\text{DLPNO-CCSD(T)/def2-TZVPP}}^{\text{T46}} + \Delta E_{\text{CBS}}^{\text{T1}} + \Delta E_{\text{DLPNO}}^{\text{T1}} \quad (3.4.6)$$

In which  $\Delta E_{\text{CBS}}^{\text{T1}} = \Delta E_{\text{CCSD/CBS(3,4)}}^{\text{T1}} - \Delta E_{\text{CCSD/def2-TZVPP}}^{\text{T1}}$  represents the complete basis-set extrapolation increment taken from the T1 cluster model (extrapolation method discussed Section 2.3.5.1 from Chapter 2) with the  $\text{CCSD}$  level of theory, as the perturbative triples increment has a very low dependence on the basis-set used.

The last extrapolation term,  $\Delta E_{\text{DLPNO}}^{\text{T1}} = E_{\text{CCSD(T)/def2-TZVPP}}^{\text{T1}} - E_{\text{DLPNO-CCSD(T)/def2-TZVPP}}^{\text{T1}}$ , represents the canonical-DLPNO shift extrapolated from the T1 cluster model. The extrapolated reaction energies shown in Equation 3.4.6 constitute our best values and is the reference method to compare different density functionals as Figure 3.4 shows.

To check the accuracy of this approach, the formation enthalpies of the molecules in Equations 3.4.3, 3.4.4 and 3.4.5 ( $\text{NO}$ ,  $\text{NO}_2$ ,  $\text{NH}_3$ ,  $\text{H}_2\text{O}$ ) were computed and agree well with experimental reference values with errors on the order of 5 kJ/mol (see Table A.7 in the appendix). Since the overall reactions in Equations 3.4.3, 3.4.4 and 3.4.5 include many broken and formed bonds, the error is larger for these reactions, on the order of 20 kJ/mol. This is an acceptable range of error as the overall reaction energies are on the order of  $> 1000$  kJ/mol.

As shown in Figure 3.4 a), the mean absolute errors and mean signed errors of the various functionals are 49 kJ/mol and 7 kJ/mol for  $\text{PBE-D3}$ . The best-performing functional,  $\text{M06}$ , is still off by 17 kJ/mol (MAE) with a MSE of 1 kJ/mol. As expected, the largest errors occur for reactions 5 and 9, where multiple bonds are broken and formed. Without these reactions (MAE\* and MSE\* in Figure 3.4 a) the accuracy is significantly improved, but reaction energies have still mean absolute

errors of  $> 10$  kJ/mol.

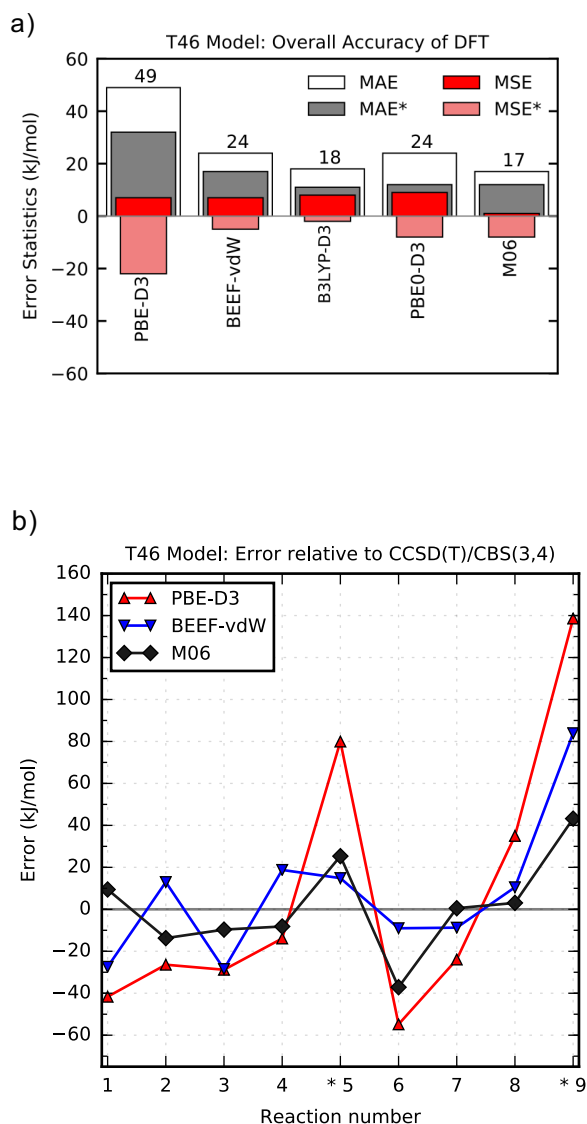


**Figure 3.4:** Comparison of CCSD(T)/CBS(3,4) with several DFT/def2-TZVPP methods along with BEEF-vdW/hard-PAWs is shown for the T46 clusters in which a) lists the mean absolute error and mean signed error. MAE\* and MSE\* represent the MAE and MSE excluding non-elementary step reactions, which are reactions 5 and 9 from Scheme 3.3. And b) lists the individual contribution of all reactions. The numbers in the x-axis represent reactions according to Scheme 3.3.

The results of both benchmarks are summarized in Figure 3.5, which shows the MAE for selected functionals.

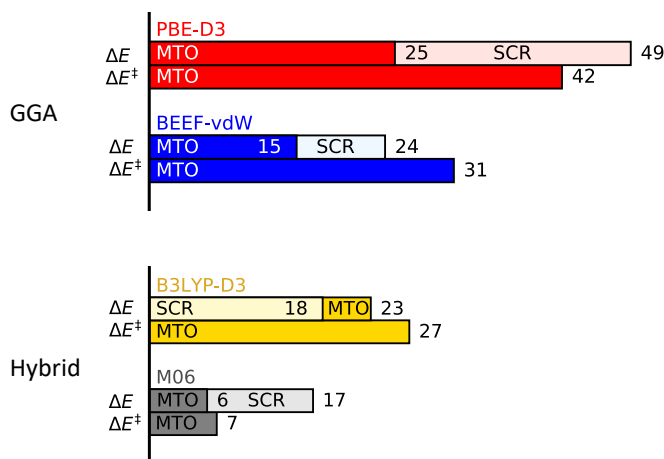


**Figure 3.5:** Overview of the mean absolute error (MAE) in kJ/mol of different functionals for reaction energies and barriers for both MTO and SCR-related reactivity catalyzed by H-SSZ-13 and Cu-SSZ-13 respectively.

Figure 3.5 shows that the error can be significantly reduced when going from PBE-D3 (GGA) to BEEF-vdW (also GGA) or hybrid functional B3LYP-D3. The best tested functional is M06 with errors only slightly above 5 kJ/mol for acid-catalyzed reactions. When using DFT to model reactions in zeolites, the M06 functional is a good alternative, while PBE-D3 functional estimated MTO and SCR reactions poorly. In OME synthesis, PBE-D3 is a good choice for estimating reaction energies with a very low MAE. However, transition states were found to be systematically underestimated by around 20 kJ/mol. MP2 methods were considered to be used in OME synthesis through homogeneous catalysis instead (study performed in Chapter 6).

The last step in the study is to obtain the most accurate reaction energies for the periodic model (final numbers are shown in Scheme 3.3, above arrows), also including thermodynamic corrections using the harmonic approximation at 473 K, which is within the range of low-temperature SCR. Having an accurate reference method for the T46 cluster model, the only step left to perform is to extrapolate those results limited by the size of the clusters, into the periodic structures using the relation  $E_{\text{PBE-D3/hard-PAW}}^{\text{PBC}} - E_{\text{PBE-D3/def2-TZVPP}}^{\text{T46}}$ , which is the extrapolation increment added into the  $E_{\text{CCSD(T)/CBS(3,4)}}^{\text{T46}}$  energies.

In this section, to calculate accurate values for reaction energies:

- A complete basis-set study was performed for CCSD;
- Comparison between MP2 and CCSD(T) with UHF and ROHF was done;
- Study of the dependency of the basis-set to calculate perturbative triples was done;
- DLPNO-CCSD(T) with different thresholds was calculated;
- Comparison between PBE-D3 using Gaussian basis-sets and PAWs was done.

For more information about convergence tests and its implications, check Section A.1.2.

### 3.5 Conclusion

The accuracy of DFT in the field of zeolite catalysis was investigated using H-SSZ-13 and Cu-SSZ-13 as an example. DLPNO-CCSD(T) is used as a reference method along with complete basis-set extrapolation for either CCSD or MP2. For acid-catalyzed reactions with relevance to DME synthesis and the MTO process both M06 and MP2 perform well with mean absolute errors below 10 kJ/mol. D3-corrected DFT (PBE-D3 and PBE0-D3) systematically overestimates adsorption by as much as 20 kJ/mol, while MP2 leads to systematic errors of around 5 kJ/mol. Barriers, on the other hand, are typically underestimated, with hybrid functionals performing better than GGA functionals, which have MAEs of up to 42 kJ/mol (in the case of PBE-D3). Importantly, it was observed that the errors are often systematic and similar for a given type of reaction. This means that they could potentially be systematically corrected without the need for expensive higher-level method calculations. This also means that energy differences across different materials can be meaningfully compared with DFT for a given class of reactions. Both M06 and MP2 perform best for barriers with mean absolute errors below 10 kJ/mol.

For Cu-SSZ-13-catalyzed redox reactions with relevance for SCR, we focused on the description of reaction energies using DFT. The tested density functionals have mean absolute errors in the range of 17 (M06) to 32 (PBE-D3) kJ/mol for elementary reactions with hybrid functionals performing best, and similar or higher errors for the corresponding reaction barriers are expected. Importantly, the active site studied in this work contains only a single copper atom. Multinuclear copper sites have also been considered and the results of our study may have limited transferability in these cases. [111] The focus of our study was on the ground-state electronic energies that have relevance for catalysis. The ranking of functionals herein is thus with respect to an accurate description of energies, [203] while other properties such as the ground-state density may actually be less well described. The best performing functionals identified herein are hence not necessarily the best choice for other properties.

Overall, our study shows that errors in barriers and reaction energies can be relatively large, depending on the density functional, and results must therefore be analyzed carefully. Some errors are systematic, e.g. for PBE-D3 barriers are too low and adsorption is too strong. These effects can therefore be qualitatively anticipated to some extent and typically allow for a comparison across a range of materials, while a quantitative analysis requires more accurate calculations.

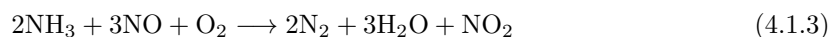
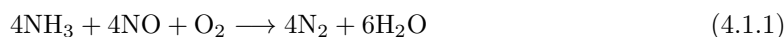


## Chapter 4

# Selective Catalytic Reduction of NO<sub>x</sub> by Ammonia using Cu-SSZ-13

### 4.1 Introduction

NO<sub>x</sub> exhaust gases, products of the oxidation of nitrogen during the combustion of fuels at high temperatures, are still one of the major contributors to local air pollution, hence their emissions are being strictly controlled. [127,204] These gases can be selectively reduced by ammonia under lean conditions over different catalysts such as transition-metal exchanged zeolites and transition-metal oxide catalysts. [41–53,197] This chapter deals with computational investigations of the reaction mechanism of NO<sub>x</sub> reduction with ammonia over copper-exchanged SSZ-13. The key reaction is the formation of nitrogen and water according to Equation 4.1.1, also called the “Standard SCR”, [45,197,198] which is a combination of Equations 4.1.2 and 4.1.3 that are depicted below.



If NO<sub>2</sub> is present, nitrogen is also formed via Equation 4.1.2, also called “fast SCR” since its efficiency, above 473 K, is at least 10 times higher than the “standard SCR”. [45,58,205] Additionally, there is the so-called “NO activation cycle” shown in Equation 4.1.3. During the standard SCR, there is no excess of NO<sub>2</sub> and as the fast cycle depends on the amount of NO<sub>2</sub> available, the standard SCR is limited to the rate of NO<sub>2</sub> formation. [45,61,62]

Herein we focus on Cu-SSZ-13 that has been shown to have a high activity in NO<sub>x</sub> reduction and a high hydrothermal stability. [34,41–43,48] Studies suggest that single-copper sites in SSZ-13 are suitable for the fast SCR, while reaction barriers were determined to be very high for the NO activation cycle, which suggests that the splitting of molecular oxygen goes through a different process. Copper ions are considered to be very mobile, and desorbed copper complexes such

---

This chapter is based on the following publication: Goncalves, T. J.; Plessow, P. N.; Studt, F., A Theoretical Study of the Selective Catalytic Reduction of Nitrogen Oxides by Ammonia using Cu-SSZ-13, in preparation.

as  $\text{Cu}(\text{NH}_3)_2^+$  pairs, have been proposed to split  $\text{O}_2$  as these barriers are considerably lower in comparison. [45, 47, 61, 62, 162]

As shown in Chapter 3, commonly used DFT functionals are prone to significant errors for this kind of systems. We therefore use hierarchical cluster models to correct energies by using higher-level methods. This procedure consists of considering different layers of the catalyst, where clusters that include the active site are cut and modeled by using accurate (and demanding) methods, while in the periodic limit (under periodic boundary conditions) lower-level methods are used. [73–77, 135, 136, 192] We focus on the reactivity of single sites, by optimizing periodic structures (PBC) with DFT. Structures with 46 tetrahedral atoms (T46) are cut from the periodic structures and saturated with hydrogen atoms in Si-terminations to perform DFT and DLPNO-CCSD(T) single-point calculations. Clusters with one tetrahedral atom (T1) are fully optimized and only model the reactive site. Accurate energies are obtained with Equation 4.1.4.

$$E_{\text{CCSD(T)}}^{\text{PBC}} = E_{\text{PBE-D3}}^{\text{PBC}} + E_{\text{DLPNO-CCSD(T)}}^{\text{T46}} - E_{\text{PBE-D3}}^{\text{T46}} \quad (4.1.4)$$

Although considering the mobility of multiple copper ions in the chabazite framework may be essential for the standard SCR reactions, we chose to investigate the activity of close-to-static single-copper sites in the vicinity of aluminum atoms, with a Si/Al ratio of 35 (same framework used in Chapter 3). With that, we evaluate reactions of the fast SCR in single-copper sites and study a complete mechanism.

## 4.2 Methods

Periodic calculations were carried out with DFT using the VASP program package [186, 187, 189–191] with the PAW method [186, 187] and the PBE-D3 functional to find minima and transition states. TS scans were performed with constrained optimizations using ARPES. [85] The dimer method [206] and Nudged Elastic Band [84, 207–209] from the Atomic Simulation Environment [87] were also used.

To improve the reaction energies and barriers, a cluster is cut from the periodic structure, so that the entire pore from the Cu-SSZ-13 is modeled and the H-terminations are at least five bonds away from the active site, containing 46 tetrahedral atoms. DLPNO-CCSD(T)/def2-TZVPP [99, 185] single-point calculations were then performed with Quasi-Restricted Orbital [107] treatment with ORCA program package [106, 107] as well as PBE-D3 with TURBOMOLE.

Geometry optimizations were performed using PBE-D3/dhf-SV(P) [89–91, 97, 179, 184] and the RI approximation [103] for the T1 cluster model, along with CCSD(T)/def2-TZVPP [178–181, 184] single-points and thermodynamic corrections at 473 K using the TURBOMOLE program package, [175, 176] to have an estimate of the Gibbs free energy profile. An optimized rhombohedral unit cell of the Cu-SSZ-13 zeolite was used. TS scans for the T1 cluster model were performed with relaxed potential surface scans and local quasi-Newton optimizations. [210, 211]

By using the DLPNO-CCSD(T) approximation, [99, 185] the performance scales well with the size of a system compared to canonical CCSD(T), with deviations in reaction energies smaller than 10 kJ/mol. [174] The formation of an H-terminated cluster that models the relevant electronic structure of the periodic zeolite, by cutting an amount of tetrahedral atoms, allows calculations in real space. To study the SCR mechanism, we employ a hierarchical cluster approach (as in Chapter 3). [73–77, 135, 136, 192] The different cluster models are depicted in Figure 3.1 b.

DFT energies on the periodic systems were corrected by extrapolating results from the T46 cluster (46 tetrahedral atoms) with the DLPNO-CCSD(T) level of theory, as shown in Equation 4.1.4.

We compared intrinsic barriers to show the deviations of T46 clusters with respect to PBC. Overall, the T46 cluster model can predict barriers with the accuracy of the periodic limit (with a MAE of close to 5 kJ/mol) as shown in Figure B.1.

We have evaluated D1 diagnostics on the CCSD level of theory for T1 cluster models to check how reliable single-reference coupled-cluster results are. Table B.2 shows D1 diagnostics for the structures used in this work. Additionally, we compared DLPNO-CCSD(T) with DLPNO-CCSD to see the contribution of perturbative triples in reaction energies and transition states for the T46 cluster models (Table B.3). Structures and barriers that may indicate multi-reference character for the fast SCR (black cycle) are 5, 9, TS\_8-9<sup>1</sup> and TS\_9-10 with D1 diagnostics of 0.19, 0.24, 0.22 and 0.28 respectively, which according to ref. [181], already indicates multi-reference character (values above 0.15 for catalysts with transition metals). We also found that structure 9 and TS\_9-10 have the biggest contributions of perturbative triples (around 50 kJ/mol). Nevertheless, the systems that indicate multi-reference character are assumed to have no impact in our conclusions for the fast SCR. However, the NO oxidation cycle has several structures with multi-reference character that may impact our conclusions.

### 4.3 Results

We investigated the mechanism of the fast SCR cycle on copper-exchanged SSZ-13 using the hierarchical cluster approach described above.

Scheme 4.1 shows various molecular steps of the investigated mechanism of the fast SCR cycle. Note that this cycle is almost identical to the earlier work of Janssens et al. [45] Several molecules can adsorb on the active site, which along the cycle can have different oxidation states, mostly +1 and +2, and +3 in rare cases. We start with the bare copper ion attached to the SSZ-13. We calculate that the adsorption free energies for NO<sub>2</sub> and NH<sub>3</sub> molecules on copper to be in the range of -100 to -50 kJ/mol, with NH<sub>3</sub> having the most exothermic adsorption (105 kJ/mol), whereas water and nitric oxide have adsorption free energies of around 0 kJ/mol.

We therefore start with the adsorption of ammonia as the first step in the catalytic cycle. After coadsorption of nitrogen dioxide, a hydrogen is transferred from ammonia, creating a copper adsorbed amino radical<sup>2</sup> and nitrous acid (HNO<sub>2</sub>) in a *cis* configuration, that is in equilibrium with the gas phase and can desorb. HNO<sub>2</sub> is eventually adsorbed on a clean copper atom and split into nitric oxide and a hydroxyl. In the next step, NO is desorbed, while the copper-adsorbed hydroxyl reacts with ammonia producing H<sub>2</sub>O and an amino radical (or azanide) adsorbed on a Cu. This is depicted in the “pink pathway” (cycle II) from Scheme 4.1. The Gibbs free energy profile for nitrous acid decomposition is depicted in Figure B.2, and we found that all transition states are reasonably low ( $\leq 140$  kJ/mol). NH<sub>2</sub> is then decomposed by adsorption of NO, where hydrogen atoms are subsequently transferred to the oxygen atom releasing molecular nitrogen and water. The process of adsorbing ammonia and NO<sub>x</sub> gases without nitrous oxide decomposition is depicted in the “black cycle” (cycle I) from Scheme 4.1. Between structures 9 and 10, multiple isomerization steps are omitted due to very low barriers (on the order of 10 kJ/mol).

Note that the copper atom is fairly mobile within the zeolite cage. While the bare copper prefers

<sup>1</sup>Indicates transition state between structures 8 and 9.

<sup>2</sup>It is unclear if Cu-NH<sub>2</sub> are copper-adsorbed amino radicals or azanides. In this work they are assumed to be amino radicals.

to adsorb at the middle of the 6-membered ring in the zeolite (40 kJ/mol more stable in Gibbs free energy than in the 8-membered ring, Figure 3.1 b), its location at the 8-membered ring is becoming energetically preferred upon adsorption of molecules such as ammonia and nitrogen dioxide. As these adsorbates have shown to form structures that are more stable than clean copper in the 6-membered ring by up to 60 kJ/mol, this isomer is not considered.

The formation of  $\text{Cu}(\text{NH}_3)_x^+$  complexes, confirmed by other authors, [45, 47, 162, 212] is also briefly investigated. According to Table B.1, the stability of Cu atoms with respect to clean Cu-SSZ-13 gets larger by increasing the quantities of ammonia adsorbed, which is slightly counter-acted by the increase of entropy. A single molecule of ammonia adsorbed on copper leads to an adsorption free energy of around -140 kJ/mol, while two and three molecules lead to copper becoming detached from the zeolite under formation of  $\text{Cu}(\text{NH}_3)_2$  and  $\text{Cu}(\text{NH}_3)_3$  complexes. While the stability of these complexes were calculated with PBE-D3 on the periodic model (Table B.1), it is expected that adsorption energies are slightly higher using higher-level methods (+40 kJ/mol for a single copper-adsorbed  $\text{NH}_3$  molecule). Note that typical amounts of ammonia during SCR are about 350-500 ppm [41–44] while our reference pressure has been set to 1 bar. By using pressure values close to those of the experiments, e.g. 350 ppm, adsorption energies will increase by about 35 kJ/mol. We note that the total correction to adsorption energies (about +75 kJ/mol) of ammonia on copper atoms do not influence our overall conclusions, as ammonia still strongly adsorbs on copper atoms.

**Scheme 4.1** a) Representation of the Cu-SSZ-13 resonant structures b) Overview of the “fast SCR” cycle, a catalytic conversion of NO<sub>x</sub> into water and N<sub>2</sub>. Copper atoms, that are connected to oxygen atoms, which are attached to aluminum, are purely represented as “Cu<sup>+</sup>”. Cycle I is the main “fast SCR” cycle (with arrows in black) and cycle II depicts HNO<sub>2</sub> decomposition (pathway with arrows in pink). From structure 3, HNO<sub>2</sub> is released and either resorbed on a different active site or resorbed on the same after the black cycle resets. Color scheme: Blue – Reactants (except 3a which is both a reactant and a product); Red – Products; Brown – Oxygen atoms that belong to the framework.

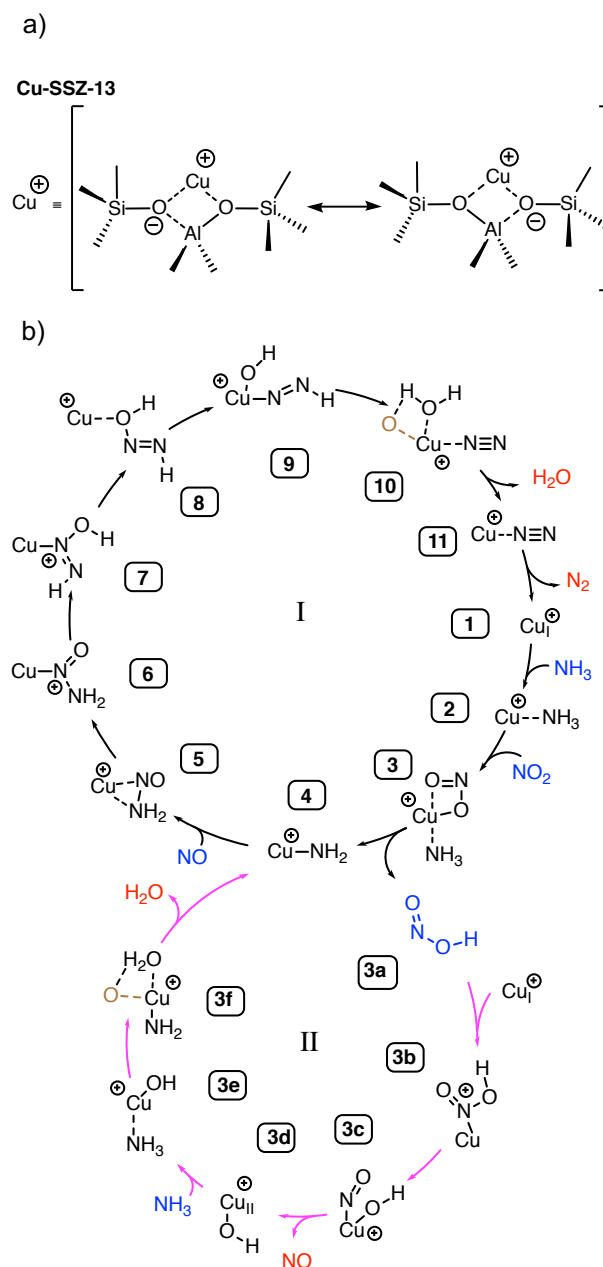
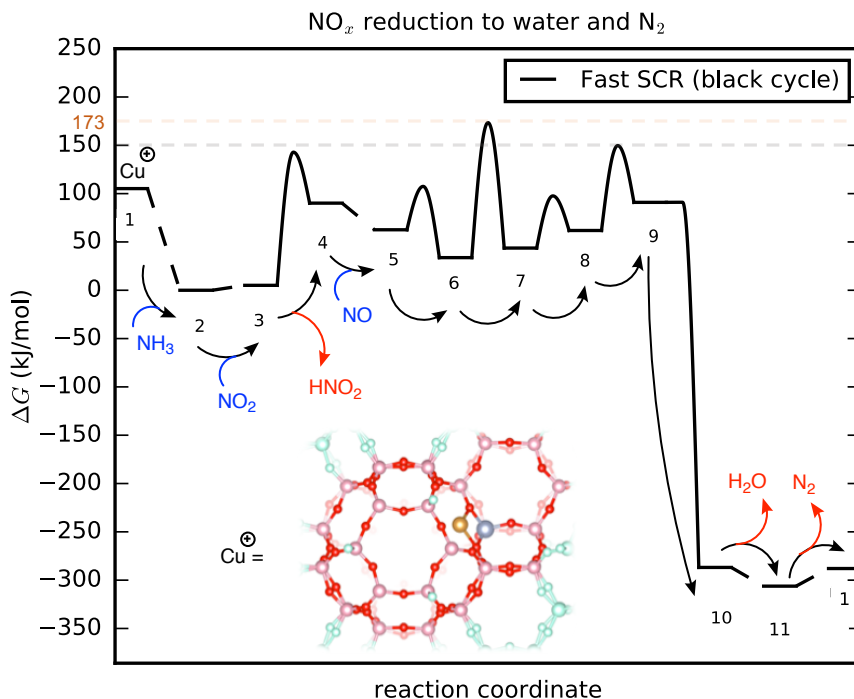


Figure 4.1 shows the free energy profile of the reaction mechanism depicted in Scheme 4.1. We find that overall, the mechanism seems feasible as all reaction barriers are below 150 kJ/mol with respect to the resting state (Cu-NH<sub>3</sub>). The only exception is found for the barrier between structures 6 and 7. This barrier corresponds to the hydrogen transfer from the amino radical to the oxygen from nitric oxide, which is calculated to 173 kJ/mol and we thus expect this to be

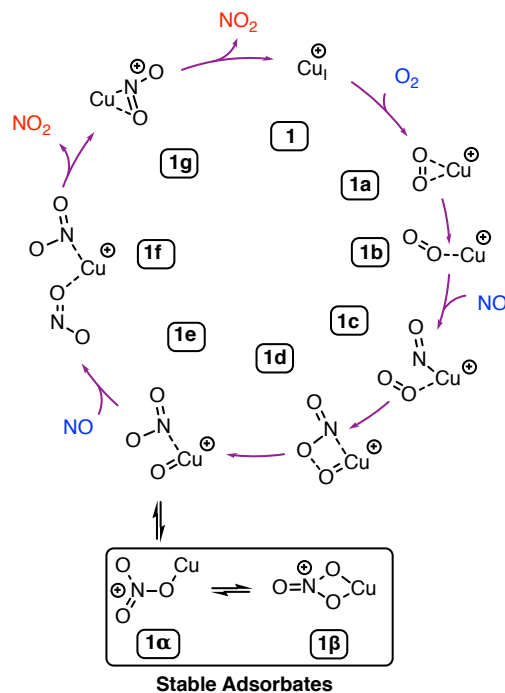
the rate-determining step in the fast SCR. Conclusive answers however, need a thorough kinetic analysis, which is beyond the scope of the present study. While it seems that the calculated free energy barrier of 173 kJ/mol is slightly higher than what one would expect for a reaction occurring readily at 473 K, we speculate that this is due to inaccuracies associated with the description of the entropy using the harmonic approximation.



**Figure 4.1:** Gibbs free energy profile at 473 K of the cycle depicted in black in Scheme 4.1. Reactions 1-11 are labeled according to Scheme 4.1. Molecules in blue show reactants while molecules in red show products. Barrier between structures 9 and 10 is only slightly higher (less than 5 kJ/mol) than the stability structure 9. Cu-NH<sub>3</sub> is considered to be the resting state ( $\Delta G=0$ ). Color scheme for the zeolite: Si – Pink; O – Red; Al – Gray; Cu – Brown; Periodicity – Green.

Reaction rates for fast SCR were reported to be almost 10 times higher than the standard SCR. This is due to the fact that the reduction of NO<sub>2</sub> will recover the resting state and occurs stoichiometrically, while the reduction of NO needs oxygen to partially oxidize NO to NO<sub>2</sub>. [213] The rate-determining step in the standard SCR is expected to be the oxidation of NO to form NO<sub>2</sub> [45] that is depicted in Scheme 4.2.

**Scheme 4.2** Illustration of the "NO activation cycle". Stable adsorbates represent energetically favorable intermediates that are formed during the oxidation process. Color scheme: Blue – Reactants; Red – Products.

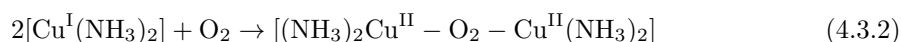


The oxidation of nitric oxide follows Equation 4.3.1. This formation is downhill by close to 32 kJ/mol, as shown in Figure 4.2.



As can be seen in Scheme 4.2, NO oxidation involves the adsorption of nitric oxide and oxygen on copper. This leads to the formation of adsorbed atomic oxygen and NO<sub>2</sub>, which react to form nitrates (depicted in "Stable Adsorbates").

The formation of nitrates therefore represents an energetic "sink" leading to blockage of the active site, rendering this reaction prohibitive at the active site investigated. One could therefore speculate that the reaction will not occur on isolated copper sites, it needs the formation of other active species. In fact, desorbed ammonia-copper complexes hint to be a feasible alternative for the oxidation of nitric oxides. These complexes react simultaneously with O<sub>2</sub>, creating a complex (depicted in Equation 4.3.2) that severs the oxygen molecular bond. Studies found that these barriers are below 50 kJ/mol. [45, 47, 162, 212]



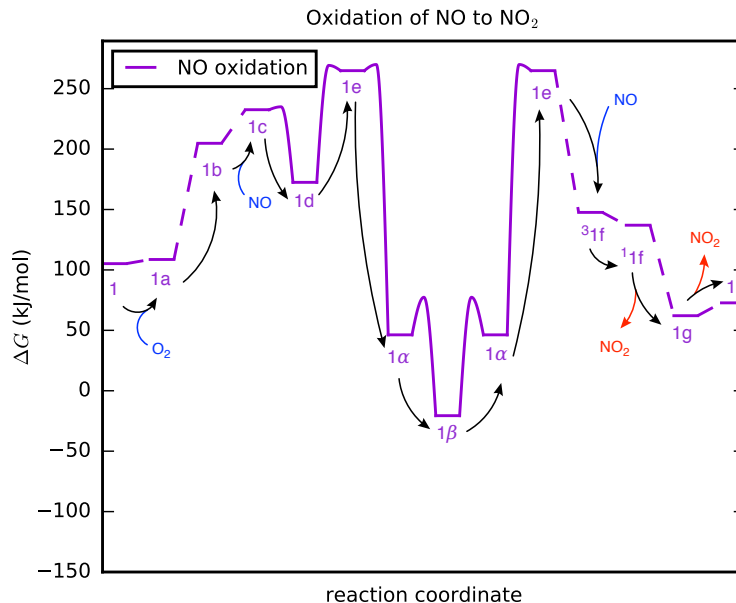


**Figure 4.2:** Gibbs free energy profile at 473 K of the cycle depicted in Scheme 4.2. Reactions 1a-1g are labeled according to Scheme 4.2. Molecules in blue show reactants while molecules in red show products. Barriers with entropy corrections that result in slightly lower free energies (1c-1d, 1d-1e and 1e-1 $\alpha$ ) than their minima are moved above 5 kJ/mol for representation purposes. <sup>3</sup>1f and <sup>1</sup>1f represent triplet and singlet states of structure “1f”.

## 4.4 Conclusion

The  $\text{NO}_x$  reduction to molecular nitrogen and water was investigated using a hierarchical cluster approach employing the higher level method DLPNO-CCSD(T) for the “fast SCR” and “NO activation cycle”. Based on the findings from our calculations, we propose a detailed reaction mechanism. We found that nitrous acid ( $\text{HNO}_2$ ) is formed and released into gas phase, which is eventually decomposed (on copper sites) into nitrogen monoxide and water by reacting with ammonia. Barriers for the fast SCR are usually less than 140 kJ/mol with the exception of the hydrogen transfer between an amino radical and nitric oxide, that leads to a barrier of 173 kJ/mol.

Our calculations on the oxidation of NO on single copper sites show that these have prohibitively high barriers [45,61] of 265 and 285 kJ/mol. This has also been found in earlier studies and indicate to the necessity for copper to form dimers to reduce reaction barriers to a reasonable level.

## Chapter 5

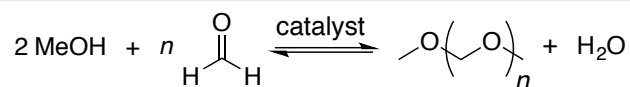
# Synthesis of Oxymethylene Dimethyl Ethers using H-BEA

### 5.1 Introduction

Oxymethylene dimethyl ethers (OMEs) are being considered as an alternative synthetic fuel for the transportation sector where they are receiving growing interest as diesel fuel substitutes owing to their favorable properties regarding the reduction of soot and NO<sub>x</sub>. [22, 23, 215–219] OME production is based on methanol which can be produced from syngas, derived from renewable resources.

Oxymethylene dimethyl ethers<sup>1</sup> were discovered early in twentieth century by Staudenger, a German chemist, and have the general formula CH<sub>3</sub>-(O-CH<sub>2</sub>)<sub>n</sub>-O-CH<sub>3</sub>. OMEs can be synthesized via oligomerization of formaldehyde (FA) and end-capping of the oligomers by acetalization with methanol. The general route for OME synthesis from MeOH and FA is shown in Scheme 5.1. The main drawback of this reaction is that it produces stoichiometric amounts of water, which promotes the formation of byproducts and lowers the OME yield. [220, 221]

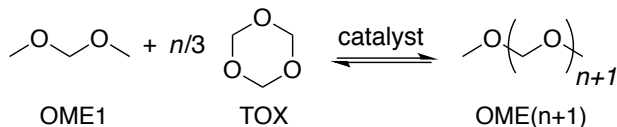
**Scheme 5.1** OME Synthesis from FA and methanol.



Variations of the synthesis route shown in 5.1 differ in the choice of FA sources and end-capping reagents. The reaction of trioxane (TOX) as the FA source with OME1 as the end-capping reagent has attracted recent interest as the reaction proceeds without the formation of water. [222] OME1 provides the end-capping groups, while TOX provides three FA units. Additionally, OME1 introduces another FA unit, formally leading to simple chain growth of OME1 to OME<sub>n</sub>, as shown in Scheme 5.2.

This chapter is based on the following publication: [214] Adapted with permission from Goncalves, T. J.; Plessow, P. N.; Studt, F., Theoretical investigation of the acid catalyzed formation of oxymethylene dimethyl ethers from trioxane and dimethoxymethane. ACS Catal. 2017, 7, 3615–3621. Copyright 2017 American Chemical Society.

<sup>1</sup>Also denoted as Polyoxymethylene Dimethyl Ethers (POMEs)

**Scheme 5.2** Synthesis of OMEs from TOX and OME1.

While the direct reaction between OME1 and integer numbers of TOX as depicted in Scheme 5.2 would produce only OME(3T+1), where T is the number of trioxane molecules added, one usually finds all OMEs according to their thermodynamic equilibrium concentration. [222] The formation of OMEs other than OME4, OME7, etc., may result from a reaction mechanism that proceeds via single FA units and therefore directly accesses all OMEs or from subsequent transacetalization between OMEs (Scheme 5.3).

**Scheme 5.3** Transacetalization that effectively transfers  $\Delta n$  FA units from one OME to the other.

Different acidic catalysts were explored for this synthesis route, most of them being based on ion exchange resins [22, 215, 216, 222–224] and acidic zeolites such as H-ZSM5 [225] and BEA. [226] Suggestions on the reaction mechanism have been reported in the literature. [223] There are, however, no theoretical studies exploring the exact nature of intermediates and transition states for zeolites. Herein, we present a density functional theory (DFT) study of the reaction mechanism using H-BEA as the catalytic material and employing an explicit solvent correction scheme.

The first steps in investigating the OME synthesis are studying the location of the active site of the catalyst considered, the influence of the solvent exerted in the catalytic reaction of the formation of OME<sub>n</sub>, followed by a thermodynamic analysis.

## 5.2 Methods

Structures were optimized using DFT, employing the PBE functional. Energies were obtained as single points from these structures using the PBE-D3 method, the PBE functional, and Grimme’s dispersion correction. [91,97] We verified that structures change only slightly upon reoptimization at the PBE-D3 level so that the employed level of theory PBE-D3//PBE is a good approximation with deviations in reaction energies below 5 kJ/mol. Periodic calculations were carried out with the projector-augmented-wave (PAW) method using the VASP program package in version 5.4 as well as the standard VASP-PAWs. [186,187] An energy cutoff of 400 eV was used for the expansion of the wave function in the plane wave basis set, and 800 eV was used if the volume of the unit cell was changed in the optimization of cells. The Brillouin-zone was sampled at the  $\Gamma$ -point and Gaussian-smearing with a width of 0.1 eV was used. Benchmark calculations at the MP2 and CCSD(T) level of theory were carried out as single-point calculations with the def2-TZVPP basis-set, the resolution-of-the-identity approximation and appropriate auxiliary basis-sets, and the TURBOMOLE program package. [178,179] Free energies in the gas phase were obtained within the usual rigid rotator and harmonic oscillator approximation at  $T = 300$  K. Harmonic force constants were obtained from a central finite difference scheme where, in addition to the adsorbate, only part of the zeolite, the involved oxygen atom, and the adjacent Al and Si atoms were included. All transition states were verified to contain only a single imaginary harmonic frequency corresponding

to the transition vector of the reaction. Because the harmonic approximation can lead to inaccurate entropies for apparent low frequency vibrations in solution, all frequencies of adsorbates on the zeolite were raised to  $100\text{ cm}^{-1}$  if they were below this value. [227] Imaginary frequencies of minima occurred in three cases, resulting from extremely soft vibrational modes, and small numerical inaccuracies of the finite difference scheme for force constants were also raised to this value. In some cases, the entropic contributions to the free energy of small activation barriers resulted in small or even formally negative activation free energies. In these cases, the activation free energies were kept at  $5\text{ kJ/mol}$ . Free energies in solution were then obtained by adding the solvation free energies, as shown in Equation 5.2.1.

$$G_1(\chi) = G_g(p) + \Delta G_{\text{solv}}(\chi, p) \quad (5.2.1)$$

We chose a reference molar fraction of  $\chi = 1$  with the exception of methanol, which is formed only in catalytic amounts during the initiation reaction. Here, we used  $\chi \approx 1.5 \times 10^{-4}$ , which is the approximate concentration of active sites in experiments. For some reactions that differ only in chain length, results were extrapolated from lower chain lengths. This concerns the reaction of  $A_4$  to  $A_7$  (abbreviations taken from Scheme 5.4), which we assume to have the same free energy profile relative to  $A_4$  as that of the reaction from  $A_1$  to  $A_4$ , which we explicitly computed. The same assumption was made for the insertion of FA, where only the first reaction ( $A_1$  to  $A_2$ ) was explicitly computed, and the subsequent reactions ( $A_2$  to  $A_3$  and  $A_3$  to  $A_4$ ) are assumed to have the same barriers and reaction free energies. Details of energies and each contribution to the energy of each molecule (e.g. ZPVE and solvation corrections) are available in Table C.3.

## 5.3 Active Site and Solvation Models

### 5.3.1 Active Site

Our investigations focus on H-BEA-25 as one of the acidic catalysts that has been used experimentally, [226] with a Si:Al ratio of 25:1. We hence expect mainly isolated aluminum atoms within the pores of this catalyst and model the material by using one aluminum atom per unit cell of the zeolite (and thus a Si:Al ratio of 63:1). The structure of BEA gives rise to nine different isomers upon exchange of silicon with aluminum. Furthermore, the reactions can generally occur at any of the oxygens adjacent to Al that are exposed toward the pores of the zeolite. For this reason, we have tested three symmetry-inequivalent substitution-positions for aluminum, which are shown in Figure 5.1 and labeled T1, T2 and T3. T1 is at the intersection of two pores which run in orthogonal directions along the (100) and (010)-direction. These positions are therefore expected to provide more room for reaction with bulky substrate due to lower steric repulsion with the surrounding walls.

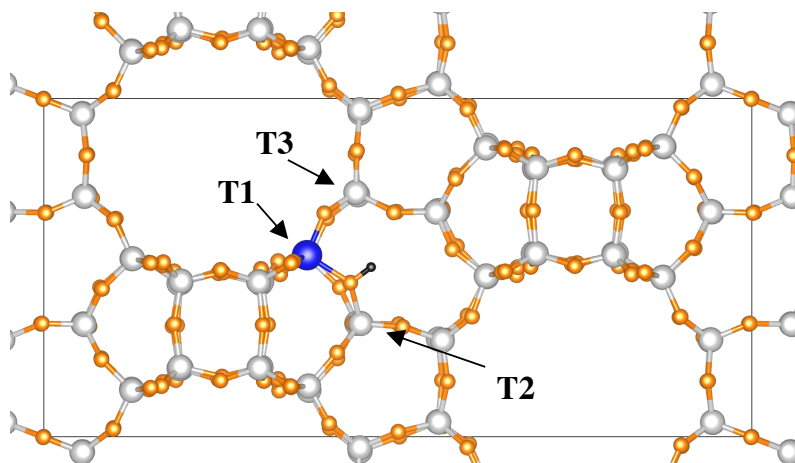


**Figure 5.1:** Model of the zeolite showing the position of aluminum (T1) to illustrate the active site position in the precatalyst, abbreviated as Al-OH or  $X_0$ . The other symmetry-inequivalent position of the Al investigated in this work are depicted as T2 and T3. The unit cell is also indicated with view along the  $(0\bar{1}0)$  direction. Color code: Al = blue, H = black, Si = gray, O = orange.

The stability of various intermediates relative to the reference energy of the T1 position are listed in Table C.1. In addition to the choice of Al-position, different reactions occur at different adjacent oxygen atoms (up to four), which are also listed in Table C.1. It can be seen that for most structures the most stable O-isomers of the three Al-isomers are within a range of 10 kJ/mol, e.g. we expect no significant difference in reactivity, when considering T1, T2 or T3. Transition state TS\_A1-B1 is an exception as all T2- and T3-isomers are at least 10 kJ/mol less stable than T1. This is due to the pore structure, where T1 provides most space for the alkylation of TOX. Despite the preferred locations of aluminum not being known experimentally, our calculations indicate that there are no significant differences for the intrinsic reactivity related to the various possible structural motifs. However, the chosen position can best accommodate bulky adsorbates and is therefore slightly more favorable for the reaction involving the ring-opening of TOX.

### 5.3.2 Explicit Solvation and Hydrogen-bonding

Since OME synthesis takes place in solution, solvation enthalpies were determined for all molecules and for selected zeolites by explicit solvation using periodic boundary conditions. This approach was chosen because the solvation enthalpy is almost entirely due to van der Waals (vdW) interactions, which is shown by comparison of the functional PBE with dispersion corrections (D3) and PBE without D3. This is deduced from the fact that solvation energies computed with PBE are negligible ( $<5$  kJ/mol) and PBE without D3 corrections do not account for vdW interactions. An exception are molecules that form hydrogen bonds and this will be discussed last in this subsection.

These kinds of interactions are generally difficult to account for with implicit solvation models, and for periodic structures, available models were validated mainly for cases where electrostatic interactions dominates. [228–230] The other issue is that the cavities constructed by most implicit solvent models, are not ideal to describe complex catalysts such as zeolites. These models usually replace the vacuum with a dielectric constant that defines the solvent, based on the constructed cavity, through a smoothed function to avoid a sudden solvent-to-solute region transition (with what would be a Heaviside step type of function). The problem is that in zeolites, for instance,

implicit models fail to predict which pores the solvent molecules cannot fit, which leads to error accumulation due to artificial interactions of the structure with a non-existent solvent.

We chose OME1 as the solvent, although initially, TOX is also present, and the composition of the solution changes with conversion and thus also contains OMEs of various chain lengths. Given the similarities between these molecules, however, we expect this to be a reasonable approximation. We have also considered two types of solvation structures. First of all, molecules such as OME, FA, and TOX have been placed in a large unit cell, where different initial structures were generated by manually rotating and translating adjacent solvent molecules into a few different orientations and by changing the number of solvent molecules per unit cell until it reaches a minimum in energy. This closely resembles the actual solvation structure and is labeled  $H_{\text{solv}}(\text{l})$ . Secondly, we have considered self-solvation, where the molecules have been placed in minimal unit cells containing only one molecule. This corresponds to a molecular crystal and is labeled  $H_{\text{solv}}(\text{s})$ . In both cases, structures as well as the volume of the unit cells were fully optimized at an increased energy cutoff of 800 eV. Since solvation is mainly due to vdW interactions and the structure of most molecules (OMEn, TOX) is similar,  $H_{\text{solv}}(\text{l})$  and  $H_{\text{solv}}(\text{s})$  deviate typically by less than 10 kJ/mol, as shown in Table C.2, giving confidence in the accuracy of the obtained solvation energies. Similar to what was found for OMEs, [231] there is a linear dependency of the solvation energy on the molecular size.

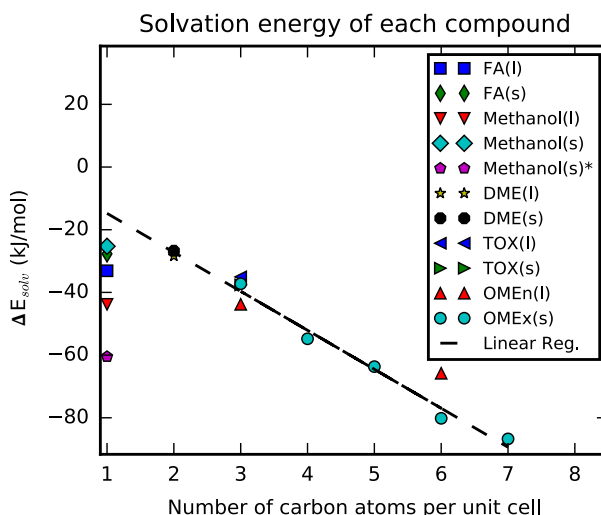


**Figure 5.2:** Solvation energies of the different molecules, methanol(s)\* contains two molecules per unit cell.

In Figure 5.2, the solvation energy increases linearly with the number of carbon atoms of the molecule. The obtained solvation energies are listed in Table C.2 and generally agree well with the experimental solvation enthalpies (between -20 to -60 kJ/mol for FA to OME4). In most cases, the computed solvation energies are more stable by around 10 kJ/mol which can be explained by the fact that the thermal motion in solution is not taken into account and that they really correspond to solvation enthalpies at  $T = 0$  K and correspond in fact to a (albeit somewhat disordered) crystal. The linear relationship of solvation energy as a function of the number of carbon atoms has been fitted (Equation 5.3.1) and used to compute all solvation enthalpies. An exception is FA, which deviates significantly and here the computed value of -33 kJ/mol has been used. The deviation of methanol molecules comes from hydrogen-bond formation, which is discussed last in this subsection. With the exception of these cases, enthalpies are in good agreement with

experimental reference values, it is also expected that this will also apply to solvation energies within zeolite pores. Choosing the number of carbon atoms,  $n_C$ , as our descriptor allows us to correlate the solvation enthalpy through Equation 5.3.1, giving a linear dependence.

$$\Delta H_{\text{solv}}^{\text{zeolite}} (\text{kJ/mol}) \approx -12.4 \times n_C - 2.3 \quad (5.3.1)$$

Solvation of zeolite structures has been carried out with the same approach, e.g. through explicit solvation with OME1 molecules. While for the molecular structures discussed above, the optimal density of the solvent (OME1) was obtained through optimization of the volume of the unit cell at a constant number of solvent molecules per unit cell, this is not possible for the zeolite structures. Here, at a constant unit cell of the zeolite structure, the number of OME1 molecules in the zeolite pore has been optimized as shown in Figure 5.3 a).

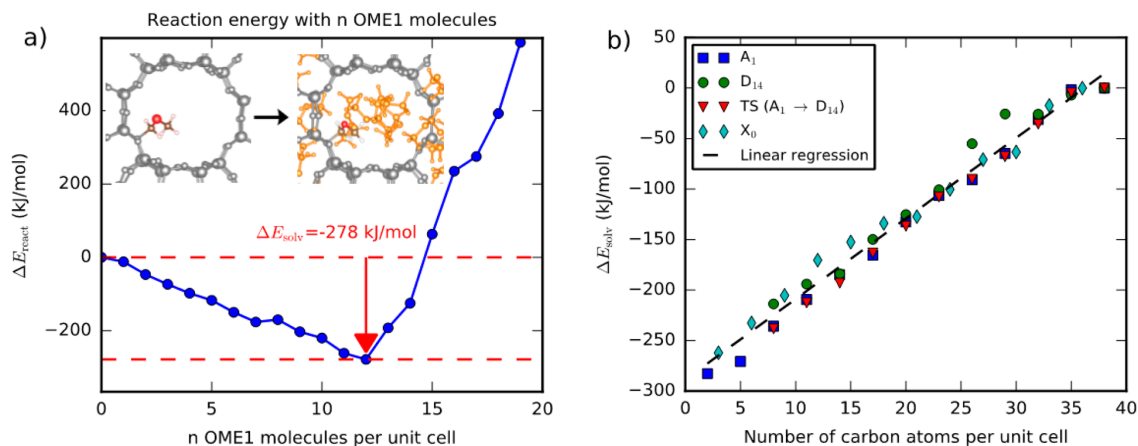


**Figure 5.3:** a) Determination of the solvation energy of a given zeolite structure by variation of the number of solvent molecules to obtain the solvation energy as the optimum (minimal) reaction energy. The inset shows the solvation process where the zeolite (structure A1) is shown in gray, the solvent in yellow, and the adsorbate color coded (C: brown, O: red, H: white). b) Solvation energy of zeolites with adsorbates as a function of the number of carbon atoms of the adsorbate. The notations  $A_n$ ,  $D_{nm}$  and  $X_n$  correspond to the labels defined in Scheme 5.4.

Using the data from Figure 5.3 b), we found a linear relationship with the size of the adsorbate in the zeolite and the solvation energy, shown in Equation 5.3.2. In contrast to Equation 5.3.1, the solvation energy of zeolite structures becomes smaller when the adsorbate is larger because fewer solvent molecules will fit into the pore. To improve our estimation of the linear relationship for the solvation of zeolite structures, we also included the structures required to determine the optimum number of solvent molecules. For example, the solvation energy of  $A_0$  (labels defined in Scheme 5.4), already solvated with two OME1 molecules is also included.

$$\Delta H_{\text{solv}}^{\text{zeolite}} (\text{kJ/mol}) \approx 8.0 \times n_C - 288.8 \quad (5.3.2)$$

Focusing on the most important structures, we have also explicitly solvated TS\_A1-A2 (labels defined in Scheme 5.4), the rate-limiting TS for the FA-pathway. The energy barriers for the TOX- and FA-pathway are 29 (32) kJ/mol and 17 (20) kJ/mol using the developed solvation model (explicit solvation). This level of agreement is certainly fortuitous but supports the validity of the approximate solvation model. A more accurate determination of the relative rates for TOX-

and FA-pathway would not only require more accurate solvation energies but also more accurate electronic energies and also entropies in solution.

As observed in Figures 5.2 and C.2, significant deviations from the trends for solvation occur when hydrogen bonds are present. This mainly concerns the zeolite precursor, Al-OH and methanol, these exceptions were excluded in obtaining the linear regression Equations 5.3.1 and 5.3.2 and were considered separately. Since the number of hydroxyl groups is always preserved (e.g., Al-OH releases methanol when initialized to Al-CH<sub>2</sub>-OMe), there is partial cancellation of the effect of hydrogen bonding. For self-solvation of methanol in the smallest unit cell, hydrogen bonding is geometrically impossible and only occurs when two methanol molecules per unit cell are used.

Since Al-OH is more acidic, the H-bond to OME1 is stronger than for methanol. Using PBE calculations to separate vdW-effects from hydrogen binding, we estimate the hydrogen binding strengths with OME1 as the acceptor to be roughly  $\Delta H = -70$  kJ/mol and  $-20$  kJ/mol for Al-OH and methanol. Importantly, directed interaction of a H-bond leads to a significant, negative association entropy that becomes generally more negative as the hydrogen bond becomes stronger. [232, 233] Measured values for association of 4-fluorophenyl with various ethers vary in the range of  $\Delta H$  of  $-20$  to  $-30$  kJ/mol with corresponding free energies  $\Delta G$  in the range of  $-10$  to  $-15$  kJ/mol. [232] The free energy  $\Delta G$  grows with  $\Delta H$ , roughly linearly with a slope of 0.5, as can also be extracted from the compilation of data available in the Supporting Information from ref. [233]. Using the approximation of this linear relationship, we extrapolate the contribution of entropic corrections,  $-T\Delta S$ , to hydrogen bonding at 300 K to be 10 kJ/mol for methanol and 35 kJ/mol for Al-OH. The discussed deviation of the solvation enthalpies of Al-OH and methanol from Equations 5.3.1 and 5.3.2 are taken into account by correcting methanol by the difference of this deviation, which is  $+40$  kJ/mol.<sup>2</sup> The difference in solvation entropies of the hydrogen bonds contributes  $-25(10-35)$  kJ/mol to the difference in solvation free energies (through  $-T\Delta S$ ). Overall, we estimate that hydrogen bonding changes the free energy of the initiation reaction by 15 (40-25) kJ/mol in favor of Al-OH. This value was added to the solvation free energy of methanol.

### 5.3.3 Thermodynamics

For all involved reactants and products (OMEn, FA, TOX) experimental solvation enthalpies and entropies are known. Experimental data as well as fitted coefficient for interpolation have been taken from ref. [215]. Vapor pressures and heats of vaporization have been calculated using Equations 5.3.3 and 5.3.4 together with the parameters in Tables 9 and 10 of ref. [215]. From the vapor pressures of the pure substances, we can deduce the free energies of solvation of the substances within themselves (Equation 5.3.3).

$$\Delta G_{\text{solv}}(\chi = 1) = -k_{\text{B}}T \ln \frac{p}{p_{\text{ref}}} \quad (5.3.3)$$

Having the solvation free energy and enthalpy, we can then deduce the solvation entropy through Equation 5.3.4.

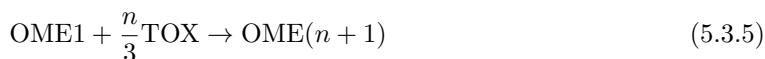
$$\Delta S_{\text{solv}}(\chi = 1) = \frac{\Delta H_{\text{solv}}(\chi = 1) - \Delta G_{\text{solv}}(\chi = 1)}{T} \quad (5.3.4)$$

<sup>2</sup>This value actually corresponds to the average of: 1) The difference between  $\Delta H_{\text{solv}}$  of Al-OH and methanol using PBE (only H-bonds), which is  $+50(-20+70)$  and 2) the difference between  $\Delta H_{\text{solv}}$  (only H-bonds) of Al-OH and methanol using the interpolated values from the stated equations (no H-bonds) and the explicit result (with H-bonds), which is around  $+30$ . As both methods should provide approximately the same result.

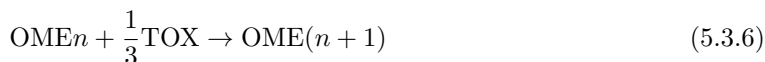
Solvation enthalpies, free energies and entropies are shown in Figures C.3-C.5 as a function of temperature. In Figure C.6, we furthermore show that the ratio of the solvation entropy to the entropy of the molecule in gas-phase is at reference pressure of 1 bar and  $T \approx 300$  K, around 0.35 for TOX and FA and around 0.25 for the OMEs. One can therefore deduce the solvation entropy from the gas phase entropy, in the rigid rotator and harmonic oscillator approximation, using a scaling factor. For TOX and FA, we found that  $\Delta S_{\text{solv}}^{\text{TOX/FA}} \approx -0.25 \times S_{\text{gas}}^{\text{TOX/FA}}$  while for OMEs  $\Delta S_{\text{solv}}^{\text{OMEn}} \approx -0.35 \times S_{\text{gas}}^{\text{TOX/FA}}$ .

Concerning solvation entropies for the zeolite, they differ only in their vibrational frequencies, which are taken into account implicitly through the shift of small harmonic frequencies to  $100 \text{ cm}^{-1}$ . [227, 234] We therefore approximate  $\Delta S_{\text{solv}}^{\text{zeolite}} \approx 0$ .

The formation of OMEn from OME1 and TOX is almost thermoneutral ( $\Delta G^{298\text{K}} = -6 \text{ kJ/mol}$ ), [222] thus limiting the equilibrium of the catalytic process. We first focus on the accuracy of modeling the thermodynamics using DFT calculations, which were confirmed to be accurate within 5 kJ/mol with MP2 and CCSD(T) calculations. The calculated formation energy of TOX is -48 kJ/mol, relative to one FA-equivalent. The stability of OMEn relative to that of OME1 is then given by the reaction from Equation 5.3.5.



Alternatively, one may study the reaction from Equation 5.3.6.

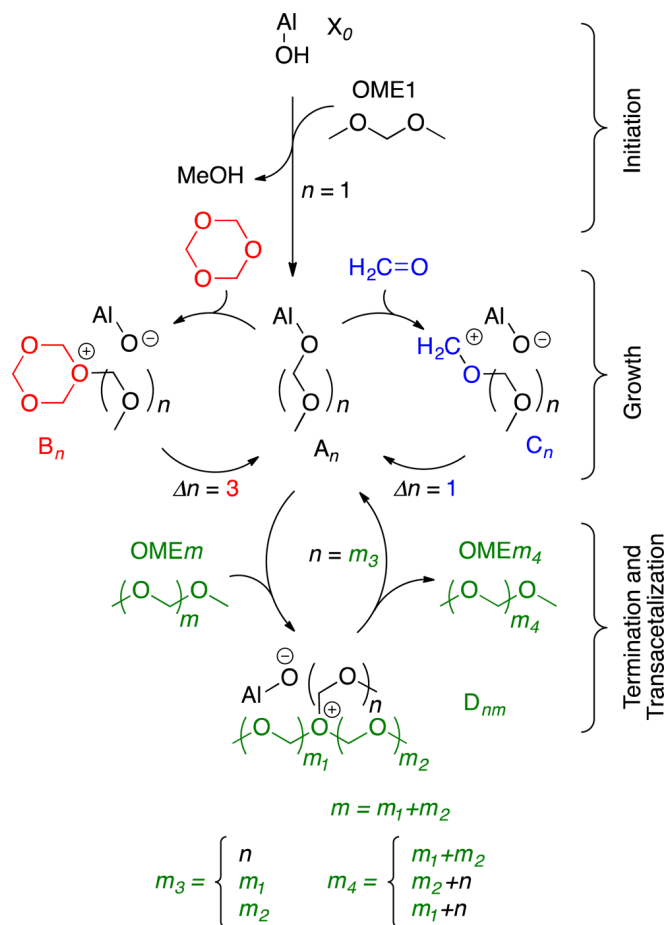


The reaction energy of the latter reaction is essentially independent of  $n$  and calculated to  $\Delta E_n = -12(-11) \text{ kJ/mol}$  using DFT-PBE-D3 (MP2) with  $n$ -dependent deviations of 1 kJ/mol. One can easily change the reference from TOX to FA by adding the relative stability of TOX to obtain  $\Delta E_n = -58 \text{ kJ/mol}$  relative to FA. At  $T > 0$  K, formation of OMEs becomes less favorable due to a loss in entropy from condensation. Higher OMEs become progressively less stable at higher temperatures. At room temperature, TOX is more stable than FA; however, with increasing temperature, FA becomes more stable for entropic reasons.

## 5.4 Results

The reaction mechanism of OME1 and TOX can be divided into initiation, chain growth, and termination, as outlined in Scheme 5.4. Initiation starts through reaction of the acid site (Al-OH) with OME1 to form Al-O-CH<sub>2</sub>-OMe thus already containing the building block of an OME, and further chain growth occurs via reaction with FA sources (FA or TOX) to give Al-(O-CH<sub>2</sub>) <sub>$n$</sub> -OMe. Termination occurs through reaction with another OME via transacetalization, releasing an OME and recovering the resting state, Al-(O-CH<sub>2</sub>) <sub>$m$</sub> -OMe, which differs only in chain length,  $m$  vs  $n$ . As the reaction proceeds and more OMEs are formed, this transacetalization gives access to OMEs of all chain lengths, as illustrated in Scheme 5.4. Two different mechanisms for chain growth are illustrated in this scheme: 1) via direct incorporation of TOX and 2) via incorporation of single FA units, with the latter requiring prior decomposition of TOX into three FA. We will now discuss the outcome of our calculations for the entire reaction mechanism starting with initiation followed by chain growth via TOX mechanism and termination.

**Scheme 5.4** Overview of reactions occurring in OME synthesis. The active site of the catalyst, a four-fold coordinated Al atom, is abbreviated by Al, omitting three oxygen atoms for clarity. Intermediates are labeled  $A_n$ ,  $B_n$ ,  $C_n$  and  $D_{nm}$  where  $D_{nm}$  includes all possible  $m_1$  and  $m_2$ .



The reaction pathway shown in Scheme 5.4 is discussed using the solvation model introduced above together with the PBE-D3 functional. Initiation starts by protonation of OME1 followed by release of methanol. This reaction is about 30 kJ/mol uphill in energy. However, because the concentration of OME1 is much higher than the resulting catalytic amount of methanol, the initiation reaction is more favorable in terms of free energy. Explicitly accounting for this, yields a free energy difference of  $\Delta G = 6$  kJ/mol at a methanol molar fraction of  $\chi \approx 1.5 \times 10^{-4}$  (Figure 5.4). Methanol, driven by entropy due to the low concentration of these species, will also react with various OMEs to produce hemiformals  $\text{Me}-(\text{O}-\text{CH}_2)_n-\text{OH}$  and OME1, thus further shifting equilibrium from protonated (Al-OH) to alkylated (Al-O-CH<sub>2</sub>-R) acid sites.

Chain growth is facilitated by reaction of the alkylated zeolite (Al-O-CH<sub>2</sub>-OMe) with TOX forming a zwitterionic species where the TOX rings stay intact (Scheme 5.4). In a subsequent step, the remaining Al-O<sup>-</sup> moiety opens the positively charged alkylated TOX ring in a nucleophilic attack, resulting in the chain growth of the alkylated zeolite (Al-(O-CH<sub>2</sub>)<sub>4</sub>-OMe). All barriers are relatively low, and the highest barrier (55 kJ/mol) results mainly from the fact that the chain growth is unfavorable in entropy. Further chain growth continues with the same mechanism with the estimated barriers being on the order of 84 kJ/mol, again mainly for entropic reasons.

Chain growth, defined by the insertion of FA units, always competes with termination processes, where the Al-(O-CH<sub>2</sub>)<sub>n</sub>-OMe moiety alkylates an OME instead of TOX. This leads to the branched

cationic intermediate shown in Scheme 5.4 ( $D_{nm}$ , depicted in green) that can react with the remaining anionic Al-O<sup>-</sup>-group. This reaction can either be degenerate, e.g. revert to the same OME and Al-(O-CH<sub>2</sub>)<sub>n</sub>-OMe-group, or yield a new OME. Initially, only OME1 is available for termination, and this can (apart from the reverse reaction) lead only to OME(1 + n) and Al-O-CH<sub>2</sub>-OMe, thus, as depicted in Figure 5.4, leading to the target molecule OME4. The barrier for OME4 formation is 70 kJ/mol and is therefore lower than that for further chain growth to A<sub>7</sub>. As various different OMEs are formed with longer reaction times, cross reactions with other OMEs also occur. Referring to Scheme 5.4, an OME(*m*) molecule can be alkylated at different positions, which can result in two different product OMEs. These reactions will hence eventually lead to the thermodynamic distribution of OMEs, as observed experimentally. [222]

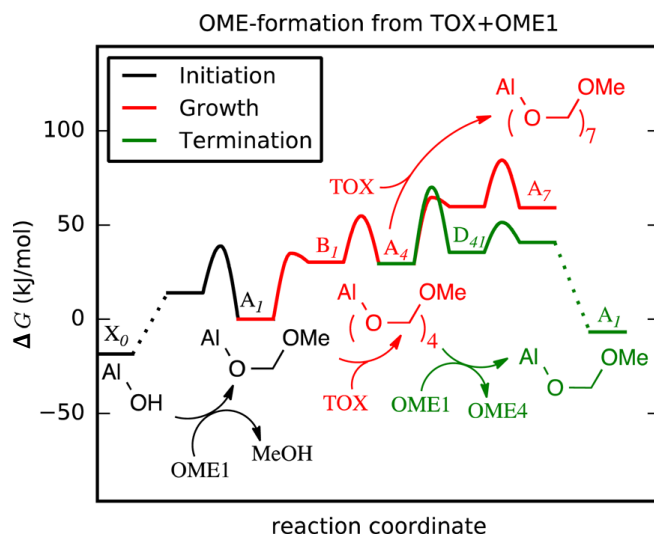


**Figure 5.4:** Free energy diagram at  $T = 300$  K for the catalytic formation of OME4. The abbreviation  $D_{41}$  is used according to the definition of  $D_{nm}$  in Scheme 5.4. The first step in initiation is the protonation of OME1 that then reacts to  $A_1 + \text{MeOH}$ . The last step in the pathway for termination and formation of OME4 is the release of formed but vdW-adsorbed OME4 into the solution. The gain in free energy is due to entropy. The free energy diagram is referenced to  $A_1$  because it likely represents the resting state of the catalyst, as discussed in the text.

As described in ref. [223] for a sulfonic acid-functionalized ionic liquid, TOX can be decomposed by catalytic activation with an acid (Figure 5.5 a). We calculated the decomposition mechanism catalyzed by a Brønsted acid accordingly: TOX is protonated by Al-OH, resulting in a zwitterionic structure, where the cationic, protonated TOX ring is subsequently opened by nucleophilic attack of Al-O<sup>-</sup> at one of the carbon atoms. This results in the intermediate formation of an Al-(O-CH<sub>2</sub>)<sub>3</sub>-OH species. The calculated reaction barrier of 61 kJ/mol relative to that of Al-OH is similar to that found for the sulfonic acid-functionalized ionic liquid (85 kJ/mol). [223] After the protonated TOX ring is opened, its decomposition into three FA units has lower barriers with the most favorable path consisting of a stepwise decomposition. This is hence equivalent to the reverse reaction (Figure 5.5 a): Al-OH protonates FA and reacts to Al-O-CH<sub>2</sub>-OH. Subsequent chain growth occurs through attack of FA at the growing chain. Importantly, the rate for TOX decomposition to FA depends on the concentration of acidic species such as water, shifting the equilibrium in favor of Al-OH and all intermediates containing protons. As mentioned initially, it is expected that in this case the stability of Al-OH is somewhat overestimated because of the concentration of methanol that will be further reduced through the formation of hemiformals is

not taken into account. From a technical perspective, it is important to note that intermediates  $X_2$  and  $X_1$  have internal hydrogen bonds which may lead to a slight overestimation of their stability ( $\approx 30$  kJ/mol) because the OH group is now not available for hydrogen bonding with the solvent, as assumed in our solvation model. However, this will not significantly increase the overall barrier for TOX decomposition, which is currently given by the reaction of  $X_0 \rightarrow X_3$  (Figure 5.5 b).

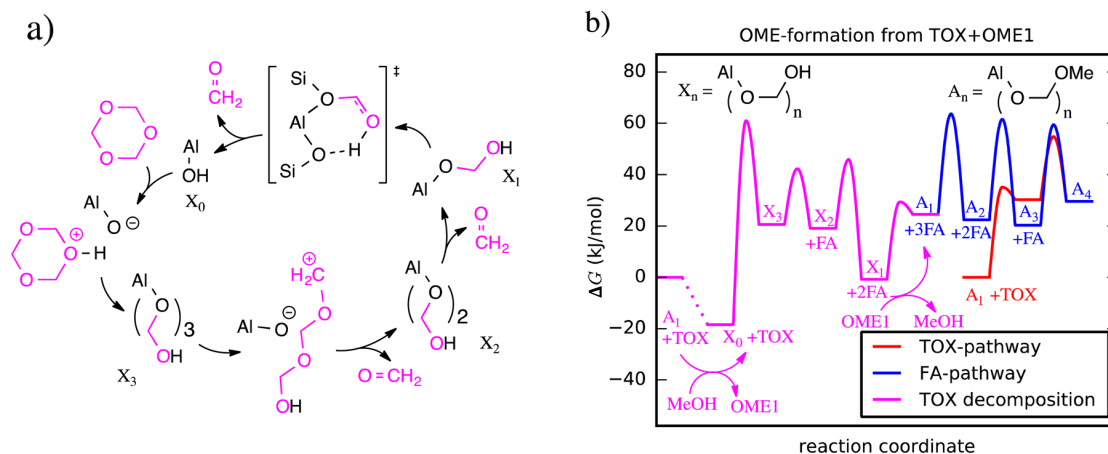


**Figure 5.5:** a) Decomposition mechanism for TOX to FA. To illustrate the mechanistic details for the last step of the actual decomposition of the opened TOX ring into FA fragments ( $X_1 \rightarrow X_0$ ) a more detailed model of the zeolite catalyst is shown. In contrast to all other reactions studied here, two oxygen atoms bound to Al are involved at the same time (this does not imply that the number of Si or O atoms in the vicinity of the Al atom would change). b) Free energy diagram at  $T = 300$  K comparing chain growth via direct TOX incorporation and via prior TOX decomposition to FA with subsequent sequential FA incorporation. For decomposition of  $X_1$  to FA and  $A_1$ , the intermediate formation of  $X_0$  is omitted for brevity. In the reaction of  $X_0 \rightarrow X_3$ , the formation of the zwitterionic intermediate with protonated TOX is also omitted, and the barrier refers to the activation barrier for opening the protonated ring.

The highest barrier for direct TOX decomposition to FA is calculated to 80 kJ/mol and therefore comparable to direct TOX incorporation (55 kJ/mol). Importantly, once FA is formed and reacts in chain-growth steps, there is no dependence on the concentration of protic species. The highest barrier for FA incorporation is 63 kJ/mol and therefore only 8 kJ/mol above that for direct TOX incorporation. This difference in activation barriers was also obtained using directly explicit solvated structures rather than the solvation model. We therefore conclude that direct TOX incorporation is more favorable. Both mechanisms may therefore contribute to the total reaction rate. Because the barrier for termination of  $A_4$  to  $A_1$  and OME4 (70 kJ/mol) is slightly higher than that for removal of an FA molecule from  $A_4$  to  $A_3$  (59 kJ/mol), the chain length of  $A_n$  may be changed by releasing FA after TOX incorporation.

The final addressed question is the rate with which transacetalization occurs between different OMEs. This depends on the differences in the reactivity of OME1 versus higher OMEs toward the fragment  $\text{Al}-(\text{O}-\text{CH}_2)_n-\text{OMe}$ . In terms of electronic factors, e.g. the intrinsic reactivity of the reacting groups, one would expect the differences to be relatively small because they are only due to the effect that the neighboring groups have on the nucleophilicity of the oxygen that is alkylated. For longer OMEs, alkylation can occur at a terminal oxygen,  $\text{Me}-(\text{O}-\text{CH}_2)_n-\text{O}^*-\text{Me}$ ,

or an internal oxygen,  $\text{Me}-(\text{O}-\text{CH}_2)_n-\text{O}^*-(\text{O}-\text{CH}_2)_m-\text{Me}$ . Certainly, the effect of  $n$  and  $m$  ( $>1$ ) can be expected to be small. Additionally, steric hindrance will play a role for larger OMEs. We compared the reactivity of  $\text{Al}-\text{O}-\text{CH}_2-\text{OMe}$  toward OME1 and the three symmetry-inequivalent oxygens in OME4. All activation energies are very similar, differing by less than 10 kJ/mol. This explains why OME synthesis after prolonged reaction times is entirely nonselective and yields a thermodynamic equilibrium mixture of OMEs with various chain lengths.

## 5.5 Conclusion

We investigated the mechanism for the zeolite-catalyzed formation of OMEs from TOX and OME1. A balanced description of vdW interactions between adsorbate and zeolite as well as with the solvent is required to calculate free energies accurately. The obtained activation barriers are reasonably low and agree well with kinetics observed in experiments. We found that incorporation of TOX can occur both directly, which is more favorable, and via prior decomposition of TOX to FA. Because direct TOX incorporation into OME1 initially generates OME4 rather than the OME equilibrium distribution, understanding and controlling the growth mechanism is one of the requirements for a potential synthesis nonequilibrium OME mixtures. For OME synthesis from MeOH and para-formaldehyde, catalyzed by ion exchange resins, experimental kinetics indicate that the FA mechanism is operative. [24] The most energy demanding reaction step for both incorporation mechanisms is the opening of the TOX ring either by protonation or alkylation (61 and 55 kJ/mol). The overall highest step in the catalytic formation of OMEs is the termination of chain growth that requires the reaction with an OME. This reaction also allows equilibration of OMEs of different lengths. The difference in activation barriers for transacetalization involving OMEs of different lengths is small ( $\approx 10$  kJ/mol). This explains the nonselective generation of all OMEs according to their thermodynamic stability over prolonged reaction times.

## Chapter 6

# OME Synthesis through Homogeneous Acid Catalysis

### 6.1 Introduction

As discussed in Chapter 5, Oxymethylene Dimethyl Ethers (OMEs) are promising candidates as diesel fuel additives, where an acidic zeolite, H-BEA is used to protonate an OME molecule that is decomposed into MeOH and a methoxymethyl cation, which is adsorbed on  $\text{BEA}^-$ . This represented the initiation step in the catalytic process. Methoxymethylated BEA was assumed to be the resting state.

In addition to heterogeneous catalysts such as acidic zeolites, [24] homogeneous acids such as sulfuric acid [236] have been explored for this process. Here, acids are assumed to protonate OMEs, while bases have no effect in the catalytic process. This study aims to investigate the role of  $\text{H}^+$ - $\text{OME}_1$  in the oligomerization process, without further interactions with the catalyst.

A central challenge is that the reaction usually yields a thermodynamic equilibrium mixture of OMEs, while it would be desirable to steer the product distribution towards OMEs in the range of  $\text{OME}_3$  to  $\text{OME}_5$ . [23, 231, 237, 238] This equilibration is due to fast transacetalization of the formed OMEs as depicted in Scheme 5.3.

In addition to the study made in Chapter 5, we have proceeded with the investigation of the reaction mechanism of the synthesis of OMEs from TOX and  $\text{OME}_1$  and the influence of the presence and the strength of a Brønsted acid with *ab initio* calculations. To investigate how accurate DFT is in OME synthesis, DFT functionals are compared with MP2. Also, in contrast to Chapter 5, where solvent corrections were applied explicitly, an implicit solvent model is used. While zeolites have porous channels in which it is often hard to predict where solvation takes place (based on the size of these channels), having a catalyst in liquid-phase will eliminate this concern. We have used the implicit solvation model, SMD, [108] which is parametrized for different solvents, including the possibility of hydrogen bonding, and takes into account entropic corrections.

---

This chapter is based on the following publication: [235] Goncalves, T. J.; Plessow, P. N.; Studt, F., A Computational Investigation of OME-synthesis through Homogeneous Acid Catalysis. *ChemCatChem* 2019, 11, 1949–1954. Copyright (2019) Wiley. Used with permission from Goncalves, T. J.; Plessow, P. N.; Studt, F., A Computational Investigation of OME-synthesis through Homogeneous Acid Catalysis. *ChemCatChem*. Wiley.

## 6.2 Methods

Structures were optimized at the PBE0-D3/dhf-SV(P) level of theory [91, 96, 97] using the TURBOMOLE program package [178, 179] employing the resolution-of-identity approximation. [103] Transition states were found using relaxed potential surface scans and local quasi-Newton optimizations. [210, 211] In order to increase the accuracy of our study, we carried out single-point energy calculations with the def2-TZVPP basis-set and the second order Møller-Plesset perturbation theory (MP2) [180, 181] for all intermediates and transition states. All results discussed thus use MP2/def2-TZVPP//PBE0-D3/dhf-SV(P) energies. [178, 179, 184]

All reported free energies are Gibbs free energies in solution at 300 K and a reference concentration of 1 mol/l. These free energies were obtained by calculating gas-phase free energies and additionally computing solvation free energies. The gas-phase Gibbs free energy for a known pressure is given by  $G(p) = G(p_0) + RT \ln(p/p_0)$  where  $p_0$  represents the reference pressure of 1 bar. The conversion of 1 bar from gas phase as reference state into 1 mol/l in solution corresponds to the relation depicted in Equation 6.2.1.

$$\Delta G_{\text{solv}}^{\text{1bar} \rightarrow \text{1mol/l}} = \Delta G_{\text{solv}}^{\text{1mol/l} \rightarrow \text{1mol/l}} + RT \ln(p/p_0) \quad (6.2.1)$$

$p$  represents the pressure of an ideal gas with a concentration of 1 mol/l. Considering the ideal gas Equation  $PV = nRT$ , the increment is then equivalent to  $RT \ln(V_0/V)$ , which is substituted in Equation 6.2.2.

$$\Delta G_{\text{solv}}^{\text{1bar} \rightarrow \text{1mol/l}} = \Delta G_{\text{solv}}^{\text{1mol/l} \rightarrow \text{1mol/l}} + RT \ln(V_0/V) \quad (6.2.2)$$

Now,  $V_0$  represents the molar volume of an ideal gas ( $\approx 22.4 \text{ dm}^3$ ) at room temperature ( $T = 300 \text{ K}$ ) and  $V$  is the molar volume corresponding to 1 mol/l, which is  $1 \text{ dm}^3$  for a quantity of 1 mol.  $R$  represents the ideal gas constant. The conversion value is then  $RT \ln(22.4) = 7.9 \text{ kJ/mol}$ .  $\Delta G_{\text{solv}}^{\text{1bar} \rightarrow \text{1mol/l}}$  is the solvation free energy which is then included in the gas-phase free energies, which corresponds to the sum of the computed solvation free energy for the reference state of 1 mol/l plus the conversion factor from the reference state of 1 bar to 1 mol/l.

Gas-phase free energies were obtained using the harmonic oscillator and rigid rotator approximation at the level of theory at which the structures were optimized, PBE0-D3/dhf-SV(P). Solvation free energies were computed with the SMD solvation model using single-point calculations with the M06 [93] functional and the cc-pVTZ basis-set. [98, 108, 239–244] The actual solution consists initially of OME1 and TOX and after the reaction of a mixture of OMEs. The parametrization that resembles this situation best is that for diethyl ether that has therefore been employed. [245–247] The SMD calculations were carried out with GAMESS-US. [248, 249] The free energies in solution were thus obtained as Equation 6.2.3 shows.

$$G_{\text{solution}} = E(\text{MP2//PBE0-D3}) + \Delta G_{\text{gas}}^{\text{harmonic}} + \Delta G_{\text{solv}}(\text{M06//PBE0-D3}) \quad (6.2.3)$$

Here, MP2 denotes MP2/def2-TZVPP, PBE0-D3 denotes PBE0-D3/dhf-SV(P) and M06 denotes M06/cc-pVTZ. Additional calculations for the determination of acidities including explicit solvation with periodic boundary conditions were performed with Vienna Ab initio Simulation Package with the Projected Augmented Wave method [186, 187] and the Atomic Simulation Environment [87] employing the PBE-D3 functional. [91, 97] Information regarding relative free energies (Tables D.3,

D.4, D.5 and D.6), free energy contributions (Table D.7) and solvation energies (Table D.8) is available in the appendix.

In this chapter, the accuracy of DFT was done and included in Section D.1. Details on solvent corrections and parametrization using the Solvent Model based on Density (SMD) are included in Section D.2.

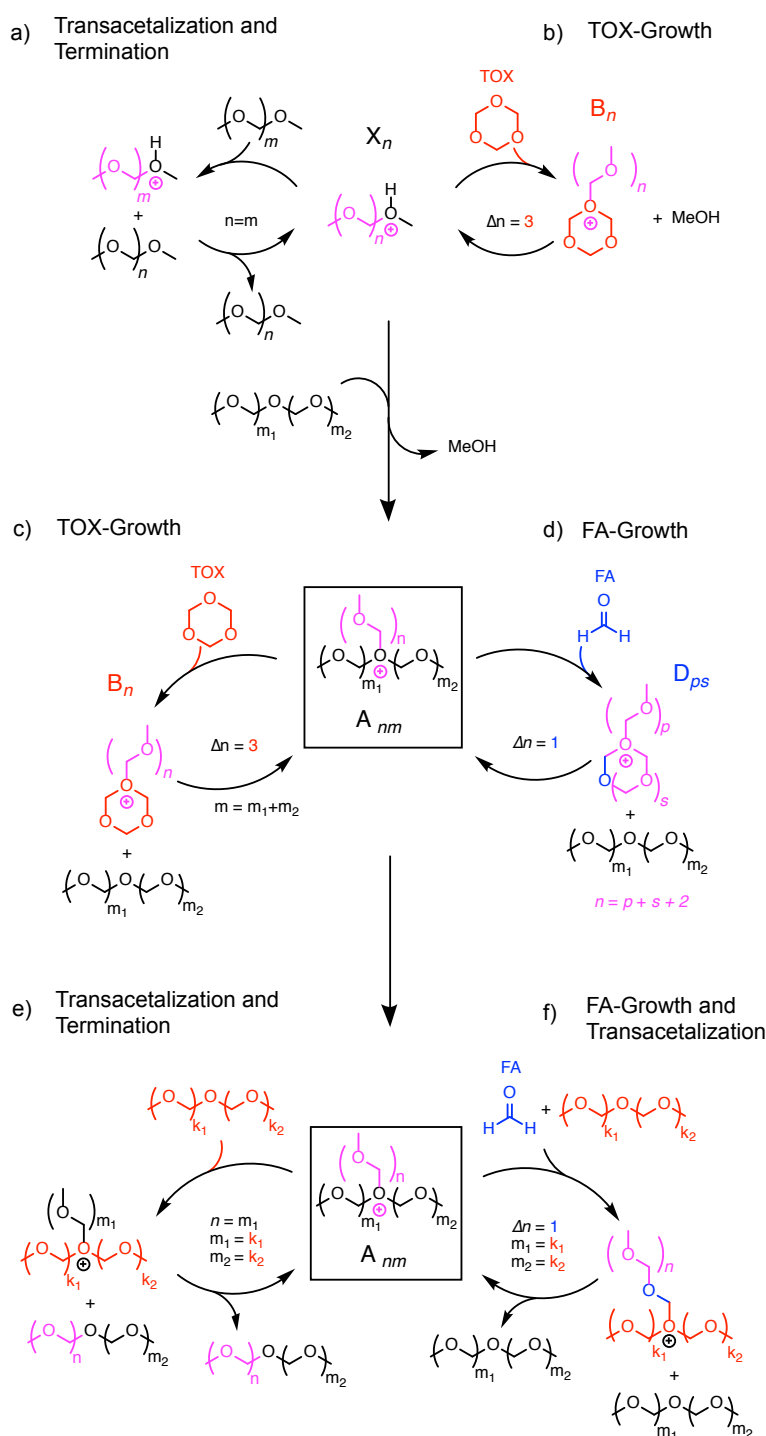
### 6.3 Results

In our investigation, we assume that a Brønsted acid (HA), acting as precatalyst, is able to protonate the reactant OME1, thus creating OME1-H<sup>+</sup> and that the corresponding base (A<sup>-</sup>) is not exerting a significant influence. With this assumption, acids differ only in their ability to protonate OME1. Therefore, it is possible to evaluate the reaction mechanism starting from OME1-H<sup>+</sup> and study the influence of acid strengths on the reaction mechanism through variation in HA. The protonation results in the formation of catalytically active species, which are always cationic but do not necessarily contain a protonated ether group.

Experimentally, OME synthesis is carried out in solution typically using ambient to elevated temperatures and often pure reactants as solvent. [24, 25, 226, 250] The reaction of OME1 and TOX will be studied without additional solvents at room temperature. Free energies in solution at a reference concentration of 1 mol/l are obtained at the MP2/def2-TZVPP//PBE0-dhf-SV(P) level of theory using the harmonic oscillator and rigid rotator approximations. Solvation free energies are computed with SMD (M06/cc-pVTZ//PBE0-dhf-SV(P)).

Scheme 6.1 gives an overview over the mechanisms for OME-formation investigated in this work. After initial protonation of OME1, there are two conceivable mechanisms. On one hand, the active species can be a protonated one, containing an O-protonated C-O-C unit, which is shown in the upper part of Scheme 6.1. On the other hand, the active species can be an O-alkylated C-O-C unit and the proton is now bound in a neutral molecule, either in methanol or as a half acetal, CH<sub>3</sub>O-(CH<sub>2</sub>O)<sub>n</sub>-CH<sub>2</sub>OH.

**Scheme 6.1** Overview over reaction mechanisms for proton-catalyzed OME formation starting from OME1 and TOX/FA. The scheme is characterized by multiple growth processes, including the incorporation of trioxane/formaldehyde into a protonated or alkylated OME (as depicted in b, c, d and f), releasing OME<sub>n</sub> through transacetalization (a,e).



For both, a protonated OME ( $X_n$ ) or an alkylated one ( $A_{nm}$ ) the principle types of reactions are the same. Growth can occur by direct reaction with TOX, where TOX reacts in an  $S_N2$ -like reaction with  $X_n$  and  $A_{nm}$ , leading to the same alkylated TOX-intermediate (Scheme 6.1 b and c). The only difference is that, as an intermediate, in the case of  $A_{nm}$ , an OME is released, while in the case of  $X_n$  a half acetal or MeOH is formed instead. This intermediate (OME or MeOH)

can now open the alkylated, cationic TOX-ring, thus forming again  $X_n$  and  $A_{nm}$ , where  $n$  is now increased to  $n + 3$ .

In addition, single FA-units can also react directly. FA may either be used directly as a reactant or can also be formed in situ from TOX. The most favorable mechanism studied for direct FA-reaction involves nucleophilic attack of FA at a carbon bound to the trivalent, cationic oxygen of  $A_{nm}$ . The intermediately formed  $\text{CH}_2^+$ -moiety of formaldehyde is immediately stabilized by reaction with another part of OME, resulting in cyclization (Scheme 6.1 d).

The growth mechanisms discussed above lead to even longer cations of  $X_n$  or  $A_{nm}$ . The release of OMEs occurs through transacetalization by the reaction of  $X_n$  and  $A_{nm}$  with reactant OME1 or other OMEs that are formed during the process. In this reaction, one of the  $\text{CH}_3\text{O}-(\text{CH}_2\text{O})_n$ -groups in  $X_n$  or  $A_{nm}$  is transferred to another OME, thus releasing the remaining part of the previous  $X_n$  or  $A_{nm}$  as a neutral OME (Scheme 6.1 a, e and f).

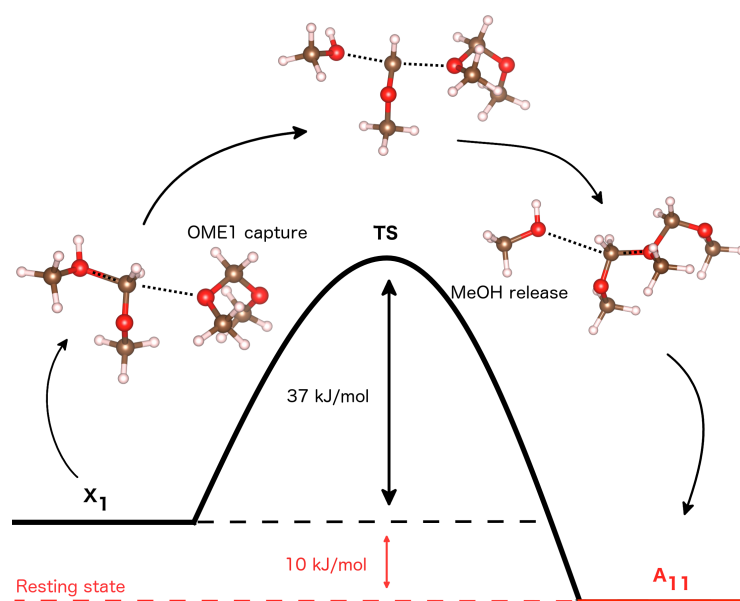


**Figure 6.1:** Example of atomic structure of reactants, transition state and product for one of the catalytic reactions, the formation of  $A_{11}$  from  $X_1$ , according to notation in Scheme 6.1. Color scheme: H–White; O–Red; C–Brown.

The pathways described in Scheme 6.1 were investigated through the calculation of minima and transition states. Figure 6.1 illustrates a barrier that corresponds to the formation of an alkylated OME1, labeled as  $A_{11}$ , from a protonated OME1,  $X_1$ , capturing OME1 from the solution and releasing methanol. This constitutes one of the first barriers in the formation of OME4 from H-OME1. Other relevant transition-state structures are shown in Figures D.5, D.6, D.7 and D.8.





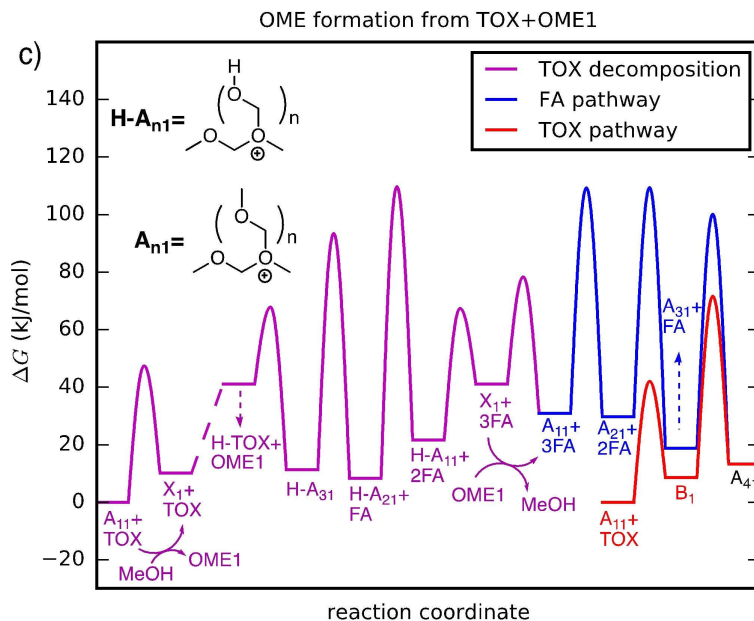


**Figure 6.4:** a) Decomposition mechanism from TOX to FA (magenta) and b) subsequent sequential FA incorporation (blue). Note that the transition states for FA-incorporation involve an additional OME1-molecule as shown in Scheme 6.1 f) and in Figure D.8, which depicts the atomic structure. c) Free energy diagram at  $T = 300$  K showing chain growth via prior TOX decomposition to FA (magenta) and subsequent sequential FA incorporation (blue), both of which mechanisms are depicted in a) and b). This is additionally compared with the free energy diagram for direct TOX incorporation (red), which is identical to the data and mechanism in Figure 6.2.

Generally, barrier heights reported here are slightly higher than those obtained previously for H-BEA, since the PBE-D3 approach used there systematically underestimates barriers [93, 136, 188] (see Figure D.1 b). Generally, similar conclusions are taken, namely that direct incorporation of TOX is more favorable than decomposition of TOX to FA with subsequent sequential FA-incorporation. However, there are some differences in the stability of certain intermediates, such as H-A<sub>31</sub>, which is an intermediate in the decomposition of TOX (see Figure 6.4). This is due to the fact that the relative entropy of this intermediate is different when the reaction occurs in a zeolite.

Up to now, our analysis is based on the existence of a protonated OME1, X<sub>1</sub>. The addressed issue now is how likely this species is to be formed from a given precatalyst. The simplest way of doing this is to consider trimethyl oxonium salts as precatalysts that have also been used in a recent experimental study. [250] Neglecting the effect of the weakly-coordinating counter-ions, the trimethyl oxonium cation can methylate OME1, which by reaction with another OME1 forms A<sub>11</sub> and DME. This reaction sequence is shown in Figure 6.2 and is mildly uphill in free energy (30 kJ/mol) confirming that trimethyl oxonium salts are viable precatalysts for this reaction.

Calculating initiation based on neutral Brønsted acids is much more challenging, since this involves charge-separation due to the formation of a cationic OME-species (X<sub>1</sub> or A<sub>11</sub>) and an anion, for example chloride if HCl is used as an acid. This is generally challenging for continuum models, in particular for solvents other than water where little experimental data exists to benchmark the solvation methods. [251] Using implicit solvation (SMD with diethyl ether as solvent) in a straightforward manner, we find that protonation of OME1 by HCl is uphill by more than 150 kJ/mol,

when free chloride is formed, as shown in Figure 6.2. Using explicit solvation with periodic boundary conditions and around 10 OME1-solvent molecules per unit cell (Figure D.3), we find that protonation of OME1 is uphill by around 80 kJ/mol, as shown before. We note here that combinations of implicit and explicit solvation can also be used. In addition, contact-ion pairs may also be important in practice, highlighting the difficulty to correctly estimate the formation of cationic intermediates when starting from neutral acid precursors. We have also studied the formation of a protonated OME1 in the pores of H-BEA, in which the protonated OME1 is displaced significantly from the protonated acid site (Figure D.2). Again, using periodic boundary conditions and explicit solvation with OME1, we calculate the protonation of OME1 to be uphill in energy by around 60 kJ/mol thus being less favorable compared to the direct reaction at the active site.

## 6.4 Conclusion

The acid catalyzed formation of higher OMEs from OME1 and TOX has been investigated using *ab initio* and DFT calculations, employing a protonated OME1 as a homogeneous catalyst that can be generated either by protonation with a Brønsted acid, or by reaction of OME1 with a trimethyl oxonium cation. Based on our findings, we expect trimethyl oxonium salts to be an active precatalyst, in agreement with a recent experimental study. [250] Once protonated OME1 is formed, we find both direct TOX incorporation and TOX-decomposition to FA and subsequent FA-incorporation to be viable reaction mechanisms for the formation of higher OMEs, similar to reactions within the pores of H-BEA. However, we find that direct TOX-incorporation is somewhat more likely. Ring-opening of the TOX-ring represents the rate-limiting step in this case and this reaction can be induced by cationic species that are either protonated or alkylated OMEs, which differ only little in their reactivity. Owing to the fast transacetalization, this is not expected to affect the product distribution significantly after prolonged reaction times.



## Chapter 7

# Final conclusion and outlook

This thesis dealt with the investigation of the synthesis of OMEs and the reduction of  $\text{NO}_x$  by ammonia SCR using quantum chemical calculations. The reactions were investigated using H-BEA and a homogeneous acid catalyst (synthesis of OMEs) as well as copper exchanged SSZ-13 (ammonia SCR). The first part of this thesis has focused on establishing a computational methodology that ensures that the employed calculations yield an acceptable accuracy. This was particularly challenging for the SCR reaction on Cu-SSZ-13, which involved calculations of systems with different spin states (singlets, doublets and triplets) that potentially have strong correlation effects. Similarly, the investigation of OME synthesis is occurring at low temperature and thus in liquid phase making the application of a solvent model necessary. As solvation occurs within the zeolite pore, standard implicit solvation models cannot be applied and this motivated the development of an explicit solvation model for molecules and zeolites. Here, explicit solvation calculations for a selected number of structures in the zeolite pores were used to parametrize a model that allows the prediction of solvation energies for all involved structures.

The investigations of the ammonia-SCR process on Cu-SSZ-13 showed that the fast SCR cycle occurs via the reaction of copper-bound ammonia with nitrogen oxides. Further intermediates include nitrous acids and the Cu-bound amino radical and hydroxyl-group. The hydrogen transfer between the amino radical and NO is a possible rate determining step in this cycle, with a calculated reaction barrier of 173 kJ/mol. Fast SCR requires stoichiometric quantities of  $\text{NO}_2$  molecules, that usually constitute around 5% of  $\text{NO}_x$  gases. The partial oxidation of nitric oxides by  $\text{O}_2$  is consequently required for the reduction process. For the investigated single-copper site, we have not found an energetically feasible mechanism for the oxidation of NO by  $\text{O}_2$ . This is in line with previous mechanistic proposals that suggests that the interaction of two copper sites is required for this reaction.

The acid catalyzed oligomerization of formaldehyde and methanol in BEA is comprised of the following steps. Protonation of OME leads to the formation of methanol and methoxymethyl cations that are extended in chain length either by trioxane ring opening and direct incorporation or decomposition into formaldehyde units and subsequent incorporation. These molecules are released as  $\text{OMEn}$  via transacetalization with other OME molecules. The direct trioxane incorporation was found to be the most favorable pathway, with lower barriers in comparison to trioxane decomposition. The trioxane ring-opening is computed to be the rate-determining step, with a reaction barrier of close to 60 kJ/mol. The Schulz-Flory distribution of OMEs in solution is explained by fast transacetalization processes between OMEs that quickly establish thermodynamic equilibrium. I furthermore investigated the synthesis of OMEs via homogeneous acid catalysis. The potential

---

mechanisms are the same as for the acidic zeolites, since both are Brønsted acid catalysts. The main difference for homogeneous catalysis is that the intermediates and transition states only react with the solvent and not with the porous structure of the zeolite. The interaction with the solvent can, in this case, be modeled with an implicit solvation model. The results are largely similar to those obtained for the acidic zeolite. This is in agreement with the experimental observation that many different acidic catalysts from sulfuric acid, over ion exchange resins to acidic zeolites are catalytically active.

In summary, I established a computational protocol that allows for an accurate description of reactions catalyzed by H-SSZ-13 and ammonia-SCR catalyzed by Cu-SSZ-13. This methodology comprises a hierarchical cluster approach allowing to employ higher level methods such as CCSD(T) or the computationally more feasible DLPNO-CCSD(T) approach. The calculated reaction mechanisms revealed an atomistic picture of the reduction of NO<sub>2</sub> to N<sub>2</sub> with ammonia and showed that the direct oxidation of NO with O<sub>2</sub> is accompanied by prohibitively high barriers. Calculations of the reaction mechanism of OME synthesis for H-BEA and homogeneous catalysis revealed that the ring-opening of the employed trioxane is most likely the rate-determining step. Importantly, all reaction barriers are calculated to be relatively small ( $\leq 60$  kJ/mol) so that one can expect fast reaction rates and an OME composition that approaches equilibrium relatively fast.

Future work will have to focus on other possible active sites for ammonia-SCR (e.g. the proposed Cu<sub>2</sub> complexes) and the influence of acidity and employed reactants in OME synthesis. The investigations have so far only focused on establishing a reaction mechanism and a first analysis through free energy diagrams, but elaborate kinetic models will need to be developed for an in-depth analysis.

# References

- [1] B. Brunekreef and S. T. Holgate, “Air pollution and health,” *The lancet*, vol. 360, no. 9341, pp. 1233–1242, 2002.
- [2] B. Forsberg, H.-C. Hansson, C. Johansson, H. Areskoug, K. Persson, and B. Järholm, “Comparative health impact assessment of local and regional particulate air pollutants in scandinavia,” *AMBIO*, vol. 34, no. 1, pp. 11–19, 2005.
- [3] H. Akimoto, “Global air quality and pollution,” *Science*, vol. 302, no. 5651, pp. 1716–1719, 2003.
- [4] A. Ghorani-Azam, B. Riahi-Zanjani, and M. Balali-Mood, “Effects of air pollution on human health and practical measures for prevention in iran,” *J. Res. Med. Sci.*, vol. 21, 2016.
- [5] H. Kan, R. Chen, and S. Tong, “Ambient air pollution, climate change, and population health in china,” *Environ. Int.*, vol. 42, pp. 10–19, 2012.
- [6] M. M. Alam, M. W. Murad, A. H. M. Noman, and I. Ozturk, “Relationships among carbon emissions, economic growth, energy consumption and population growth: Testing environmental kuznets curve hypothesis for brazil, china, india and indonesia,” *Ecol. Indic.*, vol. 70, pp. 466–479, 2016.
- [7] R. A. Begum, K. Sohag, S. M. S. Abdullah, and M. Jaafar, “Co2 emissions, energy consumption, economic and population growth in malaysia,” *Renewable Sustainable Energy Rev.*, vol. 41, pp. 594–601, 2015.
- [8] M. Shahbaz, Q. M. A. Hye, A. K. Tiwari, and N. C. Leitão, “Economic growth, energy consumption, financial development, international trade and co2 emissions in indonesia,” *Renewable Sustainable Energy Rev.*, vol. 25, pp. 109–121, 2013.
- [9] D. Lüthi, M. Le Floch, B. Bereiter, T. Blunier, J.-M. Barnola, U. Siegenthaler, D. Raynaud, J. Jouzel, H. Fischer, K. Kawamura, *et al.*, “High-resolution carbon dioxide concentration record 650,000–800,000 years before present,” *Nature*, vol. 453, no. 7193, pp. 379–382, 2008.
- [10] J.-R. Petit, J. Jouzel, D. Raynaud, N. I. Barkov, J.-M. Barnola, I. Basile, M. Bender, J. Chappellaz, M. Davis, G. Delaygue, *et al.*, “Climate and atmospheric history of the past 420,000 years from the vostok ice core, antarctica,” *Nature*, vol. 399, no. 6735, p. 429, 1999.
- [11] P. Tans and R. Keeling, “Trends in atmospheric carbon dioxide, noaa/esrl,” *URL: <http://www.esrl.noaa.gov/gmd/ccgg/trends>*, 2020.
- [12] N. G. C. Change, G. W. V. S. of the Planet. Jet Propulsion Laboratory / National Aeronautics, and S. Administration, “Global climate change: Evidence,” *URL: <http://climate.nasa.gov/evidence>*, 2017.

- [13] A. Berger, "Long-term variations of daily insolation and quaternary climatic changes," *J. Atmos. Sci.*, vol. 35, no. 12, pp. 2362–2367, 1978.
- [14] U. S. E. P. Agency, "Overview of greenhouse gases," URL: <https://www.epa.gov/ghgemissions/overview-greenhouse-gases>, 2017.
- [15] U. S. E. P. Agency, "National air pollutant emission trends, 1900-1998," *Report EPA-454/R-00-002, EPA, Research Triangle Park, NC*, 1999.
- [16] W. AAS, "Co-operative programme for monitoring and evaluation of the long-range transmission of air pollutants in europe," *Data quality*, 2001.
- [17] N. Kato and H. Akimoto, "Anthropogenic emissions of so<sub>2</sub> and no<sub>x</sub> in asia: emission inventories," *Atmos. Environ. A, Gen. Top.*, vol. 26, no. 16, pp. 2997–3017, 1992.
- [18] D. G. Streets, N. Y. Tsai, H. Akimoto, and K. Oka, "Trends in emissions of acidifying species in asia, 1985–1997," *Water, Air, Soil Pollut.*, vol. 130, no. 1-4, pp. 187–192, 2001.
- [19] O. for Economic Cooperation and D. (OECD), "Oecd environmental data compendium," *OECD, Paris, France*, 1993.
- [20] T. Bhatelia, W. J. Lee, C. Samanta, J. Patel, and A. Bordoloi, "Processes for the production of oxymethylene ethers: promising synthetic diesel additives," *Asia-Pac. J. Chem. Eng.*, vol. 12, no. 5, pp. 827–837, 2017.
- [21] W. Maus, E. Jacob, M. Härtl, P. Seidenspinner, and G. Wachtmeister, "Synthetische kraftstoffe—ome1: Ein potenziell nachhaltig hergestellter dieselmotorkraftstoff," in *35. Internationales Wiener Motorensymposium*, 2014.
- [22] J. Burger, M. Siegert, E. Ströfer, and H. Hasse, "Poly (oxymethylene) dimethyl ethers as components of tailored diesel fuel: Properties, synthesis and purification concepts," *Fuel*, vol. 89, no. 11, pp. 3315–3319, 2010.
- [23] L. Lautenschütz, D. Oestreich, P. Seidenspinner, U. Arnold, E. Dinjus, and J. Sauer, "Physico-chemical properties and fuel characteristics of oxymethylene dialkyl ethers," *Fuel*, vol. 173, pp. 129–137, 2016.
- [24] D. Oestreich, L. Lautenschütz, U. Arnold, and J. Sauer, "Reaction kinetics and equilibrium parameters for the production of oxymethylene dimethyl ethers (ome) from methanol and formaldehyde," *Chem. Eng. Sci.*, vol. 163, pp. 92–104, 2017.
- [25] L. Lautenschütz, D. Oestreich, P. Haltenort, U. Arnold, E. Dinjus, and J. Sauer, "Efficient synthesis of oxymethylene dimethyl ethers (ome) from dimethoxymethane and trioxane over zeolites," *Fuel Process. Technol.*, vol. 165, pp. 27–33, 2017.
- [26] P. Haltenort, L. Lautenschütz, U. Arnold, and J. Sauer, "(trans) acetalization reactions for the synthesis of oligomeric oxymethylene dialkyl ethers catalyzed by zeolite bea25," *Top. Catal.*, vol. 62, no. 5-6, pp. 551–559, 2019.
- [27] L. Wang, W.-T. Wu, T. Chen, Q. Chen, and M.-Y. He, "Ion-exchange resin-catalyzed synthesis of polyoxymethylene dimethyl ethers: a practical and environmentally friendly way to diesel additive," *Chem. Eng. Commun.*, vol. 201, no. 5, pp. 709–717, 2014.
- [28] J. C. Groen, W. Zhu, S. Brouwer, S. J. Huynink, F. Kapteijn, J. A. Moulijn, and J. Pérez-Ramírez, "Direct demonstration of enhanced diffusion in mesoporous zsm-5 zeolite obtained via controlled desilication," *J. Am. Chem. Soc.*, vol. 129, no. 2, pp. 355–360, 2007.

- [29] L. Zhao, B. Shen, J. Gao, and C. Xu, "Investigation on the mechanism of diffusion in mesopore structured zsm-5 and improved heavy oil conversion," *J. Catal.*, vol. 258, no. 1, pp. 228–234, 2008.
- [30] C. J. Baranowski, A. M. Bahmanpour, F. Héroguel, J. S. Luterbacher, and O. Kröcher, "Prominent role of mesopore surface area and external acid sites for the synthesis of polyoxymethylene dimethyl ethers (ome) on a hierarchical h-zsm-5 zeolite," *Catal. Sci. Technol.*, vol. 9, no. 2, pp. 366–376, 2019.
- [31] Y. Zeldovich, D. Frank-Kamenetskii, and P. Sadovnikov, *Oxidation of nitrogen in combustion*. Publishing House of the Acad of Sciences of USSR, 1947.
- [32] G. Busca, L. Lietti, G. Ramis, and F. Berti, "Chemical and mechanistic aspects of the selective catalytic reduction of nox by ammonia over oxide catalysts: a review," *Appl. Catal., B*, vol. 18, no. 1-2, pp. 1–36, 1998.
- [33] M. Shelef, "Selective catalytic reduction of nox with n-free reductants," *Chem. Rev.*, vol. 95, no. 1, pp. 209–225, 1995.
- [34] J. H. Kwak, R. G. Tonkyn, D. H. Kim, J. Szanyi, and C. H. Peden, "Excellent activity and selectivity of cu-ssz-13 in the selective catalytic reduction of nox with nh<sub>3</sub>," *J. Catal.*, vol. 275, no. 2, pp. 187–190, 2010.
- [35] H. C. Andersen, W. J. Green, and D. R. Steele, "The catalytic treatment of nitric acid plant tail gas," *Ind. Eng. Chem.*, vol. 53, no. 3, pp. 199–204, 1961.
- [36] H. Jääskeläinen, "Diesel exhaust gas," 2011.
- [37] R. Q. Long and R. T. Yang, "Superior fe-zsm-5 catalyst for selective catalytic reduction of nitric oxide by ammonia," *J. Am. Chem. Soc.*, vol. 121, no. 23, pp. 5595–5596, 1999.
- [38] M. Schwidder, M. S. Kumar, K. Klementiev, M. M. Pohl, A. Brückner, and W. Grünert, "Selective reduction of no with fe-zsm-5 catalysts of low fe content: I. relations between active site structure and catalytic performance," *J. Catal.*, vol. 231, no. 2, pp. 314–330, 2005.
- [39] M. S. Kumar, M. Schwidder, W. Grünert, U. Bentrup, and A. Brückner, "Selective reduction of no with fe-zsm-5 catalysts of low fe content: Part ii. assessing the function of different fe sites by spectroscopic in situ studies," *J. Catal.*, vol. 239, no. 1, pp. 173–186, 2006.
- [40] M. Devadas, O. Kröcher, M. Elsener, A. Wokaun, N. Söger, M. Pfeifer, Y. Demel, and L. Mussmann, "Influence of no<sub>2</sub> on the selective catalytic reduction of no with ammonia over fe-zsm5," *Appl. Catal., B*, vol. 67, no. 3-4, pp. 187–196, 2006.
- [41] A. M. Beale, F. Gao, I. Lezcano-Gonzalez, C. H. Peden, and J. Szanyi, "Recent advances in automotive catalysis for no x emission control by small-pore microporous materials," *Chem. Soc. Rev.*, vol. 44, no. 20, pp. 7371–7405, 2015.
- [42] K. A. Lomachenko, E. Borfecchia, C. Negri, G. Berlier, C. Lamberti, P. Beato, H. Falsig, and S. Bordiga, "The cu-cha deno x catalyst in action: temperature-dependent nh<sub>3</sub>-assisted selective catalytic reduction monitored by operando xas and xes," *J. Am. Chem. Soc.*, vol. 138, no. 37, pp. 12025–12028, 2016.
- [43] S. A. Bates, A. A. Verma, C. Paolucci, A. A. Parekh, T. Anggara, A. Yezerets, W. F. Schneider, J. T. Miller, W. N. Delgass, and F. H. Ribeiro, "Identification of the active cu site in standard selective catalytic reduction with ammonia on cu-ssz-13," *J. Catal.*, vol. 312, pp. 87–97, 2014.

- [44] J.-S. McEwen, T. Anggara, W. Schneider, V. Kispersky, J. Miller, W. Delgass, and F. Ribeiro, "Integrated operando x-ray absorption and dft characterization of cu-ssz-13 exchange sites during the selective catalytic reduction of nox with nh<sub>3</sub>," *Catal. Today*, vol. 184, no. 1, pp. 129–144, 2012.
- [45] T. V. Janssens, H. Falsig, L. F. Lundegaard, P. N. Vennestrøm, S. B. Rasmussen, P. G. Moses, F. Giordanino, E. Borfecchia, K. A. Lomachenko, C. Lamberti, *et al.*, "A consistent reaction scheme for the selective catalytic reduction of nitrogen oxides with ammonia," *ACS Catal.*, vol. 5, no. 5, pp. 2832–2845, 2015.
- [46] D. Berthomieu and G. Delahay, "Recent advances in cui/iyy: experiments and modeling," *Catal. Rev.*, vol. 48, no. 3, pp. 269–313, 2006.
- [47] C. Paolucci, I. Khurana, A. A. Parekh, S. Li, A. J. Shih, H. Li, J. R. Di Iorio, J. D. Albarracin-Caballero, A. Yezerets, J. T. Miller, *et al.*, "Dynamic multinuclear sites formed by mobilized copper ions in nox selective catalytic reduction," *Science*, vol. 357, no. 6354, pp. 898–903, 2017.
- [48] F. Gao, J. H. Kwak, J. Szanyi, and C. H. Peden, "Current understanding of cu-exchanged chabazite molecular sieves for use as commercial diesel engine deno x catalysts," *Top. Catal.*, vol. 56, no. 15-17, pp. 1441–1459, 2013.
- [49] S. Kieger, G. Delahay, B. Coq, and B. Neveu, "Selective catalytic reduction of nitric oxide by ammonia over cu-fau catalysts in oxygen-rich atmosphere," *J. Catal.*, vol. 183, no. 2, pp. 267–280, 1999.
- [50] T. Yu, T. Hao, D. Fan, J. Wang, M. Shen, and W. Li, "Recent nh<sub>3</sub>-scr mechanism research over cu/sapo-34 catalyst," *J. Phys. Chem. C*, vol. 118, no. 13, pp. 6565–6575, 2014.
- [51] C. Paolucci, A. A. Verma, S. A. Bates, V. F. Kispersky, J. T. Miller, R. Gounder, W. N. Delgass, F. H. Ribeiro, and W. F. Schneider, "Isolation of the copper redox steps in the standard selective catalytic reduction on cu-ssz-13," *Angew. Chem., Int. Ed.*, vol. 53, no. 44, pp. 11828–11833, 2014.
- [52] F. Gao, D. Mei, Y. Wang, J. Szanyi, and C. H. Peden, "Selective catalytic reduction over cu/ssz-13: linking homo-and heterogeneous catalysis," *J. Am. Chem. Soc.*, vol. 139, no. 13, pp. 4935–4942, 2017.
- [53] N. Tajima, M. Hashimoto, F. Toyama, A. M. El-Nahas, and K. Hirao, "A theoretical study on the catalysis of cu-exchanged zeolite for the decomposition of nitric oxide," *Phys. Chem. Chem. Phys.*, vol. 1, no. 16, pp. 3823–3830, 1999.
- [54] Y. Liu, Y. Hou, X. Han, J. Wang, Y. Guo, N. Xiang, Y. Bai, and Z. Huang, "Effect of ordered mesoporous alumina support on the structural and catalytic properties of mn-ni/oma catalyst for nh<sub>3</sub>-scr performance at low-temperature," *ChemCatChem*, 2019.
- [55] B. Guan, R. Zhan, H. Lin, and Z. Huang, "Review of state of the art technologies of selective catalytic reduction of nox from diesel engine exhaust," *Appl. Therm. Eng.*, vol. 66, no. 1-2, pp. 395–414, 2014.
- [56] T. Johnson, "Vehicular emissions in review," *SAE Int. J. Engines*, vol. 6, no. 2, pp. 699–715, 2013.
- [57] J. Han, E. Kim, T. Lee, J. Kim, N. Ahn, and H.-S. Han, "Urea-scr catalysts with improved low temperature activity," tech. rep., SAE Technical Paper, 2011.

- [58] L. Han, S. Cai, M. Gao, J.-y. Hasegawa, P. Wang, J. Zhang, L. Shi, and D. Zhang, "Selective catalytic reduction of no x with nh<sub>3</sub> by using novel catalysts: State of the art and future prospects," *Chem. Rev.*, vol. 119, no. 19, pp. 10916–10976, 2019.
- [59] J. Kornatowski, W. H. Baur, G. Pieper, M. Rozwadowski, W. Schmitz, and A. Cichowlas, "Dealumination of large crystals of zeolite zms-5 by various methods," *J. Chem. Soc., Faraday Trans.*, vol. 88, no. 9, pp. 1339–1343, 1992.
- [60] C. K. Lambert, "Perspective on scr no x control for diesel vehicles," *React. Chem. Eng.*, vol. 4, no. 6, pp. 969–974, 2019.
- [61] H. Falsig, P. N. Vennestrøm, P. G. Moses, and T. V. Janssens, "Activation of oxygen and no in nh<sub>3</sub>-scr over cu-cha catalysts evaluated by density functional theory," *Top. Catal.*, vol. 59, no. 10-12, pp. 861–865, 2016.
- [62] C. Tyrsted, E. Borfecchia, G. Berlier, K. Lomachenko, C. Lamberti, S. Bordiga, P. Vennestrøm, T. Janssens, H. Falsig, P. Beato, *et al.*, "Nitrate–nitrite equilibrium in the reaction of no with a cu-cha catalyst for nh<sub>3</sub>-scr," *Catal. Sci. Technol.*, vol. 6, no. 23, pp. 8314–8324, 2016.
- [63] J. Weitkamp, "Zeolites and catalysis," *Solid state ionics*, vol. 131, no. 1-2, pp. 175–188, 2000.
- [64] T. Armadori, L. Simon, M. Digne, T. Montanari, M. Bevilacqua, V. Valtchev, J. Patarin, and G. Busca, "Effects of crystal size and si/al ratio on the surface properties of h-zsm-5 zeolites," *Appl. Catal., A*, vol. 306, pp. 78–84, 2006.
- [65] L. Shirazi, E. Jamshidi, and M. Ghasemi, "The effect of si/al ratio of zsm-5 zeolite on its morphology, acidity and crystal size," *Cryst. Res. Technol.*, vol. 43, no. 12, pp. 1300–1306, 2008.
- [66] S. Mintova, V. Valtchev, T. Onfroy, C. Marichal, H. Knözinger, and T. Bein, "Variation of the si/al ratio in nanosized zeolite beta crystals," *Microporous Mesoporous Mater.*, vol. 90, no. 1-3, pp. 237–245, 2006.
- [67] Y. Miyamoto, N. Katada, and M. Niwa, "Acidity of  $\beta$  zeolite with different si/al<sub>2</sub> ratio as measured by temperature programmed desorption of ammonia," *Microporous Mesoporous Mater.*, vol. 40, no. 1-3, pp. 271–281, 2000.
- [68] U. Lohse, B. Parlitz, and V. Patzelova, "Y zeolite acidity dependence on the silicon/aluminum ratio," *J. Phys. Chem.*, vol. 93, no. 9, pp. 3677–3683, 1989.
- [69] W.-Q. Xu, Y.-G. Yin, S. L. Suib, J. C. Edwards, and C.-L. OYoung, "n-butene skeletal isomerization to isobutylene on shape selective catalysts: Ferrierite/zsm-35," *J. Phys. Chem.*, vol. 99, no. 23, pp. 9443–9451, 1995.
- [70] V. Blay, B. Louis, R. Miravalles, T. Yokoi, K. A. Peccatiello, M. Clough, and B. Yilmaz, "Engineering zeolites for catalytic cracking to light olefins," *ACS Catal.*, vol. 7, no. 10, pp. 6542–6566, 2017.
- [71] S. Babitz, B. Williams, J. Miller, R. Q. Snurr, W. Haag, and H. H. Kung, "Monomolecular cracking of n-hexane on y, mor, and zsm-5 zeolites," *Appl. Catal., A*, vol. 179, no. 1-2, pp. 71–86, 1999.
- [72] J. A. Van Bokhoven, B. A. Williams, W. Ji, D. C. Koningsberger, H. H. Kung, and J. T. Miller, "Observation of a compensation relation for monomolecular alkane cracking by zeolites: The dominant role of reactant sorption," *J. Catal.*, vol. 224, no. 1, pp. 50–59, 2004.

- [73] C. Tuma, T. Kerber, and J. Sauer, "The tert-butyl cation in h-zeolites: Deprotonation to isobutene and conversion into surface alkoxides," *Angew. Chem., Int. Ed.*, vol. 49, no. 27, pp. 4678–4680, 2010.
- [74] C. Tuma and J. Sauer, "Treating dispersion effects in extended systems by hybrid mp2: Dft calculations—protonation of isobutene in zeolite ferrierite," *Phys. Chem. Chem. Phys.*, vol. 8, no. 34, pp. 3955–3965, 2006.
- [75] N. Hansen, T. Kerber, J. Sauer, A. T. Bell, and F. J. Keil, "Quantum chemical modeling of benzene ethylation over h-zsm-5 approaching chemical accuracy: a hybrid mp2: Dft study," *J. Am. Chem. Soc.*, vol. 132, no. 33, pp. 11525–11538, 2010.
- [76] S. Svelle, C. Tuma, X. Rozanska, T. Kerber, and J. Sauer, "Quantum chemical modeling of zeolite-catalyzed methylation reactions: toward chemical accuracy for barriers," *J. Am. Chem. Soc.*, vol. 131, no. 2, pp. 816–825, 2009.
- [77] M. Rybicki and J. Sauer, "Ab initio prediction of proton exchange barriers for alkanes at brønsted sites of zeolite h-mfi," *J. Am. Chem. Soc.*, vol. 140, no. 51, pp. 18151–18161, 2018.
- [78] A. Szabo and N. S. Ostlund, *Modern quantum chemistry: introduction to advanced electronic structure theory*. Courier Corporation, 2012.
- [79] J. K. Nørskov, F. Studt, F. Abild-Pedersen, and T. Bligaard, *Fundamental concepts in heterogeneous catalysis*. John Wiley & Sons, 2014.
- [80] R. M. Martin and R. M. Martin, *Electronic structure: basic theory and practical methods*. Cambridge university press, 2004.
- [81] F. Jensen, *Introduction to computational chemistry*. John wiley & sons, 2017.
- [82] T. Helgaker, P. Jorgensen, and J. Olsen, *Molecular electronic-structure theory*. John Wiley & Sons, 2014.
- [83] W. Koch and M. C. Holthausen, *A chemist's guide to density functional theory*. John Wiley & Sons, 2015.
- [84] B. J. Berne, G. Ciccotti, D. F. Coker, *et al.*, *Classical and quantum dynamics in condensed phase simulations*. World Scientific, Singapore, 1998.
- [85] P. N. Plessow, "Efficient transition state optimization of periodic structures through automated relaxed potential energy surface scans," *J. Chem. Theory Comput.*, vol. 14, no. 2, pp. 981–990, 2018.
- [86] C. J. Cramer and F. Bickelhaupt, "Essentials of computational chemistry," *Angew. Chem., Int. Ed. Engl.*, vol. 42, no. 4, pp. 381–381, 2003.
- [87] A. H. Larsen, J. J. Mortensen, J. Blomqvist, I. E. Castelli, R. Christensen, M. Dulak, J. Friis, M. N. Groves, B. Hammer, C. Hargus, *et al.*, "The atomic simulation environment—a python library for working with atoms," *J. Phys.: Condens. Matter*, vol. 29, no. 27, p. 273002, 2017.
- [88] J. P. Casquilho and P. I. C. Teixeira, "Introdução à física estatística," *São Paulo: Editora Livraria da Física*, 2012.
- [89] J. P. Perdew, A. Ruzsinszky, G. I. Csonka, O. A. Vydrov, G. E. Scuseria, L. A. Constantin, X. Zhou, and K. Burke, "Restoring the density-gradient expansion for exchange in solids and surfaces," *Phys. Rev. Lett.*, vol. 100, no. 13, p. 136406, 2008.

- 
- [90] J. P. Perdew, A. Ruzsinszky, G. I. Csonka, O. A. Vydrov, G. E. Scuseria, L. A. Constantin, X. Zhou, and K. Burke, "Erratum: Restoring the density-gradient expansion for exchange in solids and surfaces [phys. rev. lett. 100, 136406 (2008)]," *Phys. Rev. Lett.*, vol. 102, no. 3, p. 039902, 2009.
- [91] J. P. Perdew, K. Burke, and M. Ernzerhof, "Generalized gradient approximation made simple," *Phys. Rev. Lett.*, vol. 77, no. 18, p. 3865, 1996.
- [92] Y. Zhao and D. G. Truhlar, "A new local density functional for main-group thermochemistry, transition metal bonding, thermochemical kinetics, and noncovalent interactions," *J. Chem. Phys.*, vol. 125, no. 19, p. 194101, 2006.
- [93] Y. Zhao and D. G. Truhlar, "The m06 suite of density functionals for main group thermochemistry, thermochemical kinetics, noncovalent interactions, excited states, and transition elements: two new functionals and systematic testing of four m06-class functionals and 12 other functionals," *Theor. Chem. Acc.*, vol. 120, no. 1-3, pp. 215–241, 2008.
- [94] A. D. Becke, "Density-functional thermochemistry. III. The role of exact exchange," *J. Chem. Phys.*, vol. 98, no. 7, pp. 5648–5652, 1993.
- [95] P. J. Stephens, F. Devlin, C. Chabalowski, and M. J. Frisch, "Ab initio calculation of vibrational absorption and circular dichroism spectra using density functional force fields," *J. Phys. Chem.*, vol. 98, no. 45, pp. 11623–11627, 1994.
- [96] C. Adamo and V. Barone, "Toward reliable density functional methods without adjustable parameters: The pbe0 model," *J. Chem. Phys.*, vol. 110, no. 13, pp. 6158–6170, 1999.
- [97] S. Grimme, J. Antony, S. Ehrlich, and H. Krieg, "A consistent and accurate ab initio parametrization of density functional dispersion correction (dft-d) for the 94 elements h-pu," *J. Chem. Phys.*, vol. 132, no. 15, p. 154104, 2010.
- [98] T. H. Dunning Jr, "Gaussian basis sets for use in correlated molecular calculations. i. the atoms boron through neon and hydrogen," *J. Chem. Phys.*, vol. 90, no. 2, pp. 1007–1023, 1989.
- [99] Y. Minenkov, G. Bistoni, C. Riplinger, A. A. Auer, F. Neese, and L. Cavallo, "Pair natural orbital and canonical coupled cluster reaction enthalpies involving light to heavy alkali and alkaline earth metals: the importance of sub-valence correlation," *Phys. Chem. Chem. Phys.*, vol. 19, no. 14, pp. 9374–9391, 2017.
- [100] A. Halkier, T. Helgaker, P. Jørgensen, W. Klopper, and J. Olsen, "Basis-set convergence of the energy in molecular hartree-fock calculations," *Chem. Phys. Letters*, vol. 302, no. 5-6, pp. 437–446, 1999.
- [101] A. Halkier, T. Helgaker, P. Jørgensen, W. Klopper, H. Koch, J. Olsen, and A. K. Wilson, "Basis-set convergence in correlated calculations on ne, n2, and h2o," *Chem. Phys. Letters*, vol. 286, no. 3-4, pp. 243–252, 1998.
- [102] V. Vasilyev, "Online complete basis set limit extrapolation calculator," *Comput. Theor. Chem.*, vol. 1115, pp. 1–3, 2017.
- [103] K. Eichkorn, O. Treutler, H. Oehm, M. Häser, and R. Ahlrichs, "Auxiliary basis sets to approximate coulomb potentials (chem. phys. letters 240 (1995) 283-290)," *Chem. Phys.*, vol. 242, pp. 652–660, 1995.

- [104] F. Neese, F. Wennmohs, A. Hansen, and U. Becker, "Efficient, approximate and parallel hartree-fock and hybrid dft calculations. a 'chain-of-spheres' algorithm for the hartree-fock exchange," *Chem. Phys.*, vol. 356, no. 1-3, pp. 98-109, 2009.
- [105] C. Riplinger and F. Neese, "An efficient and near linear scaling pair natural orbital based local coupled cluster method," *J. Chem. Phys.*, vol. 138, no. 3, p. 034106, 2013.
- [106] F. Neese, "The orca program system," *Wiley Interdiscip. Rev.: Comput. Mol. Sci.*, vol. 2, no. 1, pp. 73-78, 2012.
- [107] F. Neese, "Software update: the orca program system, version 4.0," *Wiley Interdiscip. Rev.: Comput. Mol. Sci.*, vol. 8, no. 1, p. e1327, 2018.
- [108] A. V. Marenich, C. J. Cramer, and D. G. Truhlar, "Universal solvation model based on solute electron density and on a continuum model of the solvent defined by the bulk dielectric constant and atomic surface tensions," *J. Phys. Chem. B*, vol. 113, no. 18, pp. 6378-6396, 2009.
- [109] J. K. Nørskov, F. Abild-Pedersen, F. Studt, and T. Bligaard, "Density functional theory in surface chemistry and catalysis," *Proc. Natl. Acad. Sci.*, vol. 108, no. 3, pp. 937-943, 2011.
- [110] N. K. Dandu, J. A. Reed, and S. O. Odoh, "Performance of density functional theory for predicting methane-to-methanol conversion by a tri-copper complex," *J. Phys. Chem. C*, vol. 122, no. 2, pp. 1024-1036, 2018.
- [111] K. D. Vogiatzis, G. Li, E. J. Hensen, L. Gagliardi, and E. A. Pidko, "Electronic structure of the  $[\text{Cu}_3(\mu\text{-O})_3]^{2+}$  cluster in mordenite zeolite and its effects on the methane to methanol oxidation," *J. Phys. Chem. C*, vol. 121, no. 40, pp. 22295-22302, 2017.
- [112] N. K. Dandu, O. Adeyiga, D. Panthi, S. A. Bird, and S. O. Odoh, "Performance of density functional theory for describing hetero-metallic active-site motifs for methane-to-methanol conversion in metal-exchanged zeolites," *J. Comput. Chem.*, vol. 39, no. 32, pp. 2667-2678, 2018.
- [113] C. Tuma and J. Sauer, "A hybrid mp2/planewave-dft scheme for large chemical systems: proton jumps in zeolites," *Chem. Phys. Lett.*, vol. 387, no. 4-6, pp. 388-394, 2004.
- [114] M. Sierka and J. Sauer, "Structure and reactivity of silica and zeolite catalysts by a combined quantum mechanics [ndash] shell-model potential approach based on dft," *Faraday Discuss.*, vol. 106, pp. 41-62, 1997.
- [115] S. Sklenak, J. Dědeček, C. Li, B. Wichterlova, V. Gabova, M. Sierka, and J. Sauer, "Aluminium siting in the zsm-5 framework by combination of high resolution 27al nmr and dft/mm calculations," *Phys. Chem. Chem. Phys.*, vol. 11, no. 8, pp. 1237-1247, 2009.
- [116] A. L. Dzubak, L.-C. Lin, J. Kim, J. A. Swisher, R. Poloni, S. N. Maximoff, B. Smit, and L. Gagliardi, "Ab initio carbon capture in open-site metal-organic frameworks," *Nat. Chem.*, vol. 4, no. 10, p. 810, 2012.
- [117] T. M. McDonald, J. A. Mason, X. Kong, E. D. Bloch, D. Gygi, A. Dani, V. Crocella, F. Giordanino, S. O. Odoh, W. S. Drisdell, *et al.*, "Cooperative insertion of co 2 in diamine-appended metal-organic frameworks," *Nature*, vol. 519, no. 7543, pp. 303-308, 2015.

- [118] D. J. Xiao, E. D. Bloch, J. A. Mason, W. L. Queen, M. R. Hudson, N. Planas, J. Borycz, A. L. Dzubak, P. Verma, K. Lee, *et al.*, “Oxidation of ethane to ethanol by  $n_2o$  in a metal–organic framework with coordinatively unsaturated iron (ii) sites,” *Nat. Chem.*, vol. 6, no. 7, p. 590, 2014.
- [119] N. Planas, A. L. Dzubak, R. Poloni, L.-C. Lin, A. McManus, T. M. McDonald, J. B. Neaton, J. R. Long, B. Smit, and L. Gagliardi, “The mechanism of carbon dioxide adsorption in an alkylamine-functionalized metal–organic framework,” *J. Am. Chem. Soc.*, vol. 135, no. 20, pp. 7402–7405, 2013.
- [120] Z. Li, N. M. Schweitzer, A. B. League, V. Bernales, A. W. Peters, A. B. Getsoian, T. C. Wang, J. T. Miller, A. Vjunov, J. L. Fulton, *et al.*, “Sintering-resistant single-site nickel catalyst supported by metal–organic framework,” *J. Am. Chem. Soc.*, vol. 138, no. 6, pp. 1977–1982, 2016.
- [121] B. Vlaisavljevich, L. Gagliardi, and P. C. Burns, “Understanding the structure and formation of uranyl peroxide nanoclusters by quantum chemical calculations,” *J. Am. Chem. Soc.*, vol. 132, no. 41, pp. 14503–14508, 2010.
- [122] S. Grundner, M. A. Markovits, G. Li, M. Tromp, E. A. Pidko, E. J. Hensen, A. Jentys, M. Sanchez-Sanchez, and J. A. Lercher, “Single-site trinuclear copper oxygen clusters in mordenite for selective conversion of methane to methanol,” *Nat. Commun.*, vol. 6, no. 1, pp. 1–9, 2015.
- [123] E. A. Pidko and R. A. Van Santen, “Activation of light alkanes over zinc species stabilized in zsm-5 zeolite: a comprehensive dft study,” *J. Phys. Chem. C*, vol. 111, no. 6, pp. 2643–2655, 2007.
- [124] G. Yang, E. A. Pidko, and E. J. Hensen, “The mechanism of glucose isomerization to fructose over sn-bea zeolite: a periodic density functional theory study,” *ChemSusChem*, vol. 6, no. 9, pp. 1688–1696, 2013.
- [125] Y. Zhao and D. G. Truhlar, “Benchmark data for interactions in zeolite model complexes and their use for assessment and validation of electronic structure methods,” *J. Phys. Chem. C*, vol. 112, no. 17, pp. 6860–6868, 2008.
- [126] D. Lesthaeghe, V. Van Speybroeck, G. B. Marin, and M. Waroquier, “Understanding the failure of direct c—c coupling in the zeolite-catalyzed methanol-to-olefin process,” *Angew. Chem., Int. Ed.*, vol. 45, no. 11, pp. 1714–1719, 2006.
- [127] K. Rahkamaa-Tolonen, T. Maunula, M. Lomma, M. Huuhtanen, and R. L. Keiski, “The effect of no<sub>2</sub> on the activity of fresh and aged zeolite catalysts in the nh<sub>3</sub>-scr reaction,” *Catal. Today*, vol. 100, no. 3-4, pp. 217–222, 2005.
- [128] G. Centi and S. Perathoner, “Nature of active species in copper-based catalysts and their chemistry of transformation of nitrogen oxides,” *Appl. Catal., A*, vol. 132, no. 2, pp. 179–259, 1995.
- [129] K. Tanabe and W. F. Hölderich, “Industrial application of solid acid–base catalysts,” *Appl. Catal., A*, vol. 181, no. 2, pp. 399–434, 1999.
- [130] I. Nova and E. Tronconi, *Urea-SCR technology for deNO<sub>x</sub> after treatment of diesel exhausts*, vol. 5. Springer, 2014.

- [131] K. Burke, "Perspective on density functional theory," *J. Chem. Phys.*, vol. 136, no. 15, p. 150901, 2012.
- [132] J. Wellendorff, T. L. Silbaugh, D. Garcia-Pintos, J. K. Nørskov, T. Bligaard, F. Studt, and C. T. Campbell, "A benchmark database for adsorption bond energies to transition metal surfaces and comparison to selected dft functionals," *Surf. Sci.*, vol. 640, pp. 36–44, 2015.
- [133] K. Duanmu and D. G. Truhlar, "Validation of density functionals for adsorption energies on transition metal surfaces," *J. Chem. Theory Comput.*, vol. 13, no. 2, pp. 835–842, 2017.
- [134] S. Mallikarjun Sharada, T. Bligaard, A. C. Luntz, G.-J. Kroes, and J. K. Nørskov, "Sbh10: A benchmark database of barrier heights on transition metal surfaces," *J. Phys. Chem. C*, vol. 121, no. 36, pp. 19807–19815, 2017.
- [135] P. N. Plessow and F. Studt, "Olefin methylation and cracking reactions in h-ssz-13 investigated with ab initio and dft calculations," *Catal. Sci. Technol.*, vol. 8, no. 17, pp. 4420–4429, 2018.
- [136] P. N. Plessow and F. Studt, "Unraveling the mechanism of the initiation reaction of the methanol to olefins process using ab initio and dft calculations," *ACS Catal.*, vol. 7, no. 11, pp. 7987–7994, 2017.
- [137] L. Wu, V. Degirmenci, P. C. Magusin, B. M. Szyja, and E. J. Hensen, "Dual template synthesis of a highly mesoporous ssz-13 zeolite with improved stability in the methanol-to-olefins reaction," *Chem. Commun.*, vol. 48, no. 76, pp. 9492–9494, 2012.
- [138] L. Sommer, D. Mores, S. Svelle, M. Stöcker, B. M. Weckhuysen, and U. Olsbye, "Mesopore formation in zeolite h-ssz-13 by desilication with naoh," *Microporous Mesoporous Mater.*, vol. 132, no. 3, pp. 384–394, 2010.
- [139] K. Hemelsoet, J. Van der Mynsbrugge, K. De Wispelaere, M. Waroquier, and V. Van Speybroeck, "Unraveling the reaction mechanisms governing methanol-to-olefins catalysis by theory and experiment," *ChemPhysChem*, vol. 14, no. 8, pp. 1526–1545, 2013.
- [140] V. Van Speybroeck, K. De Wispelaere, J. Van der Mynsbrugge, M. Vandichel, K. Hemelsoet, and M. Waroquier, "First principle chemical kinetics in zeolites: the methanol-to-olefin process as a case study," *Chem. Soc. Rev.*, vol. 43, no. 21, pp. 7326–7357, 2014.
- [141] U. Olsbye, S. Svelle, M. Bjørgen, P. Beato, T. V. Janssens, F. Joensen, S. Bordiga, and K. P. Lillerud, "Conversion of methanol to hydrocarbons: how zeolite cavity and pore size controls product selectivity," *Angew. Chem., Int. Ed.*, vol. 51, no. 24, pp. 5810–5831, 2012.
- [142] P. N. Plessow and F. Studt, "Theoretical insights into the effect of the framework on the initiation mechanism of the mto process," *Catal. Lett.*, vol. 148, no. 4, pp. 1246–1253, 2018.
- [143] P. N. Plessow, A. Smith, S. Tischer, and F. Studt, "Identification of the reaction sequence of the mto initiation mechanism using ab initio-based kinetics," *J. Am. Chem. Soc.*, vol. 141, no. 14, pp. 5908–5915, 2019.
- [144] F. Bleken, M. Bjørgen, L. Palumbo, S. Bordiga, S. Svelle, K.-P. Lillerud, and U. Olsbye, "The effect of acid strength on the conversion of methanol to olefins over acidic microporous catalysts with the cha topology," *Top. Catal.*, vol. 52, no. 3, pp. 218–228, 2009.
- [145] B. P. Hereijgers, F. Bleken, M. H. Nilsen, S. Svelle, K.-P. Lillerud, M. Bjørgen, B. M. Weckhuysen, and U. Olsbye, "Product shape selectivity dominates the methanol-to-olefins (mto) reaction over h-sapo-34 catalysts," *J. Catal.*, vol. 264, no. 1, pp. 77–87, 2009.

- [146] W. Wang, Y. Jiang, and M. Hunger, "Mechanistic investigations of the methanol-to-olefin (mto) process on acidic zeolite catalysts by in situ solid-state nmr spectroscopy," *Catal. Today*, vol. 113, no. 1-2, pp. 102–114, 2006.
- [147] Q. Qian, J. Ruiz-Martínez, M. Mokhtar, A. M. Asiri, S. A. Al-Thabaiti, S. N. Basahel, and B. M. Weckhuysen, "Single-catalyst particle spectroscopy of alcohol-to-olefins conversions: Comparison between sapo-34 and ssz-13," *Catal. Today*, vol. 226, pp. 14–24, 2014.
- [148] I. Yarulina, A. D. Chowdhury, F. Meirer, B. M. Weckhuysen, and J. Gascon, "Recent trends and fundamental insights in the methanol-to-hydrocarbons process," *Nat. Catal.*, vol. 1, no. 6, pp. 398–411, 2018.
- [149] C.-M. Wang, R. Y. Brogaard, B. M. Weckhuysen, J. K. Nørskov, and F. Studt, "Reactivity descriptor in solid acid catalysis: predicting turnover frequencies for propene methylation in zeotypes," *J. Phys. Chem. Lett.*, vol. 5, no. 9, pp. 1516–1521, 2014.
- [150] E. Borodina, F. Meirer, I. Lezcano-González, M. Mokhtar, A. Asiri, S. Al-Thabaiti, S. Basahel, J. Ruiz-Martínez, and B. Weckhuysen, "Influence of the reaction temperature on the nature of the active and deactivating species during methanol to olefins conversion over h-ssz-13," *ACS Catal.*, vol. 5, no. 2, pp. 992–1003, 2015.
- [151] F. Gao, E. D. Walter, M. Kollar, Y. Wang, J. Szanyi, and C. H. Peden, "Understanding ammonia selective catalytic reduction kinetics over cu/ssz-13 from motion of the cu ions," *J. Catal.*, vol. 319, pp. 1–14, 2014.
- [152] F. Gao, N. M. Washton, Y. Wang, M. Kollár, J. Szanyi, and C. H. Peden, "Effects of si/al ratio on cu/ssz-13 nh<sub>3</sub>-scr catalysts: Implications for the active cu species and the roles of brønsted acidity," *J. Catal.*, vol. 331, pp. 25–38, 2015.
- [153] H. Zhu, J. H. Kwak, C. H. Peden, and J. Szanyi, "In situ drifts-ms studies on the oxidation of adsorbed nh<sub>3</sub> by nox over a cu-ssz-13 zeolite," *Catal. Today*, vol. 205, pp. 16–23, 2013.
- [154] I. Lezcano-Gonzalez, U. Deka, B. Arstad, A. Van Yperen-De Deyne, K. Hemelsoet, M. Waroquier, V. Van Speybroeck, B. M. Weckhuysen, and A. M. Beale, "Determining the storage, availability and reactivity of nh<sub>3</sub> within cu-chabazite-based ammonia selective catalytic reduction systems," *Phys. Chem. Chem. Phys.*, vol. 16, no. 4, pp. 1639–1650, 2014.
- [155] T. Yu, J. Wang, M. Shen, and W. Li, "Nh<sub>3</sub>-scr over cu/sapo-34 catalysts with various acid contents and low cu loading," *Catal. Sci. Technol.*, vol. 3, no. 12, pp. 3234–3241, 2013.
- [156] E. Borfecchia, K. Lomachenko, F. Giordanino, H. Falsig, P. Beato, A. Soldatov, S. Bordiga, and C. Lamberti, "Revisiting the nature of cu sites in the activated cu-ssz-13 catalyst for scr reaction," *Chem. Sci.*, vol. 6, no. 1, pp. 548–563, 2015.
- [157] U. Deka, I. Lezcano-Gonzalez, B. M. Weckhuysen, and A. M. Beale, "Local environment and nature of cu active sites in zeolite-based catalysts for the selective catalytic reduction of no<sub>x</sub>," *ACS Catal.*, vol. 3, no. 3, pp. 413–427, 2013.
- [158] C. W. Andersen, M. Bremholm, P. N. R. Vennestrøm, A. B. Blichfeld, L. F. Lundegaard, and B. B. Iversen, "Location of cu<sup>2+</sup> in cha zeolite investigated by x-ray diffraction using the rietveld/maximum entropy method," *IUCrJ*, vol. 1, no. 6, pp. 382–386, 2014.
- [159] F. Giordanino, E. Borfecchia, K. A. Lomachenko, A. Lazzarini, G. Agostini, E. Gallo, A. V. Soldatov, P. Beato, S. Bordiga, and C. Lamberti, "Interaction of nh<sub>3</sub> with cu-ssz-13 catalyst:

- A complementary ftir, xanes, and xes study,” *J. Phys. Chem. Lett.*, vol. 5, no. 9, pp. 1552–1559, 2014.
- [160] F. Gao, E. D. Walter, E. M. Karp, J. Luo, R. G. Tonkyn, J. H. Kwak, J. Szanyi, and C. H. Peden, “Structure–activity relationships in nh<sub>3</sub>-scr over cu-ssz-13 as probed by reaction kinetics and epr studies,” *J. Catal.*, vol. 300, pp. 20–29, 2013.
- [161] S. T. Korhonen, D. W. Fickel, R. F. Lobo, B. M. Weckhuysen, and A. M. Beale, “Isolated cu 2+ ions: active sites for selective catalytic reduction of no,” *Chem. Commun.*, vol. 47, no. 2, pp. 800–802, 2011.
- [162] L. Chen, T. V. Janssens, and H. Grönbeck, “A comparative test of different density functionals for calculations of nh<sub>3</sub>-scr over cu-chabazite,” *Phys. Chem. Chem. Phys.*, vol. 21, no. 21, pp. 10923–10930, 2019.
- [163] F. Göttl and J. Hafner, “Structure and properties of metal-exchanged zeolites studied using gradient-corrected and hybrid functionals. i. structure and energetics,” *J. Chem. Phys.*, vol. 136, no. 6, p. 064501, 2012.
- [164] F. Göttl and J. Hafner, “Structure and properties of metal-exchanged zeolites studied using gradient-corrected and hybrid functionals. iii. energetics and vibrational spectroscopy of adsorbates,” *J. Chem. Phys.*, vol. 136, no. 6, p. 064503, 2012.
- [165] T. Anggara, C. Paolucci, and W. F. Schneider, “Periodic dft characterization of no x adsorption in cu-exchanged ssz-13 zeolite catalysts,” *J. Phys. Chem. C*, vol. 120, no. 49, pp. 27934–27943, 2016.
- [166] A. Grüneis, M. Marsman, and G. Kresse, “Second-order möller–plesset perturbation theory applied to extended systems. ii. structural and energetic properties,” *J. Chem. Phys.*, vol. 133, no. 7, p. 074107, 2010.
- [167] M. Marsman, A. Grüneis, J. Paier, and G. Kresse, “Second-order möller–plesset perturbation theory applied to extended systems. i. within the projector-augmented-wave formalism using a plane wave basis set,” *J. Chem. Phys.*, vol. 130, no. 18, p. 184103, 2009.
- [168] T. Schäfer, B. Ramberger, and G. Kresse, “Quartic scaling mp2 for solids: A highly parallelized algorithm in the plane wave basis,” *J. Chem. Phys.*, vol. 146, no. 10, p. 104101, 2017.
- [169] T. Schäfer, B. Ramberger, and G. Kresse, “Laplace transformed mp2 for three dimensional periodic materials using stochastic orbitals in the plane wave basis and correlated sampling,” *J. Chem. Phys.*, vol. 148, no. 6, p. 064103, 2018.
- [170] R. Lazarski, A. M. Burow, and M. Sierka, “Density functional theory for molecular and periodic systems using density fitting and continuous fast multipole methods,” *J. Chem. Theory Comput.*, vol. 11, no. 7, pp. 3029–3041, 2015.
- [171] R. Lazarski, A. M. Burow, L. Grajciar, and M. Sierka, “Density functional theory for molecular and periodic systems using density fitting and continuous fast multipole method: Analytical gradients,” *J. Comput. Chem.*, vol. 37, no. 28, pp. 2518–2526, 2016.
- [172] M. Del Ben, M. Schönherr, J. Hutter, and J. VandeVondele, “Bulk liquid water at ambient temperature and pressure from mp2 theory,” *J. Phys. Chem. Lett.*, vol. 4, no. 21, pp. 3753–3759, 2013.

- [173] M. Del Ben, J. Hutter, and J. VandeVondele, "Second-order mller–plesset perturbation theory in the condensed phase: An efficient and massively parallel gaussian and plane waves approach," *J. Chem. Theory Comput.*, vol. 8, no. 11, pp. 4177–4188, 2012.
- [174] T. J. Goncalves, P. N. Plessow, and F. Studt, "On the accuracy of density functional theory in zeolite catalysis," *ChemCatChem*, vol. 11, no. 17, pp. 4368–4376, 2019.
- [175] R. Ahlrichs, M. Br, M. Hser, H. Horn, and C. Klmele, "Electronic structure calculations on workstation computers: The program system turbomole," *Chem. Phys. Lett.*, vol. 162, no. 3, pp. 165–169, 1989.
- [176] M. Von Arnim and R. Ahlrichs, "Performance of parallel turbomole for density functional calculations," *J. Comput. Chem.*, vol. 19, no. 15, pp. 1746–1757, 1998.
- [177] F. Weigend, F. Furche, and R. Ahlrichs, "Gaussian basis sets of quadruple zeta valence quality for atoms h–kr," *J. Chem. Phys.*, vol. 119, no. 24, pp. 12753–12762, 2003.
- [178] F. Weigend and R. Ahlrichs, "Balanced basis sets of split valence, triple zeta valence and quadruple zeta valence quality for h to rn: Design and assessment of accuracy," *Phys. Chem. Chem. Phys.*, vol. 7, no. 18, pp. 3297–3305, 2005.
- [179] F. Weigend, M. Hser, H. Patzelt, and R. Ahlrichs, "Ri-mp2: optimized auxiliary basis sets and demonstration of efficiency," *Chem. Phys. Lett.*, vol. 294, no. 1-3, pp. 143–152, 1998.
- [180] C. L. Janssen and I. M. Nielsen, "New diagnostics for coupled-cluster and mller–plesset perturbation theory," *Chem. Phys. Lett.*, vol. 290, no. 4-6, pp. 423–430, 1998.
- [181] W. Jiang, N. J. DeYonker, and A. K. Wilson, "Multireference character for 3d transition-metal-containing molecules," *J. Chem. Theory Comput.*, vol. 8, no. 2, pp. 460–468, 2012.
- [182] A. Hellweg, C. Httig, S. Hfener, and W. Klopper, "Optimized accurate auxiliary basis sets for ri-mp2 and ri-cc2 calculations for the atoms rb to rn," *Theor. Chem. Acc.*, vol. 117, no. 4, pp. 587–597, 2007.
- [183] C. Httig, "Optimization of auxiliary basis sets for ri-mp2 and ri-cc2 calculations: Core–valence and quintuple- $\zeta$  basis sets for h to ar and qzvpp basis sets for li to kr," *Phys. Chem. Chem. Phys.*, vol. 7, no. 1, pp. 59–66, 2005.
- [184] F. Weigend, "Accurate coulomb-fitting basis sets for h to rn," *Phys. Chem. Chem. Phys.*, vol. 8, no. 9, pp. 1057–1065, 2006.
- [185] Y. Minenkov, E. Chermak, and L. Cavallo, "Accuracy of dlpno–ccsd (t) method for noncovalent bond dissociation enthalpies from coinage metal cation complexes," *J. Chem. Theory Comput.*, vol. 11, no. 10, pp. 4664–4676, 2015.
- [186] G. Kresse and J. Furthmller, "Efficient iterative schemes for ab initio total-energy calculations using a plane-wave basis set," *Phys. Rev. B*, vol. 54, no. 16, p. 11169, 1996.
- [187] G. Kresse and D. Joubert, "From ultrasoft pseudopotentials to the projector augmented-wave method," *Phys. Rev. B*, vol. 59, no. 3, p. 1758, 1999.
- [188] J. Wellendorff, K. T. Lundgaard, A. Mgelhj, V. Petzold, D. D. Landis, J. K. Nrskov, T. Bligaard, and K. W. Jacobsen, "Density functionals for surface science: Exchange–correlation model development with bayesian error estimation," *Phys. Rev. B*, vol. 85, no. 23, p. 235149, 2012.

- [189] G. Kresse and J. Hafner, "Ab initio molecular dynamics for liquid metals," *Phys. Rev. B*, vol. 47, no. 1, p. 558, 1993.
- [190] G. Kresse and J. Hafner, "Ab initio molecular-dynamics simulation of the liquid-metal–amorphous-semiconductor transition in germanium," *Phys. Rev. B*, vol. 49, no. 20, p. 14251, 1994.
- [191] G. Kresse and J. Furthmüller, "Efficiency of ab-initio total energy calculations for metals and semiconductors using a plane-wave basis set," *Comput. Mater. Sci.*, vol. 6, no. 1, pp. 15–50, 1996.
- [192] F. J. Keil, "Molecular modelling for reactor design," *Annu. Rev. Chem. Biomol. Eng.*, vol. 9, pp. 201–227, 2018.
- [193] S. L. Moors, K. De Wispelaere, J. Van der Mynsbrugge, M. Waroquier, and V. Van Speybroeck, "Molecular dynamics kinetic study on the zeolite-catalyzed benzene methylation in zsm-5," *ACS Catal.*, vol. 3, no. 11, pp. 2556–2567, 2013.
- [194] M. W. Erichsen, S. Svelle, and U. Olsbye, "H-sapo-5 as methanol-to-olefins (mto) model catalyst: Towards elucidating the effects of acid strength," *J. Catal.*, vol. 298, pp. 94–101, 2013.
- [195] I. Hill, A. Malek, and A. Bhan, "Kinetics and mechanism of benzene, toluene, and xylene methylation over h-mfi," *ACS Catal.*, vol. 3, no. 9, pp. 1992–2001, 2013.
- [196] R. L. Espinoza, "Oligomerization vs. methylation of propene in the conversion of dimethyl ether (or methanol) to hydrocarbons," *Ind. Eng. Chem. Prod. Res. Dev.*, vol. 23, no. 3, pp. 449–452, 1984.
- [197] A. Kato, S. Matsuda, T. Kamo, F. Nakajima, H. Kuroda, and T. Narita, "Reaction between nitrogen oxide (nox) and ammonia on iron oxide-titanium oxide catalyst," *J. Phys. Chem.*, vol. 85, no. 26, pp. 4099–4102, 1981.
- [198] L. Arnarson, H. Falsig, S. B. Rasmussen, J. V. Lauritsen, and P. G. Moses, "A complete reaction mechanism for standard and fast selective catalytic reduction of nitrogen oxides on low coverage vox/tio<sub>2</sub> (0 0 1) catalysts," *J. Catal.*, vol. 346, pp. 188–197, 2017.
- [199] M. Radon and E. Broclawik, "Mono-and dinitrosyls on copper (i) site in a zeolite model: Effects of static correlation," *J. Phys. Chem. A*, vol. 115, no. 42, pp. 11761–11774, 2011.
- [200] W. Schneider, K. Hass, R. Ramprasad, and J. Adams, "Density functional theory study of transformations of nitrogen oxides catalyzed by cu-exchanged zeolites," *J. Phys. Chem. B*, vol. 102, no. 19, pp. 3692–3705, 1998.
- [201] W. Schneider, K. Hass, R. Ramprasad, and J. Adams, "First-principles analysis of elementary steps in the catalytic decomposition of no by cu-exchanged zeolites," *J. Phys. Chem. B*, vol. 101, no. 22, pp. 4353–4357, 1997.
- [202] A. Pulido and P. Nachtigall, "Theoretical investigation of dinitrosyl complexes in cu-zeolites as intermediates in deno x process," *Phys. Chem. Chem. Phys.*, vol. 11, no. 9, pp. 1447–1458, 2009.
- [203] M. G. Medvedev, I. S. Bushmarinov, J. Sun, J. P. Perdew, and K. A. Lyssenko, "Density functional theory is straying from the path toward the exact functional," *Science*, vol. 355, no. 6320, pp. 49–52, 2017.

- [204] C. Ciardelli, I. Nova, E. Tronconi, D. Chatterjee, B. Bandl-Konrad, M. Weibel, and B. Krutzsch, "Reactivity of no/no<sub>2</sub>-nh<sub>3</sub> scr system for diesel exhaust aftertreatment: Identification of the reaction network as a function of temperature and no<sub>2</sub> feed content," *Appl. Catal., B*, vol. 70, no. 1-4, pp. 80–90, 2007.
- [205] M. Koebel, M. Elsener, and G. Madia, "Reaction pathways in the selective catalytic reduction process with no and no<sub>2</sub> at low temperatures," *Ind. Eng. Chem. Res.*, vol. 40, no. 1, pp. 52–59, 2001.
- [206] G. Henkelman and H. Jónsson, "A dimer method for finding saddle points on high dimensional potential surfaces using only first derivatives," *J. Chem. Phys.*, vol. 111, no. 15, pp. 7010–7022, 1999.
- [207] G. Henkelman and H. Jónsson, "Improved tangent estimate in the nudged elastic band method for finding minimum energy paths and saddle points," *J. Chem. Phys.*, vol. 113, no. 22, pp. 9978–9985, 2000.
- [208] G. Henkelman, B. P. Uberuaga, and H. Jónsson, "A climbing image nudged elastic band method for finding saddle points and minimum energy paths," *J. Chem. Phys.*, vol. 113, no. 22, pp. 9901–9904, 2000.
- [209] S. Smidstrup, A. Pedersen, K. Stokbro, and H. Jónsson, "Improved initial guess for minimum energy path calculations," *J. Chem. Phys.*, vol. 140, no. 21, p. 214106, 2014.
- [210] T. Helgaker, "Transition-state optimizations by trust-region image minimization," *Chem. Phys. Lett.*, vol. 182, no. 5, pp. 503–510, 1991.
- [211] F. Jensen, "Locating transition structures by mode following: A comparison of six methods on the ar<sub>8</sub> lennard-jones potential," *J. Chem. Phys.*, vol. 102, no. 17, pp. 6706–6718, 1995.
- [212] C. Paolucci, A. A. Parekh, I. Khurana, J. R. Di Iorio, H. Li, J. D. Albarracin Caballero, A. J. Shih, T. Anggara, W. N. Delgass, J. T. Miller, *et al.*, "Catalysis in a cage: condition-dependent speciation and dynamics of exchanged cu cations in ssz-13 zeolites," *J. Am. Chem. Soc.*, vol. 138, no. 18, pp. 6028–6048, 2016.
- [213] M. F. Irfan, J. H. Goo, and S. D. Kim, "Co<sub>3</sub>o<sub>4</sub> based catalysts for no oxidation and nox reduction in fast scr process," *Appl. Catal., B*, vol. 78, no. 3-4, pp. 267–274, 2008.
- [214] T. J. Goncalves, U. Arnold, P. N. Plessow, and F. Studt, "Theoretical investigation of the acid catalyzed formation of oxymethylene dimethyl ethers from trioxane and dimethoxymethane," *ACS Catal.*, vol. 7, no. 5, pp. 3615–3621, 2017.
- [215] J. Burger, E. Ströfer, and H. Hasse, "Production process for diesel fuel components poly (oxymethylene) dimethyl ethers from methane-based products by hierarchical optimization with varying model depth," *Chem. Eng. Res. Des.*, vol. 91, no. 12, pp. 2648–2662, 2013.
- [216] J. Burger and H. Hasse, "Multi-objective optimization using reduced models in conceptual design of a fuel additive production process," *Chem. Eng. Sci.*, vol. 99, pp. 118–126, 2013.
- [217] K. Gaukel, D. Pélerin, M. Härtl, G. Wachtmeister, J. Burger, W. Maus, and E. Jacob, "The fuel ome<sub>2</sub>: an example to pave the way to emission-neutral vehicles with internal combustion engine," in *37th international Vienna motor symposium, Vienna*, 2016.
- [218] M. Härtl, K. Gaukel, D. Pélerin, and G. Wachtmeister, "Oxymethylene ether as potentially co<sub>2</sub>-neutral fuel for clean diesel engines part 1: Engine testing," *MTZ worldwide*, vol. 78, no. 2, pp. 52–59, 2017.

- [219] E. Jacob and W. Maus, "Oxymethylenether als potenziell co 2-neutraler kraftstoff für saubere dieselmotoren teil 2: Erfüllung des nachhaltigkeitsanspruchs," *MTZ-Motortechnische Zeitschrift*, vol. 78, no. 3, pp. 54–61, 2017.
- [220] N. Schmitz, F. Homberg, J. Berje, J. Burger, and H. Hasse, "Chemical equilibrium of the synthesis of poly (oxymethylene) dimethyl ethers from formaldehyde and methanol in aqueous solutions," *Ind. Eng. Chem. Res.*, vol. 54, no. 25, pp. 6409–6417, 2015.
- [221] N. Schmitz, J. Burger, and H. Hasse, "Reaction kinetics of the formation of poly (oxymethylene) dimethyl ethers from formaldehyde and methanol in aqueous solutions," *Ind. Eng. Chem. Res.*, vol. 54, no. 50, pp. 12553–12560, 2015.
- [222] J. Burger, E. Ströfer, and H. Hasse, "Chemical equilibrium and reaction kinetics of the heterogeneously catalyzed formation of poly (oxymethylene) dimethyl ethers from methylal and trioxane," *Ind. Eng. Chem. Res.*, vol. 51, no. 39, pp. 12751–12761, 2012.
- [223] F. Wang, G. Zhu, Z. Li, F. Zhao, C. Xia, and J. Chen, "Mechanistic study for the formation of polyoxymethylene dimethyl ethers promoted by sulfonic acid-functionalized ionic liquids," *J. Mol. Catal. A: Chem.*, vol. 408, pp. 228–236, 2015.
- [224] X. Zhang, A. O. Oyedun, A. Kumar, D. Oestreich, U. Arnold, and J. Sauer, "An optimized process design for oxymethylene ether production from woody-biomass-derived syngas," *Biomass Bioenergy*, vol. 90, pp. 7–14, 2016.
- [225] J. Wu, H. Zhu, Z. Wu, Z. Qin, L. Yan, B. Du, W. Fan, and J. Wang, "High si/al ratio hzsm-5 zeolite: an efficient catalyst for the synthesis of polyoxymethylene dimethyl ethers from dimethoxymethane and trioxymethylene," *Green Chem.*, vol. 17, no. 4, pp. 2353–2357, 2015.
- [226] P. Haltenort, K. Hackbarth, D. Oestreich, L. Lautenschütz, U. Arnold, and J. Sauer, "Heterogeneously catalyzed synthesis of oxymethylene dimethyl ethers (ome) from dimethyl ether and trioxane," *Catal. Commun.*, vol. 109, pp. 80–84, 2018.
- [227] R. F. Ribeiro, A. V. Marenich, C. J. Cramer, and D. G. Truhlar, "Use of solution-phase vibrational frequencies in continuum models for the free energy of solvation," *J. Phys. Chem. B*, vol. 115, no. 49, pp. 14556–14562, 2011.
- [228] K. Mathew, R. Sundararaman, K. Letchworth-Weaver, T. Arias, and R. G. Hennig, "Implicit solvation model for density-functional study of nanocrystal surfaces and reaction pathways," *J. Chem. Phys.*, vol. 140, no. 8, p. 084106, 2014.
- [229] J. Tomasi, B. Mennucci, and R. Cammi, "Quantum mechanical continuum solvation models," *Chem. Rev.*, vol. 105, no. 8, pp. 2999–3094, 2005.
- [230] O. Andreussi, I. Dabo, and N. Marzari, "Revised self-consistent continuum solvation in electronic-structure calculations," *J. Chem. Phys.*, vol. 136, no. 6, p. 064102, 2012.
- [231] R. H. Boyd, "Some physical properties of polyoxymethylene dimethyl ethers," *J. Polym. Sci.*, vol. 50, no. 153, pp. 133–141, 1961.
- [232] C. Laurence, J. Graton, M. Berthelot, F. Besseau, J.-Y. Le Questel, M. Luçon, C. Ouvrard, A. Planchat, and E. Renault, "An enthalpic scale of hydrogen-bond basicity. 4. carbon  $\pi$  bases, oxygen bases, and miscellaneous second-row, third-row, and fourth-row bases and a survey of the 4-fluorophenol affinity scale," *J. Org. Chem.*, vol. 75, no. 12, pp. 4105–4123, 2010.

- [233] A. Klamt, J. Reinisch, F. Eckert, J. Graton, and J.-Y. Le Questel, "Interpretation of experimental hydrogen-bond enthalpies and entropies from cosmo polarisation charge densities," *Phys. Chem. Chem. Phys.*, vol. 15, no. 19, pp. 7147–7154, 2013.
- [234] J. Ho, A. Klamt, and M. L. Coote, "Comment on the correct use of continuum solvent models," *J. Phys. Chem. A*, vol. 114, no. 51, pp. 13442–13444, 2010.
- [235] T. J. Goncalves, P. N. Plessow, and F. Studt, "A computational investigation of ome-synthesis through homogeneous acid catalysis," *ChemCatChem*, vol. 11, no. 7, pp. 1949–1954, 2019.
- [236] D. J. Stanonis, W. D. King, and S. L. Vail, "Influence of chain length on the rate of hydrolysis of polyoxymethylene ethers," *J. Appl. Polym. Sci.*, vol. 16, no. 6, pp. 1447–1456, 1972.
- [237] B. Lump, D. Rothe, C. Pastötter, R. Lämmermann, and E. Jacob, "Oxymethylenether als dieselkraftstoffzusätze der zukunft," *MTZ-Motortechnische Zeitschrift*, vol. 72, no. 3, pp. 198–203, 2011.
- [238] K. D. Vertin, J. M. Ohi, D. W. Naegeli, K. H. Childress, G. P. Hagen, C. I. McCarthy, A. S. Cheng, and R. W. Dibble, "Methylal and methylal-diesel blended fuels for use in compression-ignition engines," tech. rep., SAE Technical Paper, 1999.
- [239] A. A. Oliferenko, P. V. Oliferenko, J. G. Huddleston, R. D. Rogers, V. A. Palyulin, N. S. Zefirov, and A. R. Katritzky, "Theoretical scales of hydrogen bond acidity and basicity for application in qsar/qspr studies and drug design. partitioning of aliphatic compounds," *J. Chem. Inf. Comput. Sci.*, vol. 44, no. 3, pp. 1042–1055, 2004.
- [240] R. A. Kendall, T. H. Dunning Jr, and R. J. Harrison, "Electron affinities of the first-row atoms revisited. systematic basis sets and wave functions," *J. Chem. Phys.*, vol. 96, no. 9, pp. 6796–6806, 1992.
- [241] D. E. Woon and T. H. Dunning Jr, "Gaussian basis sets for use in correlated molecular calculations. iii. the atoms aluminum through argon," *J. Chem. Phys.*, vol. 98, no. 2, pp. 1358–1371, 1993.
- [242] K. A. Peterson, D. E. Woon, and T. H. Dunning Jr, "Benchmark calculations with correlated molecular wave functions. iv. the classical barrier height of the  $\text{h} + \text{h}_2 \rightarrow \text{h}_2 + \text{h}$  reaction," *J. Chem. Phys.*, vol. 100, no. 10, pp. 7410–7415, 1994.
- [243] A. K. Wilson, T. van Mourik, and T. H. Dunning Jr, "Gaussian basis sets for use in correlated molecular calculations. vi. sextuple zeta correlation consistent basis sets for boron through neon," *J. Mol. Struct.: THEOCHEM*, vol. 388, pp. 339–349, 1996.
- [244] E. R. Davidson, "Comment on "comment on dunning's correlation-consistent basis set"," *Chem. Phys. Lett.*, vol. 260, no. 3-4, pp. 514–518, 1996.
- [245] P. Winget, D. M. Dolney, D. J. Giesen, C. J. Cramer, and D. G. Truhlar, "Minnesota solvent descriptor database," *Dept. of Chemistry and Supercomputer Inst., University of Minnesota, Minneapolis, MN*, vol. 55455, 1999.
- [246] M. H. Abraham, "Hydrogen bonding. 31. construction of a scale of solute effective or summation hydrogen-bond basicity," *J. Phys. Org. Chem.*, vol. 6, no. 12, pp. 660–684, 1993.
- [247] R. Weast *et al.*, "Crc handbook of chemistry and physics, crc press1, boca raton, 1989, p," *B196 F*, vol. 187.

- [248] M. W. Schmidt, K. K. Baldridge, J. A. Boatz, S. T. Elbert, M. S. Gordon, J. H. Jensen, S. Koseki, N. Matsunaga, K. A. Nguyen, S. Su, *et al.*, “General atomic and molecular electronic structure system,” *J. Comput. Chem.*, vol. 14, no. 11, pp. 1347–1363, 1993.
- [249] M. S. Gordon and M. W. Schmidt, “Advances in electronic structure theory: Gamess a decade later,” in *Theory Appl. Comput. Chem.*, pp. 1167–1189, Elsevier, 2005.
- [250] A. Peter, S. M. Fehr, V. Dybbert, D. Himmel, I. Lindner, E. Jacob, M. Ouda, A. Schaadt, R. J. White, H. Scherer, *et al.*, “Towards a sustainable synthesis of oxymethylene dimethyl ether by homogeneous catalysis and uptake of molecular formaldehyde,” *Angew. Chem., Int. Ed.*, vol. 57, no. 30, pp. 9461–9464, 2018.
- [251] P. Deglmann and S. Schenk, “Thermodynamics of chemical reactions with cosmo-rs: The extreme case of charge separation or recombination,” *J. Comput. Chem.*, vol. 33, no. 14, pp. 1304–1320, 2012.
- [252] P. Linstrom and E. W.G. Mallard, “NIST Chemistry WebBook, NIST Standard Reference Database Number 69, National Institute of Standards and Technology, Gaithersburg MD, 20899.” <https://doi.org/10.18434/T4D303>, 2020. last accessed: 2020-01-23.

## Appendix A

# Accuracy of Density Functional Theory in Zeolite Catalysis

### A.1 Details on Convergence Tests

#### A.1.1 MTO

The reference energies from Figures 3.2 and 3.3 require a meticulous evaluation so that DFT is compared to the best possible value. For that, the accuracy of the approximate HF exchange (COSX) is examined, along with the error of the size of the basis-sets. The set of parameters for the DLPNO calculations, as well as the comparison between the PAW method and basis-sets, are also carefully evaluated in Section A.1.2. The chain of spheres algorithm [104] was used in the ORCA program package since the Hartree Fock exchange calculation is significantly sped up for large molecules. The default COSX grid (grid S2) leads to a deviation of up to 6 kJ/mol for the DLPNO-MP2 energies, compared to the exact exchange energies, as observed in Figure A.1 for adsorption and reaction energies and Figure A.2 for transition states, whereas using an improved COSX grid (grid 6) can reduce the error up to 2 kJ/mol without a significant impact on the performance.

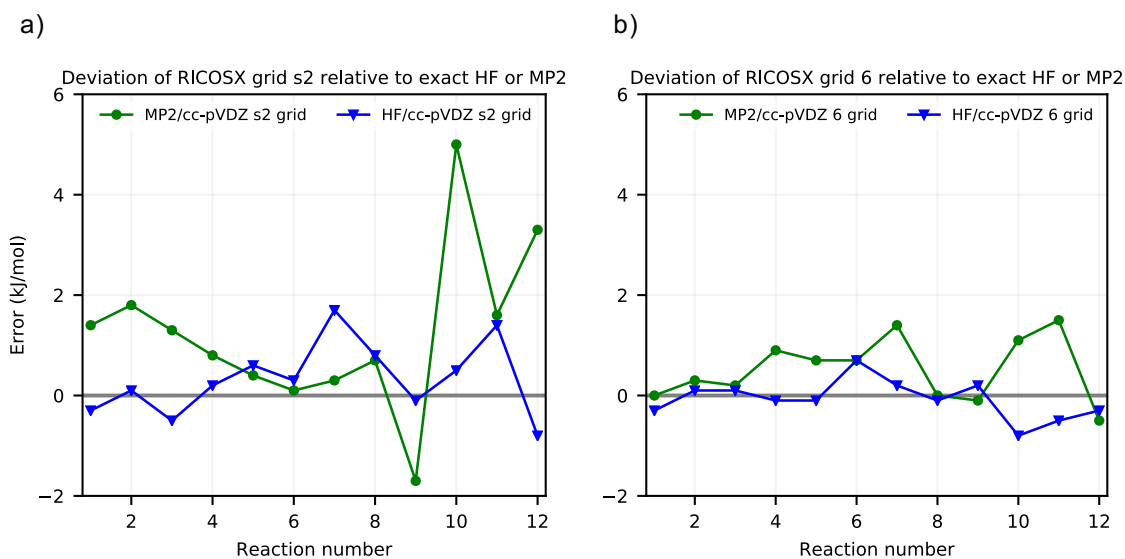


**Figure A.1:** Accuracy of RIJCOSX using different grid parameters for adsorption and reaction energies relative to exact Hartree-Fock or MP2 correlation. Reaction numbers labeled in the x-axis represent reactions depicted in Scheme 3.1.

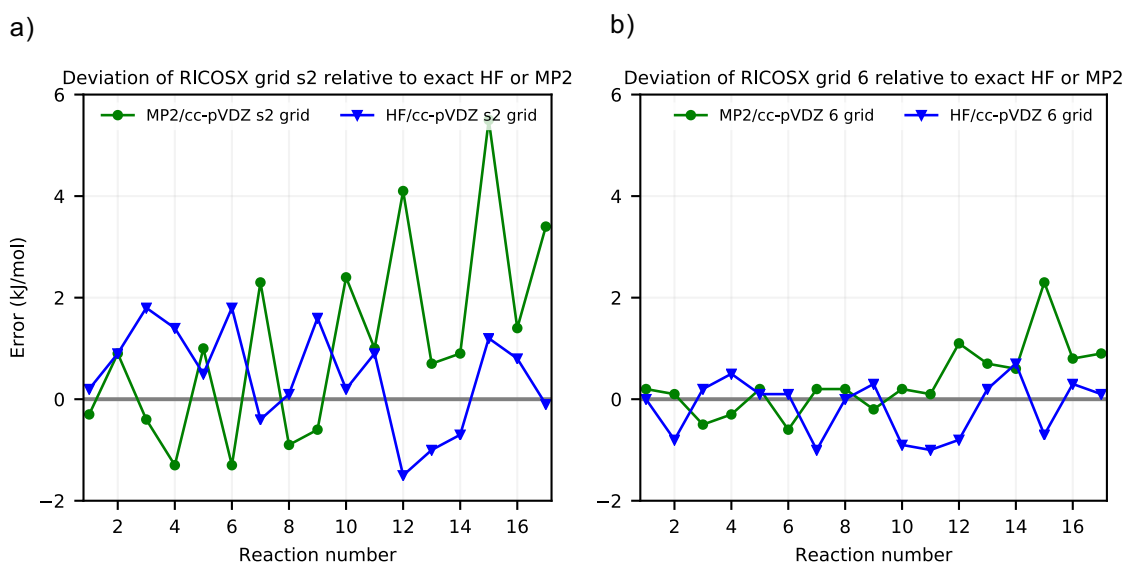


**Figure A.2:** Accuracy of RIJCOSX using different grid parameters for transition states relative to exact Hartree-Fock or MP2 correlation. Reaction numbers labeled in the x-axis represent transition states depicted in Scheme 3.2.

A complete basis-set extrapolation study was performed on the tier 2 models. Figure A.3 shows the error of different basis-sets, cc-pVXZ and def2-TZVPP compared to the CBS extrapolation from cc-pVXZ for the adsorption and reaction energies shown in Scheme 3.1. The CBS study is split into the HF energy component (Figure A.13), the correlation component (Figure A.14) and the full DLPNO-MP2 energy, given by the sum of the HF component with the correlation component, depicted in Figure A.3. The CBS extrapolation approach used in the MTO reactions is the same as in the SCR mechanism, following Equations 2.3.55 and 2.3.56 depicted in Section 2.3.5.1 from

## Chapter 2.

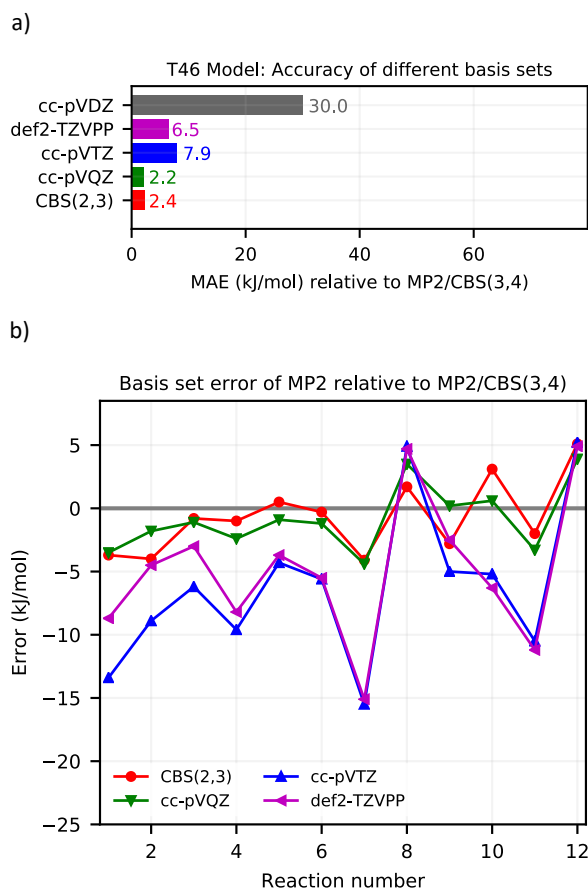


**Figure A.3:** Basis-set error a) and individual deviation of all adsorption and reaction energies b) depicted in Scheme 3.1 for the DLPNO-MP2 energies ( $\text{HF} + \text{DLPNO-MP2}_{\text{corr}}$ ) with respect to the complete basis-set limit extrapolated using Dunning’s basis-sets  $\text{cc-pVDZ}$ ,  $\text{cc-pVTZ}$  and  $\text{cc-pVQZ}$  (2,3,4).

Similar to the adsorption and reaction energies, Figure A.4 shows the error of different basis-sets with respect to the CBS extrapolated values from the  $\text{cc-pVXZ}$  Dunning’s basis-sets for the transition-state energies, in which the convergence of Hartree-Fock (Figure A.15) and the correlation component from DLPNO-MP2 (Figure A.16) were done separately. Both Figures A.3 and A.4 show that the double-zeta basis-set is too small to accurately compute HF and post-HF reaction/adsorption and transition-state energies, with a mean absolute error of 30 and 19 kJ/mol respectively. Triple-zeta basis-sets perform significantly better with a MAE of 3 to 8 kJ/mol, whereas the quadruple-zeta basis-set has similar accuracy to CBS(2,3), which indicates that the CBS(2,3) extrapolation gives already converged values, with MAE of 1-2 kJ/mol with respect to CBS(3,4).

Despite the SCR reactions in Section 3.4.2 being studied with the same zeolite framework and using the same approach, several reactions involve spin-polarized calculations with a transition-metal ( $\text{Cu}^+$ ). For this reason, errors associated with basis-sets or methods may not be consistent with convergence studies here.

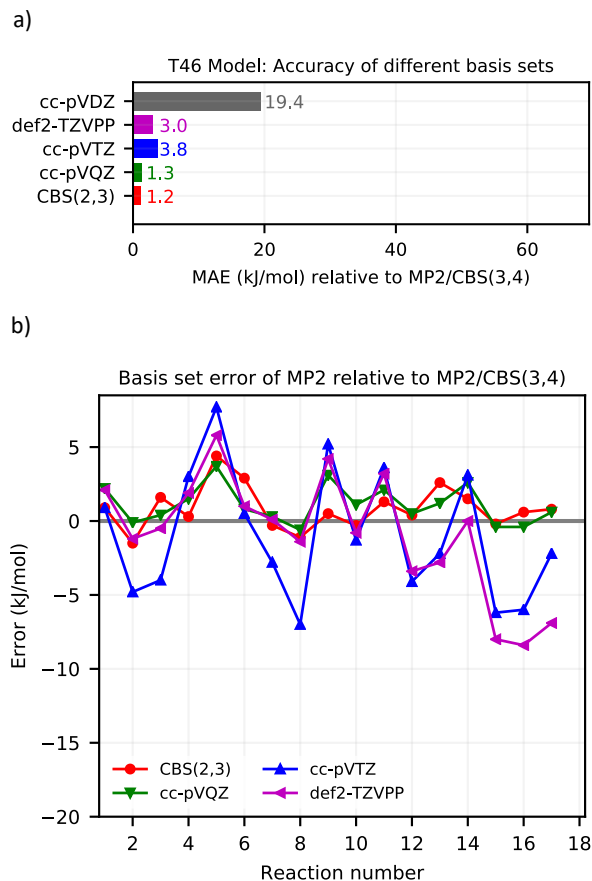


**Figure A.4:** Basis-set error a) and individual deviation of all transition-state energies b) depicted in Scheme 3.2 for the DLPNO-MP2 energies (HF + DLPNO-MP2<sub>corr</sub>) with respect to the complete basis-set limit extrapolated using Dunning’s basis-sets cc-pVDZ, cc-pVTZ and cc-pVQZ (2,3,4).

The accuracy of  $E_{\text{CCSD(T)}}^{\text{PBC}}$  depends on how well converged basis-sets are. The  $E_{\text{CCSD(T)}}^{\text{T46}}$  is complete basis-set extrapolated while the  $E_{\text{PBE-D3}}^{\text{T46}}$  uses the def2-TZVPP basis-set. As the convergence rate differs between DFT and other methods, CBS extrapolation used in Equation 3.4.1 cannot be used for DFT. We assessed the basis-set convergence of DFT with a functional that has a small error (M06), where the basis-set incompleteness would lead to a relatively large impact.

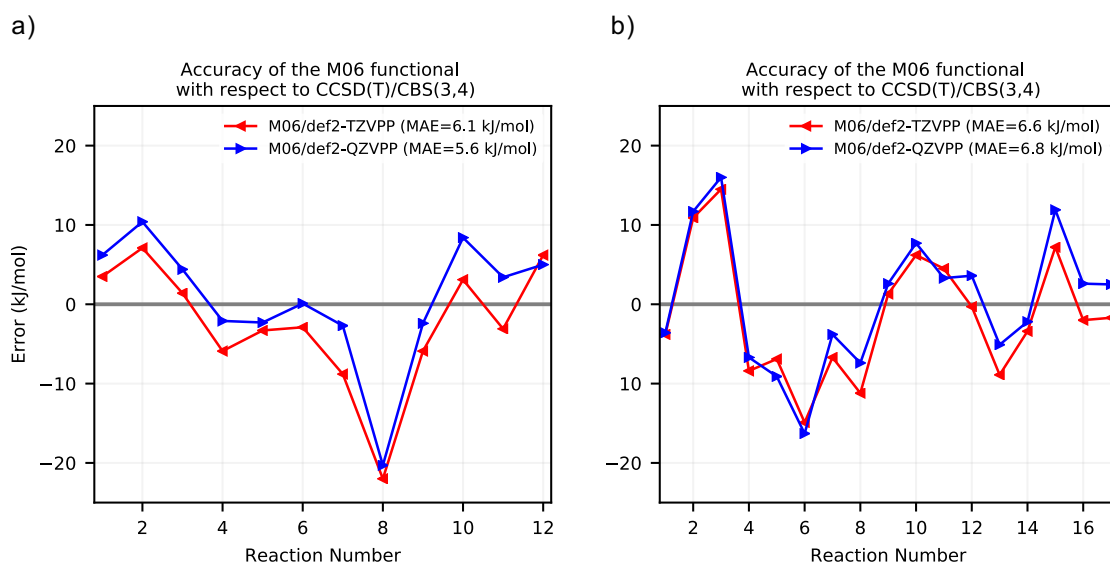


**Figure A.5:** M06 differences calculated using Orca with respect to CCSD(T)/CBS(3,4). a) lists the error in kJ/mol of adsorption and reaction energies depicted in Scheme 3.1, while b) lists the error in kJ/mol of transition states depicted in Scheme 3.2.

Figures A.5 a) and b) show the error obtained with the def2-TZVPP basis-set (also shown in Figures 3.2 b and 3.3 b) and def2-QZVPP basis-set. We observe that the MAE of M06 shifts around 0.5 kJ/mol, which means that the def2-TZVPP basis-set is already converged for DFT and does not need further extrapolation.

We will study the dependency on the basis-set into calculating the difference between CCSD(T) and MP2 next.

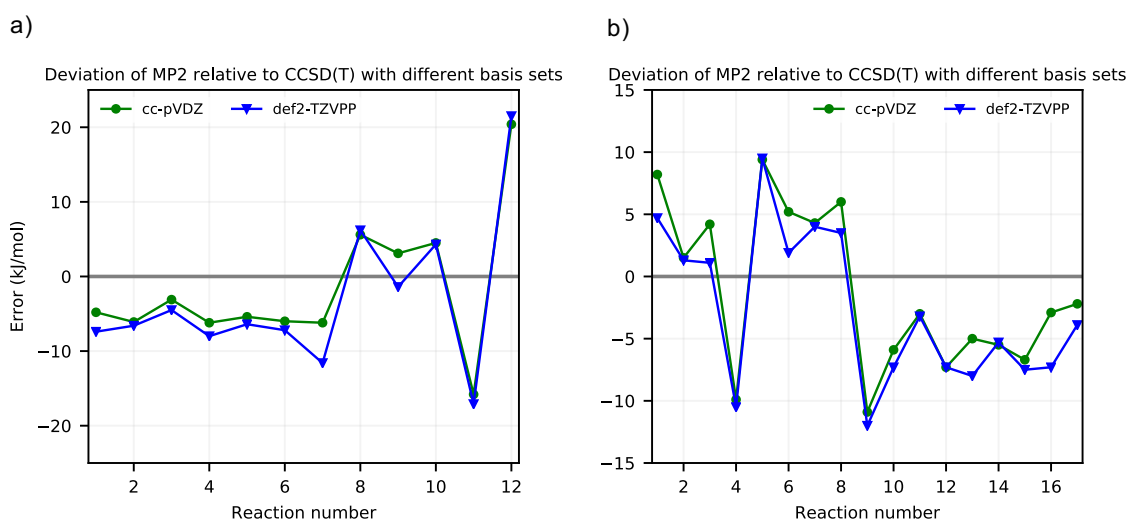


**Figure A.6:** DLPNO-MP2/basis deviation with respect to DLPNO-CCSD(T)/basis for the reactions a) and transition states b) depicted in Scheme 3.1 and 3.2 respectively.

Figures A.6 a) and b) show the difference between DLPNO-MP2 and DLPNO-CCSD(T) for the T46 cluster model using different basis-sets. The difference is only weakly dependent on the basis-

set, as the green and blue lines almost overlap. This means that it is a good approximation to determine the difference between DLPNO-MP2 and DLPNO-CCSD(T) with a smaller basis-set and perform the CBS extrapolation using MP2, as described by Equation 3.4.1.

To extrapolate coupled-cluster results from the T46 cluster model into the periodic model, a consistency check was performed for the different methods. In principle, the extrapolation from T46 to PBC may be different if the PBE-D3 or the BEEF-vdW functionals are used. If that was indeed the case, it would mean that the PBE-D3 extrapolation cannot be used to convert T46 using coupled-cluster theory into the periodic result.

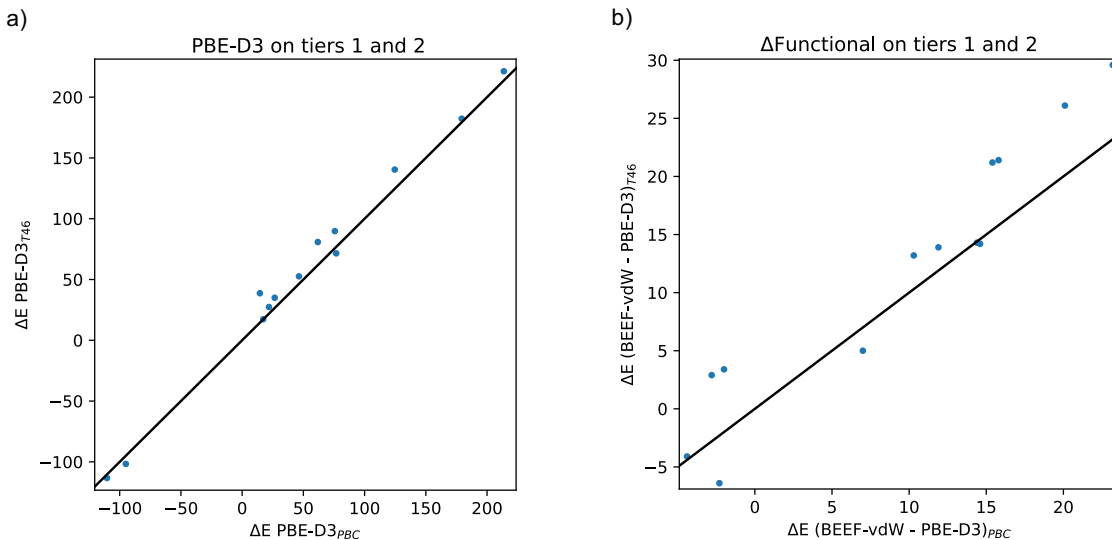


**Figure A.7:** Comparison of a) the PBE-D3 functional for H-SSZ-13 under periodic boundary conditions and for the T46 cluster model and b) the difference between BEEF-vdW and PBE-D3 functionals for H-SSZ-13 under periodic boundary conditions and for the T46 cluster model. The results are also explicitly shown in Table A.3.

Ideally, the difference between BEEF-vdW and PBE-D3 under PBC and on the T46 cluster model would have the same values so that the extrapolation is consistent, which is in agreement with Figure A.7 b) and Table A.3 column G, where the biggest deviation is 7 kJ/mol. We can also observe that the  $E_{\text{PBE-D3}}^{\text{PBC}}$  results do not fall far off from the  $E_{\text{PBE-D3}}^{\text{T46}}$  results, as shown in Figure A.7 a).

### A.1.2 SCR

In Section 3.4.2, MP2 with an unrestricted HF-reference is not used as the reference method because of its inaccuracy. Figure A.8 shows that the deviation in the MP2 energies are as large as 145 kJ/mol with a mean absolute error of around 50 kJ/mol when compared to CCSD(T) if an unrestricted Hartree-Fock reference is used.

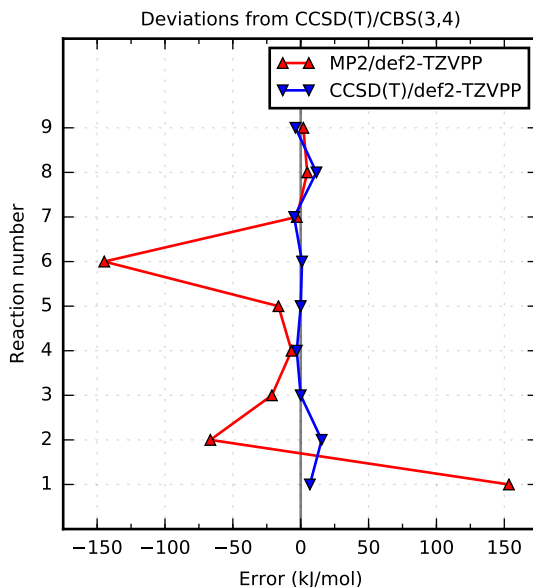


**Figure A.8:** Deviation in energy of MP2 and CCSD(T) using an UHF-reference with the def2-TZVPP basis-set with respect to CCSD(T) with the complete basis-set extrapolation from cc-pVXZ for the T1 chabazite. The CBS extrapolation for the CCSD(T) level follows Equations 2.3.55 and 2.3.56. Reaction number refers to SCR reactions using Cu-SSZ-13 labeled in Scheme 3.3.

We additionally tested a Restricted Open-shell Hartree-Fock (ROHF) reference for gas-phase reactions (Table A.5). We observe that the CCSD(T) depends only weakly on the reference, with deviations below 5 kJ/mol, while MP2 deviations are on the order of 100 kJ/mol and are significantly improved if a ROHF reference is used. This suggests that the MP2 results for the catalyzed reactions shown in Figure A.8 could potentially be improved with a ROHF reference. However, due to SCF-convergence problems, we have not pursued this possibility further. The disadvantage of using UHF wavefunctions are that they may lead to spin contamination. Table A.6 shows the expectation value  $\langle S \cdot S \rangle$  for DFT, using different functionals and for HF, using the T46 cluster model. Spin contamination is almost non-existent, with its highest value of around 0.05 for the Cu-NO<sub>3</sub> structure, using UHF wavefunctions. DLPNO-CCSD(T) and DLPNO-MP2 calculations have no spin contamination due to the Quasi-Restricted Orbitals (QRO) used.

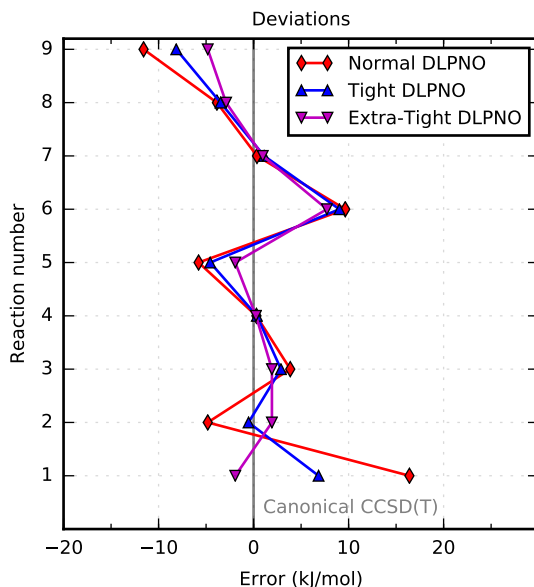


**Figure A.9:** DLPNO-CCSD(T) with normal accuracy, ORCA’s default parameters ( $\text{TCutPairs} = 10^{-4}$ ,  $\text{TCutMKN} = 10^{-3}$ ,  $\text{TCutPNO} = 3.33 \times 10^{-7}$ ) in red, DLPNO-CCSD(T) with keyword "Tight" ( $\text{TCutPairs} = 10^{-5}$ ,  $\text{TCutMKN} = 10^{-3}$ ,  $\text{TCutPNO} = 10^{-7}$ ) in blue and DLPNO-CCSD(T) with manually set parameters ( $\text{TCutPairs} = 10^{-6}$ ,  $\text{TCutMKN} = 10^{-3}$ ,  $\text{TCutPNO} = 10^{-8}$ ) in purple (termed "extra-tight" here) compared to canonical CCSD(T)/def2-TZVPP for the T1 cluster model. Reaction number refers to SCR reactions using Cu-SSZ-13 labeled in Scheme 3.3.

- $\text{TCutPNO}$  – Cutoff for PNO occupation numbers. This is the main truncation parameter. [106]
- $\text{TCutPairs}$  – Cutoff for estimated pair correlation energies. [106]
- $\text{TCutMKN}$  – This is a technical parameter that controls the domain size for the local fit to the PNOs. It is conservative. [106]

In Figure A.9, we compare the results of canonical and DLPNO-CCSD(T), using different thresholds for the latter. The parameters that correspond to 'Normal' DLPNO yield the largest deviation, up to around 15 kJ/mol. The errors are reduced if the thresholds according to the keyword 'Tight' are used and further reduced with manually set parameters, which were termed 'Extra-tight' here. In practice 'Tight' thresholds were used in all benchmark calculations since it leads to the best accuracy-cost ratio, agreeing well with canonical CCSD(T) ( $\text{MAE} = 4$  kJ/mol).

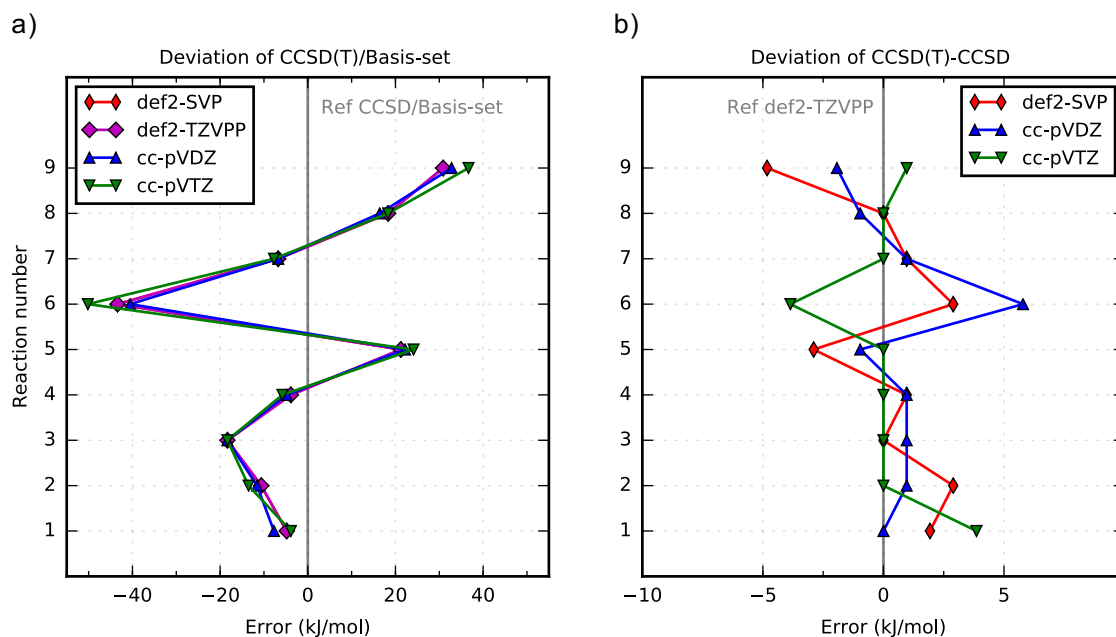


**Figure A.10:** a) Energy increment from the perturbative triples "CCSD(T)–CCSD" for different basis-sets. b) Deviation of the energy increment from the perturbative triples "CCSD(T)–CCSD" on CCSD energies with the def2-TZVPP basis-set as reference. Reaction number refers to SCR reactions using Cu-SSZ-13 labeled in Scheme 3.3.

Figure A.10 a) shows that the difference between reaction energies computed with CCSD(T) and CCSD can be as large as 40 kJ/mol, showing that the CCSD level of theory is not accurate enough for benchmark purposes. Figure A.10 b) shows that the difference between CCSD and CCSD(T) depends only weakly on the employed basis-set and can be evaluated with relatively small basis-set (def2-SV(P) or cc-pVDZ) with an error of only 5 kJ/mol.

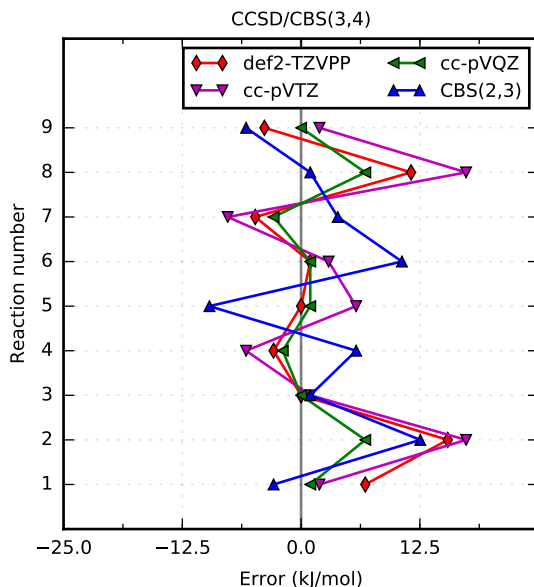


**Figure A.11:** Deviation of the reaction energies in the T1 model, obtained with the CCSD treatment using the def2-TZVPP, cc-pVTZ, cc-pVQZ and CBS(2,3) compared to the CBS(3,4) extrapolation using cc-pVTZ and cc-pVQZ. Reaction number refers to SCR reactions using Cu-SSZ-13 labeled in Scheme 3.3.

While the CBS extrapolation using double and triple-zeta basis-sets has better performance than regular triple-zeta basis-sets, due to error cancellation, it still deviates considerably with respect to the CBS(3,4), while the cc-pVQZ has small deviations in reaction energies. Another interesting observation is that the def2-TZVPP has a slightly better performance than the Dunning’s triple-zeta basis-set.

The extrapolation that corresponds to the  $E_{\text{PBE-D3/hard-PAW}}^{\text{PBC}} - E_{\text{PBE-D3/def2-TZVPP}}^{\text{T46}}$  difference, raises questions of its consistency since the VASP and TURBOMOLE use different methods to perform calculations. In principle, programs that use PAW potentials or Gaussian basis-sets should give the same result, however each method has different types of approximations. PAWs have a cutoff on the number of plane-waves and radius of the PAW spheres, while Gaussian basis-sets are limited to the number of basis functions used.

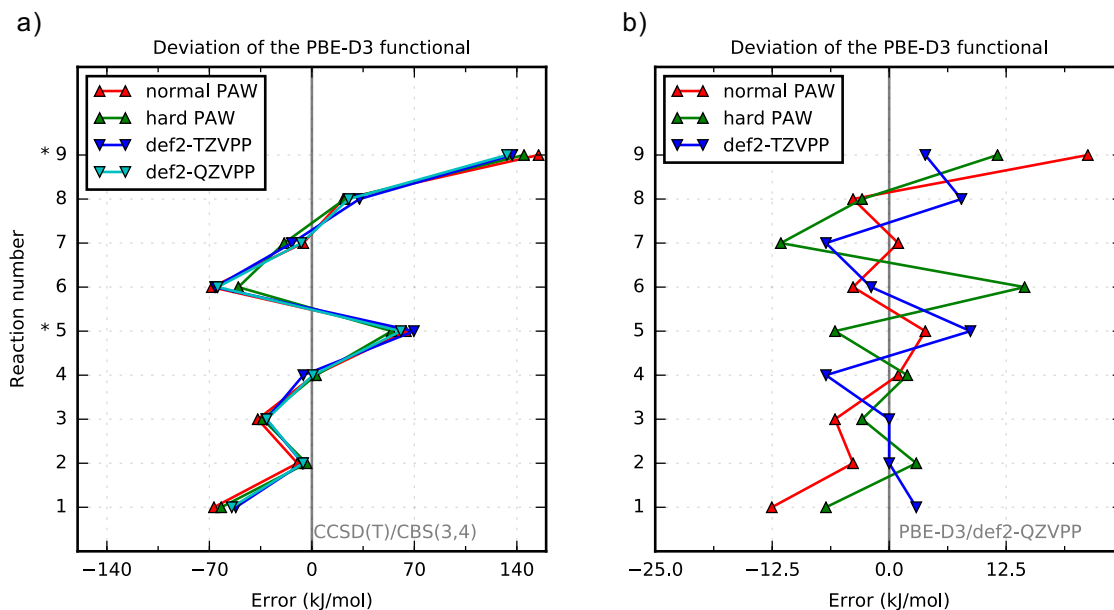


**Figure A.12:** Comparison of the PBE-D3 functional using PAW with different accuracy and basis-sets with respect to the CCSD(T) level of theory, with the complete basis-set extrapolation from cc-pVXZ (a) and with respect to the def2-QZVPP basis-set (b) for the T1 cluster model. Reaction number refers to SCR reactions using Cu-SSZ-13 labeled in Scheme 3.3.

Despite the normal and hard PAWs having very similar mean absolute errors (both around 7 kJ/mol) with respect to the def2-QZVPP basis-set, as observed in Figure A.12, the hard-PAWs were used for calculations with plane-waves. The def2-TZVPP basis has reasonable accuracy for most cases, showing a MAE value of 5 kJ/mol with respect to def2-QZVPP because DFT is less sensitive to the size of the basis-set than HF or post-HF methods. We have performed the same study for the B3LYP-D3 functional (Figure A.18) and found again that the differences between PAWs and Gaussian basis-sets are smaller than the deviation from CCSD(T)/CBS(3,4), although the differences are up to 20 kJ/mol in the worst cases.

## A.2 Tables and Figures

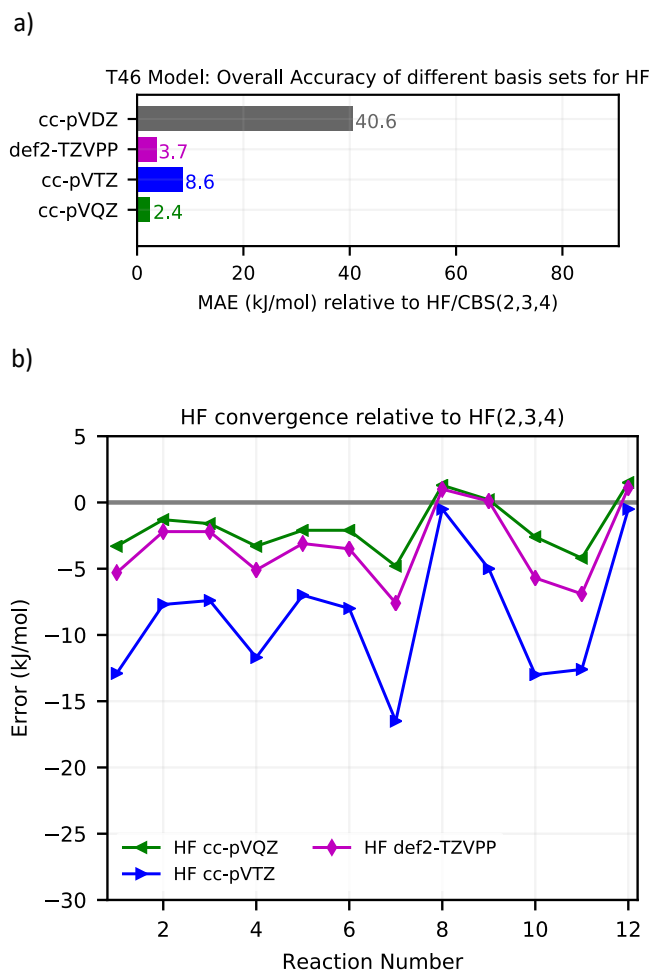


**Figure A.13:** Basis-set error a) and individual deviation of all adsorption and reaction energies b) depicted in Scheme 3.1 for the Hartree-Fock energies with respect to the complete basis-set limit extrapolated using Dunning's basis-sets cc-pVDZ, cc-pVTZ and cc-pVQZ (2, 3, 4).

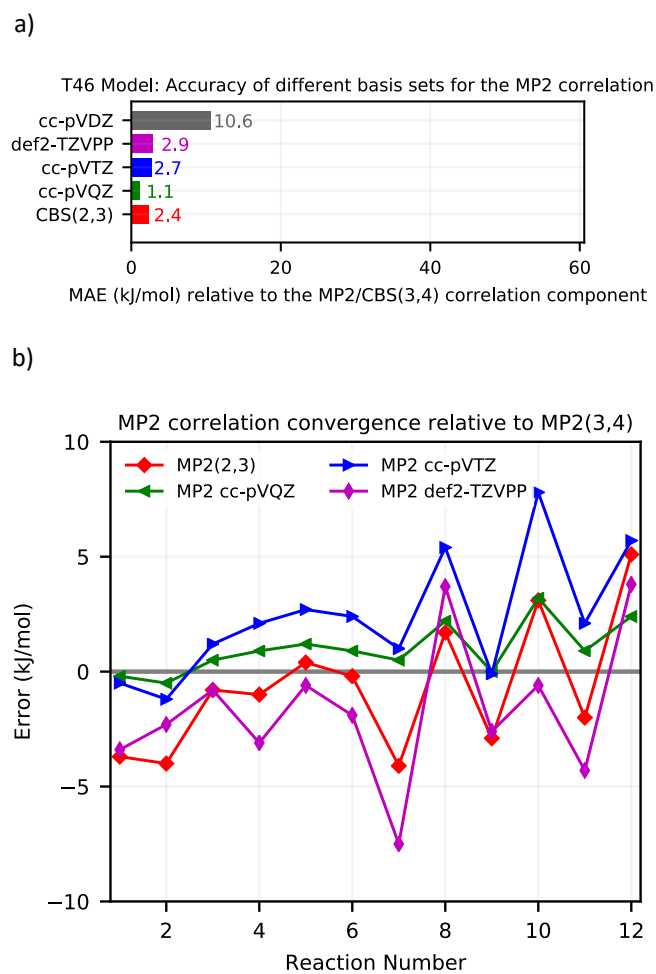


**Figure A.14:** Basis-set error a) and individual deviation of all adsorption and reaction energies b) depicted in Scheme 3.1 for the DLPNO-MP2 correlation energies with respect to the complete basis-set limit extrapolated using Dunning's basis-sets cc-pVDZ, cc-pVTZ and cc-pVQZ (2, 3, 4).

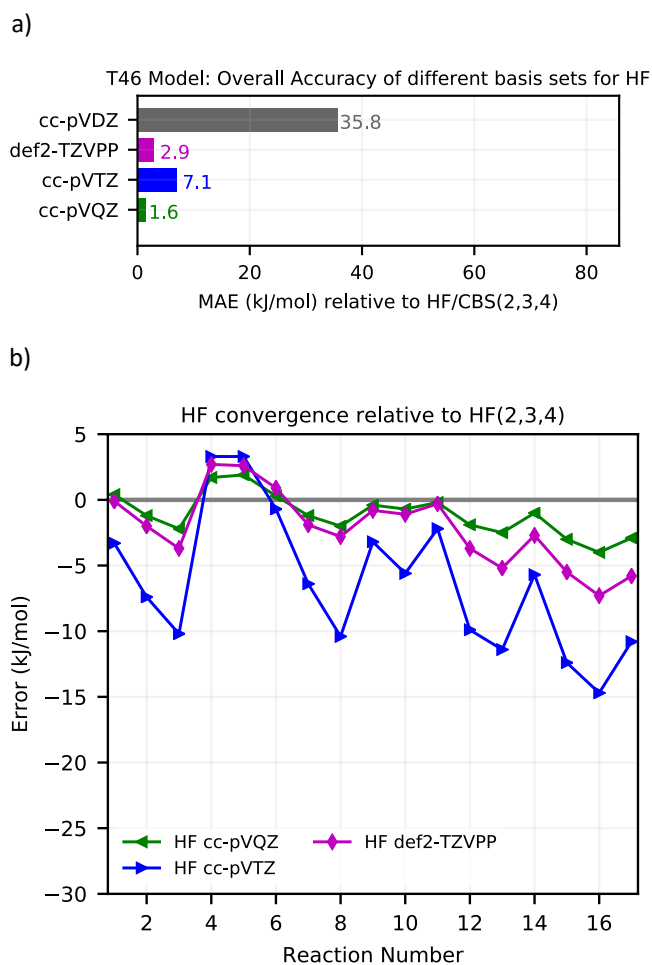


**Figure A.15:** Basis-set error a) and individual deviation of all transition-state energies b) depicted in Scheme 3.2 for the Hartree-Fock energies with respect to the complete basis-set limit extrapolated using Dunning's basis-sets cc-pVDZ, cc-pVTZ and cc-pVQZ (2, 3, 4).

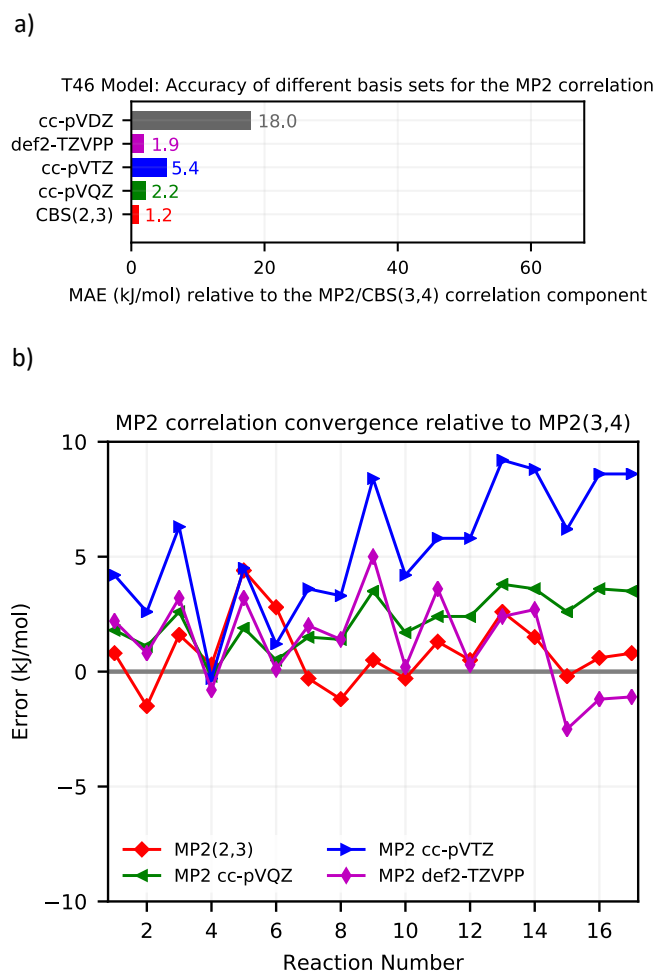


**Figure A.16:** Basis-set error a) and individual deviation of all transition-state energies b) depicted in Scheme 3.2 for the DLPNO-MP2 correlation energies with respect to the complete basis-set limit extrapolated using Dunning's basis-sets cc-pVDZ, cc-pVTZ and cc-pVQZ (2, 3, 4).

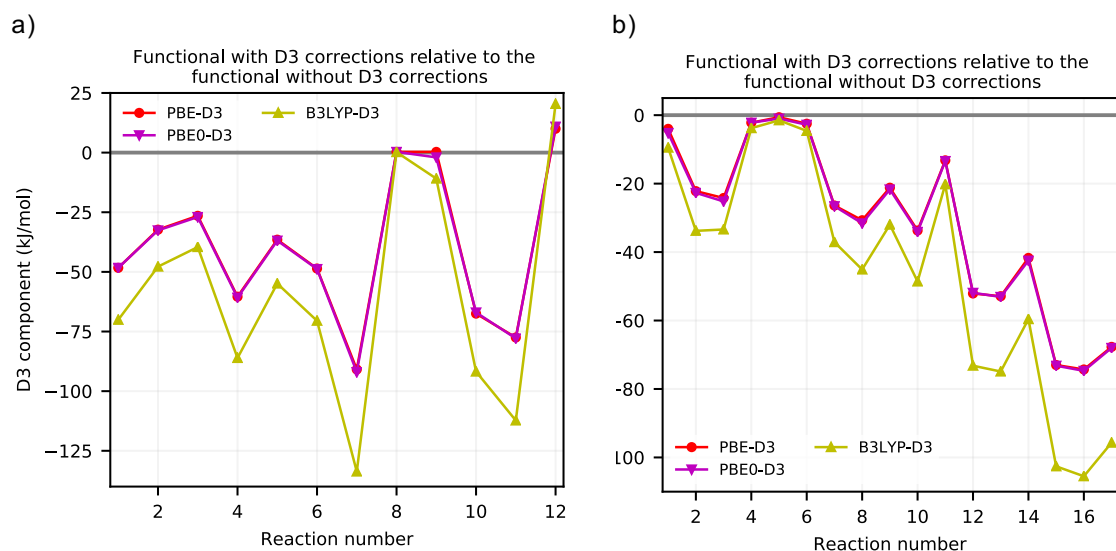


**Figure A.17:** Grimme's dispersion corrections D3 for PBE, PBE0 and B3LYP functionals involving a) adsorption and reaction energies depicted in Scheme 3.1 and b) transition states depicted in Scheme 3.2.

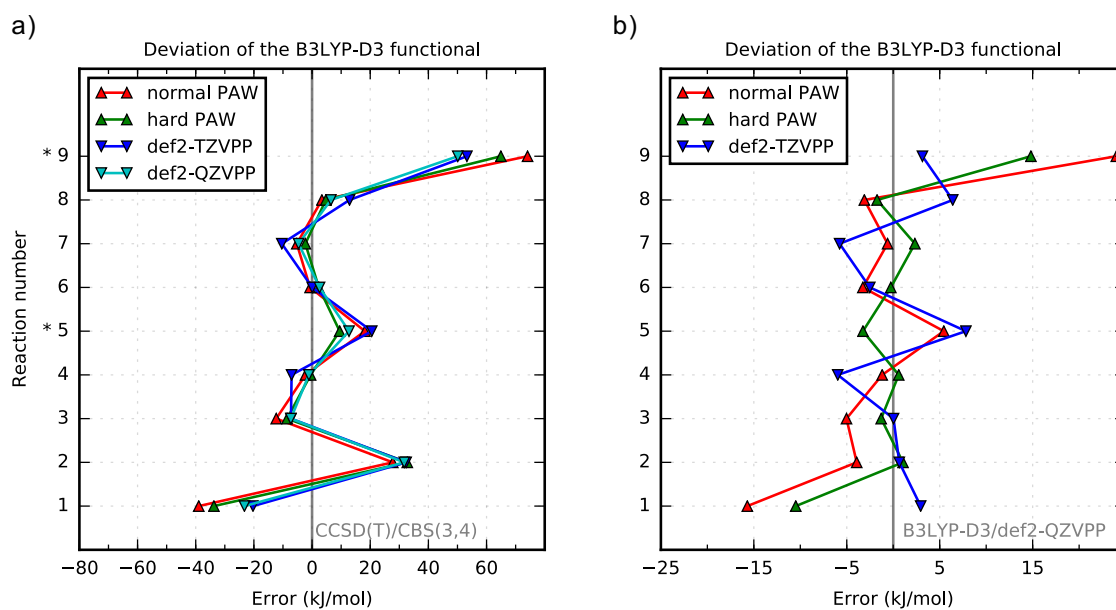


**Figure A.18:** Comparison of the B3LYP functional using PAW with different accuracy and basis-sets with respect to the CCSD(T) level of theory, with the complete basis-set extrapolation from cc-pVXZ (a) and with respect to the def2-QZVPP basis-set (b) for the T1 cluster model. Reaction number refers to SCR reactions using Cu-SSZ-13 labeled in Scheme 3.3.

|                  | PBE-D3 | BEEF-vdW | PBE0-D3 | B3LYP-D3 | M06  | MP2  |
|------------------|--------|----------|---------|----------|------|------|
| <b>Max error</b> | 48.7   | 48.3     | 28.5    | 39.0     | 22.0 | 21.5 |
| <b>MAE</b>       | 25.3   | 15.4     | 18.3    | 23.4     | 6.1  | 8.5  |
| <b>MSE</b>       | -22.7  | -5.3     | -16.4   | -19.7    | -2.6 | -3.2 |

**Table A.1:** Maximum error, mean absolute error and mean signed error in kJ/mol for adsorption and reaction energies depicted in Scheme 3.1 with respect to DLPNO-CCSD(T)/CBS(3, 4).

|                  | PBE-D3 | BEEF-vdW | PBE0-D3 | B3LYP-D3 | M06  | MP2  |
|------------------|--------|----------|---------|----------|------|------|
| <b>Max error</b> | 65.6   | 47.9     | 35.7    | 41.4     | 12.0 | 12.0 |
| <b>MAE</b>       | 42.2   | 31.3     | 16.8    | 27.0     | 6.6  | 5.8  |
| <b>MSE</b>       | -42.2  | -31.3    | -15.0   | -27.0    | -1.4 | -2.7 |

**Table A.2:** Maximum error, mean absolute error and mean signed error in kJ/mol for transition states depicted in Scheme 3.2 with respect to DLPNO-CCSD(T)/CBS(3, 4).

|                                       | PBC    |          | T46    |          | B – A | D – C | E – F |
|---------------------------------------|--------|----------|--------|----------|-------|-------|-------|
|                                       | PBE-D3 | BEEF-vdW | PBE-D3 | BEEF-vdW |       |       |       |
|                                       | A      | B        | C      | D        | E     | F     | G     |
| <b><math>\Delta E</math></b>          |        |          |        |          |       |       |       |
| 1                                     | -110.4 | -94.6    | -113.3 | -91.8    | 15.8  | 21.4  | -5.6  |
| 2                                     | -95.0  | -71.8    | -101.7 | -72.0    | 23.2  | 29.6  | -6.5  |
| <b><math>\Delta E^\ddagger</math></b> |        |          |        |          |       |       |       |
| 1                                     | 124.6  | 120.2    | 140.4  | 136.3    | -4.4  | -4.1  | -0.3  |
| 2                                     | 14.5   | 26.4     | 38.7   | 52.6     | 11.9  | 13.9  | -2.0  |
| 3                                     | 46.4   | 43.6     | 52.6   | 55.5     | -2.8  | 2.9   | -5.7  |
| 4                                     | —      | —        | —      | —        | —     | —     | —     |
| 5                                     | 213.7  | 211.3    | 221.3  | 214.9    | -2.3  | -6.4  | 4.1   |
| 6                                     | 179.3  | 186.2    | 182.3  | 187.3    | 7.0   | 5.0   | 2.0   |
| 7                                     | 61.8   | 81.9     | 80.8   | 106.9    | 20.1  | 26.1  | -6.0  |
| 8                                     | 76.8   | 92.2     | 71.5   | 92.7     | 15.4  | 21.2  | -5.8  |
| 9                                     | —      | —        | —      | —        | —     | —     | —     |
| 10                                    | 21.9   | 36.5     | 27.4   | 41.5     | 14.6  | 14.2  | 0.4   |
| 11                                    | 75.7   | 90.0     | 89.8   | 104.1    | 14.4  | 14.3  | 0.0   |
| 12                                    | 17.2   | 27.5     | 17.3   | 30.5     | 10.3  | 13.2  | -2.9  |
| 13                                    | 26.6   | 24.6     | 35.0   | 38.4     | -2.0  | 3.4   | -5.4  |
| 14                                    | 61.4   | 72.3     | 68.9   | 80.8     | 10.9  | 11.9  | -1.0  |
| 15                                    | 16.3   | 26.9     | 20.0   | 33.7     | 10.6  | 13.7  | -3.1  |
| 16                                    | 33.5   | 29.9     | 43.6   | 47.0     | -3.6  | 3.4   | -7.0  |
| 17                                    | 61.8   | 66.7     | 76.5   | 83.6     | 4.9   | 7.1   | -2.2  |

**Table A.3:** Comparison of tier 1 (PBC) and tier 2 (T46) using PBE-D3 and BEEF-vdW. Minima are labeled according to Scheme 3.1 and barriers according to Scheme 3.2. Reaction energies and transition states are given in kJ/mol.

| Structure                          | ORCA T1 diagnostics | TM D1 diagnostics | ORCA T1 diagnostics |
|------------------------------------|---------------------|-------------------|---------------------|
|                                    | T1 cluster model    | T1 cluster model  | T46 cluster model   |
| Cu                                 | 0.015               | 0.079             | 0.012               |
| Cu-NO <sub>2</sub>                 | 0.021               | 0.089             | 0.013               |
| Cu-NO <sub>3</sub>                 | 0.020               | 0.077             | 0.013               |
| Cu-OH                              | 0.022               | 0.063             | 0.013               |
| Cu-NONH <sub>2</sub>               | 0.020               | 0.117             | 0.013               |
| Cu-NOOHNH <sub>3</sub>             | 0.022               | 0.157             | 0.013               |
| Cu-NO <sub>2</sub> NH <sub>3</sub> | 0.020               | 0.090             | 0.013               |
| Cu-NH <sub>3</sub>                 | 0.017               | 0.108             | 0.012               |
| Cu-O <sub>2</sub>                  | 0.028               | 0.064             | 0.014               |
| Cu-HONO                            | 0.023               | 0.148             | 0.013               |

**Table A.4:** T1 and D1 diagnostics for the T1 and T46 cluster models using ORCA and TURBO-MOLE program packages for CCSD(T).

|   | MP2              |                   | CCSD(T)          |                   |
|---|------------------|-------------------|------------------|-------------------|
|   | UHF <sup>†</sup> | ROHF <sup>‡</sup> | UHF <sup>†</sup> | ROHF <sup>‡</sup> |
| Standard SCR  | -1755.8          | -1612.0           | -1595.8          | -1592.8           |
| NO activation cycle                                   | -969.9           | -867.2            | -848.7           | -847.0            |
| NO <sub>2</sub> → 1/2 N <sub>2</sub> + O <sub>2</sub> | -23.2            | -53.7             | -40.8            | -40.2             |
| NO <sub>2</sub> → NO + 1/2 O <sub>2</sub>             | 92.0             | 61.2              | 50.8             | 50.6              |
| NO → 1/2 N <sub>2</sub> + 1/2 O <sub>2</sub>          | -115.3           | -114.9            | -91.7            | -90.9             |

**Table A.5:** Reaction energies (kJ/mol) for MP2 and CCSD(T) with the def2-TZVPP basis-set and UHF or ROHF reference. <sup>†</sup> represents a RHF treatment for closed-shell and UHF treatment for open-shell molecules while <sup>‡</sup> represents a RHF treatment for closed-shell and ROHF treatment for open-shell molecules.

| Structure                          | PBE-D3                      | PBE0-D3                     | B3LYP-D3                    | M06                         | HF                          |
|------------------------------------|-----------------------------|-----------------------------|-----------------------------|-----------------------------|-----------------------------|
|                                    | $\langle S \cdot S \rangle$ |
| Cu                                 | 0.00                        | 0.00                        | 0.00                        | 0.00                        | 0.00                        |
| Cu-NO <sub>2</sub>                 | 0.75                        | 0.75                        | 0.75                        | 0.75                        | 0.75                        |
| Cu-NO <sub>3</sub>                 | 0.75                        | 0.75                        | 0.75                        | 0.75                        | 0.80                        |
| Cu-OH                              | 0.75                        | 0.76                        | 0.76                        | 0.76                        | 0.75                        |
| Cu-NONH <sub>2</sub>               | 0.00                        | 0.00                        | 0.00                        | 0.00                        | 0.00                        |
| Cu-NOOHNH <sub>3</sub>             | 0.00                        | 0.00                        | 0.00                        | 0.00                        | 0.00                        |
| Cu-NO <sub>2</sub> NH <sub>3</sub> | 0.75                        | 0.75                        | 0.75                        | 0.75                        | 0.75                        |
| Cu-NH <sub>3</sub>                 | 0.00                        | 0.00                        | 0.00                        | 0.00                        | 0.00                        |
| Cu-O <sub>2</sub>                  | 2.01                        | 2.01                        | 2.01                        | 2.01                        | 2.04                        |
| Cu-HONO                            | 0.00                        | 0.00                        | 0.00                        | 0.00                        | 0.00                        |

**Table A.6:** Expectation values of  $\langle S \cdot S \rangle$  for DFT using different functionals and HF to show the spin contamination on the T46 cluster models.

|                  | Exp.<br>Values | PBE-D3<br>def2-TZVPP | M06     | CCSD(T)<br>CBS(3,4) | Difference       |               |                   |
|------------------|----------------|----------------------|---------|---------------------|------------------|---------------|-------------------|
|                  |                |                      |         |                     | PBE-D3<br>- exp. | M06<br>- exp. | CCSD(T)<br>- exp. |
| NO <sub>2</sub>  | 33.1           | -15.0                | 12.0    | 38.3                | -48.1            | -21.1         | -5.2              |
| NH <sub>3</sub>  | -45.9          | -60.7                | -58.3   | -49.1               | -14.8            | -12.4         | 3.2               |
| NO               | 90.3           | 89.6                 | 90.7    | 90.2                | -0.7             | 0.4           | 0.1               |
| H <sub>2</sub> O | -241.8         | -216.6               | -238.5  | -248.5              | 25.2             | 3.3           | 6.7               |
| N <sub>2</sub>   | 0.0            | 0.0                  | 0.0     | 0.0                 | 0.0              | 0.0           | 0.0               |
| O <sub>2</sub>   | 0.0            | 0.0                  | 0.0     | 0.0                 | 0.0              | 0.0           | 0.0               |
| Reaction 1       | -1628.4        | -1415.3              | -1560.5 | -1655.5             | 213.1            | 67.9          | 27.1              |
| Reaction 2       | -871.4         | -812.3               | -859.0  | -879.6              | 59.1             | 12.4          | 8.2               |
| Reaction 3       | -757.0         | -603.0               | -701.5  | -775.8              | 154.0            | 55.5          | 18.8              |

**Table A.7:** Enthalpies of formation at 298.15 K in kJ/mol. Reactions 1, 2 and 3 correspond to the reactions from Equations 3.4.3, 3.4.4 and 3.4.5 respectively. Experimental values were taken from the NIST Chemistry Webbook. [252] Geometries were optimized with PBE-D3/dhf-SV(P).

| Model                     | Method           | PW/Basis-sets                        |
|---------------------------|------------------|--------------------------------------|
| PBC                       | PBE-D3           | Hard PAWs                            |
| Large Cluster model (T46) | DFT <sup>†</sup> | Hard PAWs<br>def2-TZVPP / def2-QZVPP |
|                           | DFT <sup>‡</sup> | Hard PAWs                            |
|                           | DLPNO-MP2        | def2-TZVPP / cc-pVXZ                 |
|                           | DLPNO-CCSD(T)    | def2-TZVPP / cc-pVDZ                 |

**Table A.8:** Methods and planewaves/basis-sets represented for each model of the H-SSZ-13 for MTO reactions. <sup>†</sup> corresponds to PBE-D3, B3LYP-D3, PBE0-D3 and M06 functionals while <sup>‡</sup> corresponds to BEEF-vdW.

| Model                     | Method            | PW/Basis-sets                               |
|---------------------------|-------------------|---|
| PBC                       | PBE-D3            | Hard PAWs                                   |
| Large Cluster model (T46) | DFT <sup>†</sup>  | Hard PAWs                                   |
|                           | DFT <sup>‡</sup>  | Hard PAWs                                   |
|                           | DLPNO-CCSD(T)     | def2-TZVPP                                  |
| Small Cluster model (T1)  | DFT <sup>†</sup>  | Normal/Hard PAWs<br>def2-TZVPP / def2-QZVPP |
|                           | Canonical CCSD(T) | def2-TZVPP                                  |
|                           | DLPNO-CCSD(T)     | def2-TZVPP                                  |
|                           | Canonical CCSD    | def2-TZVPP / cc-pVXZ                        |
|                           | MP2               | def2-TZVPP                                  |

**Table A.9:** Methods and planewaves/basis-sets represented for each model of the Cu-SSZ-13 for SCR reactions. <sup>†</sup> corresponds to PBE-D3, B3LYP-D3, PBE0-D3 and M06 functionals while <sup>‡</sup> corresponds to BEEF-vdW.



## Appendix B

# Selective Catalytic Reduction of NO<sub>x</sub> by Ammonia using Cu-SSZ-13

### B.1 Tables and Figures

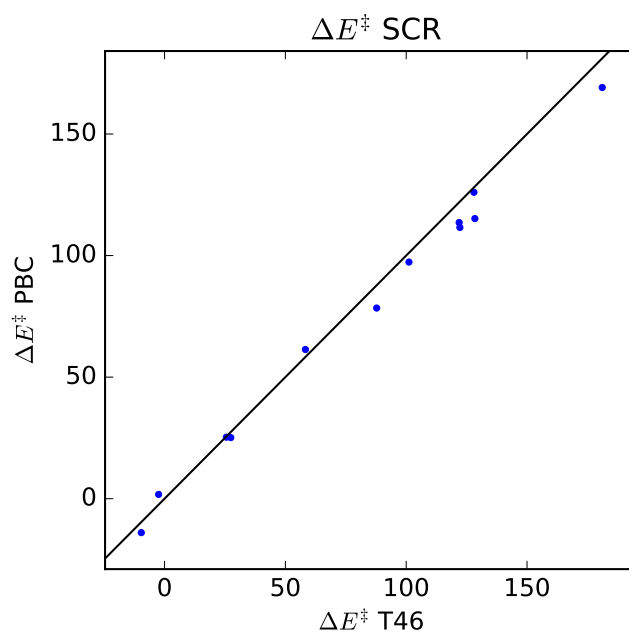


**Figure B.1:** Relation of intrinsic transition states between the T46 cluster model and PBC, for the fast SCR and NO activation cycle. The PBE-D3 functional is used for both models. The black line corresponds to a linear fit of  $y = mx + b$  with  $m = 1$  and  $b = 0$ . The mean absolute error with respect to PBC is 4.9 kJ/mol with its biggest deviation being around 12 kJ/mol.

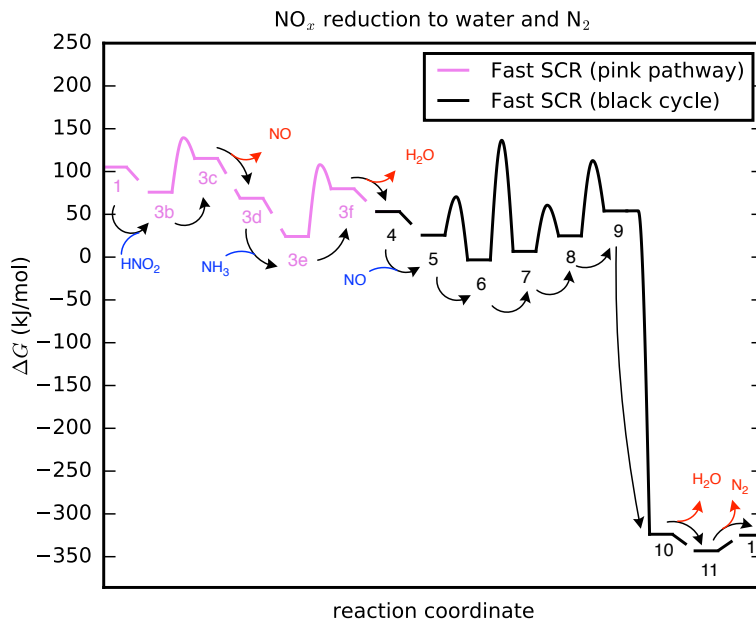


**Figure B.2:** Gibbs free energy profile at 473 K of the pink pathway and subsequent black cycle depicted in Scheme 4.1. Reactions 3b-3f are labeled according to Scheme 4.1. Molecules in blue show reactants while molecules in red show products.

| Molecule  | $\Delta E$ | $\Delta G$ |
|---|------------|------------|
| $\text{Cu}^+$ (adsorbed in zeolite)             | 0          | 0          |
| $\text{NH}_3\text{-Cu}^+$ (adsorbed in zeolite) | -223       | -139       |
| $(\text{NH}_3)_2\text{-Cu}^+$ (desorbed)        | -345       | -176       |
| $(\text{NH}_3)_3\text{-Cu}^+$ (desorbed)        | -416       | -175       |

**Table B.1:** Reaction energies without entropic contributions ( $\Delta E$ ) and with entropic contributions ( $\Delta G$ ) of copper complexes in kJ/mol, with respect to “clean” copper adsorbed on the zeolite. Reaction energies were calculated using the periodic model with PBE-D3.

| Molecule/structure | D1 Diagnostics (T1 cluster model) <sup>†</sup> |
|--------------------|--|
| H <sub>2</sub> O   | 0.0140   |
| N <sub>2</sub>     | 0.0273   |
| NH <sub>3</sub>    | 0.0124   |
| NO                 | 0.1182   |
| NO <sub>2</sub>    | 0.0729   |
| O <sub>2</sub>     | 0.0434   |
| 1                  | 0.0788   |
| 1 $\beta$          | 0.0768   |
| 1a                 | 0.0643   |
| 1b                 | 0.2352   |
| 1c                 | 0.3085   |
| 1e                 | 0.2664   |
| <sup>1</sup> 1f    | 0.3029   |
| <sup>3</sup> 1f    | 0.2268   |
| 1g                 | 0.2182   |
| 2                  | 0.1079   |
| 3                  | 0.0821   |
| 3a                 | 0.0651   |
| 3b                 | 0.1361   |
| 3c                 | 0.1875   |
| 3d                 | 0.0631   |
| 3e                 | 0.0554   |
| 3f                 | 0.0561   |
| 4                  | 0.0624   |
| 5                  | 0.1853   |
| 6                  | 0.1174   |
| 7                  | 0.1158   |
| 9                  | 0.2383   |
| 10                 | 0.0868   |
| 11                 | 0.0919   |
| TS.1c-1e           | 0.2914   |
| TS.1e-1 $\beta$    | 0.2713   |
| TS.3b-3c           | 0.1820   |
| TS.3e-3f           | 0.0596   |
| TS.5-6             | 0.1510   |
| TS.6-7             | 0.1309   |
| TS.7-9             | 0.2210   |
| TS.9-10            | 0.2805   |

**Table B.2:** D1 diagnostics for molecules depicted in Schemes 4.1 and 4.2, using the T1 cluster model (active site only). In catalysts with transition metals, structures with values above 0.15 are considered to have multi-reference character. [181] Labels are defined in Schemes 4.1 and 4.2. 1 $\alpha$ , 1d and 8 do not exist in the T1 cluster model, however diagnostics of TS.7-9 from T1 model are related with TS.8-9 from PBC model as this corresponds to a molecular dissociation barrier. <sup>†</sup> D1 diagnostics on CCSD that are based on the largest single excitation amplitudes.

| Structure        | $\Delta E$ of Perturbative Triples (T) |
|------------------|--|
| 1                | 12                                     |
| 2                | 0                                      |
| 3                | 16                                     |
| 4                | 15                                     |
| 5                | -5                                     |
| 6                | -7                                     |
| 7                | -3                                     |
| 8                | -1                                     |
| 9                | -47                                    |
| 10               | -1                                     |
| 11               | 4                                      |
| 1 <sub>end</sub> | 23                                     |
| TS_3-4           | 16                                     |
| TS_5-6           | -11                                    |
| TS_6-7           | -19                                    |
| TS_7-8           | -2                                     |
| TS_8-9           | -23                                    |
| TS_9-10          | -54                                    |

**Table B.3:** Contribution of perturbative triples (DLPNO-CCSD(T) – DLPNO-CCSD) for reaction energies and barriers (in kJ/mol) depicted in Scheme 4.1, for the T46 cluster model. Cu-NH<sub>3</sub> is assumed to be the resting state ( $\Delta E = 0$ ), and 1<sub>end</sub> is  $\Delta E$  of  $\text{NH}_3 + \text{NO} + \text{NO}_2 - \text{HNO}_2 \rightarrow \text{H}_2\text{O} + \text{N}_2$ .

## Appendix C

# Synthesis of Oxymethylene Dimethyl Ethers using H-BEA

### C.1 Gas phase free energy diagrams

The reaction takes place in solution in conditions under which all species (except FA) are themselves liquid in their pure substances. Figure C.1 a) shows a unsolvated free energy profile for the reaction using PBE-D3 and standard states of  $p = 1$  bar. The free energy profile is completely different from that discussed in the main text for solvation. This is not surprising since the empty zeolite used in the calculation represents an unstable species and the diagram from Figure C.1 a) essentially predicts that all molecules will condensate in the zeolite. The obtained diagram in Figure C.1 a) mainly depicts the magnitude of this condensation energy and has not much to do with the actual reaction profile in solution. Using PBE to obtain gas-phase free energies gives the profile shown in Figure C.1 b). This profile agrees much better with the one in solution (Figure 5.4). This is due to error cancellation: Both the vdW interaction with the solvent and within the solute is entirely neglected since GGAs such as PBE do not describe vdW interactions at all.

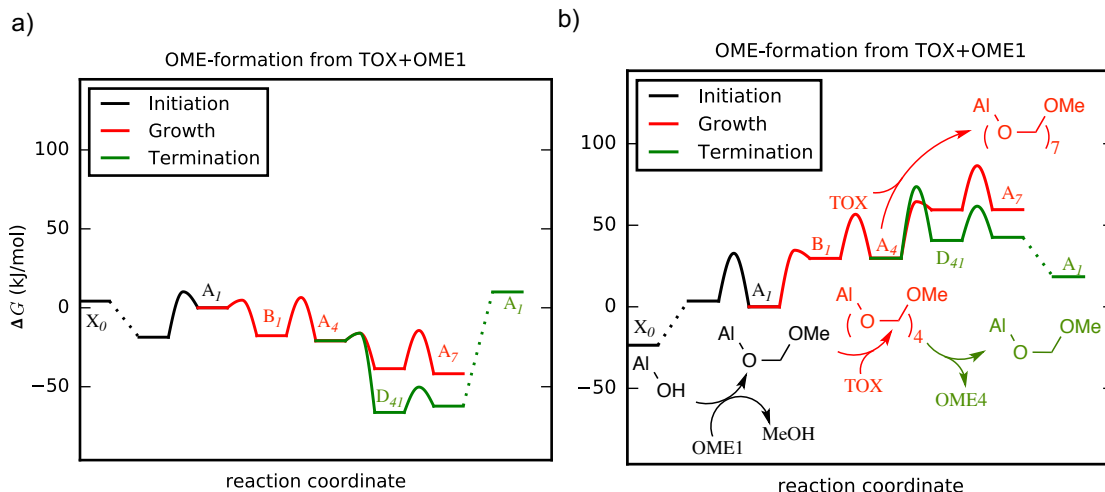


**Figure C.1:** Gas phase free energy diagram using a) PBE-D3 and b) PBE functionals at  $T = 300$  K.

## C.2 Tables and Figures

| Al | O    | X0 | Al-OMe | A1 | TS A1-B1 | TS A1-A2 |
|----|------|----|--------|----|----------|----------|
| T1 | O1   | 0  | 0      | 0  | 13       | 11       |
| T1 | O1 * | 3  | —      | 5  | 0        | 0        |
| T1 | O2   | 3  | -4     | -2 | 18       | 0        |
| T1 | O3   | 0  | 0      | 21 | 16       | 28       |
| T2 | O1   | -3 | -13    | -2 | 10       | -6       |
| T2 | O2   | 4  | —      | —  | —        | —        |
| T3 | O1   | 12 | 3      | 7  | 24       | 3        |
| T3 | O2   | 12 | 13     | 45 | 36       | 47       |
| T3 | O3   | 9  | -7     | 4  | 20       | 9        |

**Table C.1:** Relative energies in kJ/mol obtained with PBE for different substitution of Si with Al. The position of Al is explained in Figure 5.1, different isomers arising from the choice of adjacent oxygen positions have been included. O1 \* refers to a different conformer for the same isomer of O1.

| $n_c$ | Molecule | $H_{\text{solv}}(\text{s})$ | $H_{\text{solv}}(\text{exp.})$ | $H_{\text{solv}}(\text{l})$ |
|-------|----------|-----------------------------|--------------------------------|-----------------------------|
| 1     | FA       | -28                         | -20                            | -33                         |
| 1     | MeOH     | -25(-61*)                   | -43                            | -43                         |
| 2     | DME      | -27                         | -19                            | -28                         |
| 3     | TOX      | -38                         | -43                            | -35                         |
| 3     | OME1     | -38                         | -29                            | -43                         |
| 4     | OME2     | -55                         | -40                            | —                           |
| 5     | OME3     | -64                         | -48                            | —                           |
| 6     | OME4     | -80                         | -58                            | -66                         |
| 7     | OME5     | -87                         | -67                            | —                           |

**Table C.2:** Computed solvation energies of molecules with  $n_c$  carbons in kJ/mol.  $H_{\text{solv}}(\text{s})$  refers to structures containing only one molecule per unit cell which closely resembles a molecular crystal. Since methanol cannot form hydrogen bonds in this minimal unit cell, a larger unit cell containing two methanol molecules has also been considered. This leads to a significant stabilization (labeled with \*).  $H_{\text{solv}}(\text{l})$  refers to structures where the molecule is solvated in a large number of OME1 molecules that have been initially placed in random orientation and therefore closely resembles a solution. The experimental values of methanol and DME are obtained from NIST Standard Reference Database Number 69. [252]

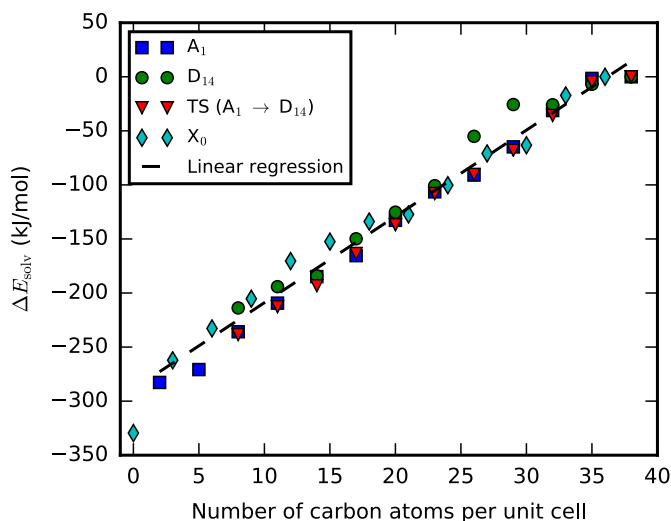


**Figure C.2:** Solvation energy of zeolites with adsorbates as a function of the number of carbon atoms of the adsorbate. Hydrogen-bond formation in  $X_0$  is included. The notations  $A_n$ ,  $D_{nm}$  and  $X_n$  correspond to the labels defined in Scheme 5.4.

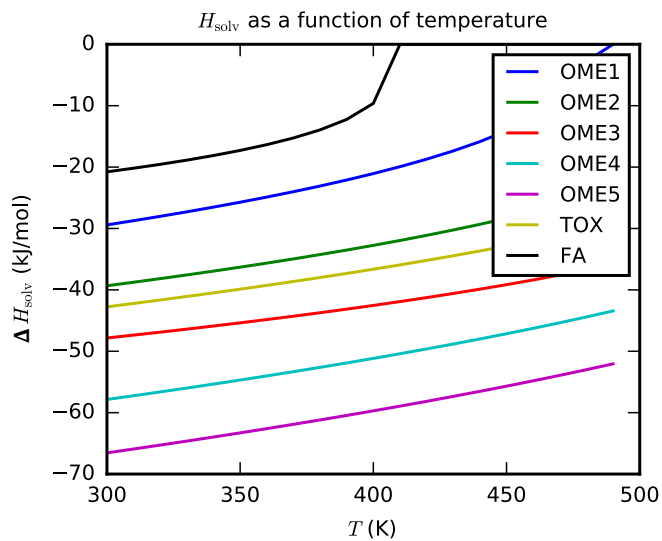


**Figure C.3:** Solvation enthalpy, interpolation data taken from ref [215]. Discontinuities occur for FA and OME1 beyond their boiling points but are not relevant for this work ( $T \approx 300$  K).

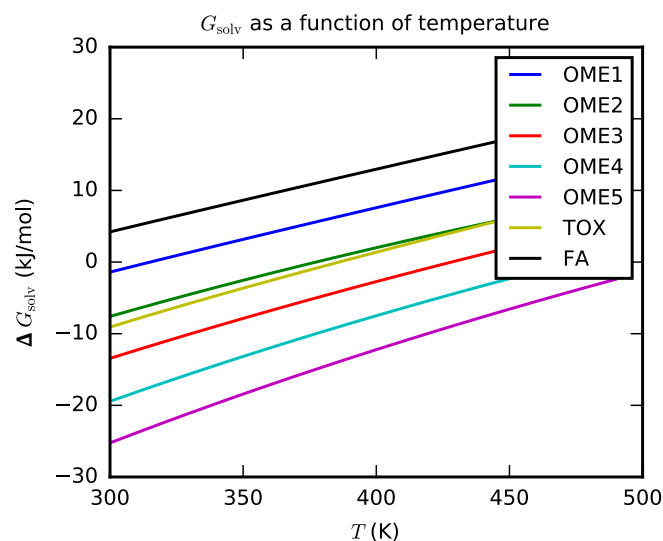


**Figure C.4:** Solvation free energy, interpolation data taken from ref [215]. Discontinuities occur for FA and OME1 beyond their boiling points but are not relevant for this work ( $T \approx 300$  K).

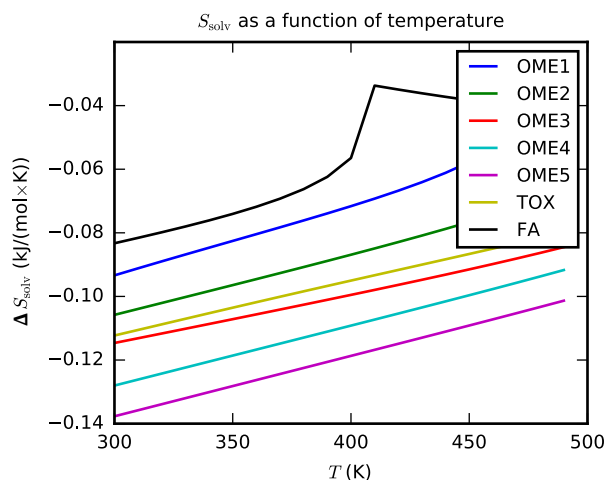


**Figure C.5:** Solvation entropy, interpolation data taken from ref [215]. Discontinuities occur for FA and OME1 beyond their boiling points but are not relevant for this work ( $T \approx 300$  K).

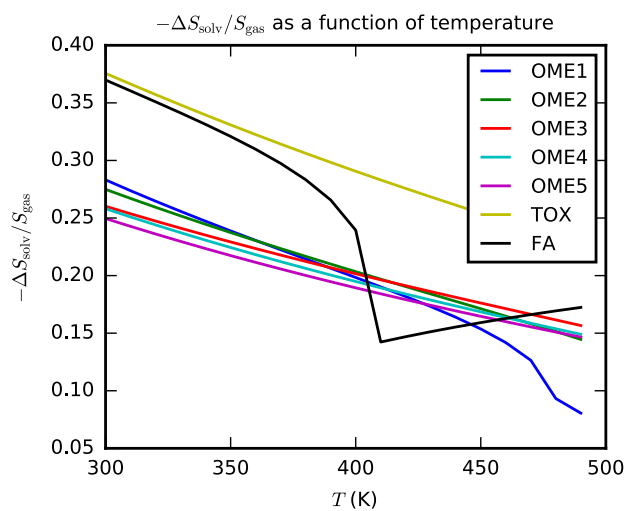


**Figure C.6:** Ratio of solvation entropy to gas phase entropy (computed based on the rigid-rotator, harmonic oscillator approximation). Interpolation data taken from ref [215]. Discontinuities occur for FA and OME1 beyond their boiling points but are not relevant for this work ( $T \approx 300$  K).

| Molecule                               | $E$      | ZPVE | $\Delta G_{\text{solv}}$ | $\Delta G_{\text{harm}}$ |
|--|----------|------|--------------------------|--------------------------|
| X2                                     | -1579.21 | 2.37 | -2.85                    | -0.15                    |
| TOX                                    | -68.43   | 2.61 | -0.41                    | -0.45                    |
| TS_X0-A1                               | -1603.01 | 3.59 | -2.77                    | -0.29                    |
| FA                                     | -22.15   | 0.71 | -0.34                    | -0.36                    |
| TS_X1-X0                               | -1555.99 | 1.38 | -2.93                    | -0.08                    |
| Al-O <sup>-</sup> +OME1-H <sup>+</sup> | -1603.40 | 3.68 | -2.77                    | -0.25                    |
| TS_A4-D41                              | -1711.49 | 7.83 | -2.35                    | -0.54                    |
| D41                                    | -1711.91 | 7.89 | -2.35                    | -0.54                    |
| TS_A1-D11                              | -1642.37 | 5.21 | -2.60                    | -0.37                    |
| X0                                     | -1533.24 | 0.61 | -3.01                    | -0.04                    |
| A4                                     | -1641.55 | 4.86 | -2.60                    | -0.29                    |
| B1                                     | -1641.53 | 4.86 | -2.60                    | -0.31                    |
| A4+OME1                                | -1711.73 | 7.87 | -2.35                    | -0.55                    |
| TS_A1-B1                               | -1641.49 | 4.83 | -2.60                    | -0.32                    |
| methanol                               | -30.24   | 1.36 | -0.43                    | -0.38                    |
| A1+OME4                                | -1711.86 | 7.88 | -2.35                    | -0.53                    |
| TS_A1-D41                              | -1711.71 | 7.85 | -2.35                    | -0.54                    |
| TS_X2-X1                               | -1578.66 | 2.17 | -2.85                    | -0.22                    |
| A4+TOX                                 | -1641.60 | 4.85 | -2.60                    | -0.32                    |
| TS_X0-X3                               | -1601.79 | 3.22 | -2.77                    | -0.21                    |
| X1                                     | -1556.25 | 1.38 | -2.93                    | -0.09                    |
| TS_B1-A4                               | -1641.23 | 4.82 | -2.60                    | -0.31                    |
| A1                                     | -1572.44 | 2.23 | -2.85                    | -0.14                    |
| OME1                                   | -69.40   | 2.99 | -0.41                    | -0.57                    |
| A1+OME1                                | -1642.54 | 5.29 | -2.60                    | -0.31                    |
| OME5                                   | -161.12  | 6.51 | -0.93                    | -0.83                    |
| OME4                                   | -138.20  | 5.62 | -0.80                    | -0.78                    |
| TS_A1-A2                               | -1594.83 | 2.93 | -2.77                    | -0.27                    |
| X3                                     | -1602.23 | 3.25 | -2.77                    | -0.22                    |
| A2                                     | -1595.49 | 3.10 | -2.77                    | -0.21                    |
| TS_X3-X2                               | -1601.75 | 3.06 | -2.77                    | -0.28                    |
| Al-OMe                                 | -1549.26 | 1.37 | -2.93                    | -0.08                    |

**Table C.3:** Contribution to the total free energies in eV. Total energy PBE-D3//PBE, ZPVE (PBE), solvation free energy, harmonic correction to free energy (PBE), excluding ZPVE.

## Appendix D

# OME Synthesis through Homogeneous Acid Catalysis

### D.1 Accuracy of DFT

The PBE-D3, PBE0-D3 and M06-2X hybrid functionals were compared with second order Møller-Plesset perturbation theory (MP2) to investigate reaction energies and transition states for OME synthesis. All calculations were performed as single-point energy calculations with the def2-TZVPP basis-set using geometries optimized with PBE0-D3/dhf-SV(P).

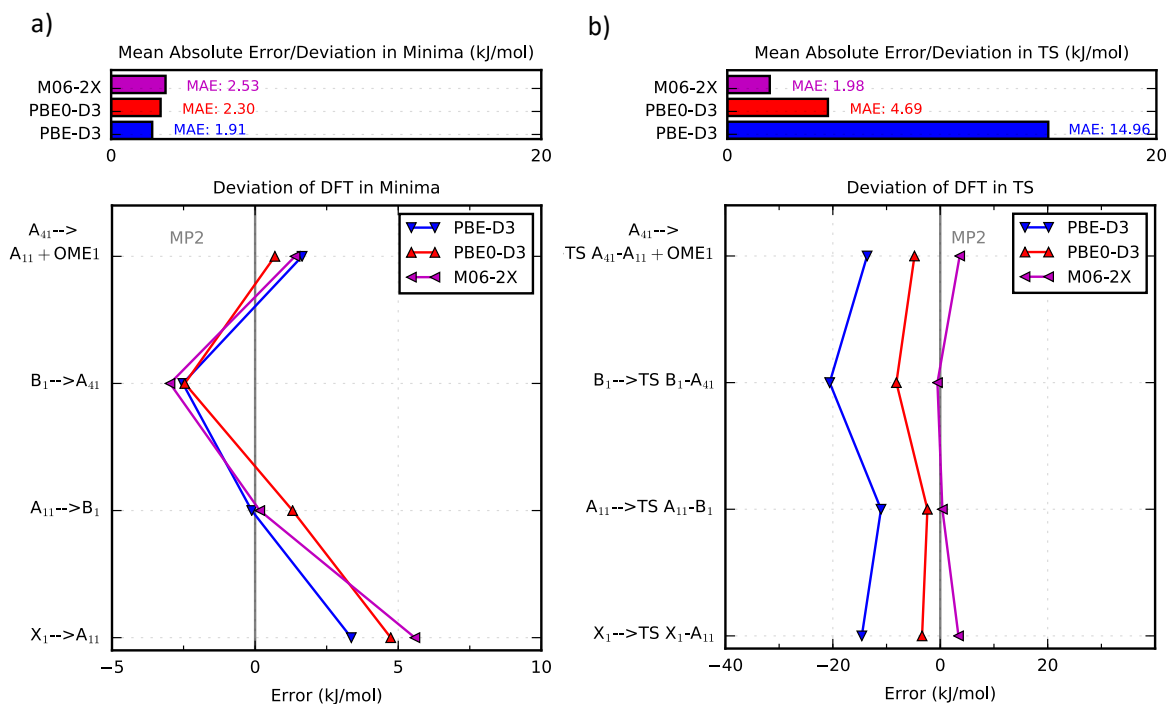


**Figure D.1:** Deviation of the PBE-D3 GGA DFT functional and PBE0-D3, M06-2X hybrid functionals with respect to MP2, with calculated MAE values in kJ/mol both for a) Reaction energies and b) Barriers.

As Figures D.1 a) and b) indicate, minima are usually well described using PBE-D3, PBE0-D3 and M06-2X functionals for the OME synthesis, having both a mean absolute deviation and mean absolute error lower than 5 kJ/mol. Transition states are, however, systematically underestimated by around 15 kJ/mol using the PBE-D3 functional (MAE  $\sim$  15 kJ/mol). M06-2X agrees well with MP2, with a mean absolute error of around 2 kJ/mol. To have an accurate description of the transition states in this work, MP2 was used in single-point energy calculations.

## D.2 Solvent corrections

### D.2.1 Calculation of Protonation Energies with Solvation

The protonation of OME1 is the first step in initiation of the catalytic formation of OME<sub>n</sub> (Scheme 6.1). Different acids, such as the H-BEA and HCl, were explored with the assumption that its corresponding base does not exert significant influence in the OME synthesis. The transfer of a proton from BEA into OME1, which is now distant from the active site, is around 70 kJ/mol uphill in energy, as shown in Figure D.2.

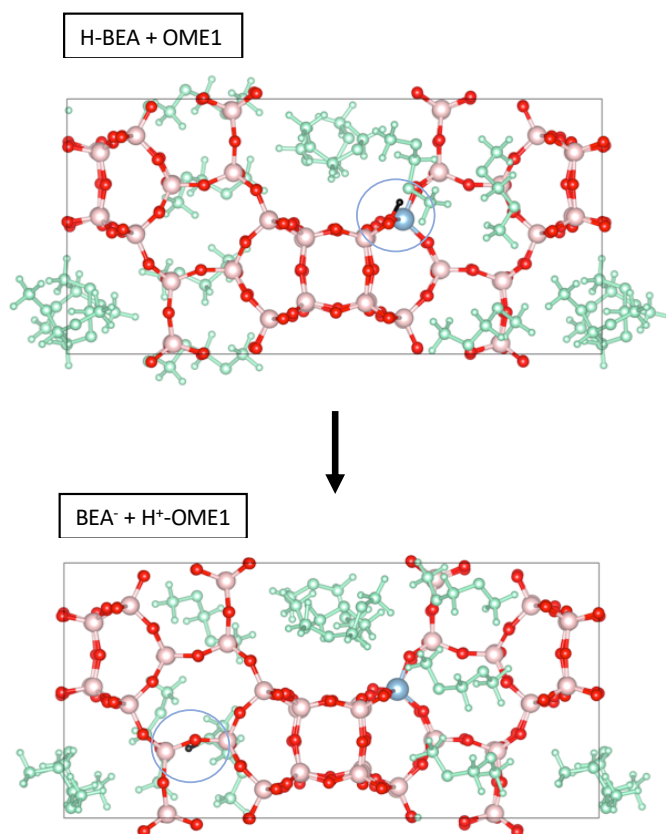


**Figure D.2:** OME protonation with H-BEA in periodic boundary conditions. Color scheme: H – Black; O – Red; Si – Pink; Al – Gray; OME – Green.

The fully solvated HCl in 11 OME1 molecules is also considered and shown in Figure D.3. The protonation of OME1 under these conditions is 90 kJ/mol uphill in energy, which means that in this case, the zeolite is a stronger acid when compared to hydrochloric acid by 20 kJ/mol. However, the protonation reaction from HCl, using one explicit solvent OME1 molecule in addition to the

implicit solvation model described in Section D.2.2, results in a reaction free energy that is 170 kJ/mol uphill. Reaction energies between these two different approaches (explicit solvation with PBC and mixed implicit and explicit solvation) do not agree very well, having an energy difference of close to 80 kJ/mol. The reason for this difference may be due to entropic correction not being considered in the explicit solvation case, however it already provides a crude estimate of how acid HCl is. These protonation energies are shown in the Gibbs free energy profile from Figure 6.2.

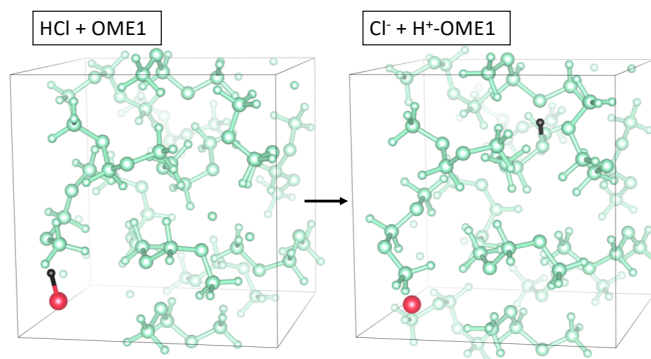


**Figure D.3:** OME protonation with HCl in periodic boundary conditions. Color scheme: H – Black; Cl – Red; OME – Green.

## D.2.2 Solvent parameterizations in the SMD model

With different molecules in solution, it is difficult to find descriptors, that simulate the interaction of the whole solvent mixture with the solute accurately. The solvent database for the SMD model [108] implemented in GAMESS quantum chemistry package is limited to 179 molecules, in which the best descriptors found were the ones from the Diethyl Ether solvent, as its descriptors (depicted in Table D.1) are most identical to molecules in liquid phase that are present during OME synthesis. The descriptors are defined in Table D.2. A comparison of the reaction energies for the formation of OME4 from OME1+TOX using different solvent descriptors was also performed (Figure D.4), since MeOH and the remaining "ether-like" molecules have slightly different properties, as observed in Table D.1.

| Molecule             | $n$   | $n_{25}$ | $\alpha, \beta$ | $\gamma$ | $\epsilon$ | $\phi$ | $\psi$ |
|----------------------|-------|----------|-----------------|----------|------------|--------|--------|
| <b>Diethyl Ether</b> | 1.353 | 1.350    | 0.00, 0.45      | 24.0     | 4.24       | 0.0    | 0.0    |
| <b>OME1</b>          | 1.353 | 1.348    | 0.00, 0.53      | 21.3     | 2.70       | 0.0    | 0.0    |
| <b>FA</b>            | 1.377 | —        | —               | 27.4     | —          | 0.0    | 0.0    |
| <b>TOX</b>           | 1.385 | —        | 0.00, —         | 35.3     | 15.55      | 0.0    | 0.0    |
| <b>MeOH</b>          | 1.329 | 1.327    | 0.40, 0.47      | 31.8     | 32.61      | 0.0    | 0.0    |

**Table D.1:** Descriptors for the molecules present in the solvent. [245–247] Diethyl ether and methanol are 2 out of the 179 molecules that can be found in the solvent database for the SMD model.

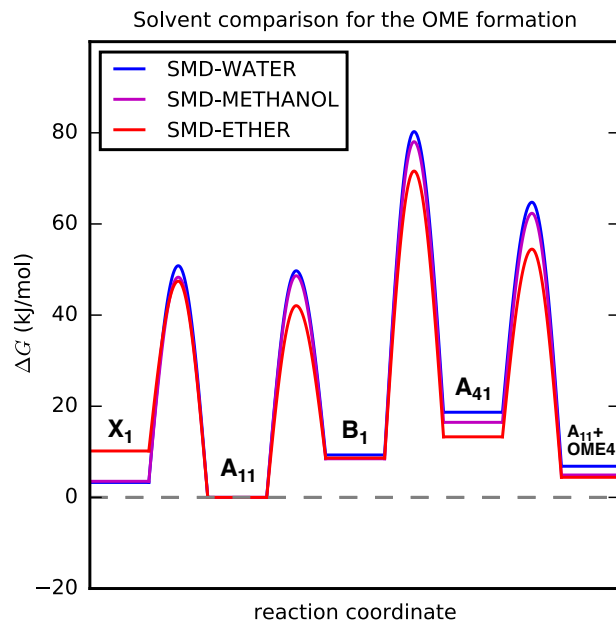


**Figure D.4:** Free energy diagram at  $T = 300$  K, using MP2 with the def2-TZVPP basis-set, for the catalytic conversion of OME4 through OME1+TOX, using diethyl ether, water or methanol as solvent. This diagram and the corresponding labels are based on Scheme 6.1.

While the overall reaction free energies are similar, larger differences are found for the reaction barriers and in the stability of  $X_1$  and  $A_{41}$  when compared to the resting state  $A_{11}$ . Here, water and methanol behave similarly, while results with diethyl ether differ on the order of 10 kJ/mol, which still does not exert any significant influence in our results.

### D.3 Tables and Figures

|            |   |
|------------|---|
| n          | Index of refraction at optical frequencies at 293 K, This is sometimes called $n_{20}^D$ .  |
| $\alpha$   | Abraham's hydrogen bond acidity. In particular, in Abraham's notation this is called $\sum \alpha_2^H$ .  |
| $\beta$    | Abraham's hydrogen bond basicity. In particular, in Abraham's notation this is called $\sum \beta_2^H$ .  |
| $\gamma$   | $\gamma = \gamma_m / \gamma^0$ , where $\gamma_m$ is macroscopic surface tension at liquid-air interface at 298 K, and $\gamma^0$ is $1 \text{ cal mol}^{-1} \text{ \AA}^{-2}$ . Conversion factor: $1 \text{ dyne/cm} = 1.43932 \text{ cal mol}^{-1} \text{ \AA}^{-2}$ . |
| $\epsilon$ | Dielectric constant at 298 K. Note that dielectric constant is also called relative permittivity.   |
| $\phi$     | Aromaticity: fraction of non-hydrogenic solvent atoms that are aromatic carbon atoms.   |
| $\psi$     | Electronegative halogenicity: fraction of non-hydrogenic solvent atoms that are F, Cl, or Br.   |
| $n_{25}$   | Index of refraction at optical frequencies at 298 K, This is sometimes called $n_{25}^D$ .  |

**Table D.2:** Descriptors for solvent molecules in the universal model based on density (SMD).

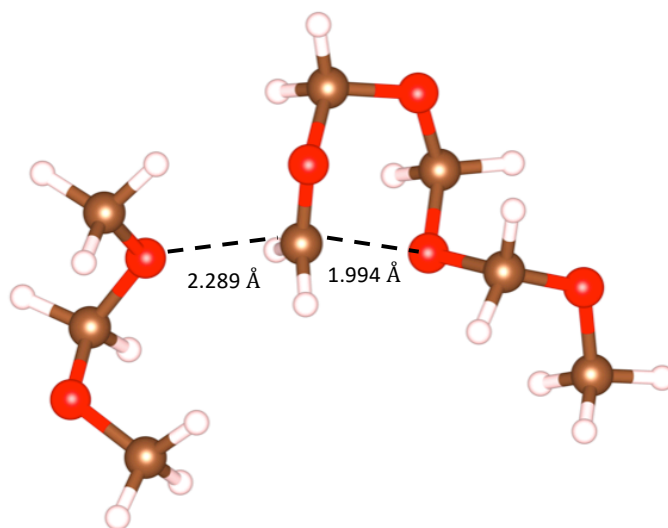


**Figure D.5:** 3D representation of the TOX ring-opening transition state ( $B_1 \rightarrow A_{41}$ ) from the direct TOX incorporation pathway with  $A_{11}$  as the catalytic species (Figure 6.2). Color scheme : H – White; O – Red; C – Brown.

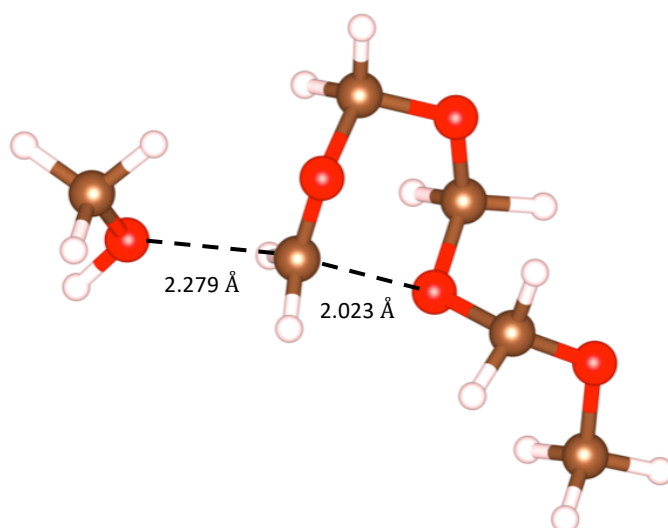


**Figure D.6:** 3D representation of the TOX ring-opening transition state ( $B_1 \rightarrow X_4$ ) from the direct TOX incorporation pathway with protonated OME1 ( $X_1$ ) as the catalytic species (Figure 6.3). Color scheme : H – White; O – Red; C – Brown.

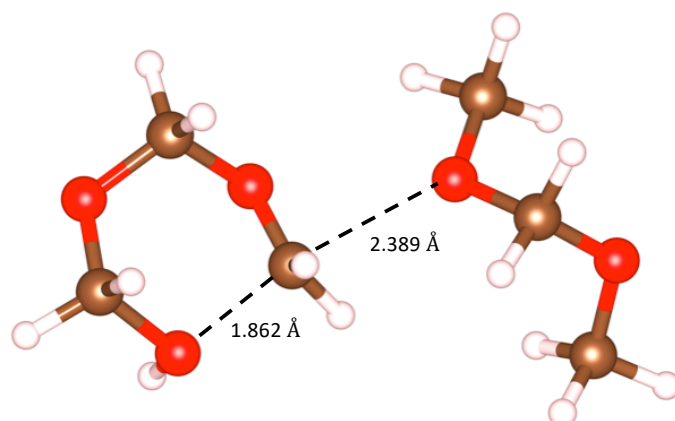


**Figure D.7:** 3D representation of the TOX ring-opening transition state ( $\text{H-TOX} + \text{OME1} \rightarrow \text{H-A}_{31}$ ) from the chain growth pathway via TOX decomposition to FA and subsequent sequential FA incorporation (Figure 6.4 c). Color scheme : H – White; O – Red; C – Brown.

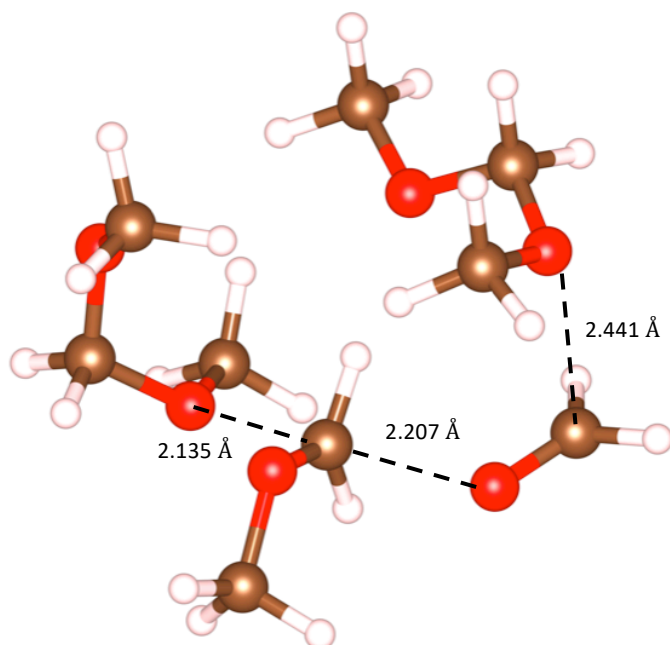


**Figure D.8:** 3D representation of the FA-incorporation transition state ( $\text{A}_{11} + 3\text{FA} \rightarrow \text{A}_{21} + 2\text{FA}$ ) from the chain growth pathway via TOX decomposition to FA and subsequent sequential FA incorporation (Figure 6.4 c). Color scheme : H – White; O – Red; C – Brown.

| Molecule   | Relative $\Delta G$ |
|--|---------------------|
| X <sub>1</sub>                                   | 10.18               |
| A <sub>11</sub>                                  | 0.00                |
| TS A <sub>11</sub> - B <sub>1</sub>              | 42.07               |
| B <sub>1</sub>                                   | 8.64                |
| TS B <sub>1</sub> - A <sub>41</sub>              | 71.61               |
| A <sub>41</sub>                                  | 13.29               |
| TS A <sub>41</sub> - A <sub>11</sub> +OME4       | 54.48               |
| A <sub>11</sub> +OME4                            | 4.41                |
| Trimethyloxonium                                 | -29.65              |
| H-BEA  | -61.35              |
| HCl implicit TM (reference to X <sub>1</sub> )   | -156.44             |
| HCl explicit VASP (reference to X <sub>1</sub> ) | -72.69              |

**Table D.3:** Relative Gibbs free energies of the TOX pathway (Figure 6.2) using MP2/def2-TZVPP in kJ/mol

| Molecule                            | Relative $\Delta G$ |
|-------------------------------------|---------------------|
| A <sub>11</sub>                     | 0.00                |
| TS A <sub>11</sub> - X <sub>1</sub> | 47.44               |
| X <sub>1</sub>                      | 10.18               |
| TS X <sub>1</sub> - B <sub>1</sub>  | 40.39               |
| B <sub>1</sub>                      | 8.64                |
| TS B <sub>1</sub> - X <sub>4</sub>  | 67.55               |
| X <sub>4</sub>                      | 20.89               |
| X <sub>1</sub> + OME4               | 14.59               |

**Table D.4:** Relative Gibbs free energies of the MeOH pathway (Figure 6.3) using MP2/def2-TZVPP in kJ/mol

| Molecule  | Relative $\Delta G$ |
|---|---------------------|
| A <sub>11</sub> +TOX                              | 0.00                |
| TS A <sub>11</sub> +TOX - X <sub>1</sub> +TOX     | 47.44               |
| X <sub>1</sub> +TOX                               | 10.18               |
| H-TOX+OME1  | 41.15               |
| TS H-TOX+OME1 - H-A <sub>31</sub>                 | 67.86               |
| H-A <sub>31</sub>                                 | 11.37               |
| TS H-A <sub>31</sub> - H-A <sub>21</sub> +FA      | 93.44               |
| H-A <sub>21</sub> +FA                             | 8.34                |
| TS H-A <sub>21</sub> +FA - H-A <sub>11</sub> +2FA | 109.77              |
| H-A <sub>11</sub> +2FA                            | 21.58               |
| TS H-A <sub>11</sub> +2FA - X <sub>1</sub> +3FA   | 67.41               |
| X <sub>1</sub> +3FA                               | 41.1                |
| TS X <sub>1</sub> +3FA - A <sub>11</sub> +3FA     | 78.34               |
| A <sub>11</sub> +3FA                              | 30.90               |

**Table D.5:** Relative Gibbs free energies of TOX decomposition (Figure 6.4 c) using MP2/def2-TZVPP in kJ/mol

| <b>Molecule</b>                                | <b>Relative <math>\Delta G</math></b> |
|--|---------------------------------------|
| A <sub>11</sub> +3FA                           | 30.90                                 |
| TS A <sub>11</sub> +3FA - A <sub>21</sub> +2FA | 109.34                                |
| A <sub>21</sub> +2FA                           | 29.67                                 |
| TS A <sub>21</sub> +2FA - A <sub>31</sub> +FA  | 109.40                                |
| A <sub>31</sub> +FA                            | 18.82                                 |
| TS A <sub>31</sub> +FA - A <sub>41</sub>       | 100.14                                |
| A <sub>41</sub>                                | 13.29                                 |

**Table D.6:** Relative Gibbs free energies of formaldehyde insertion (Figure 6.4 c) using MP2/def2-TZVPP in kJ/mol

| Molecule                     | Total Energies |             |             |             | $\Delta G_{\text{PBE0}}^{\text{1bar harm}}$ | $\Delta G_{\text{M06,SMD-ETHER}}^{\text{1bar solv} \rightarrow \text{1mol/l}}$ |
|------------------------------|----------------|-------------|-------------|-------------|---|--|
|                              | PBE-D3         | MP2         | PBE0-D3     | M06-2X      |   |  |
| TS_OME4+H-A4+OME1            | -2316636.85    | -2314305.58 | -2316752.61 | -2318341.45 | 734.54                                      | -154.14  |
| tetroxane                    | -1201879.79    | -1200725.96 | -1201923.27 | -1202765.50 | 268.73                                      | -14.23   |
| pentoxane                    | -1502349.73    | -1500902.96 | -1502401.13 | -1503451.28 | 347.24                                      | -19.29   |
| TS_B1-A4+OME1                | -2012983.90    | -2010950.52 | -2013080.12 | -2014468.85 | 622.77                                      | -155.10  |
| TS_A1+OME1-tetroxane_CH2OCH3 | -2313450.68    | -2311125.71 | -2313559.39 | -2315159.80 | 701.22                                      | -163.22  |
| TS_A4+OME1-A3+OME1           | -3321193.89    | -3317875.56 | -3321367.41 | -3323668.38 | 1062.01                                     | -141.34  |
| TS_A3OH+OME1-A2OH+OME1       | -2316608.61    | -2314269.47 | -2316708.88 | -2318297.47 | 728.05                                      | -149.24  |
| TS_A2+OME1-A3+OME1           | -2419698.05    | -2417223.56 | -2419818.17 | -2421481.63 | 805.82                                      | -134.22  |
| A2+OME1                      | -1412057.82    | -1410620.69 | -1412145.89 | -1413123.88 | 471.69                                      | -156.40  |
| TS_A2+OME1-A3                | -1712483.63    | -1710732.39 | -1712557.54 | -1713736.65 | 524.93                                      | -150.83  |
| OME5                         | -1909059.99    | -1907188.26 | -1909153.25 | -1910484.30 | 530.18                                      | -19.96   |
| TS_H.DME-CH3_TOX             | -1308907.22    | -1307595.89 | -1308967.44 | -1309860.19 | 403.92                                      | -166.36  |
| TS_A3+OME1-A1+OME1           | -2419729.03    | -2417267.37 | -2419867.20 | -2421535.96 | 814.17                                      | -145.56  |
| TS_A1OH+OME1-OME1+H          | -1008457.30    | -1007433.80 | -1008505.38 | -1009193.55 | 319.07                                      | -165.98  |
| TS_CH3.DME-CH3_TOX           | -1411990.91    | -1410546.20 | -1412070.14 | -1413041.19 | 473.74                                      | -158.07  |
| A1+OME1                      | -1111571.38    | -1110421.43 | -1111648.40 | -1112414.17 | 391.39                                      | -164.43  |
| TS_OME1+CH3-A1+OME1          | -1518270.88    | -1516673.18 | -1518376.12 | -1519413.99 | 575.15                                      | -147.32  |
| FA                           | -300410.11     | -300121.28  | -300408.17  | -300618.62  | 12.97                                       | -1.38  |
| A3                           | -1005281.04    | -1004264.34 | -1005319.13 | -1006016.68 | 266.96                                      | -173.13  |
| A5+OME1                      | -2313523.64    | -2311221.42 | -2313643.69 | -2315250.19 | 718.91                                      | -149.03  |
| TS_A3+OME1-A2+OME1           | -2720216.72    | -2717472.93 | -2720368.10 | -2722249.13 | 896.27                                      | -142.84  |
| TS_CH3_TOX-CH3_OME3          | -1412013.02    | -1410559.60 | -1412091.02 | -1413061.70 | 468.18                                      | -157.36  |
| TS_TOX_CH3.opening           | -1712491.68    | -1710748.30 | -1712579.52 | -1713760.11 | 545.42                                      | -161.34  |
| TS_A4+OME1-A2+OME1           | -3020712.84    | -3017685.91 | -3020877.81 | -3022972.53 | 986.72                                      | -139.91  |
| 2OME+H                       | -1415181.14    | -1413733.98 | -1415278.20 | -1416247.97 | 509.17                                      | -169.66  |
| A4+OME1                      | -2013027.11    | -2011011.79 | -2013135.67 | -2014532.56 | 627.85                                      | -157.23  |
| A3+OME1                      | -1712545.27    | -1710818.40 | -1712642.62 | -1713828.27 | 551.69                                      | -159.24  |
| TS_CH3_OME3-OME3+CH3.DME     | -1818709.55    | -1816831.71 | -1818827.35 | -1820079.87 | 666.73                                      | -150.62  |
| DME+H                        | -407482.59     | -407056.63  | -407528.82  | -407802.36  | 175.19                                      | -197.90  |
| MeOH                         | -303593.34     | -303300.30  | -303613.28  | -303815.73  | 74.00                                       | -3.35  |
| OME3+CH3                     | -1412052.71    | -1410619.19 | -1412142.77 | -1413122.33 | 474.29                                      | -161.96  |
| OME2                         | -1007633.28    | -1006625.76 | -1007693.50 | -1008393.43 | 297.62                                      | -6.65  |
| DME+CH3                      | -510585.88     | -510030.15  | -510651.88  | -511005.37  | 242.74                                      | -183.01  |
| A1OH+OME1                    | -1008493.20    | -1007483.11 | -1008552.36 | -1009244.61 | 326.94                                      | -170.37  |
| TS_A1+OME1-A2+OME1           | -2119210.74    | -2117029.38 | -2119323.32 | -2120780.12 | 725.33                                      | -138.28  |
| A2OH+OME1                    | -1308989.55    | -1307688.21 | -1309058.01 | -1309956.67 | 403.55                                      | -164.81  |
| A3OH+OME1                    | -1609474.98    | -1607882.70 | -1609553.62 | -1610662.32 | 486.86                                      | -160.29  |
| OME3                         | -1308114.78    | -1306819.54 | -1308185.92 | -1309096.11 | 375.91                                      | -10.04   |
| TS_A4+OME1-pentoxane_CH3     | -2313458.54    | -2311126.10 | -2313551.44 | -2315150.44 | 692.01                                      | -147.15  |
| tetroxane_CH2OCH3            | -1606308.15    | -1604724.58 | -1606378.75 | -1607498.85 | 442.05                                      | -163.09  |
| A5                           | -1606239.53    | -1604643.09 | -1606295.21 | -1607411.21 | 418.41                                      | -168.07  |
| TS_DME+CH3-OME1+CH3          | -1217733.59    | -1216429.93 | -1217829.29 | -1218660.77 | 503.99                                      | -155.48  |
| TS_ome1h+tox-meoh+prottox    | -1609451.15    | -1607850.99 | -1609522.47 | -1610627.28 | 475.71                                      | -151.84  |
| A1+TOX                       | -1305807.27    | -1304512.12 | -1305865.49 | -1306772.40 | 362.09                                      | -167.95  |
| TOX+H                        | -902202.80     | -901329.61  | -902234.42  | -902854.07  | 216.54                                      | -196.69  |
| A1                           | -404276.30     | -403846.94  | -404300.62  | -404580.62  | 119.60                                      | -201.17  |
| TS_CH3_OME3-OME3+H.DME       | -1715624.88    | -1713880.73 | -1715724.21 | -1716898.53 | 597.95                                      | -157.36  |
| OME1+H                       | -707987.31     | -707260.28  | -708036.10  | -708515.18  | 247.45                                      | -184.51  |
| A2                           | -704787.01     | -704054.72  | -704809.24  | -705293.09  | 185.25                                      | -178.87  |
| trioxane_CH3                 | -1005307.11    | -1004305.66 | -1005359.63 | -1006058.42 | 284.64                                      | -182.92  |
| TS_A4+OME1-A1+OME1           | -2720217.38    | -2717469.12 | -2720366.67 | -2722245.12 | 896.47                                      | -143.93  |
| DME                          | -406668.48     | -406236.65  | -406707.16  | -406986.19  | 146.23                                      | 0.67   |
| TS_A5+OME1-A1+OME1           | -3020691.82    | -3017659.68 | -3020854.99 | -3022948.48 | 980.27                                      | -142.38  |
| TS_A3+OME1-A4+OME1           | -2720181.10    | -2717420.53 | -2720312.30 | -2722187.11 | 883.96                                      | -134.35  |
| D14                          | -2013022.11    | -2011006.77 | -2013131.20 | -2014528.31 | 624.56                                      | -160.71  |
| TS_pentoxane_CH3.opening     | -2313505.42    | -2311183.74 | -2313613.61 | -2315213.91 | 713.03                                      | -146.90  |
| tetroxane_CH3                | -1305825.75    | -1304537.49 | -1305889.88 | -1306802.84 | 366.39                                      | -167.86  |
| OME1+CH3                     | -811086.07     | -810230.85  | -811155.69  | -811714.45  | 317.07                                      | -171.13  |
| TS_A2+OME1-A1+OME1           | -2119246.26    | -2117075.09 | -2119374.93 | -2120834.90 | 737.16                                      | -143.01  |
| B1                           | -1305814.96    | -1304521.48 | -1305874.06 | -1306780.44 | 361.09                                      | -168.82  |
| TS_Tetroxane_CH3.opening     | -2013014.71    | -2010984.77 | -2013113.55 | -2014506.34 | 626.71                                      | -150.25  |
| TS_A2OH+OME1-A1OH+OME1       | -2016111.71    | -2014061.19 | -2016203.89 | -2017582.61 | 653.32                                      | -156.77  |
| A4                           | -1305764.56    | -1304448.77 | -1305802.45 | -1306703.86 | 333.53                                      | -167.78  |
| TS_A1+OME1-B1                | -2013007.33    | -2010983.61 | -2013108.75 | -2014501.18 | 624.86                                      | -153.64  |
| TS_A3+OME1-tetroxane_CH3     | -2012976.50    | -2010935.25 | -2013059.22 | -2014449.85 | 608.65                                      | -146.65  |
| OME4+H                       | -1609446.44    | -1607850.30 | -1609524.05 | -1610632.01 | 479.87                                      | -176.19  |
| TS_2OME1+H-A1+OME1+MeOH      | -1415189.55    | -1413728.59 | -1415276.66 | -1416238.95 | 506.05                                      | -154.14  |
| TS_B1-OME4+H                 | -1609427.84    | -1607821.07 | -1609495.47 | -1610598.68 | 477.60                                      | -156.48  |
| OME1                         | -707151.69     | -706432.37  | -707201.23  | -707691.21  | 218.99                                      | -3.22  |
| TS_TOX+H+OME1-A3OH+OME1      | -1609413.25    | -1607808.57 | -1609484.41 | -1610589.94 | 477.50                                      | -168.57  |
| pentoxane_CH3                | -1606312.71    | -1604731.75 | -1606386.19 | -1607508.83 | 448.55                                      | -161.00  |
| TS_DME.H-DME-CH3             | -814173.03     | -813294.10  | -814240.09  | -814783.72  | 359.22                                      | -164.22  |
| FA+OME1                      | -1007580.40    | -1006570.28 | -1007627.02 | -1008328.71 | 276.84                                      | -9.54  |
| TS_tetroxane_CH2OCH3.opening | -2313464.86    | -2311147.16 | -2313576.05 | -2315181.95 | 704.30                                      | -154.01  |
| OME4                         | -1608596.17    | -1607013.12 | -1608678.21 | -1609798.60 | 454.29                                      | -133.35  |
| TS_DME+CH3-A1+OME1           | -1518188.36    | -1516581.53 | -1518277.41 | -1519312.79 | 567.52                                      | -149.33  |
| TOX                          | -901406.35     | -900543.62  | -901439.39  | -902068.84  | 194.14                                      | -10.50   |

**Table D.7:** Contribution to the total free energies in kJ/mol. Electronic energies are calculated using DFT and MP2 with the def2-TZVPP basis-set, harmonic contribution with the zero-point vibrational energy is included at 1 bar of reference state ( $\Delta G_{\text{harm}}^{\text{1bar}}$ ) using the dhf-SV(P) basis-set and solvent corrections are included using diethyl ether as solvent at a reference pressure of 1 bar and a reference concentration of 1 mol/l and using the cc-pVTZ Dunning's basis-set.

| Molecule                     | $\Delta G_{\text{sol}}^{\text{(1bar} \rightarrow \text{1mol/l)}} \text{ (M06/cc-PVTZ SMD)}$ |         |          |
|------------------------------|---|---------|----------|
|                              | ETHER   | WATER   | METHANOL |
| TS_OME4+H-A4+OME1            | -154.14   | -166.31 | -187.57  |
| tetroxane                    | -14.23  | -10.79  | -13.31   |
| pentoxane                    | -19.29  | -16.32  | -19.41   |
| TS_B1-A4+OME1                | -155.10   | -168.36 | -182.67  |
| TS_A1+OME1-tetroxane-CH2OCH3 | -163.22   | -179.49 | -193.51  |
| TS_A4+OME1-A3+OME1           | -141.34   | -138.41 | -160.67  |
| TS_A3OH+OME1-A2OH+OME1       | -149.24   | -159.54 | -179.58  |
| TS_A2+OME1-A3+OME1           | -134.22   | -134.72 | -155.44  |
| A2+OME1                      | -156.40   | -175.69 | -187.86  |
| TS_A2+OME1-A3                | -150.83   | -165.85 | -179.74  |
| OME5                         | -19.96  | -5.82   | -16.11   |
| TS_H_DME-CH3_TOX             | -166.36   | -196.02 | -204.51  |
| TS_A3+OME1-A1+OME1           | -145.56   | -151.80 | -171.71  |
| TS_A1OH+OME1-OME1+H          | -165.98   | -197.90 | -206.27  |
| TS_CH3_DME-CH3_TOX           | -158.07   | -179.20 | -189.28  |
| A1+OME1                      | -164.43   | -189.12 | -200.62  |
| TS_OME1+CH3-A1+OME1          | -147.32   | -159.87 | -179.70  |
| FA                           | -1.38   | 3.81    | 2.64     |
| A3                           | -173.13   | -211.33 | -215.94  |
| A5+OME1                      | -149.03   | -160.46 | -174.39  |
| TS_A3+OME1-A2+OME1           | -142.84   | -141.25 | -164.14  |
| TS_CH3_TOX-CH3_OME3          | -157.36   | -176.82 | -189.49  |
| TS_TOX_CH3_opening           | -161.34   | -179.87 | -192.72  |
| TS_A4+OME1-A2+OME1           | -139.91   | -139.16 | -160.58  |
| 2OME+H                       | -169.66   | -196.40 | -212.34  |
| A4+OME1                      | -157.23   | -173.76 | -188.07  |
| A3+OME1                      | -159.24   | -177.78 | -191.71  |
| TS_CH3_OME3-OME3+CH3_DME     | -150.62   | -161.46 | -179.20  |
| DME+H                        | -197.90   | -251.54 | -257.82  |
| MeOH                         | -3.35   | -4.48   | -8.37    |
| OME3+CH3                     | -161.96   | -186.19 | -197.82  |
| OME2                         | -6.65   | 4.60    | -3.72    |
| DME+CH3                      | -183.01   | -221.38 | -229.41  |
| A1OH+OME1                    | -170.37   | -205.69 | -214.35  |
| TS_A1+OME1-A2+OME1           | -138.28   | -143.13 | -163.13  |
| A2OH+OME1                    | -164.81   | -195.48 | -205.56  |
| A3OH+OME1                    | -160.29   | -185.10 | -195.39  |
| OME3                         | -10.04  | 3.05    | -6.07    |
| TS_A4+OME1-pentoxane-CH3     | -147.15   | -155.35 | -170.54  |
| tetroxane-CH2OCH3            | -163.09   | -189.37 | -196.86  |
| A5                           | -168.07   | -195.98 | -203.55  |
| TS_DME+CH3-OME1+CH3          | -155.48   | -173.38 | -189.16  |
| TS_ome1h+tox-meoh+prottox    | -151.84   | -174.47 | -186.23  |
| A1+TOX                       | -167.95   | -199.28 | -204.76  |
| TOX+H                        | -196.69   | -255.48 | -257.40  |
| A1                           | -201.17   | -257.02 | -258.99  |
| TS_CH3_OME3-OME3+H_DME       | -157.36   | -177.82 | -194.30  |
| OME1+H                       | -184.51   | -226.73 | -234.47  |
| A2                           | -178.87   | -219.99 | -223.97  |
| trioxane-CH3                 | -182.92   | -220.58 | -224.35  |
| TS_A4+OME1-A1+OME1           | -143.93   | -146.06 | -167.99  |
| DME                          | 0.67  | 8.62    | 1.76     |
| TS_A5+OME1-A1+OME1           | -142.38   | -140.12 | -163.64  |
| TS_A3+OME1-A4+OME1           | -134.35   | -126.48 | -150.16  |
| D14                          | -160.71   | -175.94 | -190.41  |
| TS_pentoxane-CH3_opening     | -146.90   | -157.78 | -173.47  |
| tetroxane-CH3                | -167.86   | -199.87 | -205.81  |
| OME1+CH3                     | -171.13   | -201.42 | -211.50  |
| TS_A2+OME1-A1+OME1           | -143.01   | -149.29 | -169.08  |
| B1                           | -168.82   | -199.58 | -205.10  |
| TS_Tetroxane-CH3_opening     | -150.25   | -163.13 | -177.49  |
| TS_A2OH+OME1-A1OH+OME1       | -156.77   | -174.72 | -191.21  |
| A4                           | -167.78   | -197.48 | -204.18  |
| TS_A1+OME1-B1                | -153.64   | -167.90 | -181.08  |
| TS_A3+OME1-tetroxane-CH3     | -146.65   | -157.36 | -172.17  |
| OME4+H                       | -176.19   | -210.66 | -222.51  |
| TS_2OME1+H-A1+OME1+MeOH      | -154.14   | -176.56 | -194.47  |
| TS_B1-OME4+H                 | -156.48   | -180.54 | -192.80  |
| OME1                         | -3.22   | 6.28    | -1.13    |
| TS_TOX+H+OME1-A3OH+OME1      | -168.57   | -201.42 | -211.92  |
| pentoxane-CH3                | -161.00   | -188.78 | -196.06  |
| TS_DME-H-DME-CH3             | -164.22   | -193.34 | -206.98  |
| FA+OME1                      | -9.54   | 3.51    | -5.06    |
| TS_tetroxane-CH2OCH3_opening | -154.01   | -160.83 | -176.36  |
| OME4                         | -13.35  | 1.34    | -8.58    |
| TS_DME+CH3-A1+OME1           | -149.33   | -162.13 | -179.70  |
| TOX                          | -10.50  | -7.74   | -8.33    |

**Table D.8:** Contribution of different solvents to the Gibbs free energy in kJ/mol at 1 mol/l, using the implicit Solvent Model based on Density (SMD) implemented in GAMESS-US.

# Acknowledgments

First of all, I would like to acknowledge my two supervisors, Prof. Dr. Felix Studt and Dr. Philipp Plessow, not only for giving the opportunity to work with them, but also for being my mentors and role models as researchers throughout these years. Without them, none of this work would be possible.

I would like to thank my colleagues at work for all the great time spent together and enlightening discussions.

I would like to thank the Helmholtz association for the financial support and the state of Baden-Württemberg through bwHPC (bwunicluster and JUSTUS, RV bw17D011).

I would like to thank my friends from Germany and Portugal for the emotional support and great times.

Specifically, I would like to thank Mário Marques for being an amazing friend and a great person. Please never change. And also Jao Lope for being a great positive influence in my life.

Furthermore, I would like to thank my family. Specially my mother and brother for always being there for me.

And most importantly, I would like to thank my beloved soon to be wife. Ana, I love you.



# Acronyms

|         |   |
|---------|---|
| ASE     | Atomic Simulation Environment                         |
| AO      | Atomic Orbital  |
| ARPESS  | Automated Relaxed Potential Energy Surface Scan       |
| B3LYP   | Becke, 3-parameter, Lee-Yang-Parr hybrid functional   |
| BEA     | Beta Zeolite  |
| BEEF    | Bayesian Error Estimation Functional                  |
| CBS     | Complete Basis-Set                                    |
| CCSD    | Coupled Cluster Single and Double                     |
| CCSD(T) | Coupled Cluster Single-Double and perturbative Triple |
| CHA     | Chabazite   |
| DLPNO   | Domain-based Local Pair Natural Orbital               |
| DME     | Dimethyl Ether  |
| DFT     | Density Functional Theory                             |
| FA      | Formaldehyde  |
| GTO     | Gaussian-Type Orbitals                                |
| GGA     | Generalized Gradient Approximation                    |
| HF      | Hartree-Fock  |
| HK      | Hohenberg-Kohn  |
| HTST    | Harmonic Transition State Theory                      |
| IKFT    | Institute of Catalysis Research and Technology        |
| KIT     | Karlsruhe Institute of Technology                     |
| KS      | Kohn-Sham   |
| LCAO    | Linear Combination of Atomic Orbitals                 |
| LDA     | Local Density Approximation                           |
| LPNO    | Local Pair Natural Orbitals                           |
| M06     | Minnesota 2006 hybrid functional                      |
| MAE     | Mean Absolute Error                                   |
| MO      | Molecular Orbital                                     |
| MP2     | Second order Møller-Plesset perturbation theory       |
| MTO     | Methanol to Olefins                                   |
| MSE     | Mean Signed Error                                     |
| NEB     | Nudged Elastic Band                                   |
| OME     | Oxymethylene Dimethyl Ether                           |
| PAO     | Projected Atomic Orbitals                             |

|       |  |
|-------|--|
| PAW   | Projector Augmented Wave                   |
| PBC   | Periodic Boundary Conditions               |
| PBE   | Perdew-Burke-Ernzerhof functional          |
| PCM   | Polarized Continuum Model                  |
| PES   | Potential Energy Surface                   |
| PNO   | Pair Natural Orbitals                      |
| POME  | Polyoxymethylene Dimethyl Ether            |
| PP    | Pseudo-Potential                           |
| QMC   | Quantum Monte Carlo                        |
| QRO   | Quasi-Restricted Orbitals                  |
| RHF   | Restricted Hartree-Fock                    |
| ROHF  | Restricted Open-Shell Hartree-Fock         |
| SCF   | Self-Consistent Field                      |
| SCR   | Selective Catalytic Reduction              |
| STO   | Slater-Type Orbitals                       |
| SMD   | Universal Solvation Model Based on Density |
| SP    | Single-Point                               |
| TM    | TURBOMOLE                                  |
| TOX   | Trioxane                                   |
| TS    | Transition State                           |
| TST   | Transition State Theory                    |
| UHF   | Unrestricted Hartree-Fock                  |
| VASP  | Vienna Ab initio Simulation Package        |
| vdW   | Van der Waals                              |
| WF    | Wave-Function                              |
| XC    | Exchange and Correlation                   |
| ZSM-5 | Zeolite Socony Mobil-5                     |
| ZPE   | Zero-point Energy                          |

# List of Publications

- [1] T. J. Goncalves, P. N. Plessow, and F. Studt. “On the accuracy of density functional theory in zeolite catalysis.” *ChemCatChem*, 11(17):4368–4376, **2019**.

The results from this publication are presented in Chapter 3; reproduced with permission.

- [2] T. J. Goncalves, P. N. Plessow, and F. Studt. “A Theoretical Study of the Selective Catalytic Reduction of Nitrogen Oxides by Ammonia using Cu-SSZ-13.” *In preparation*.

The results from this publication are presented in Chapter 4.

- [3] T. J. Goncalves, U. Arnold, P. N. Plessow, and F. Studt. Theoretical investigation of the acid catalyzed formation of oxymethylene dimethyl ethers from trioxane and dimethoxymethane. *ACS Catal.*, 7(5):3615–3621, **2017**.

The results from this publication are presented in Chapter 5; reproduced with permission.

- [4] T. J. Goncalves, Philipp N Plessow, and Felix Studt. A computational investigation of ome-synthesis through homogeneous acid catalysis. *ChemCatChem*, 11(7):1949–1954, **2019**.

The results from this publication are presented in Chapter 6; reproduced with permission.



# Eidesstattliche Erklärung

Hiermit versichere ich eidesstattlich, dass ich die vorgelegte Dissertation selbständig angefertigt habe und keine anderen als die angegebenen Quellen und Hilfsmittel benutzt habe. Die wörtlichen oder inhaltlich übernommenen Stellen wurden als solche kenntlich gemacht. Weiterhin habe ich die Satzung des Karlsruher Instituts für Technologie (KIT) zur Sicherung guter wissenschaftlicher Praxis in der gültigen Fassung beachtet und die Primärdaten gemäß Abs.A (6) gesichert. Die elektronische Version der Arbeit stimmt mit der schriftlichen überein. Die Arbeit wurde in gleicher oder anderer Form keiner anderen Prüfungsbehörde zur Erlangung eines akademischen Grades vorgelegt.

Karlsruhe, den 24.04.2020

